
**An investigation of traveling ionospheric
disturbances (TIDs) in the SANAE HF
radar data**

Tsige Yared Atilaw

A thesis submitted in fulfilment of the requirements for the degree of
Doctor of Philosophy
in the Department of Physics and Electronics
Rhodes University
Makhanda, South Africa, 2021

Abstract

This thesis aims to study the characteristics of traveling ionospheric disturbances (TIDs) as identified in the radar data of the South African National Antarctic Expedition (SANAE) Super Dual Auroral Radar Network (SuperDARN) radar located in Antarctica. For this project, 22 TIDs were identified from visual inspection of range time-intensity (RTI) plots of backscattered power and Doppler velocity parameters of the SANAE radar between 2005–2015. These events were studied to determine their characteristics and driving mechanisms. Where good quality data were available, the SANAE HF radar data were supplemented by Halley radar data, which has large area of overlapping field of view (FOV) with the SANAE radar, and also by GPS TEC data. This provided a multi-instrument data analysis of some TID events.

Different spectral analysis methods, namely the multitaper method (MTM), Fast Fourier transform (FFT) and the Lomb-Scargle periodogram were used to obtain spectral information of the observed waves. The advantage of using multiple windowing in MTM over the traditional windowing method was illustrated using one of the TID events. In addition, the analytic signal of the wave from the MTM method was used to estimate the instantaneous phase velocity and propagation azimuth of the wave, which was able to track the change in the characteristics of the medium-scale TID (MSTID) efficiently throughout the duration of the event. This is a clear advantage over other windowing techniques. The energy contribution by this MSTID through Joule heating was estimated over the region where spectral analysis of both SANAE and Halley data showed it to be present.

The majority of the TIDs (65.4%) could be classified as MSTIDs with periods of 20–60 minutes, velocities of 50–333 ms^{-1} and wavelengths of 129–833 km. The TID occurrence rate was high around the March equinox with 12 out of the 16 event days being during March–May. March had a particularly high number of occurrences of TIDs (46%). The majority of the TIDs observed during this month propagated northward or southeastward. In terms of prevailing geomagnetic conditions, 6 out of 16 event days were geomagnetically quiet, while 10 occurred during geomagnetic storms and substorms. During quiet conditions, TIDs could be linked to Es and polarised electric fields in 2 of these events. The other quiet time events could not be related to Es instability and polarised electric field either because their exact propagation direction could not be determined or data quality from the Es region

scatter was too poor to perform spectral analysis. The storm-/substorm-related TIDs are possibly generated through Joule heating, the Lorentz force and energetic particle precipitation.

Publication from this thesis

- Atilaw, T.Y., Stephenson, J.A. & Katamzi-Joseph, Z.T. (2021). Multitaper analysis of an MSTID event above Antarctica on 17 March 2013. *Polar Science*, 28, 100643. <https://doi.org/10.1016/j.polar.2021.100643>

Acknowledgement

I would like to express my sincere appreciation and thanks to my supervisors, Dr Zama T. Katamzi-Joseph and Dr Judy A.E. Stephenson, for their continuous support and mentorship throughout my study.

I am thankful to OWSD (Organization for Women in Science for the Development World) and Sida (Swedish International Development Cooperator Agency) for the PhD fellowship. I am also grateful for the financial supports I received from Rhodes University and SANAP (South African National Antarctic Program) to attend national conferences during my study. I wish to express my sincere thanks to SANSA (South African National Space Agency) Space Science Directorate for providing me with all the necessary facilities for my research and for creating a positive environment during my study.

I take this opportunity to express my gratitude to all my colleagues who helped me in different ways throughout my PhD study. I would like to thank Mrs Jeanne Cilliers for proofreading my work and for giving me a lot of helpful feedback.

Special thanks to the members of my lovely family who are always in my thoughts. Your prayers have strengthened me throughout these years. Thank you for all the support, encouragement and attention. My heartfelt gratitude goes to my late father Yared Atilaw, who always reminded me I could do better.

Above all, I would like to thank the one and only almighty God for His everlasting love and blessing.

Contents

1	Introduction	1
1.1	Introduction to Space Weather	1
1.2	Thesis Background and Motivation	2
1.3	Thesis Objective	3
1.4	Thesis Outline	4
2	Theoretical Background	6
2.1	Introduction	6
2.2	Ionosphere	7
2.3	Atmospheric Gravity Waves	10
2.3.1	Dispersion relation equation for gravity waves	11
2.3.2	Propagation of AGWs	13
2.3.3	Common Sources of AGWs	14
2.4	Traveling Ionospheric Disturbances (TIDs)	15
2.4.1	Large-scale TIDs	15
2.4.2	Medium-scale TIDs	17
2.5	Neutral Wind	21
2.6	Joule heating	22
2.7	Magnetic storms and substorms	23

2.8	Summary	24
3	Instrumentation and Models	25
3.1	Introduction	25
3.2	SuperDARN HF radar network	25
3.2.1	SANAE and Halley HF radars	30
3.3	Global Positioning System	33
3.3.1	GPS use in ionospheric studies	34
3.3.2	TEC measurement derived from GPS	36
3.4	Defense Meteorological Satellite Program (DMSP)	37
3.5	Magnetometer	38
3.5.1	Geomagnetic indices	38
3.6	International Geomagnetic Reference Field (IGRF)	40
3.7	Horizontal wind model (HWM14)	40
3.8	Summary	41
4	Data Analysis Methods	43
4.1	Identifying TIDs from radar data	44
4.2	FFT and CSD	46
4.3	Lomb-Scargle analysis	51
4.4	Multitaper analysis	52
4.5	Analytic signals	56
4.6	GPS TEC	58
4.6.1	Detrending VTEC	61
4.7	Summary	61

5	Multitaper analysis of an MSTID event above Antarctica on 17 March 2013	63
5.1	Introduction	63
5.2	Results and discussion	64
5.2.1	Characteristics of the MSTID	64
5.2.2	Estimation of energy dissipation by MSTID	72
5.2.3	Source mechanism	75
5.3	Summary	80
6	GPS data analysis of TID events	81
6.1	Introduction	81
6.2	Results and discussion	83
6.2.1	15 July 2012 event	83
6.2.2	17 March 2013 event	87
6.2.3	6 April 2015 event	89
6.3	Summary	92
7	Survey of TID events as observed in SANA E HF radar data and their associated source mechanism	94
7.1	Introduction	94
7.2	Results and discussion	97
7.2.1	Characteristics of TIDs	97
7.2.2	Dependence of the occurrence of TIDs on seasonal and geomagnetic activity	100
7.2.3	Source Mechanisms	101
7.3	Summary	111
8	Conclusion and future work	112

8.1 Summary and conclusion	112
8.2 Future work	115

List of Figures

2.1	Layers of Earth’s atmosphere and the ionosphere electron density variation representing a typical mid-latitude ionosphere during the day (solid line) and night (broken line) (Kelley and Heelis, 1989).	8
2.2	Propagation modes of AGWs (Mayr <i>et al.</i> , 1990)	14
2.3	Schematic illustration of the coupling between E and F region both in northern and southern hemisphere (Narayanan <i>et al.</i> , 2018).	21
3.1	Applications of SuperDARN (Nishitani <i>et al.</i> , 2019).	26
3.2	Field of view plot of the SuperDARN network in the north and south hemispheres (credit: http://vt.superdarn.org/tiki-list_file_gallery.php?galleryId=81)	27
3.3	Schematic illustration of the different paths backscatter signals will follow for 0.5 hop, 1 hop, 1.5 hop and 2 hop backscatters. The diagram is based on ray paths shown in the ray tracing model (http://vt.superdarn.org/tiki-index.php?page=Ray-tracing).	28
3.4	The raw ACF data and the fitted data for the 17 March 2013 TID event at 02:02:49 UT from SANAE radar beam 7, gate number 20. The data was plotted with the VT SuperDARN ACF plotting and fitting tool (http://vt.superdarn.org/tiki-index.php?page=ACF+Plotting+Tools).	29
3.5	Field of view of the SANAE and Halley HF radars in magnetic coordinate.	31
3.6	Photographs of the SANAE radar (a) log-periodic antennas, and (b) twin-terminated folded-dipole antennas, as well as (c) a full view of the SANAE IV base.	32
3.7	The main segments of GPS: ground-control segment, space segment and user segment (El-Rabbany, 2002).	34

3.8	Components of Earth's magnetic field.	39
4.1	RTI plots of backscattered power (top panel), Doppler velocity (middle panel) and spectral width (bottom panel) of the SANA E (left) and Halley (right) radar data for 17 March 2013.	45
4.2	Plots showing the geographic location of the three cells used for the spectral analysis (a) and the time series (in blue) and the interpolated data (in red) for cells bm=9 & G=21 (b), bm=11 & G=23 (c) and bm=14 & G=21 (d).	48
4.3	Plots of the time series data as used in Figure 4.2 after subtracting the mean (in black) and windowed data using the Hanning window method (in red) for cells bm=9 & G=21 (a), bm=11 & G=23 (b and bm=14 & G=21 (c)	49
4.4	Plots of (a) FFT of the time series data shown in Figure 4.3, (b) CSD for each pair of time series and (c) the respective phases derived from the CSD analysis for the 17 March 2013 event using Halley radar data.	50
4.5	The event of 15 July 2012 from beam 0 of the SANA E radar, (a) RTI plot of the backscatter power and Doppler velocity with overlying lines used to calculate the slope and (b) the Lomb-Scargle periodogram for gates 39 to 48.	52
4.6	The three tapers from the SSA-MTM toolkit that were used to analyse the 17 March 2013 event.	54
4.7	Reconstructed data using the SSA-MTM toolkit (in black) and applying a Hanning window on the reconstructed signal (in red) for cells (a) bm=8 & G=20, (b) bm=12 & G=20 and (c) bm=10 & G=24. Data is from SANA E radar FOV for the 17 March 2013 TID event.	55
4.8	Hilbert transform of the reconstructed signals with the envelope (red lines) for cell 1 identified by bm=8 & G=20 (top panel), cell 2 identified by bm=12 & G=20 (middle panel) and cell 3 identified by bm=10 & G=24 (bottom panel) for the 17 March 2013 TID event. The grey shade marks the time interval when the amplitude of all three SANA E HF radar cells are large.	57
4.9	The instantaneous frequency for the respective cells where the instantaneous amplitudes are shown in Figure 4.8. The grey shade marks the same time interval as in Figure 4.8	57
4.10	Geometry of STEC to VTEC mapping (adapted from Hofmann-Wellenhof <i>et al.</i> (1992))	58

4.11	VTEC and elevation angle versus time plots for PRN (a) 1 and (b) 32 as observed by GPS receiver located at Amundsen-Scott South Pole, Antarctica, on 15 July 2012.	60
4.12	These plots show the GPS data processing steps in the study of TIDs. (a) and (b) VTEC (in black) and 15-minute running mean (in red), (c) and (d) dVTEC (in black) and windowed data using Hanning window (in red), and (e) and (f) FFT of the windowed data for PRN 1 and 32, respectively, as observed from Amundsen-Scott South Pole, Antarctica, on 15 July 2012.	62
5.1	Range gate versus time plots of power backscatter (top panel), Doppler velocity (middle panel) and spectral width (bottom panel) from the SANAE (left) and Halley (right) radars on 17 March 2013.	65
5.2	Field of view scan plots using geographic coordinates, of the backscattered power for the time period 04:26-04:42 UT plotted in Geographical coordinates. The solid black lines on the figure are used to indicate the wavefronts of the MSTIDs at different timestamps.	66
5.3	The three cells used for cross-spectral analysis from SANAE and Halley are shown in blue and red stars respectively, and the field of view of the respective radars are indicated by the blue and red lines. The beam number and range gate of each cell on the map can be found on the label (e.g., Cell1 bm=8; G=20, refers to beam number (bm) 8 and range gate (G) 20).	67
5.4	MTM spectrum of the time series data taken from 3 different cells, cell 1 (a), cell 2 (b) and cell 3 (c) where the red, blue, magenta and green horizontal lines represent the confidence levels of the median, 90 %, 95 %, 99 % respectively. The MTM spectrum of all three cells are plotted on a single graph (d) with the axis limited to a frequency range between 0.2 and 1.08 mHz.	68
5.5	Reconstructed signal at the central frequency of 0.78 mHz using the SSA-MTM toolkit. The original signals are plotted in black and the reconstructed signals are plotted in red for (a) cell 1 (bm=8; G=20), (b) cell 2 (bm=12; G=20), (c) cell 3 (bm=10; G=24) and (d) the three reconstructed signals on a single graph/plot.	69
5.6	The phase differences for each pair of reconstructed signals, derived from the instantaneous phase. The grey shade marks the same time interval as in Figure 4.8	70

5.7	RTI plot of the backscatter power from SANAE radar beam 10 on 17 March 2013 between 02:04 and 06:14 UT (top panel). Calculated phase velocity (2 nd panel), wavelength (3 rd panel) and azimuth angle (bottom panel) for the time interval are indicated by the grey shaded area in Figure 5.6.	71
5.8	FFT of the three cells taken from the Halley radar field of view: in blue cell 1 (beam number 9 and range gate 21), in red, cell 2 (beam number 14 and range gate 21) and in green, cell 3 (beam number 11 and range gate 23).	72
5.9	The field of view of the SANAE and Halley radars together with the location of cells that observed TIDs with a frequency of 0.72 mHz with a confidence level of above 90%.	73
5.10	Joule heating (a) due to MSTID: the instantaneous amplitude of the Doppler velocity taken from cell with bm=8 & G=20 (top panel), estimation of energy dissipated per unit area by MSTID (Q _c + Q _{w1}) (middle panel) and the total Joule heating over the area where TID was observed ($636.43 \times 10^6 \text{ m}^2$) (last panel), (b) background: same Doppler velocity as cell in (a) (top panel), estimation of the background Joule heating per unit area (Q _c + Q _{w1} + Q _{w2}) (middle panel) and the total energy dissipation over the area where the MSTID was observed (last panel)	77
5.11	Geomagnetic conditions during 16 to 17 March 2013, (a) SW speed (1 st panel), Dst index (2 nd panel), AE index (3 rd panel) PC index for southern hemisphere (4 th panel) and Kp10 (5 th panel) (b) B _z in blue, B _y in red, B _x in magenta and B _T in black	78
5.12	Map potential for the time of the event based on the model by Thomas and Shepherd (2018) and produced by RST 4.3 software with FITACF V2.5 data. The total energy flux and the equatorward auroral oval boundary (red dot-dash) from POES are overlaid. Map produced by K. Sterne (Virginia Tech).	79
5.13	Ray tracing plot for SANAE radar beam 8 on 17 March 2013 at 04:00 UT. The pink lines indicate magnetic field lines. The black lines represent segments of computed ray paths where aspect condition is satisfied within 1°.	79
5.14	Lomb-Scargle periodogram of the backscattered power data from beam 12 and gate number 1 (blue), 2 (orange), 3 (green) and 4 (red).	80

6.1	VTEC versus IPP latitude and longitude of all GPS satellites observed from station AMU2 (a), CRDI (b), HOWE (c) and PECE (d) on 16 March 2013. Note that coordinates in brackets are geographic coordinates.	82
6.2	RTI plots of backscattered power data (top panel), Doppler velocity (middle panel) and spectral width (bottom panel) for the (a) SANAE and (b) Halley radars on 15 July 2012.	83
6.3	Lomb-Scargle periodogram of power measurements by (a) SANAE beam 2, range gates 41 to 45 and (b) Halley beam 14, range gates 28 to 35.	84
6.4	Hourly solar wind data (top panel), IMF B_y (2 nd panel), IMF B_z (3 rd), Dst (4 th panel), AE index (5 th panel), PCS index (6 th panel) and Kp10 index (last panel) from 14 to 18 July 2012. The vertical dash lines indicate the time period when the TIDs were observed by the SANAE radar.	85
6.5	TEC map for Antarctica plotted over backscatter power data from SANAE and Halley radars for 15 July 2012 at 15:00 UT. Plot taken from Virginia Tech SuperDARN website. Note that the map displays magnetic coordinates.	85
6.6	Plots showing (a) time series data of VTEC from different PRNs detected by AMU2 and HOWE GPS receiver stations on 15 July 2012, (b) detrended VTEC data, (c) ray path of each PRN with respect to the observation area of the HF radars and (d) FFT of detrended data.	86
6.7	TEC map for Antarctica plotted over backscatter power data from the SANAE and Halley radars for 17 March 2013 at 03:00 UT. Plot taken from Virginia Tech SuperDARN website. Note that map uses magnetic coordinates.	87
6.8	Plots showing (a) time series data of VTEC from different PRNs detected over AMU2, PECE and CRDI GPS receiver stations on 17 March 2013, (b) detrended VTEC data, (c) ray path of each PRN with respect to the locations where TIDs were observed by the HF radars and (d) the FFT of the detrended VTEC data.	88
6.9	RTI plots of backscattered power (top panel), Doppler velocity (middle panel) and spectral width (bottom panel) of data from SANAE radar on 6 April 2015.	89
6.10	FFT plot of backscatter power data from SANAE radar for the period between 01:00 and 06:00 UT on 6 April 2015.	90

6.11	Solar wind speed (1 st panel), total IMF magnitude (2 nd panel), IMF Bz (3 rd panel) and AE index (4 th panel) for the time period between 02 and 05 April 2015. The start of the HSSs/CIRs event is marked by the vertical red dash line. The vertical black dash line indicates the start and end of the TID event in the SANA E radar data.	90
6.12	TEC map for Antarctica plotted over backscatter power data from the SANA E and Halley radars for 6 April 2015 at 03:00 UT. Plot taken from Virginia Tech SuperDARN website. Note that the map uses magnetic coordinates.	91
6.13	Plot showing (a) time series data of VTEC from PRN 07, 09 and 30 that were detected by the PECE GPS receiver station on 6 April 2015, (b) detrended VTEC data, (c) FFT of the detrended data and (d) ray path of each PRN with respect to the locations where TIDs were observed in the HF radar data.	92
7.1	Number of sunspots for solar cycles 23 and 24 (credit: https://www.swpc.noaa.gov/products/solar-cycle-progression).	95
7.2	Histogram of (a) frequencies, (b) periods, (c) phase velocities and (d) wavelengths for all TIDs events observed between 2005 and 2015.	98
7.3	Polar plot which shows variation of period and azimuth with phase velocity. The circumference represents the propagation azimuth (with 0° corresponding to northward direction), phase velocity (in ms ⁻¹) is represented using the radial distance, and the period is indicated by the colour bar.	99
7.4	Polar plot showing the variation of (a) period and azimuth and (b) phase velocity and azimuth with day of the year (seasonal variation). Note that in this case the radii represent months and the colour bars indicate period and phase velocity of TIDs in (a) and (b) respectively. The size of the circles represent the period in (a) and phase velocity in (b).	101
7.5	Hourly data of solar wind (1 st panel), IMF By (2 nd panel), IMF Bz (3 rd), Dst (4 th panel), AE index (5 th panel), PC South index (6 th panel) and Kp10 index (last panel) for the events on (a) 4 March 2005, (b) 6 May 2005, (c) 7 May 2005, (d) 19 March 2007 and (e) 14 September 2007. The vertical dash lines indicate the starting and ending time of the TID events from the SANA E radar.	103
7.6	Frequency spectrum plots of the 19 March 2007 event (a) using FFT for gate numbers between 23 and 27 and (b) using Lomb-Scargle for gate numbers between 0 and 2.	104

7.7	Sketch of the propagation direction of the MSTIDs together with the neutral wind (\mathbf{U}) and field line-integrated current (\mathbf{J}) for the 17 Mar 2013 event. Sketch adapted from Otsuka <i>et al.</i> (2009).	104
7.8	RTI plots of backscatter power (top panel), Doppler velocity (middle panel) and spectral width (bottom panel) based on the SANAE radar data of 26 March 2010.	105
7.9	Hourly data of solar wind (1 st panel), IMF By (2 nd panel), IMF Bz (3 rd), Dst (4 th panel), AE index (5 th panel), PC South index (6 th panel) and Kp10 index (last panel) for 25 to 26 March 2010. The vertical dash lines indicate the time interval when the TIDs occurred as identified in the SANAE radar.	106
7.10	Auroral images produced by Syowa station in the southern hemisphere (a) at 19:53 on 25 March 2010 and (b) at 00:40 on 26 March 2010 (http://polaris.nipr.ac.jp/~protect/unhbox/voidb@x\penalty\@M\{}acaurora/syowa_CDC_QL/).	107
7.11	Precipitating particle flux data from DMSP satellites (a) F17 for 25 March 2010 and (b) F16 for 26 March 2010. 1 st panel Electron flux, 2 nd panel Ion flux, 3 rd panel Ni and N[O ⁺] density, 4 th panel vertical and horizontal ion drift velocity and 5 th panel magnetic field components (image taken from Boston college space weather data survey site https://dmsp.bc.edu/html2/index.html).	107
7.12	RTI plots of backscatter power (top panel), Doppler velocity (middle panel) and spectral width (bottom panel) from SANAE radar from 11 March 2012.	108
7.13	Hourly data of solar wind (1 st panel), IMF By (2 nd panel), IMF Bz (3 rd), Dst (4 th panel), AE index (5 th panel), PC South index (6 th panel) and Kp10 index (last panel) for 10 to 11 March 2012. The black dash lines indicate the time interval during which the TIDs observed in the SANAE radar data. The red line indicates the sudden impulse (or arrival of the shock wave) on 8 March 2012 and the red dash line indicates the commencement of the storm on 9 March 2012.	109
7.14	Map potential plot for the southern hemisphere between 13:58 and 14:00 UT on 15 July 2012 (image taken from VT SuperDARN website http://vt.superdarn.org/tiki-index.php?page=DaViT+Map+Potential+Plot).	110
7.15	Map potential plot for the Southern hemisphere (a) and DMSP data from satellite F16 (b) for 5 April 2015.	110

-
- 7.16 Magnetometer data from the SANA E station, showing the H (top panel), Z (middle panel) and D (bottom panel) components of the magnetic field. The red dashed lines indicate the time interval during which the substorm occurred. The black dashed lines indicate the time interval of the TID event as identified in the SANA E radar data. . . . 111

Abbreviations and acronyms

AE	Auroral electrojet
ACE	Advanced Composition Explorer
ACF	Autocorrelation function
AGWs	Atmospheric gravity waves
C/A	Code/acquisition
CIRs	Corotating interaction regions
CME	Coronal mass ejections
CSD	Cross-spectral density
DFT	Discrete Fourier Transform
DMSP	Defense Meteorological Satellite Program
Dst	Disturbance storm-time
DWM	Disturbed wind model
Es	Sporadic E
EUV	Extreme ultraviolet
FFT	Fast Fourier Transform
FAIs	Field-aligned irregularities
FPIs	Fabry-Perot interferometers
FOV	Field of view
GLONASS	Global Orbiting Navigation Satellite System
GNSS	Global Navigation Satellite Systems
GOCE	Gravity field and steady state Ocean Circulation Explorer
GEONET	GPS Earth Observation Network
GPS	Global Positioning System
HF	High frequency
HSSs	High speed streams
HWM	Horizontal wind model
IGRF	International Geomagnetic Reference Field
IMF	Interplanetary magnetic field
LSTIDs	Large-scale traveling ionospheric disturbances
LT	Local time
MLT	Magnetic local time
MSTIDs	Medium-scale traveling ionospheric disturbances
MTM	Multitaper method
PI	Principal investigator

POES Polar orbiting environmental satellites
PRN Pseudo-random number
RTI Range time-intensity
RST Radar software toolkit
RINEX Receiver Independent Exchange
SSA-MTM Singular spectrum analysis -MTM
SNR Signal-to-noise ratio
STEC Slant TEC
SANAE South African National Antarctic Expedition
SANSA South African National Space Agency
STEC Slant total electron content
SuperDARN Super Dual Auroral Radar Network
TEC Total electron content
TIDs Traveling ionospheric disturbances
UV Ultraviolet
UHF Ultra-high frequency
UT Universal time
VHF Very high frequency
VLf very low frequency
VTEC Vertical total electron content
WAGS Worldwide atmospheric gravity-wave study

Chapter 1

Introduction

1.1 Introduction to Space Weather

The Sun's activity has been studied since 1755 by counting the number of sunspots, which is used to trace the solar cycle (Cander, 2019). Sunspots are regions on the Sun with a stronger magnetic field (≈ 0.4 T) and are observed by means of a telescope as relatively dark regions; they are slightly cooler than the surrounding areas (Moldwin, 2008; Cander, 2019). The temporal variation in the monthly mean sunspot number is used to determine the activity level on the Sun. The solar cycle is determined by sunspot activity, which is related to the number of sunspots. Over an average period of 11 years the activity on the Sun gradually increases and decreases again. The year 2021 is in solar cycle 25. Space weather involves activity on the Sun, such as expulsions of electromagnetic energy and plasma clouds, and their subsequent interactions with the Earth's magnetosphere and ionosphere (Moldwin, 2008; Cander, 2019). Severe space weather events may impact our day-to-day lives by means of the disruption or even damage to space-borne and ground-based technological systems, such as power grids and oil pipelines, and the degradation of the performance of global navigation and communications systems (Moldwin, 2008; Ngwira *et al.*, 2013). Some examples of solar activity/events are solar x-ray flares, solar energetic particles, coronal mass ejections (CMEs), and high-speed streams (HSSs) from coronal holes and associated corotating interaction regions (CIRs) (Cander, 2019). The type of technologies or radio frequency ranges that will be affected by the solar event, and the time it will take to reach the Earth's magnetosphere differ (usually varying from 8 minutes to several days), depending on the type of event and the position of the source on the Sun. By monitoring solar activity it is possible to observe early warning of severe solar events in order that their impact may be mitigated with minor damage to our technological systems. Space weather information can be used to produce nowcasts and forecasts.

The effects of space weather on the ionosphere are a major concern as signals that are used for communication and navigation systems traverse or are reflected by the ionosphere. An extensive understanding of ionospheric variability helps us reduce navigation and communication systems disruptions during space weather events. Therefore, much research has and is being done on space weather events and their effects on the ionosphere (e.g., Cliver and Svalgaard, 2004; Doherty *et al.*, 2004; Lopez *et al.*, 2004; Balan *et al.*, 2014). Ionospheric phenomena that have been widely studied includes plasma bubbles (e.g., McClure *et al.*, 1977; Kil, 2015), scintillation (e.g., Beach and Kintner, 1999; Spogli *et al.*, 2009), atmospheric gravity waves (AGWs) and traveling ionospheric disturbances (TIDs) (e.g., Borries *et al.*, 2009; Tang *et al.*, 2016; Jonah *et al.*, 2018). The latter is the focus of this thesis and therefore will be discussed in more detail.

1.2 Thesis Background and Motivation

TIDs are quasi-periodic perturbations of the ionospheric electron density with periods between 15 minutes and 3 hours, wavelengths of several hundred to thousands of kilometres, and horizontal velocities between 100 and 1000 ms^{-1} (Francis, 1975; Hunsucker, 1982; Ogawa *et al.*, 1987; Hocke and Schlegel, 1996). Studies on TIDs have shown their association with F region electrodynamic processes, electrical coupling between E and F regions, and AGWs (Perkins, 1973; Samson *et al.*, 1989; Kelley and Miller, 1997; Tsunoda and Cosgrove, 2001; Otsuka *et al.*, 2007; Ogawa *et al.*, 2009; Suzuki *et al.*, 2009). AGWs are waves in the neutral atmosphere caused when gravity acts as a restoring force on an air parcel displaced from its equilibrium position (Beer, 1974; Nappo, 2002; Schunk and Nagy, 2009). Propagation of AGWs in the neutral atmosphere manifests at the ionospheric altitudes as TIDs. TIDs play an essential role in energy coupling/distribution between low and high altitudes, as well as between polar and more equatorial latitudes through attenuation as they propagate from one region to another (Richmond, 1978, 1979; Crowley *et al.*, 1987; Hocke and Schlegel, 1996; Fritts and Alexander, 2003; Vadas and Fritts, 2006). TIDs are one of the sources of error for systems using trans-ionospheric radio signals, such as navigation and communication satellites, as well as radio astronomy instruments (Afraimovich *et al.*, 1992; Skone *et al.*, 2004; Hernández-Pajares *et al.*, 2006; Nickisch *et al.*, 2016; Belehaki *et al.*, 2019). These systems are sensitive to ionospheric irregularities that reflect and scatter the traversing radio signals. In addition, it has been shown that atmospheric and ionospheric models should take into consideration the effect of TIDs if they are to accurately represent atmospheric/ionospheric conditions (e.g., Uwamahoro *et al.*, 2019). Therefore, a better understanding of the sources and scale sizes of energy coupling due to TIDs is vital to estimate the upper atmospheric energy balance and improve atmospheric and/or ionospheric models.

TIDs have been extensively studied using various instruments, including airglow imagers (e.g., Shiokawa *et al.*, 2003; Katamzi-Joseph *et al.*, 2019), ionosondes (e.g.,

Bowman, 1992; MacDougall *et al.*, 2009), global navigation satellite systems (GNSS) (e.g., Tsugawa *et al.*, 2004, 2007; Ding *et al.*, 2008; Habarulema *et al.*, 2016) and high frequency (HF) radar such as Super Dual Auroral Radar Network (SuperDARN) (e.g., Samson *et al.*, 1989; Bristow *et al.*, 1994; He *et al.*, 2004; Ishida *et al.*, 2008; Grocott *et al.*, 2013). Studies of TIDs at northern high latitudes using SuperDARN have appeared numerous times in the literature (e.g., Samson *et al.*, 1989, 1990; Bristow *et al.*, 1994, 1996; Chisham *et al.*, 2007; Nishitani *et al.*, 2019). However, studies of TIDs above Antarctica are sparse in the literature. Therefore, for this project, two SuperDARN radars on Antarctica and some Global Positioning System (GPS) receivers within the radars' fields of view were used to conduct a statistical study of polar TIDs. The South African National Antarctic Expedition (SANAE) radar (Geographic: 71.68° S, 2.85° W), and the Halley radar (Geographic: 75.52° S, 26.63° W) have a large common field of view (FOV) and provide velocity vectors of ionospheric irregularities. The SANAE radar and the Halley radar have a large common FOV and provide velocity vectors of ionospheric irregularities. The use of two radars to study a common area is rare, and the use of multi-instruments (the radars plus GPS total electron content (TEC)) measurements present a unique opportunity for optimal detection and characterization of TIDs over this region. This study also provides insight into the characteristics of TIDs and their common source mechanisms over Antarctica by utilizing ten years of SuperDARN data between 2005 and 2015.

1.3 Thesis Objective

The main objectives of this project are to study the spatial distribution and temporal variability of TIDs over Antarctica and to identify their source mechanisms. The questions which relate to these objectives and that the study aims to answer are:

- What are the most common frequencies and wavelengths of TIDs over Antarctica?
- In which direction do the TIDs mostly propagate?
- Which mechanisms are involved in the excitation of TIDs?

The following procedures are done to address the above questions:

- Identify possible TID events from the SANAE SuperDARN radar data and study their characteristics.
- Perform a detailed study of one of the TID events using MTM analysis.
- Make an estimation of the Joule heating dissipated by a MSTID.

- Investigate TID events observed concomitantly by SANA E and Halley HF radars.
- Investigate TID events selected from the SANA E HF radar that can also be observed in TEC measurements.
- Look into ground and satellite data to identify the possible source mechanisms.

1.4 Thesis Outline

The outline of the following chapters of this thesis is given here.

Chapter 2 starts by introducing the theoretical background of AGWs and TIDs, along with literature reviews of their characteristics and source mechanisms in different regions. This chapter also contains short descriptions of neutral winds, Joule heating and magnetic storms and substorms in relation to the study of TIDs.

Chapter 3 describes the different instruments and models used to extract information on TIDs and their sources. A basic introduction to the SuperDARN radar is given, namely how it works and its use in ionospheric-magnetospheric study. A description of the use of GPS to measure TEC of the ionosphere is given. The use of the Defense Meteorological Satellite Program (DMSP) and magnetometer data to determine the source mechanisms of TIDs is explained. A brief introduction to the IGRF (International Geomagnetic Reference Field) model and the Horizontal wind model (HWM14), which are utilised for the Joule heating estimation, is included.

Chapter 4 presents data analysis methods for identification of TIDs in radar data. These methods, of signal analysis nature, include Fast Fourier analysis, Lomb-Scargle analysis, multitapering and analytic signal analysis.

Chapter 5 consists of the results of an event analysis of a TID structure identified by both the SANA E and Halley on 17 March 2013, a geomagnetically quiet day. The TID characteristics obtained by means of the multitaper signal analysis method and the identification of source mechanisms by means of ground- and satellite-based data are discussed. Lastly, an estimation of the energy dissipation by the observed TID is made.

Chapter 6 comprises the results of multi-instrument observations of three TID events identified in HF radar data from SANA E and Halley stations, as well as TEC data from GPS receivers within the FOV of these radars.

Chapter 7 presents a survey of TIDs events that were observed by both the SANA E (22 events) and Halley radars (9 events) over a 10 year period (2005-2015). It includes a discussion of the characteristics of all the identified events and their

possible source mechanisms.

Chapter 8 contains a summary of all the results and discussions of this study. It also presents a short discussion on possible future work.

Chapter 2

Theoretical Background

2.1 Introduction

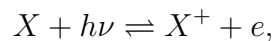
Our planet Earth is surrounded by a deep blanket of air, the atmosphere, which is crucial for the existence of life on Earth. The atmosphere is composed of layers, differing in composition, ionisation level, density and temperature. The atmosphere is divided into layers based on their temperature profile. Figure 2.1 shows typical temperature and electron density profiles that illustrate different layers of the atmosphere. The lowest part of the atmosphere is the troposphere, which extends from the ground up to 10 km altitude (Kelley and Heelis, 1989). The troposphere is a meteorologically active layer where the temperature decreases with altitude. Above the troposphere to ~ 50 km sits the stratosphere, where the temperature increases with altitude because of the ozone layer that absorbs ultraviolet (UV) radiation from the Sun. The third layer of the atmosphere is the mesosphere, located between 50 and 80 km, where the temperature decreases with altitude at a rate of 3.5 K/km (Ondoh and Marubashi, 2001). The temperature starts increasing again in the thermospheric region, which is located above 80 km. The thermosphere is a highly ionised and hot part of the atmosphere due to short wavelength UV radiation from the Sun. The absorbed UV radiation is responsible for ionising the neutral atmosphere and, at the same time, heating the thermosphere. The ionised layer (the ionosphere) extends from the mesospheric to the thermospheric region, where the region with maximum electron density is located at ~ 300 km altitude (Ondoh and Marubashi, 2001; Moldwin, 2008). The ionospheric layer plays a vital role in our radio communication and navigation systems. At the same time, the ionosphere is susceptible to space weather events and other atmospheric conditions that can cause electron density irregularities. Traveling ionospheric disturbances (TIDs) and/or atmospheric gravity waves (AGWs) are among the main causes of ionospheric irregularities in the ionosphere. Some TIDs/AGWs arise from space weather events, which will be discussed in subsequent sections. This project focuses on understanding the characteristics of TIDs,

in particular at Antarctica.

The rest of this chapter comprises the following sections: An introduction to the ionosphere is followed by a section on AGWs, which discusses their formation, their theoretical wave equation, propagation and source mechanisms. The section on TIDs includes a literature review of the characteristics of large-scale and medium-scale TIDs. This is followed by a section on neutral winds, Joule heating caused by TIDs and magnetic storms and substorms.

2.2 Ionosphere

The ionosphere has a significant effect on trans-ionospheric signals, which are used for radio communication and navigation. The ionosphere is the layer of the Earth's atmosphere located at altitude of ~ 50 km to 1,000 km, and characterized by the abundance of free electrons. These free electrons are primarily generated by photo-ionisation, which is the ionisation of the atmospheric molecules and atoms by radiation from the Sun (McNamara, 1991). The photo-ionisation process may be expressed as



where X represents an atom or a molecule and $h\nu$ a photon, which produces free ions (X^+) and electrons (e). The other mechanism which produces free electrons in the ionosphere is collision ionisation, where precipitation of energetic particles at high latitudes frees electrons by means of collision (McNamara, 1991; Hunsucker and Hargreaves, 2003).

The electron density in the ionosphere varies depending on time of day, season and altitude as the production rate of free electrons depends on the intensity of the photons and the number of neutral atoms (Georges, 1969; McNamara, 1991). The seasonal and diurnal variability of the ionosphere is directly related to the intensity of the UV radiation, whereas variation with respect to altitude is due to both the variation of the photon intensity and density of neutral atoms at different altitudes. As the altitude changes from low to high, neutral atoms becomes scarce, due to the decrease in gravitational force with increase in altitude, and the intensity of EUV becomes stronger as there is less absorption. At an altitude where these two opposing processes balance, the rate of production of free electrons reaches its maximum and electron density maximizes (McNamara, 1991). Thus layers with differing electron densities are formed in the ionosphere, as shown in Figure 2.1. Based on the ionisation level, the ionosphere is divided into 4 regions/layers known as D, E, and F. The latter splits into F1 and F2, as will be explained later.

The ionosphere also varies with latitude, solar activity and geomagnetic conditions. Solar activity variation manifests itself in that the ionisation level is higher

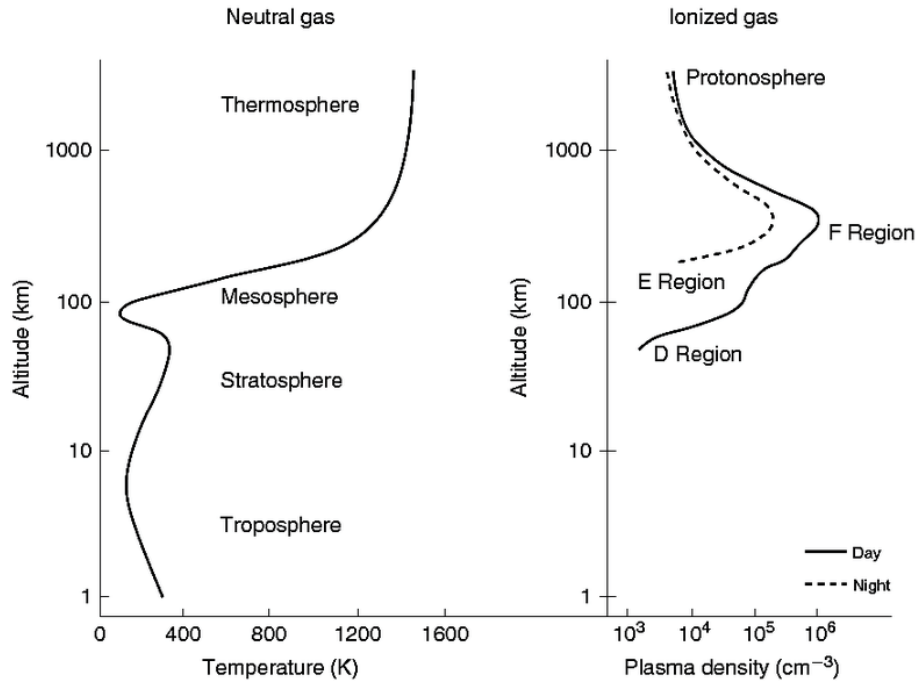


Figure 2.1: Layers of Earth's atmosphere and the ionosphere electron density variation representing a typical mid-latitude ionosphere during the day (solid line) and night (broken line) (Kelley and Heelis, 1989).

during solar maximum than solar minimum, because then the intensity of the solar radiation is greater and leads to an increase in the production rate of free electrons and ions (MacDougall *et al.*, 2009). The latitudinal variation of the ionosphere has partly to do with the change in the solar zenith angle with latitude. As the latitude increases for the same local time, the zenith angle becomes greater and the intensity of the radiation decreases (McNamara, 1991). There are other phenomena that control the latitudinal variation of the ionosphere, such as the fountain effect, which moves the electrons from the equatorial region through $\mathbf{E} \times \mathbf{B}$ vertical drift and redistributes them to latitudes between $\pm 10^\circ$ and $\pm 20^\circ$ (McNamara, 1991). This leads to regions of low electron density at the equator and of high electron density north and south of the equator. At high latitudes precipitation of energetic particles through the magnetosphere contributes to enhanced ionisation because of collision ionisation (McNamara, 1991; Hunsucker and Hargreaves, 2003). Magnetic storms contribute to the complex ionospheric variation observed at all latitudes. Relative to the background electron density, enhancement or depletion of the electron density may be observed during geomagnetic storms, known as positive and negative ionospheric storms, respectively (Habarulema *et al.*, 2013; Matamba *et al.*, 2015).

The electron density of the ionosphere depends not only on the rate of electron production, but also on that of the recombination and attachment processes. One type of recombination process occurs when the free electrons are lost due to combination with positively charged ions, a process known as radiation recombination

(McNamara, 1991). The recombination process can also occur in two stages, where first a positive ion (X^+) interacts with a neutral molecule A_2 and replaces one of the atoms in the molecule. Then the positively charged molecule AX^+ , created in the first reaction, combines with a free electron to give two neutral atoms. This type of recombination is called dissociative recombination and it is more efficient than radiative recombination (McNamara, 1991). Another electron loss process is the attachment process, prevalent in the D layer, in which electrons are attached to a neutral atom and produces a negatively charged ion (McNamara, 1991).

The D layer is the lower part of the ionosphere, ranging from 50 km to 90 km in altitude. The main sources of ionisation in the D layer are ionisation of nitric oxide by EUV photons, ionisation of molecular nitrogen and oxygen by solar hard X-rays and cosmic rays (Moldwin, 2008). The D layer has the property of absorbing lower frequency radio signals which degrade long-distance high frequency (HF) radio communication.

The E layer of the ionosphere is located between 90 km and 140 km in altitude (Ondoh and Marubashi, 2001). Ionisation of molecular oxygen and nitrogen by low energy or soft X-ray and solar UV radiation is the main source of charged particles in this region. Precipitation of energetic particles, mainly at high latitudes, also contributes to the ionisation of the E layer.

The sporadic E (Es) layer is observed as a narrow high electron density layer that occurs randomly in the E layer and lasts for short periods of time (few minutes to several hours) (Beer, 1974; Moldwin, 2008). This layer has different sources at different latitudes including plasma instability at low latitudes (e.g. Abdu *et al.*, 1996), neutral wind shears in the E region at mid-latitudes (e.g. Whitehead, 1989) and charged particle precipitation at high latitudes (e.g. Rodger *et al.*, 1983). The Es layer may affect radio communication by fading the signal and creating multipath effects (Cander, 2019).

The F layer extends from 120 km and the density peaks at approximately 300 km (Moldwin, 2008). The F layer is produced mainly by EUV ionisation of atomic oxygen. During the daytime, especially in the summer and when the Sun is low, the F layer splits into the F1 and F2 layers, with the highest electron density being in the F2 layer (Davies, 1990; Hunsucker and Hargreaves, 2003). At higher altitudes only the F2 layer exist at night, while the other three lower layers disappear because of the increase in the loss rate of free electrons relative to the production rate, which is caused by recombination and attachment mechanisms (McNamara, 1991).

2.3 Atmospheric Gravity Waves

Vertical displacement of an air parcel in a stratified atmosphere which is stable, generates gravity waves due to the Buoyancy force, which acts to restore the equilibrium (Nappo, 2002; Schunk and Nagy, 2009). The restoring force creates an oscillation of the air parcel at its equilibrium position at the Brunt-Väisälä frequency. For a parcel displaced from its equilibrium position (s_e) with a distance δs and an angle of α from the vertical, the Buoyancy force acting on the displaced air is expressed by:

$$m_p \frac{d^2(\delta s)}{dt^2} = -g \sin \alpha (m_p - m_a), \quad (2.1)$$

where $g \sin \alpha$ is the gravity component along the direction of the displacement, m_p is the mass of an air parcel in equilibrium with its environment at height s_e and m_a is the mass of the displaced air in the parcel (Nappo, 2002). Using the ideal gas law $p = \rho RT$, where p is pressure, ρ is density, R is the universal gas constant (287 J/kg K) and T is temperature, and expressing the mass of the air parcel using ρ and volume (V), the equation is reduced to (Nappo, 2002):

$$\rho_p V_p \frac{d^2(\delta s)}{dt^2} = -g \sin \alpha (\rho_p V_p - \rho_a V_a). \quad (2.2)$$

This equation can be simplified by assuming that the air pressure of the air parcel is equal to that of the environment and that the volume stays the same:

$$\frac{d^2(\delta s)}{dt^2} = -g \sin \alpha \frac{(T_a - T_p)}{T_a}, \quad (2.3)$$

where T_a and T_p are the environmental and parcel temperatures, respectively. The Taylor series expansion of T_a and T_p to the first degree substituted in Equation 2.3 leads to:

$$\frac{d^2(\delta s)}{dt^2} = \frac{-g \sin \alpha}{T_a} \left(\frac{\partial T_a}{\partial s} - \frac{\partial T_p}{\partial s} \right) \delta s. \quad (2.4)$$

By applying the adiabatic lapse rate, $\Gamma = \frac{\partial T_p}{\partial s} = \frac{g \sin \alpha}{C_p}$, where C_p is the specific heat capacity at constant pressure, the expression can be written as follows:

$$\frac{d^2(\delta s)}{dt^2} = \frac{-g \sin \alpha}{T_a} \left(\frac{\partial T_a}{\partial s} - \frac{g \sin \alpha}{C_p} \right) \delta s. \quad (2.5)$$

Equation 2.5 can be rewritten using the potential temperature ($\theta = T_a(1000/p)^{R/c_p}$), which is the temperature of an air parcel that is moved adiabatically from an altitude with pressure p to the ground where the pressure is 1000 mb (Beer, 1974; Nappo, 2002):

$$\frac{d^2(\delta s)}{dt^2} = \frac{-g}{\theta} \frac{\partial \theta}{\partial s} \sin^2 \alpha \delta s. \quad (2.6)$$

Then the motion of the parcel along the displacement direction is expressed by:

$$\delta s(t) = Ae^{i\omega_b t} + Be^{-i\omega_b t}, \quad (2.7)$$

where $\omega_b^2 = \frac{g\partial\theta}{\theta\partial s} \sin^2 \alpha$ is the Brunt-Väisälä frequency, or it can be rewritten by using the frequency for purely vertical displacement (i.e. $\omega_v^2 = \frac{g\partial\theta}{\theta\partial s}$)

$$\omega_b = \omega_v \sin \alpha. \quad (2.8)$$

Therefore, for $\alpha = 0^\circ$ then $\omega_b = 0$ and the motion is horizontal with no oscillation, and if $\alpha = 90^\circ$, which means a vertical displacement, then $\omega_b = \omega_v$.

2.3.1 Dispersion relation equation for gravity waves

Propagation of the gravity waves in the atmosphere is characterised by the interaction between the pressure gradient (∇p), the buoyancy force (ρg) and the inertia force (Hocke and Schlegel, 1996). Linear theory, where variables are expressed as background and perturbed states, is used to derive the dispersion relation equation for gravity waves (Nappo, 2002). Euler equations for a frictionless atmosphere and irrotational Earth (i.e. ignoring the Coriolis force and centripetal acceleration) are the governing equations used to derive the dispersion relation of gravity waves (Beer, 1974; Nappo, 2002; Schunk and Nagy, 2009). The Coriolis force and centripetal acceleration are not taken into account because gravity wave periods (10 min to 3 hrs) are much less than planetary rotation periods (24 hrs) (Schunk and Nagy, 2009). In addition, the atmosphere has to be isothermal, compressible and inviscid to disregard the source and dissipation mechanisms (Hines, 1959; Schunk and Nagy, 2009). The continuity, momentum and energy equations for a single-component neutral gas are expressed by (Schunk and Nagy, 2009):

$$\frac{\partial \rho}{\partial t} + \nabla \cdot (\rho \mathbf{u}) = 0, \quad (2.9)$$

$$\rho \left(\frac{\partial}{\partial t} + \mathbf{u} \cdot \nabla \right) \mathbf{u} + \nabla p - \rho \mathbf{G} = 0, \quad (2.10)$$

$$\left(\frac{\partial}{\partial t} + \mathbf{u} \cdot \nabla \right) p + \gamma p (\nabla \cdot \mathbf{u}) = 0, \quad (2.11)$$

where \mathbf{u} is atmospheric velocity, \mathbf{G} gravitational acceleration and $\gamma = 5/3$ is the ratio of specific heats.

From the linearisation theory, the atmospheric variables can be expanded to a background and perturbed state $\rho = \rho_0 + \rho_1$, $p = p_0 + p_1$ and $\mathbf{u} = \mathbf{u}_1$. The subscript 0

and 1 represent the unperturbed (or initial) and perturbed states of the atmosphere, respectively (Schunk and Nagy, 2009). p_0 and ρ_0 expressed in terms of the scale height, i.e. $p_0, \rho_0 \propto e^{-z/H_0}$ where $H_0 = kT_0/mg$ and $k = 1.381 \times 10^{-23} J/K$, which indicates that the initial atmospheric state only varies with z exponentially. Using the above expressions for the terms containing $\nabla \rho_0$ and ∇p_0 yields $\mathbf{u}_1 \cdot \nabla \rho_0 = -\frac{\rho_0}{H_0} u_{1z}$ and $\mathbf{u}_1 \cdot \nabla p_0 = -\frac{p_0}{H_0} u_{1z}$. The equations of continuity, momentum and energy become,

$$\frac{\partial}{\partial t} \left(\frac{\rho_1}{\rho_0} \right) - \frac{1}{H_0} u_{1z} + (\nabla \cdot \mathbf{u}_1) = 0, \quad (2.12)$$

$$\frac{\partial \mathbf{u}_1}{\partial t} + \frac{p_1}{\rho_0 p_0} \nabla p_0 + \frac{p_0}{\rho_0} \nabla \frac{p_1}{p_0} - \frac{\rho_1}{\rho_0} \mathbf{G} = 0, \quad (2.13)$$

$$\frac{\partial}{\partial t} \left(\frac{p_1}{p_0} \right) - \frac{1}{H_0} u_{1z} + \gamma (\nabla \cdot \mathbf{u}_1) = 0, \quad (2.14)$$

where u_{1z} is the vertical component of the perturbed velocity. The plane wave equation may be used to represent the small perturbations in density, pressure and velocity (Schunk and Nagy, 2009) as given here,

$$\frac{\rho_1}{\rho_0}, \frac{p_1}{p_0}, \mathbf{u}_1 \propto \exp^{i(\mathbf{K} \cdot \mathbf{r} - \omega t)}, \quad (2.15)$$

where \mathbf{K} is the wave vector and ω is the wave frequency. Assuming that the gravity wave propagates in x-z plane ($\mathbf{K} = (K_x, K_z)$), the momentum equation becomes two equations with the velocity having both x and z components ($\mathbf{u} = (u_x, u_z)$). Hence, there will be four equations with four unknowns (Schunk and Nagy, 2009):

$$-i\omega \left(\frac{\rho_1}{\rho_0} \right) + iK_x u_{1x} + (iK_z - 1/H_0) u_{1z} = 0, \quad (2.16)$$

$$ik_x c_0^2 / \gamma \left(\frac{p_1}{p_0} \right) - i\omega u_{1x} = 0, \quad (2.17)$$

$$(iK_z - 1/H_0) \frac{c_0^2 p_1}{\gamma p_0} - i\omega u_{1z} + g \left(\frac{\rho_1}{\rho_0} \right) = 0, \quad (2.18)$$

$$-i\omega \left(\frac{p_1}{p_0} \right) + i\gamma K_x u_x + (i\gamma K_z - 1/H_0) u_z = 0, \quad (2.19)$$

where c_0 is the speed of sound in the neutral gas, K_x and K_z are the horizontal and vertical wave numbers, respectively. Solving the above equations gives us the solution for the dispersion relation. The dispersion relation for internal gravitational waves, that relate K and ω is expressed by (Hines, 1959; Schunk and Nagy, 2009):

$$\omega^4 - \omega c_0^2 (K_x^2 + K_z^2) + (\gamma - 1) g^2 K_x^2 - i\gamma g \omega^2 K_z^2 = 0. \quad (2.20)$$

Equation 2.20 can be solved by ignoring gravity ($g = 0$) which gives the dispersion

relation of sound waves. In the case of sound waves both K and ω are real and the wave propagates without growth or attenuation ($\omega^2 = c_0^2 \mathbf{K}^2$) (Hines, 1960; Schunk and Nagy, 2009). There will be no solution where both K_x and K_y are purely real and different from zero, if gravity is not set to zero in Equation 2.20. This is the case for gravity waves, where waves experience attenuation as they propagate. Therefore, one of the wave vector components has to be complex ($K_z = K_{zr} + iK_{zi}$), where K_{zr} is the real part and K_{zi} is the imaginary part. Equation 2.20 then becomes

$$\omega^4 - \omega c_0^2 (K_x^2 + K_{zr}^2 + K_{zi}^2) + (\gamma - 1)g^2 K_x^2 + \gamma g K_{zi}^2 \omega^2 - i\omega^2 K_{zr}^2 (\gamma g + 2c_0^2 K_{zi}) = 0, \quad (2.21)$$

where the imaginary part of the equation becomes

$$K_{zi} = -\frac{\gamma g}{2c_0^2} = -\frac{1}{2H_0}, \quad (2.22)$$

and the velocity perturbation equation ($\mathbf{u}_1 \propto \exp(i\mathbf{K}\cdot\mathbf{r} - \omega t)$) becomes

$$\mathbf{u}_1 \propto \exp^{z/2H_0} \exp^{i(K_x x + K_{zr} z - \omega t)}. \quad (2.23)$$

Gravity waves are characterized by constant wave perturbation energy ($\frac{1}{2}\rho_0 u_{1z}^2$) because $\rho_0 \propto \exp^{-z\gamma g/c_0^2}$ and $u_{1z} \propto \exp^{-z\gamma g/2c_0^2}$ (Schunk and Nagy, 2009). The amplitude of the wave increases exponentially as the wave propagates towards higher altitudes where the density decreases ($\exp^{(z\gamma g/2c_0^2)}$) (Hines, 1960; Nappo, 2002; Schunk and Nagy, 2009).

2.3.2 Propagation of AGWs

AGWs exist at different altitudes, from tropospheric altitudes to thermospheric altitudes. Thermospheric gravity waves have a larger vertical wavelength than mesospheric gravity waves (Francis, 1974; Bristow *et al.*, 1996; Bristow and Greenwald, 1997). Gravity waves in the atmosphere move with oscillations that are perpendicular to the direction of the energy transfer, i.e. they are transverse waves (Hunsucker and Hargreaves, 2003). As waves propagate from a high density region, i.e. the lower atmosphere, to a less dense region their amplitudes increase and demonstrate instability (Vadas and Fritts, 2006).

Figure 2.2 shows different propagation modes of AGWs, namely upper mode and lower mode. The upper propagation mode includes direct and lower thermosphere waves, whereas the lower modes are Earth-reflected and ducted waves. Waves originating in the thermospheric region can have different propagation modes. These are direct, lower thermospheric, Earth-reflected and ducted modes. The direct and lower thermospheric modes are waves that travel obliquely to higher altitudes, as shown in Figure 2.2. For Earth-reflected and ducted modes, the wave first goes down to the

ground and is reflected before it propagates obliquely to the thermosphere or propagates horizontally with some portion of the wave penetrating the thermosphere in the case of the ducted mode (see Figure 2.2). Direct waves have longer wavelengths and propagate quasi-horizontally (Mayr *et al.*, 1990). Wave reflection occurs if the background flow characteristics change quickly with altitude (Nappo, 2002). Ducted waves travel long horizontal distances from their source as they propagate through the non-dissipative part of the atmosphere (Francis, 1974; Mayr *et al.*, 1990; Nappo, 2002). Due to geomagnetic attenuation, the amplitude of ducted waves decreases as the waves propagate to the equator (Mayr *et al.*, 1990). When it comes to the Earth-reflected waves, they have shorter wavelengths than the ducted waves and dissipate fast (Mayr *et al.*, 1990). Long-period waves with high horizontal velocity propagate long-distance in the thermosphere without dissipation. In contrast, slow moving and short-period waves dissipate faster and cannot travel a long distance from their source (Richmond, 1978).

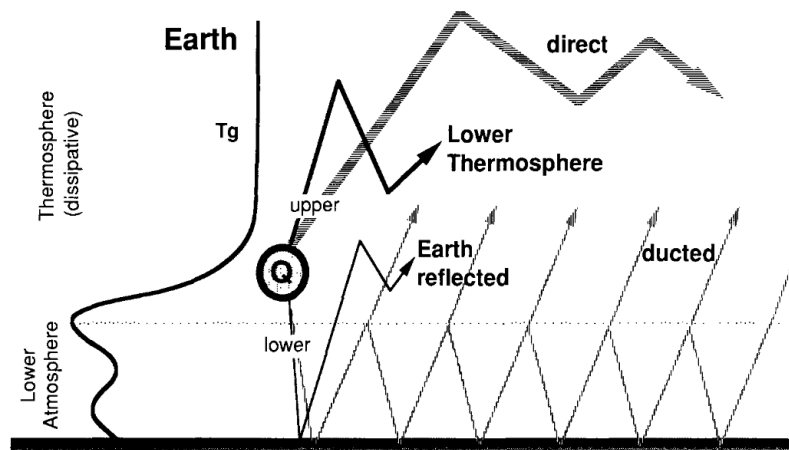


Figure 2.2: Propagation modes of AGWs (Mayr *et al.*, 1990)

2.3.3 Common Sources of AGWs

AGWs play a significant role in the dynamics of the atmosphere by transporting energy and momentum vertically, through different layers of the atmosphere and horizontally across the globe. AGWs transport energy from the source region to where dissipation occurs (Vadas and Fritts, 2006). At high latitudes, heat is deposited through precipitation of charged particles, causing heating up of the neutral atmosphere. Gravity waves are one of the mechanisms that is responsible for distributing these energies from high-latitudes regions to the middle and low latitudes (Richmond, 1979; Hunsucker, 1982). The other mechanism is meridional circulation through compressional heating and advection (Richmond, 1979). The air in the auroral region rises to higher altitudes and travels horizontally because of the heating effect of the auroral electrojet current, and then sinks to a lower altitude, where it creates compressional heating, and circles back to high latitudes at a lower altitude (Richmond, 1979).

Mesospheric AGWs are primarily generated in the tropospheric region and propagate upward (Bristow and Greenwald, 1997). Source of AGWs in the lower atmosphere include volcanoes, earthquakes, nuclear explosion, perturbation in the jetstream and mountain turbulence (Hunsucker, 1982; Nappo, 2002). AGWs can be triggered by upper atmospheric sources, such as the solar terminator, solar eclipses, the equatorial electrojet, the auroral electrojet and particle precipitation (Nappo, 2002). Particle precipitation and Joule heating and the Lorentz force associated with the auroral electrojet are common sources at high latitudes (Hunsucker, 1982). Both Joule heating ($\mathbf{J} \cdot \mathbf{E} = J^2 / \sigma_p$) and Lorentz force ($\mathbf{J} \times \mathbf{B}$ force transfer to neutrals through collision) introduce a local time-dependent disturbance into the neutral atmosphere that triggers gravity waves (Chimonas and Hines, 1970). Researchers have investigated the most dominant source during an auroral electrojet (e.g. Chimonas and Hines, 1970; Francis, 1975; Richmond, 1978). These studies concluded that the Lorentz force dominates in exciting AGW's in the auroral region.

2.4 Traveling Ionospheric Disturbances (TIDs)

TIDs transfer energy and momentum from their origin to the region where they dissipate, through molecular viscosity, thermal conductivity and ion drag (Ding *et al.*, 2008). The observation of wave motions in the upper atmosphere and their manifestation in the ionosphere started during the 1940s (Waldock and Jones, 1986; Nappo, 2002). The first study to relate AGW to TIDs was done by Hines (1960), in which he explained ionospheric irregularities in terms of internal gravity waves. Since then TIDs have been extensively studied theoretically, using models and observations. For more information or highlights refer to review papers (e.g. Francis, 1975; Hunsucker, 1982; Hocke and Schlegel, 1996; Nishitani *et al.*, 2019). Studies reveal that TIDs have diverse properties and thus are usually classified into large-scale TIDs and medium-scale TIDs, based on their wave velocity and periods (e.g. Hunsucker, 1982; MacDougall *et al.*, 2009).

2.4.1 Large-scale TIDs

TIDs with horizontal velocities between 400 and 1000 ms^{-1} , wave periods within the range of 0.5 to 3 hours, and a horizontal wavelength greater than 1000 km are classified as large-scale TIDs (LSTIDs) (Ogawa *et al.*, 1987; Samson *et al.*, 1989; Hocke and Schlegel, 1996). The speed of LSTIDs is similar to the speed of sound propagation in the thermospheric layer (Hocke and Schlegel, 1996).

LSTIDs are known to travel long distances as they travel at high speeds and have long horizontal wavelengths. Studies have shown that LSTIDs can travel from the polar region all the way to the equatorial region or the other way around and

can even propagate across the equator to the opposite hemisphere (Francis, 1975; Hunsucker, 1982; Bruinsma and Forbes, 2007). The first case is more common, as equatorward propagating LSTIDs are primarily associated with geomagnetic storms and auroral substorms and also high-latitude processes, such as energetic particle precipitation (Francis, 1974; Hunsucker, 1982). Habarulema *et al.* (2016) reported on observations of storm-time LSTIDs propagating both equatorward and poleward, using total electron content (TEC) maps derived from the Global Positioning System (GPS) covering American, African and Asian longitudinal sectors (low to high latitudes). They reported that the LSTIDs originating in the equatorial region result from low-latitude electrodynamics, specifically from the change in the $\mathbf{E} \times \mathbf{B}$ vertical drift. In a study over Antarctica, equatorward and poleward propagating LSTIDs were observed on days in October and November 2003 that were related to severe magnetic storm events (Momani *et al.*, 2010). The LSTID observed between the 30 and 31 October 2003 propagated towards the equator with a velocity of $\sim 1000 \text{ ms}^{-1}$, contrary to the event observed on the 20 November 2003 which propagated poleward with a velocity of $\sim 350 \text{ ms}^{-1}$.

A statistical study by Tsugawa *et al.* (2004), which used the GPS network in Japan (covering the area from 124°E to 148°E longitude and from 24°N to 48°N latitude), showed LSTIDs that had a mean velocity of $475 \pm 171 \text{ ms}^{-1}$, a period of $80 \pm 29 \text{ min}$ and a wavelength of $2131 \pm 863 \text{ km}$, propagating $3 \pm 19^\circ$ East from South. A study of LSTIDs by Ding *et al.* (2008), which used the GPS network in North America (geographical latitudes of 25°N - 55°N), found that the LSTIDs had a slower mean velocity than those observed by Tsugawa *et al.* (2004) at lower latitudes. Most of the LSTIDs reported by Ding *et al.* (2008) observed during the major magnetic storms from 2003 to 2005 have a mean velocity of 300 ms^{-1} and a mean period of 1.8 hours. The occurrence of LSTIDs at mid-latitudes showed local time (LT) and universal time (UT) dependence due to the UT dependence of the auroral disturbance occurrence (Ding *et al.*, 2008).

Borries *et al.* (2009) studied storm induced LSTIDs over Europe (10°W - 30°E , 30°N - 70°N), using TEC data from the GNSS network. Most of the LSTIDs had periods of 59 minutes and propagated towards the equator with a mean phase speed of 684 ms^{-1} . The phase speed of the LSTIDs was faster than those over Japan during a geomagnetically active period. Based on the high correlation between the AE index and amplitude of the LSTIDs observed during daytime of the solar maximum, it was suggested that the LSTIDs were mainly excited by Joule heating (Borries *et al.*, 2009). The correlation between the AE index and the increment in the amplitude of the LSTIDs was low during the night.

The characteristics of LSTIDs observed during the Worldwide atmospheric gravity wave study (WAGS), between 11 and 18 October 1985, were reported by Williams *et al.* (1988). For the campaign, a combination of incoherent scatter radar (in the auroral oval region), ionosondes, HF Doppler radar and a radio telescope (in the mid-latitude region) were utilized to cover both the source region and long-distance

propagation. LSTIDs with periods of 40 to 70 minutes that propagated from high latitudes to mid-latitudes (a distance of over 200 km) at speeds between 400 and 500 ms^{-1} were reported. They also observed LSTIDs with short periods, between 17 and 33 minutes, and a phase velocity of 350 ms^{-1} at lower latitudes (propagating equatorward), with a significant attenuation effect on the waves. The attenuation effect is significant especially for the 17 minutes LSTIDs. They concluded that the similarity in periodicity of the disturbance in the auroral electric field and the waves at mid-latitudes was a good indication that auroral activity, such as Joule heating, the Lorentz force and particle heating, generated the LSTIDs. Similar shorter period LSTIDs (17 to 33 minutes), generated by high latitude sources, were studied by [Bowman \(1992\)](#), using mid-latitude ionosondes in Australia and Japan. The results showed that the LSTIDs propagate equatorward in both hemispheres with an average speed of 473 ms^{-1} .

A multi-instrument study by [Katamzi-Joseph *et al.* \(2019\)](#) used GPS TEC data, observation by the Fabry-Perot interferometer (FPI) and all-sky camera and magnetometer data for Svalbard in the Arctic polar cap and reported poleward propagating LSTIDs generated by auroral sources (Joule heating and/or particle precipitation). The GPS TEC showed that the LSTIDs had periods between 29 and 65 min and propagated at a mean velocity of $\approx 755 \text{ms}^{-1}$, whereas the periods of the AGWs measured by the FPI were slightly greater, namely between 42 minutes and 2 hours 22 minutes. Similar periods and propagation speeds were observed in the horizontal magnetic field data and auroral intensity data provided by the all-sky camera, thus correlating with the observed LSTIDs.

[Hayashi *et al.* \(2010\)](#) were the first to observe LSTIDs events using SuperDARN radar (Hokkaido radar) and GPS TEC data that covered high to low latitudes. The study presented three LSTIDs observed during the main phase of a geomagnetic storm on 15 December 2006. They found two LSTIDs propagating southward (equatorward) and one propagating northward (from the southern hemisphere to the northern hemisphere).

2.4.2 Medium-scale TIDs

Relative to LSTIDs, medium-scale TIDs are characterized by a low horizontal velocity (100-250 ms^{-1}) and shorter periods, in the range of 15 minutes to 1 hour, and they have wavelengths of several hundreds of kilometres ([Francis, 1974](#); [Ogawa *et al.*, 1987](#)). MSTIDs travel slower than the speed of sound in the lower atmosphere ([Hocke and Schlegel, 1996](#)). Meteorological processes such as thunderstorms, vortices, cold fronts and hurricanes are usually listed as the main source of AGWs, which create MSTIDs ([Ding *et al.*, 2011](#)).

MSTIDs are observed more often than LSTIDs, in all latitudes, and at any time of the day ([Francis, 1974](#); [MacDougall *et al.*, 2009](#)). It is often difficult to relate

them with a specific source mechanism as they may travel a significant distance before they are damped (Francis, 1974, 1975). For example, Vadas (2007) determined that MSTIDs can travel a horizontal distance of up to 2000 km from their source before dissipating. Ogawa *et al.* (2009) presented evidence that nighttime MSTIDs can propagate horizontally over a distance of up to 4000 km. Ducted mode wave propagation of AGWs, shown in Figure 2.2, allows for the propagation of MSTIDs over long horizontal distances from their sources (Francis, 1974, 1975). Earth-reflected AGWs (waves that are reflected downward to Earth and propagate back to thermospheric altitude) propagate over a longer horizontal distance from the source without dissipation than direct waves, as the viscosity is small at altitudes below 200 km (Bristow *et al.*, 1996).

Samson *et al.* (1990) and Bristow *et al.* (1996) showed that high-latitude MSTIDs are mostly observed during winter and the late fall months, and are most commonly excited by auroral processes. However, MSTIDs at high latitudes have also been observed during magnetically quiet conditions, as well (such conditions are pertinent to this study). For example, the statical analysis of MSTIDs by Ogawa *et al.* (1987) over Syowa station (50° to 85° S), Antarctica, showed that there is a more frequent occurrence of MSTIDs during geomagnetically quiet and moderately disturbed times as well as during winter (specifically August). They also found that the time that the most MSTIDs occur, is between 14:00 and 16:00 LT with a second maximum around midnight. They propagated mostly equatorward. However, they also pointed out that their results may be biased, because the differential-Doppler satellites are highly affected by scintillation, therefore making it difficult to identify TIDs during geomagnetically disturbed periods. Bristow *et al.* (1996) reported that during the northern summer MSTIDs propagate mainly out of the south and vice versa for the southern summer, which leads to a conclusion that summer MSTIDs are mainly excited by sources in the winter hemisphere at tropospheric altitudes. The study further explained the seasonal dependence by showing that the stronger temperature gradient in the summer mesosphere causes the vertical wave vector of the AGWs to become imaginary, in which case the wave would be reflected; whereas the same wave could penetrate the mesosphere during a winter season. However, this theory did not include AGWs excited at altitudes higher than the mesosphere (Bristow *et al.*, 1996).

A study by Crowley *et al.* (1987), which used the HF Doppler network over the Antarctic Peninsula showed that the morphology of short-period TIDs (between 10-30 min) depended on geomagnetic conditions. During geomagnetically quiet periods, the TIDs had horizontal speeds of less than 300 ms⁻¹, while during geomagnetically active periods, they had higher speeds. It was suggested that this could be due to the existence of different wave sources and perturbations of the neutral wind pattern (azimuth of the wind propagation influenced by high-latitude heat and momentum) during geomagnetically disturbed periods. Besides the low speeds, they reported that short-period TIDs observed during quiet conditions propagate in an anti-windward direction (anticlockwise diurnal azimuth rotation) and reached higher altitudes within a short time period. In contrast, short-period TIDs with high speeds that were

observed during disturbed conditions did not exhibit the same anticlockwise diurnal azimuth rotation.

Davies and Jones (1971) showed that the most dominant propagation direction of MSTIDs at mid-latitudes is equatorward during local winter, poleward during local summer and westward during the equinox season in Colorado (USA). Similar findings were reported by Georges (1968) using seven months of data from a network of HF Doppler sounders in Greenwood, also in the mid-latitudes of the northern hemisphere. Both studies therefore suggest that MSTIDs originate in the winter hemisphere, which means that during the local summer, waves generated in the opposite hemisphere propagate across the equator. This theory seems to be supported by a statistical study by Munro (1958), which depicted a mean daytime north-east and south-east propagation direction for MSTIDs during the winter and summer seasons, respectively, and which changed to north-west and south-west at night over Australia in the southern hemisphere. The study also found a low MSTID occurrence rate during equinox and no clear preferred propagation direction. Francis (1974) pointed out that there are other fundamental sources of MSTIDs besides auroral sources, since MSTIDs that propagate from the winter auroral region to the equator, pass through it and then propagate poleward in the opposite hemisphere, face a linear increase in period with range. The same goes for east-west propagating MSTIDs; they do not have auroral sources (Francis, 1974).

MSTIDs associated with polarised electric field

Ogawa *et al.* (2009) reported nighttime MSTIDs that propagate southwest (from the northern high latitudes to lower latitudes) during geomagnetically quiet conditions. Measurements by the Hokkaido SuperDARN radar (in Japan), the all-sky camera and GPS TEC were used. The event was observed from ionospheric scatter echoes as it had high Doppler velocities and wide spectral width. These echoes were related to 15-m-scale F region field-aligned irregularities (FAIs). At the same time, echoes from FAIs in sporadic E layers were observed, implying the existence of electrical coupling between the E and F regions along the geomagnetic field lines at night. Similarly, Suzuki *et al.* (2009) observed, by means of the Hokkaido radar (43.5°N, 143.6°E) and an OI 630-nm airglow imager based in Russia (53°N, 158.2°E), nighttime MSTIDs propagating in the southwest direction. The polarity of the Doppler velocity of the F region FAIs, caused by gradient drift instability, changed in a manner similar to the intensity of the airglow imager, i.e. positive and negative Doppler velocities coincided with airglow enhancement and the depletion region, respectively. The airglow intensity was proportional to the F layer conductivity (field-line-integrated Pedersen conductivity), with high intensity corresponding to high conductivity. In order to maintain continuity of electric current, in the region of perturbed conductivity, polarised electric field (\mathbf{E}_p) is generated perpendicular to the MSTIDs wavefront (Otsuka *et al.*, 2004, 2009; Suzuki *et al.*, 2009). All these studies, therefore, concluded that

the observed undulation could be due to the polarised electric field induced by the $\mathbf{E} \times \mathbf{B}$ plasma drift, as its direction is the same as the drift in the Doppler velocity data. Furthermore, [Suzuki *et al.* \(2009\)](#) showed that MSTIDs accompanied by FAIs and associated to polarised electric fields are common over a wide range of latitudes (from $\sim 35^\circ\text{N}$ to 53°N).

The contribution of polarised electric fields and gradient drift instability to the generation and development of nighttime MSTIDs have been reported, both with the use of instruments (e.g., optical imagers, GPS, DMSP satellites, VHF and Doppler radars) and theoretically (e.g., [Kelley and Miller, 1997](#); [Kelley *et al.*, 2003](#); [Shiokawa *et al.*, 2003](#); [Cosgrove *et al.*, 2004](#); [Otsuka *et al.*, 2007](#); [Saito *et al.*, 2007](#); [Otsuka *et al.*, 2009](#)). The mechanism involved in the generation and the development of nighttime MSTIDs can be explained as by [Otsuka *et al.* \(2007, 2009\)](#) and [Ogawa *et al.* \(2009\)](#): Ionospheric instabilities that acts through electrodynamical processes trigger MSTIDs, which causes perturbations in the Pedersen conductivity. Perturbations of the Pedersen conductivity result in an electric current flow discontinuity. Therefore, to maintain continuity of the current flow a polarised electric field is generated perpendicular to the wavefront of the MSTIDs. These electric fields are mapped along geomagnetic field lines and push the F region upward or downward by $\mathbf{E} \times \mathbf{B}$ drifts, causing undulation of the electron density. The other known source of mid-latitude nighttime MSTIDs is the Perkins instability ([Perkins, 1973](#)). The Perkins instability is introduced in the nighttime F region when a north-south electric field exists in addition to the eastward electric field component, which can cause spread F and gradients in the Pedersen conductance that leads to $\mathbf{E} \times \mathbf{B}$ instability ([Perkins, 1973](#)). In addition to the electric field, neutral wind velocity and gradient in the background density and Pedersen conductivity, produce Perkins instability with enhanced growth rate ([Hamza, 1999](#)). Nighttime MSTIDs at mid-latitudes that are generated by Perkins instabilities have wave fronts aligned in the northeast-southwest (northwest-southeast) in the southern (northern) hemisphere, similar to the MSTIDs caused by Es instabilities ([Cosgrove *et al.*, 2004](#)). [Figure 2.3](#) illustrates the mechanism in which the MSTIDs are generated in both hemispheres. The characteristics of this type of MSTIDs cannot be explained using the classical theory of gravity waves ([Kelley and Miller, 1997](#); [Otsuka *et al.*, 2004](#); [Suzuki *et al.*, 2009](#)) The linear growth rate of the Perkins instability is relatively small compared to the growth rate due to Es layer electric field polarisation ([Tsunoda and Cosgrove, 2001](#); [Cosgrove *et al.*, 2004](#)). [Huang *et al.* \(1994\)](#) showed that gravity wave seeding enhances the growth rate of the Perkins instability. Also, [Cosgrove and Tsunoda \(2004\)](#) showed that the electrodynamical coupling between the E and F region along the geomagnetic field lines significantly enhances the Perkins instability.

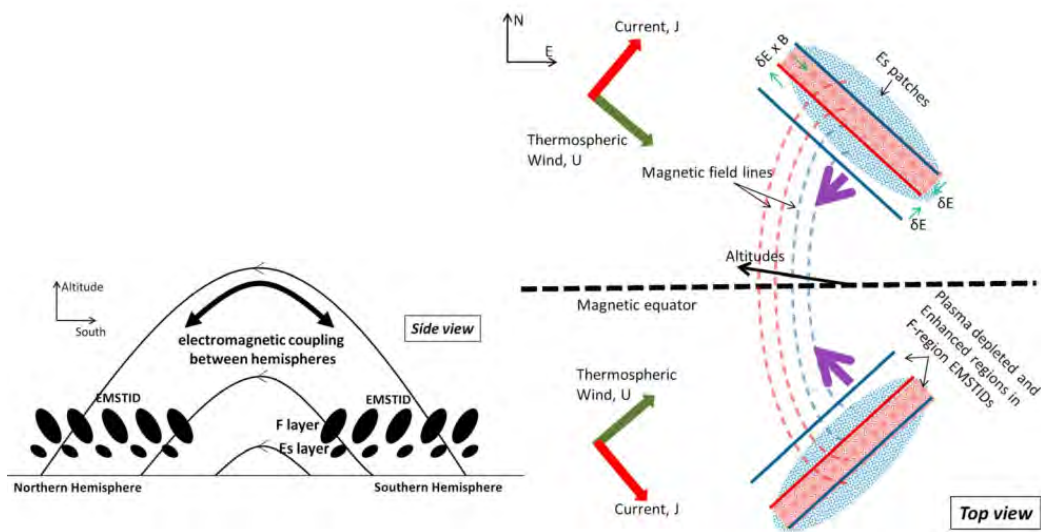


Figure 2.3: Schematic illustration of the coupling between E and F region both in northern and southern hemisphere (Narayanan *et al.*, 2018).

2.5 Neutral Wind

Neutral winds and electric fields imposed by the magnetosphere are two of the primary sources of plasma motion in high latitudes (Danskin, 2004). Neutral winds drive the motion of charged particles, or the other way round, by means of neutral-ion collision (Davies, 1990; Lu *et al.*, 1995; Drob *et al.*, 2015). The horizontal wind has two components based on its propagation direction; meridional (south-north) wind and zonal (east-west) wind. High-latitude heating causes the meridional wind, which plays a significant role in moving ionised particles along the magnetic field lines and transferring heat from high to lower latitudes. Vertical winds during storm or sub-storm time play an important role in changing the composition of the thermosphere and ionospheric density (Richmond and Matsushita, 1975).

Strong neutral winds may act as directional filters for waves propagating from the lower atmosphere by reflecting and trapping it and only permitting waves propagating in a specific direction to reach the ionosphere (Yeh *et al.*, 1972; Vadas, 2007; Figueiredo *et al.*, 2018). Theoretical studies by Waldock and Jones (1984) and Cowling *et al.* (1971), who used atmospheric models, demonstrated that the diurnal variation and hemisphere-specific propagation direction of MSTIDs is influenced by the neutral wind filtering effect. The neutral wind vector rotates clockwise in the northern hemisphere and counterclockwise in the southern hemisphere, which gives a similar diurnal variation of the MSTID propagation direction in each hemisphere (Cowling *et al.*, 1971; Yeh *et al.*, 1972; Waldock and Jones, 1984). In addition, Waldock and Jones (1984) showed that faster and longer-period waves and those propagating at 90° to the mean flow of the neutral wind are least affected by neutral winds. Neutral wind significantly affects the propagation direction of MSTIDs, since they have

phase velocities that are comparable to the speed of neutral winds (up to 200 ms^{-1}) (Cowling *et al.*, 1971; Yeh and Liu, 1974; Vadas, 2007).

Neutral wind can affect the propagation of MSTIDs in three ways; critical coupling (wave energy lost), reflection and penetration (Cowling *et al.*, 1971). When the propagation speed of a MSTID is the same as the speed of the neutral wind, which is called a critical level, the MSTID is blocked from propagating vertically due to the filtering effect of the wind (Figueiredo *et al.*, 2018). Experimental investigations confirm the directional filtering by neutral winds described in theoretical studies. Kalikhman (1980) showed that daytime MSTIDs are filtered by neutral winds and directed in the opposite direction. The results were obtained by means of Doppler radars in Irkutsk, Russia. Waldock and Jones (1986) reported similar results that show the effect of neutral wind on the propagation direction of F region TIDs by using the HF Doppler network in Leicester, U.K. (52.53°N , 1.13°W). They found that TIDs commonly propagate $130\text{-}140^\circ$ clockwise from the wind azimuth with clockwise rotation through the day, as described in the theoretical studies. This proved that the lower atmosphere wind has a more significant influence on thermospheric waves than previously expected.

2.6 Joule heating

The main causes of energy dissipation in the thermosphere are ion drag, viscosity and thermal diffusivity (Hines, 1960; Vadas, 2007). TIDs are a secondary cause of energy dissipation, through Joule heating, with the energy dissipating as they travel through the ionosphere. Joule dissipation causes attenuation of TIDs, but the most important cause of wave attenuation is the viscosity and heat conduction effects (Richmond, 1978). Joule heating ($\mathbf{J} \cdot \mathbf{E}$) is a function of the electric field (\mathbf{E}) and the Pedersen conductivity (σ_P) that is parallel to \mathbf{E} . The Joule heating dissipation rate (W_J) at a specific altitude can be calculated from the Pedersen conductivity, the electric field, geomagnetic field (\mathbf{B}) and neutral wind (\mathbf{V}_N) using the following formula (Baker *et al.*, 2004):

$$W_J = \sigma_P [\mathbf{E} + \mathbf{V}_N \times \mathbf{B}]^2. \quad (2.24)$$

The height-integrated Joule heating rate can be estimated by assuming that the electric field, geomagnetic field and neutral wind velocity are constant over the height range where Joule heating is being determined (Baker *et al.*, 2004). Therefore the height-integrated Joule heating is calculated by:

$$Q_J = \sum_P E^2 + 2 \sum_P \mathbf{E} \cdot (\mathbf{V}_N \times \mathbf{B}) + \sum_P (\mathbf{V}_N \times \mathbf{B})^2, \quad (2.25)$$

where \sum_P is the height-integrated Pedersen conductance. The first term of Equation 2.25 represents the energy contribution by plasma convection against a zero neutral velocity (Q_C), which is always a positive value (Baker *et al.*, 2004; Billett *et al.*, 2018). The contribution by the motion of the neutral wind relative to the plasma is expressed in the second term (Q_{W1}), while the third term represents the heating due to neutrals moving against a motionless plasma (Q_{W2}). Stephenson and Walker (2002) reported an estimation of power dissipation due to a Pc5 pulsation (with a central frequency of 3.3 mHz) over a defined area covered by the pulsation as observed by the SANA HF radar. They used the Doppler velocity analytic signal amplitude together with the magnetic field, taken from the International Geomagnetic Reference Field (IGRF) model, to estimate the electric field over the area where pulsations were observed. For the Joule heating estimation by Stephenson and Walker (2002) the neutral wind term was neglected, as previous work suggested that at high altitudes the dynamo of the neutral wind is smaller than the magnetospheric dynamo. This would imply that the first term in Equation 2.25 is the most dominant (Aruliah *et al.*, 2004; Baker *et al.*, 2004). However, work done by Lu *et al.* (1995), Cierpka *et al.* (2000), Aruliah *et al.* (2004) and Billett *et al.* (2018) showed it is important to include the neutral wind component in Joule heating estimation.

The electric field in the Joule heating estimation shown in Equation 2.25 is known as the polarised electric field in the case of TIDs (Otsuka *et al.*, 2007; Suzuki *et al.*, 2009). The polarised electric field is generated perpendicular to the wave front of the TIDs to keep the flow of current in the F region that is disrupted by the propagation of TIDs. Upward and downward movement of the plasma is a result of $\mathbf{E}_p \times \mathbf{B}$, where the direction of E_p alters 180° (parallel or anti-parallel to TID's propagation direction).

2.7 Magnetic storms and substorms

Magnetic storms are intense magnetospheric disturbances that are caused by solar activity, such as flares, CMEs, CIRs, or changes in the solar wind. During these forms of solar activity a southward interplanetary magnetic field (IMF) reconnects with the dayside northward Earth magnetic field lines, which increases the energy transfer into the magnetosphere. This will cause enhancement of the ring current, i.e. the current caused by the motion of charged particles that are trapped by Earth's magnetic field. This is characterized by a decrease in the disturbance storm-time (Dst) index (Moldwin, 2008). Commonly, there are three phases in a magnetic storm, namely the onset(compression) phase, main phase and recovery phase. The onset of a magnetic storm occurs when the magnetosphere is compressed suddenly due to the passing of interplanetary shock waves and the region of high pressure behind the shock waves (Akasofu, 1968). The main phase of a storm is characterized by an increase in the ring current, whereas a decrease in the ring current marks the recovery phase.

Contrary to magnetic storms, substorms have a shorter lifetime which lasts for 1 to 3 hours (Akasofu, 1968). They are characterized by enhanced auroral behaviour due to an increase in auroral ionospheric currents (Akasofu, 1968; Moldwin, 2008). During a substorm, the auroral arc expands poleward and westward (Akasofu, 1968; Moldwin, 2008). The effects of magnetic substorms are localized to nightside of the Earth's magnetosphere and ionosphere (Moldwin, 2008). Substorms can also be identified by the horizontal component of the magnetic field as high-latitude negative magnetic bays, mid-latitude positive bays and low-latitude Pi2 pulsations (Wu *et al.*, 2004; Forsyth *et al.*, 2015).

2.8 Summary

This chapter presented a brief introduction to Earth's atmosphere and ionosphere. The formation mechanism and characteristics of AGWs and TIDs at different regions are discussed. The literature review on TIDs has shown that we know very little about TIDs generated at southern hemispheric high-latitudes. Discussion on neutral wind and how it can affect the propagation direction of MSTIDs has been covered. The chapter also briefly explains how TIDs dissipate energy through Joule heating. In the later chapter, the estimation of the energy dissipated from an MSTID will be shown using the equations given in this chapter. Lastly, a short introduction to magnetic storms and substorms were given.

Chapter 3

Instrumentation and Models

3.1 Introduction

In this chapter, the Super Dual Auroral Radar Network (SuperDARN), and specifically the South African National Antarctic Expedition (SANAE) radar, and the Halley radar which were used to determine characteristics of TIDs will be described. The radar data were supplemented with TEC data from GPS receivers collocated within the radars' common field of view, and therefore GPS and TEC are also discussed in this chapter. A brief explanation of the DMSP satellites that were used to determine the energy input in the region where the TIDs were observed, is included. A general overview of magnetometers and their measurements, as well as the global indices that were obtained from those measurements (e.g. Dst, AE, Kp and PC south/north) will be presented since these were used to determine the mechanisms that generated the observed TIDs events. Lastly, a brief introduction to the horizontal wind model version 2014 (HWM14) and the international geomagnetic reference field (IGRF) models will be offered, as these models were used to estimate energy dissipation by an MSTID.

3.2 SuperDARN HF radar network

SuperDARN has been used for several decades to study the dynamics of the Earth's magnetosphere, plasma convection and the upper atmosphere, i.e. ionosphere, thermosphere and mesosphere (Greenwald *et al.*, 1995; Chisham *et al.*, 2007; Lester, 2013; Nishitani *et al.*, 2019). Figure 3.1 illustrates how SuperDARN may be used to study different ionospheric-magnetospheric phenomena. GWS/TIDs are one of the phenomena that has been studied widely using SuperDARN at high and mid-latitudes (Samson *et al.*, 1989; Ogawa *et al.*, 2009; Suzuki *et al.*, 2009). The radars operate

between 8 and 20 MHz, which is in the HF band. These frequencies are preferable for the study of high latitude irregularities as they can be easily refracted by the ionosphere, allowing for the transmitted signal to be quasi-perpendicular to the magnetic field lines, which is a condition necessary for backscatter of the signal to the radar (Chisham *et al.*, 2007).

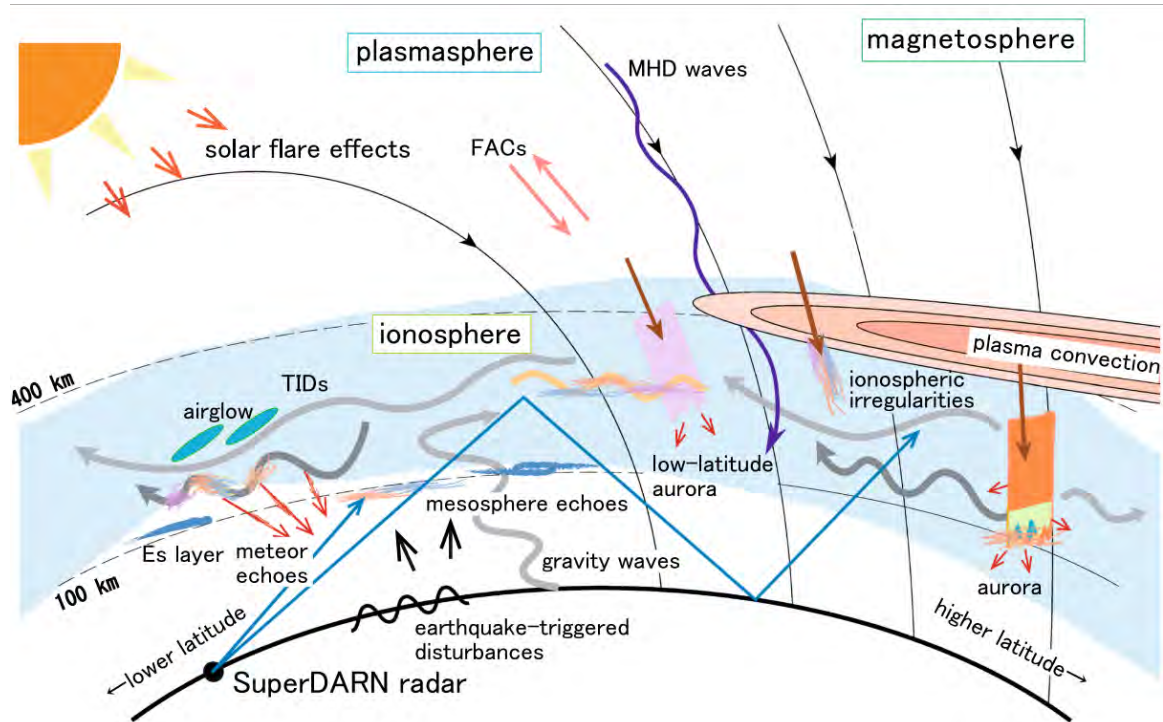


Figure 3.1: Applications of SuperDARN (Nishitani *et al.*, 2019).

SuperDARN radars are coherent scatter radars since echoes backscatter from magnetic field-aligned irregularities separated by half the wavelength of the transmitted radar signal (Liu *et al.*, 2012), as well as from ground surface irregularities. This means that a radar operating at the frequency of 12 MHz will have a wavelength of 25 m, and therefore can observe irregularities separated by 12.5 m. In standard mode, a SuperDARN radar typically scans through 16 beams of azimuthal separation 3.24° , with a dwell time of 3 s or 7 s on each beam, thus completing a full scan of $\sim 52^\circ$ azimuths in 1 and 2 minutes, respectively. A transmitted pulse length of 300 μs implies a range resolution of 45 km along each beam, with the possibility of measurements up to 75 range gates (3500 km). The radars are thus able to detect TID wavelengths in the range of ~ 100 to ~ 1000 km (Grocott *et al.*, 2013). Many of the SuperDARN radars have two arrays, the main array and interferometer array, which are separated by some distance. The main array consists of electronically phased antennas that are used to send and receive signals. The interferometer array is used only for receiving backscattered signals which are then cross-correlated with signals received at the main array in order to measure the phase difference between these received signals (Chisham *et al.*, 2008). The phase difference is used to determine the

elevation angle of the backscattered signal, which enables estimation of the altitude of the irregularities responsible for the backscatter (Baker *et al.*, 2008; Chisham *et al.*, 2008).

SuperDARN consists of HF radars located in the mid- to high latitudes of the northern and southern hemispheres. The radars' field of view (FOV) are shown in Figure 3.2, with the different colours indicating the latitudes where the radars are located (i.e. green for polar cap, blue for high latitude and orange for mid-latitude). As of 1 July 2020, there are 38 HF radars, i.e. 24 in the northern hemisphere and 14 in the southern hemisphere, operated collaboratively by 10 countries. The collaborating countries are Australia, Canada, China, France, Italy, Japan, Norway, South Africa, United Kingdom and the United States of America.

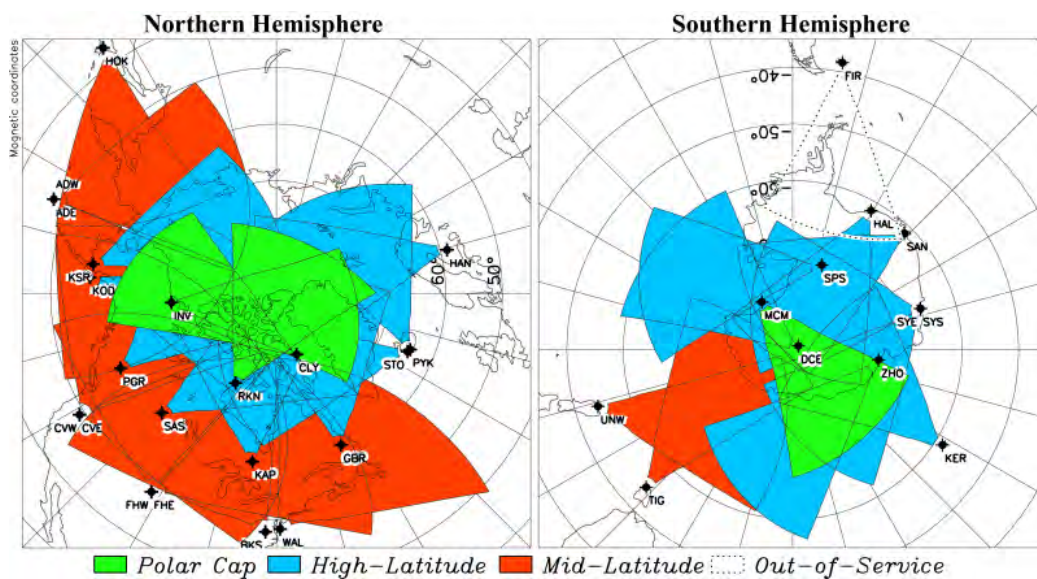


Figure 3.2: Field of view plot of the SuperDARN network in the north and south hemispheres (credit: http://vt.superdarn.org/tiki-list_file_gallery.php?galleryId=81)

SuperDARN works at different operation mode settings. The radars work in common-time mode 50% of the time, which means the radars operate in standardized settings (Ruohoniemi and Baker, 1998). The other 50% of the time the operation is divided into a special mode (20%) and discretionary mode (30%). The special mode is used to do specific experiments agreed upon by the group, whereas individual experiments can be run in the discretionary mode.

Depending on the ionosphere's horizontal and vertical electron density, there are three possible propagation paths for HF signals backscattered from ionospheric irregularities. Figure 3.3 illustrates the possible paths a backscattered signal can follow. The backscattered signal can be directly backscattered from the ionosphere to the transmitter, which is called 0.5-hop path. The signal can get refracted to the ground from the ionosphere and backscatter to the radar, which is called 1-hop

path, or backscatter to the ionosphere and down to the ground again. The signal that backscatters to the radar from this point will have 2-hop propagation path. The other propagation mode is the 1.5-hop, which means the signal is first refracted to the ground and then to the ionosphere from where it will backscatter to the radar. Depending on the altitude at which the signal was backscattered to the radar, it can be 1.5 E or 1.5 F (E and F representing the E and F ionospheric regions). The 1E, 1F and 2F propagation modes are known as ground scatter, since the received signal is reflected from the ground (Danskin, 2004).

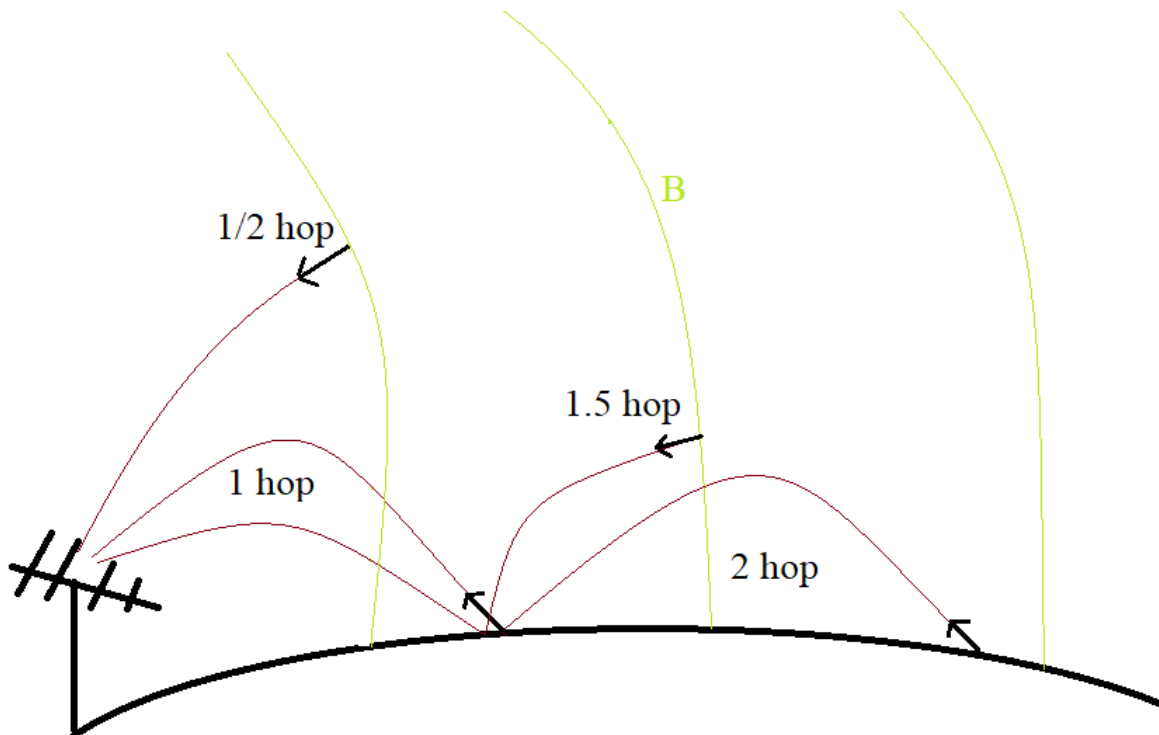


Figure 3.3: Schematic illustration of the different paths backscatter signals will follow for 0.5 hop, 1 hop, 1.5 hop and 2 hop backscatters. The diagram is based on ray paths shown in the ray tracing model (<http://vt.superdarn.org/tiki-index.php?page=Ray-tracing>).

The primary data of SuperDARN radars are a complex temporal autocorrelation function (ACF) of the backscattered signal calculated for each range gate (Baker *et al.*, 1995; Vallieres *et al.*, 2004). The complex ACF signal is calculated by autocorrelating signals received at different lags (from non-evenly spaced pulses) for a specific range gate. The backscattered power (or signal-to-noise ratio, SNR), the Doppler velocity and the width of the Doppler power spectrum (or spectral width) for each range are calculated from ACFs that are fitted with standard functions (FITACF). Figure 3.4 shows the raw ACF data and the fitted data for the 17 March 2013 TID event at 02:02:49 UT as observed from beam 7 and gate 20 of the SANAE radar. The real part ($\text{Re}\{R\}$) and the imaginary part ($\text{Im}\{R\}$) of the raw ACF data are plotted in red and blue, respectively, in the top panel of Figure 3.4. The phase shown in Figure

3.4 is calculated from the angle between the real and imaginary part of the complex ACF data ($\phi(\tau) = \tan^{-1}(\text{Im}\{R(\tau)\}/\text{Re}\{R(\tau)\})$), and the magnitude of the signal is used to determine the power ($P(\tau) = |R(\tau)|$), as shown in the bottom right panel of Figure 3.4. The phase variation with lag indicates the Doppler shift on the returned signal frequency (Ribeiro *et al.*, 2013).

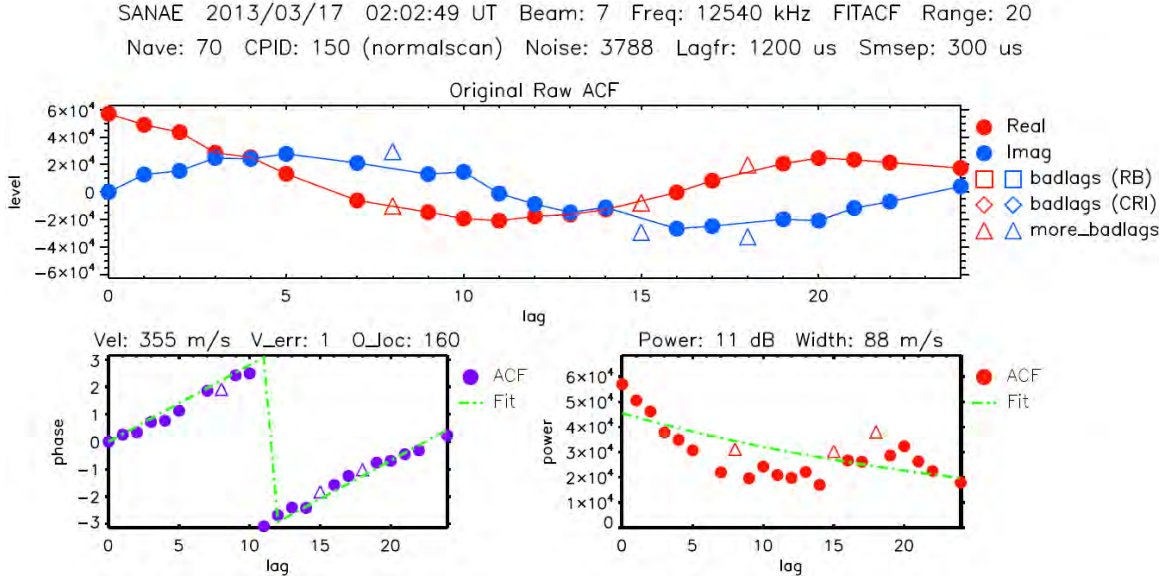


Figure 3.4: The raw ACF data and the fitted data for the 17 March 2013 TID event at 02:02:49 UT from SANAE radar beam 7, gate number 20. The data was plotted with the VT SuperDARN ACF plotting and fitting tool (<http://vt.superdarn.org/tiki-index.php?page=ACF+Plotting+Tools>).

The methodology used to calculate the Doppler velocity and spectral width briefly described here can be found in Baker *et al.* (1995) and Ribeiro *et al.* (2013). The Doppler velocity is calculated from the slope of the fit to the phase variation with lag time (shown by the green dash line in bottom left panel of Figure 3.4) as follows:

$$V = \frac{\lambda}{4\pi} \frac{\partial\phi}{\partial\tau}, \quad (3.1)$$

where V is the Doppler velocity, λ is the radar wavelength and $\frac{\partial\phi}{\partial\tau}$ is the change in phase with lag (τ) estimated from a least-squares fit. The factor of 4 represents the path of the signal (two-way path). The spectral width is calculated by fitting the exponential or Gaussian function to the exponential decay of power/amplitude of the ACF data, since the power variation of the ACF data shows an exponential decay ($|R(\tau)| = R_0 \exp(-\tau/t_d)$). The equation for the spectral width is:

$$w = \frac{\lambda}{2\pi t_d}, \quad (3.2)$$

where w is the spectral width and t_d is a decay-time constant from the slope of the least-squares fit of log of power ($\log(R(\tau))$). By using a linear least-squares fit on the natural logarithm of the ACF power data, the backscatter power or the SNR in dB is estimated as:

$$\text{SNR} = 10\log_{10}(R_0/N), \quad (3.3)$$

where R_0 is the fitted lag zero power, which is the y-intercept of the fitting, and N is the noise power level.

The Doppler velocity measurements of the irregularities are a proxy for the line-of-sight component of the $\mathbf{E} \times \mathbf{B}$ drift velocity of the plasma in which they are embedded (Ruohoniemi and Baker, 1998). Positive (negative) Doppler velocity indicates that the target is traveling towards (away from) the radar (Samson *et al.*, 1989). Ground scatter signals, i.e. signals reflected to the ground from the ionosphere and backscattered with twice the distance to the ionospheric reflection point, are identified from radar data as having a low Doppler velocity between -50 & 50 ms^{-1} and a spectral width of less than 20 ms^{-1} (Milan *et al.*, 1997). In the case ground scatter, Doppler velocities imply vertical movement of layers of the ionosphere, whereas for ionospheric scatter, Doppler velocities translate to a movement away from or toward the radar along any beam (Samson *et al.*, 1989).

3.2.1 SANAE and Halley HF radars

The South African National Antarctic Expedition (SANAE) and Halley HF radars are part of the SuperDARN network based in Antarctica. The principal investigator (PI) for the SANAE HF radar is Prof. Michael Kosch from the South African National Space Agency (SANSA). The PI for the Halley radar is Dr Gareth Chisham from the British Antarctic Survey (BAS), Antarctica. For this study, data from the SANAE and Halley SuperDARN radars, which have a substantial common FOV, as shown in Figure 3.5, were used. Note that the area encompassed by the blue (red) lines shows the SANAE (Halley) HF radar's FOV, while the numbers 0 and 15 indicate the first and last beams, respectively, of the radars.

The Halley radar made the first observation using 16 HF log-periodic antennas in January 1988 (Baker *et al.*, 1989). The radar was switched off between December 2007 and February 2011 during the rebuilding of the Halley BAS station. The SANAE SuperDARN radar saw first light on 3 March 1997 at the SANAE IV base located in Vesleskarvet, Antarctica (Walker *et al.*, 1998). The radar has implemented two antenna designs so far, namely the log-periodic antenna and twin-terminated folded-dipole antenna. The twin-terminated folded-dipole antennas replaced the log-periodic antennas after being destroyed by a storm during the 2008 Austral winter. The new antenna start operating in July 2009. Pictures of the log-periodic and twin-terminated folded-dipole antennas installed at the SANAE IV base are shown in Figure 3.6. The twin-terminated folded-dipole antenna design is simple and inexpensive relative to the

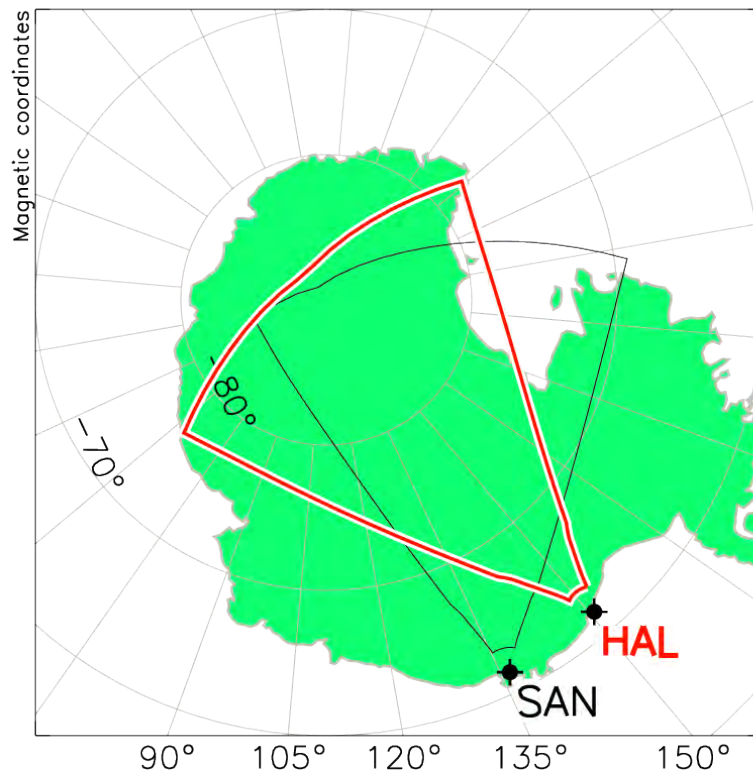


Figure 3.5: Field of view of the SANA E and Halley HF radars in magnetic coordinate.

previous log-period antenna design (Baker *et al.*, 2008). The SANA E SuperDARN radar was upgraded to digital transceivers during the 2013/2014 Australian summer. The first data from the new digital radar was recorded on 18 February 2014.



(a)



(b)



(c)

Figure 3.6: Photographs of the SANAE radar (a) log-periodic antennas, and (b) twin-terminated folded-dipole antennas, as well as (c) a full view of the SANAE IV base.

3.3 Global Positioning System

The Global Positioning System (GPS) is a space-based satellite navigation system for the provision of position, time and velocity information 24/7 worldwide. GPS is one of the first satellite-based navigation systems, and owned by the United States of America. Other global navigation satellite systems include GLONASS from Russia, Galileo from the European Union and Compass/BeiDou Navigation Satellite System (CNSS/BDS) from China. The GPS project was started in the late 1970s and reached its full operation in early 1995 (Kaplan and Hegarty, 2006; Gleason and Gebre-Egziabher, 2009). The constellation of GPS satellites includes 24 satellites on six evenly-space orbital planes (Hofmann-Wellenhof *et al.*, 1992; Kaplan and Hegarty, 2006). GPS satellites orbit the Earth at an orbital radius of approximately 26,600 km using a nearly circular orbit with an inclination of 55° (Mohinder *et al.*, 2001; Misra and Enge, 2006).

GPS consists of three main segments: the space segment, the ground-control or monitoring segment and the user segment (see Figure 3.7). The ground-control segment is used to monitor the status of satellites by uploading navigation and other data to the satellite (Kaplan and Hegarty, 2006). The space segment refers to the GPS satellites that are orbiting the Earth twice a day (one rotation taking 11.96 hours). The GPS satellites receive navigation data from the control segments and send signals to both the user and control segments. GPS satellites transmit signals in the ultra-high frequency (UHF) band using at least two L-band channels with carrier frequencies of L1=1.575 GHz, L2=1.227 GHz and L5=1.176 GHz, the latter being broadcast only by newer satellites. However, only L1 and/or L2 are generally used in ionospheric studies. Each GPS satellite generates a short and a long code referred to as coarse-acquisition (C/A) and precision (P(Y)) code, respectively (Kaplan and Hegarty, 2006). The L1 carrier signal is modulated by two pseudo-random noise (PRN) sequences: the P code with a chip frequency of 10.23 MHz and the C/A code with a chip frequency of 1.023 MHz. The L2 channel is modulated using the C/A code only (Hofmann-Wellenhof *et al.*, 1992; Elósegui *et al.*, 1995). The C/A code is reserved for civilian use, whereas the P(Y) code is reserved for military and authorised users only. The main advantage of using two carrier signals, e.g. L1 and L2, with different frequencies, is the ability to measure propagation delay of the signals as they traverse the ionosphere relative to signals propagating at the speed of light in free space. Because the ionosphere is dispersive, the propagation delay is directly proportional to the total electron content (TEC) of the ionosphere and inversely proportional to the square of the signal frequency (Hofmann-Wellenhof *et al.*, 1992; Mohinder *et al.*, 2001). The ionospheric delays can be corrected by using the information from both the L1 and L2 signals. The user segment comprises the GPS receivers, which use the L-band signals transmitted from the satellites to determine the user's position (Kaplan and Hegarty, 2006). Receivers use navigation data modulated onto the ranging signal to determine the location of the satellite at the time of signal transmission. The satellite-to-user range is determined from the

signal's transit time calculated from the ranging code (Kaplan and Hegarty, 2006). Caesium and/or rubidium atomic clocks are used by GPS satellites to give accurate timing information (Hofmann-Wellenhof *et al.*, 1992; Mohinder *et al.*, 2001). There are two basic types of receivers: dual-frequency receivers which track the L1 C/A codes and P(Y) code on L1 and L2, and single-frequency receivers which only track the C/A code (Kaplan and Hegarty, 2006).

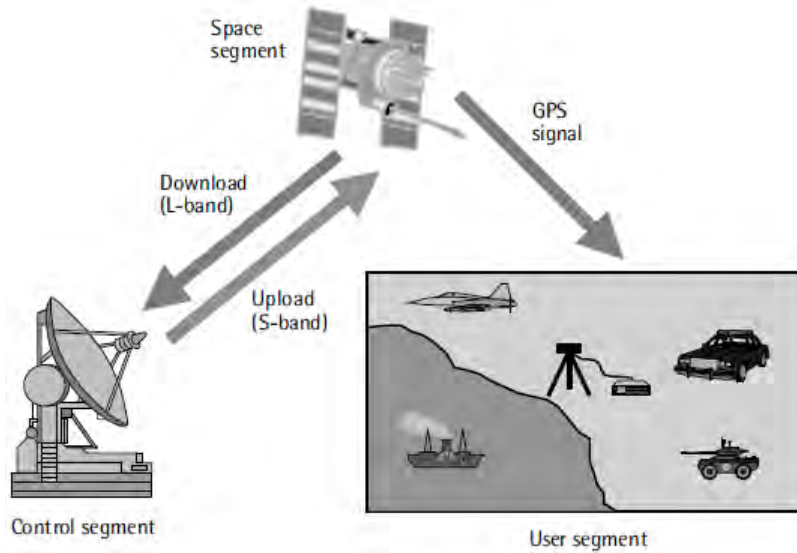


Figure 3.7: The main segments of GPS: ground-control segment, space segment and user segment (El-Rabbany, 2002).

3.3.1 GPS use in ionospheric studies

GPS provides continuous (24/7) ionospheric measurements at high temporal resolution and has good global coverage (land), where usually the data are available in near-real-time (Mannucci *et al.*, 1999; Mendillo, 2006). GPS data have been used for ionospheric studies since the 1980s after the deployment of GPS satellites (Lanyi, 1986; Klobuchar *et al.*, 1987; Lanyi and Roth, 1988; Mannucci *et al.*, 1999). The processing of GPS signals can yield the integrated electron density of the ionosphere along the ray path of the signal (Mannucci *et al.*, 1999).

A radio signal experiences refraction, reflection and attenuation as it propagates through the ionosphere. The expression for the refractive index (n) is given by Appleton-Hartree formula as follows, when both collisions and magnetic field effects are neglected (Davies, 1990):

$$n^2 = 1 - X, \quad (3.4)$$

where $X = \frac{N_e e^2}{\epsilon_0 m \omega^2}$, which can also be expressed using the plasma frequency and the wave frequency $X = f_p^2 / f^2$. The phase refractive index can be written by approxi-

mating to the first order as:

$$n_p \approx (1 - 1/2 \frac{f_p^2}{f^2}), \quad (3.5)$$

Substituting all the parameters (i.e electron mass, electron charge and permittivity of free space) in the plasma frequency equation gives $f_p = 8.98\sqrt{N_e}$, where N_e is the electron density in m^{-3} .

$$n_p = (1 - 40.3N_e/f^2). \quad (3.6)$$

The phase and group refractive indices, can be related by means of the following equation:

$$n_g = n_p + f \frac{dn_p}{df}. \quad (3.7)$$

Therefore the phase and group velocity of the radio wave is expressed as

$$n_p = 1 - 40.3N_e/f^2, \quad (3.8)$$

$$n_g = 1 + 40.3N_e/f^2, \quad (3.9)$$

Equations 3.8 and 3.9 show that $n_g > n_p$. Therefore there will be a group delay and a phase advance ($v_g < v_p$) because the electron density (N_e) is always positive (Hofmann-Wellenhof *et al.*, 1992). The phase delay ($\Delta\tau_p$ in seconds) can be calculated by calculating the difference between the travel time of a signal in a varying refractive index ($n(l)$) and the same signal in a vacuum ($n(l) = 1$), which can be expressed as (Misra and Enge, 2006):

$$\begin{aligned} \Delta\tau_p &= 1/c \int_S^R (n_p(l) - 1)dl, \\ &= -\frac{40.3}{cf^2} \int_S^R N_e(l)dl, \end{aligned} \quad (3.10)$$

where the travel time of the signal from the satellite to the receiver is derived by integrating the refractive index along the path ($\tau = 1/c \int n(l)dl$). The number of free electrons in the path of the radio signal, known as total electron content (TEC), is defined as (Misra and Enge, 2006):

$$\text{TEC} = \int_S^R N_e(l)dl, \quad (3.11)$$

where $N_e(l)$ is the variable electron density along the signal path, and the integration is along the signal path from the satellite to the receiver. TEC is measured in TEC units (1 TEC units = 10^{16} electrons/ m^2). Therefore, by substituting TEC in equation 3.10 the phase delay becomes:

$$\Delta\tau_p = -\frac{40.3\text{TEC}}{cf^2}. \quad (3.12)$$

This shows that the time delay experienced by a GPS signal with frequency f is directly proportional to TEC encountered along the signal path and inversely proportional to the square of the signal frequency. The negative sign in equation 3.12 implies the phase is advanced (Misra and Enge, 2006). The phase delay (I_p) in length is expressed as,

$$I_p = c\Delta\tau_p = -40.3\text{TEC}/f^2. \quad (3.13)$$

Similarly, the group delay (I_g) can be determined from the group refractive index as:

$$I_g = 40.3\text{TEC}/f^2. \quad (3.14)$$

Equations 3.13 and 3.14 show that the code measurements are delayed, and the carrier phases are advanced, respectively, for the GPS signals, and the delay is in direct proportion to TEC along the signal path (Hofmann-Wellenhof *et al.*, 1992; Misra and Enge, 2006). This means that the code pseudoranges are measured too long, and that the carrier phase pseudoranges are measured too short relative to the straight-line path length from the satellite to the receiver (Hofmann-Wellenhof *et al.*, 1992).

3.3.2 TEC measurement derived from GPS

The code and carrier phase measurements are given below with all error sources, as shown in Gao and Liu (2002):

$$P_i = \rho + c(dt - dT) + d_{orb} + d_{trop} + k_i I + b_{P_i} - B_{P_i} + d_{mult/P_1} + \varepsilon(P_i), \quad (3.15)$$

$$\Phi_i = \rho + c(dt - dT) + \lambda_i N_i + d_{orb} + d_{trop} - k_i I + b_{\Phi_i} - B_{\Phi_i} + d_{mult/\Phi_i} + \epsilon(\Phi_i), \quad (3.16)$$

where

ρ is the true geometric range between receiver and satellite in metres

dt and dT are the satellite and receiver clock error with respect to GPS time in seconds, respectively

λ_i is the wavelength of GPS signal on L1 and L2 in metres

N_i is the carrier phase integer ambiguity in cycles

d_{orb} is the satellite orbit error in metre

d_{trop} is the tropospheric delay

$$k_i = \frac{f_i^2}{f_1^2 - f_2^2}, i = 1, 2$$

I is the ionospheric delay in metre

b and B are the satellite and receiver hardware delay in metres, respectively

d_{mult} is the multipath effect

$\epsilon(P)$ and $\epsilon(\Phi)$ are the measurement noise on code and phase in metres.

TEC can be estimated from the difference between the L1 and L2 code observables of the dual frequency receivers:

$$P_1 - P_2 = -I + b - B + \epsilon(P_1 - P_2), \quad (3.17)$$

where $b = b_{p_1} - b_{p_2}$ and $B = B_{p_1} + B_{p_2}$ are the differential hardware delays between the L1 and L2 frequency bands. They are stable biases in time scale of days and months (Gao and Liu, 2002). After replacing the ionospheric delay I with equation 3.14, equation 3.17, becomes:

$$P_1 - P_2 = 40.28 \left(\frac{1}{f_1^2} - \frac{1}{f_2^2} \right) \text{TEC} + b - B + \epsilon(P_1 - P_2). \quad (3.18)$$

Ignoring the other error sources and rewriting the equation in terms of TEC gives:

$$\begin{aligned} \text{TEC} &= \frac{1}{40.28} \left(\frac{f_1^2 f_2^2}{f_2^2 - f_1^2} \right) [P_1 - P_2], \\ &= 9.5 \times 10^{16} [P_1 - P_2]. \end{aligned} \quad (3.19)$$

Similarly, TEC from the carrier phase measurement is expressed as:

$$\text{TEC} = 9.5 \times 10^{16} [\Phi_1 - \Phi_2 + \lambda_2 N_2 - \lambda_1 N_1]. \quad (3.20)$$

Both the code and phase measurements of L1 and L2 can be utilized to estimate TEC of the ionosphere. The advantage of using the code measurement is that it is unambiguous, but it is noisy. On the other hand, the carrier phase measurement gives estimate of TEC, but with an ambiguity of integer values (Mannucci *et al.*, 1999; Misra and Enge, 2006).

3.4 Defense Meteorological Satellite Program (DMSP)

The Defense Meteorological Satellite Program (DMSP) comprises Sun-synchronous satellites with polar orbit at an altitude of ~ 840 km (Yin *et al.*, 2009). DMSP spacecraft started operating in the 1960s, and have been providing space weather information since 1977 using the auroral particle spectrometer (SSJ5), the top-side ionospheric plasma monitor (SSIES), the fluxgate magnetometer (SSM), and downward-looking (SSUSI) and horizon-looking (SSULI) ultraviolet imaging systems. The SSJ5 (5 represents the version of the sensor) sensor measures ion and electron precipitation in the range of 0.03 - 30keV. The SSIES sensors measure the plasma density, cross-track drift and scintillation (Ferdousi *et al.*, 2019). There are up to 4 DMSP spacecrafts active at any given time, with the satellites currently operational being

F15 (since December 1999), F16 (since October 2003), F17 (since November 2006) and F18 (since October 2009). F19 only ran between April 2014 and February 2016 (refer to <https://dmsp.bc.edu/html2/index.html> accessed on 27-05-2021). The electron and ion flux data from the DMSF satellites were used to obtain the energy input in the areas where the TIDs were observed, thus enabling the determination of possible TID source mechanisms.

3.5 Magnetometer

A magnetometer is used to monitor the Earth's magnetic field strength and direction. These can be used to indirectly measure ionospheric currents since the Earth's magnetic field strength and direction are altered by currents flowing in the ionosphere. The fluxgate magnetometer and the proton precession magnetometer represent the two main magnetometer types. The fluxgate magnetometers measure relative changes in the geomagnetic field, whereas the proton precession magnetometers measure absolute values of the geomagnetic field. The fluxgate magnetometers measure three different components of the Earth's magnetic field, namely northward (X), eastward (Y), and downward (Z), which are used to derive the H (horizontal field), I (inclination angle), D (declination angle) and F ($\sqrt{H^2 + Z^2}$) components (see Figure 3.8). The H component is a good indicator of storm, substorm and ULF pulsation events and it is used in the derivation of geomagnetic indices, such as the AE index, Kp index, Dst index, SYM/H and ASY/H (Davis and Sugiura, 1966; Sutcliffe, 1998; Mtumela *et al.*, 2015). For this project, data from the SANAE and Halley fluxgate magnetometers, located in Antarctica, and geomagnetic indices were used to determine the geomagnetic condition prior to the occurrence of the TID events.

3.5.1 Geomagnetic indices

Dst index

The Dst index measures the fluctuations of the ring current using the hourly averaged measurements of the H component of the magnetic field from 4 stations; Hermanus (-33.3° , 80.3°), Kakioka (26.0° , 206°), Honolulu (21.0° , 266.4°), and San Juan (29.9° , 3.2°) in magnetic dipole latitude and geomagnetic latitude (Saba *et al.*, 1997; Wanliss and Showalter, 2006). The magnitude of the Dst index is used to classify geomagnetic storms according to their intensity. Magnetic conditions where $Dst \leq -100$ nT are classified as great storms, conditions where Dst ranges between -50 nT and -100 nT as moderate storms, and between -30 nT and -50 nT are classified as weak storms (De Campra and De Artigas, 2004). The Dst index is also used to identify the different phases of a storm. The onset of a storm is characterised by an increase of up to tens of nT in the Dst index that lasts for 10 minutes to hours (Moldwin, 2008; De Campra and De Artigas, 2004). A sharp decrease in the Dst index indicates the main phase,

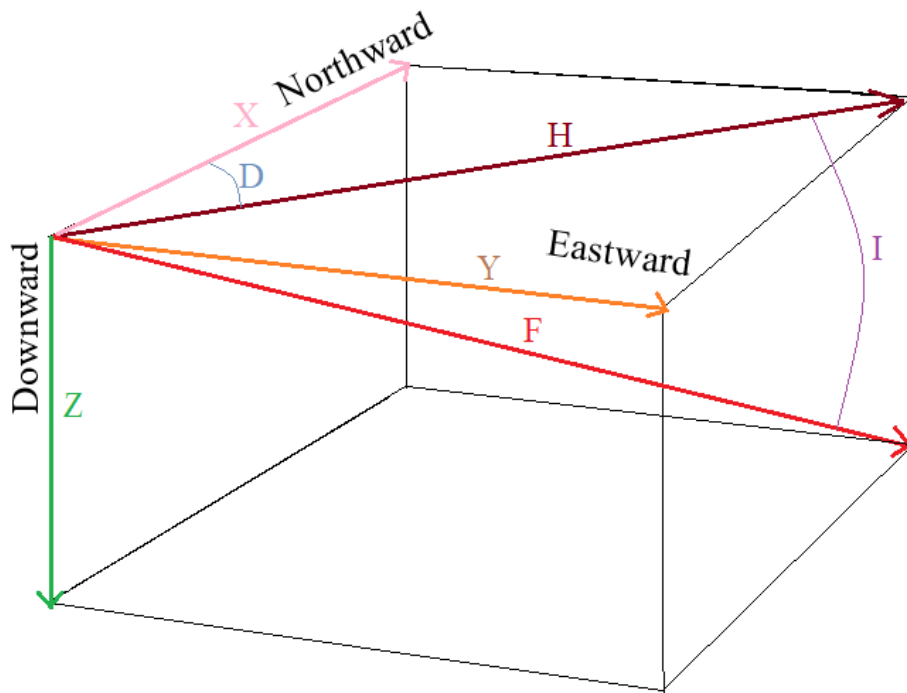


Figure 3.8: Components of Earth's magnetic field.

and at the same time the AE index increases. The recovery phase occurs when the Dst index slowly recovers to a pre-storm level and can last for several days (Saba *et al.*, 1997; Moldwin, 2008).

Kp index

The Kp index is a 3-hourly index based on the H component of the magnetic field measurements derived from subauroral-zone magnetometer stations located in Australia, Canada, Denmark, Germany, Netherlands, New Zealand, Sweden, United Kingdom and United States. The Kp index measures the storm contribution by both the ring current and auroral electrojet (Rostoker, 1972). This index is derived from the quasi-logarithmic relation with the amplitude of the disturbance (Davis and Sugiura, 1966). The linear version of the Kp index is the ap index. The Kp index varies from 0 to 9 and a value less than 4 characterises a geomagnetically quiet period, while minor to extreme storms have Kp values between 4 and 9.

AE index

The auroral electrojet (AE) index is used to study auroral zone ionospheric currents, which are known as auroral electrojet currents. The AE index is a good alternative for direct auroral observations to determine the onset of a substorm, as it is almost continuously available (Forsyth *et al.*, 2015). The AE index is derived from the H component of the magnetic field measurements taken from 12 auroral zone stations in the northern hemisphere (Ballatore and Maclellan, 1999). The derivation uses the difference between the maximum westward auroral ionospheric currents, represented

by the upper envelope (i.e. AU index), and maximum eastward ionospheric currents, represented by the lower envelope (i.e. AL index): $AE = AU - AL$ (Davis and Sugiura, 1966).

PC indices

The PC indices for the northern hemisphere (PCN) and the southern hemisphere (PCS) are derived using magnetic field measurements from a single magnetometer located close to the northern and southern pole, respectively (Ballatore and MacLennan, 1999; Stauning, 2007). The PC index is measured in mV/m, similar to the interplanetary merging electric field and dissimilar to the AE and Dst indices which are measured in nT (Stauning, 2007). These indices have been proposed to be a good proxy for Joule heating as they measure the energy input in the polar caps of each hemisphere (Chun *et al.*, 1999).

3.6 International Geomagnetic Reference Field (IGRF)

The International Geomagnetic Reference Field (IGRF) is an empirical model used since 1965 to model the internal geomagnetic field strength on and above Earth's surface worldwide as a function of geographic location, altitude and time. The model is capable of providing estimates of the Earth's magnetic field, beginning from 1900 A.D to the present (Thébault *et al.*, 2015). The IGRF model is made up of a set of spherical harmonic coefficients derived from magnetic field data which is collected from the international network of ground magnetic observatories, ground surveys, low Earth orbiting (LEO) satellites, and also geomagnetic indices (Thébault *et al.*, 2015; Alken *et al.*, 2021). The model gets updated every five years to account for the changes in the Earth's magnetic field with time. The latest version is the thirteenth generation of IGRF, IGRF-13, which was released in December 2019 (Alken *et al.*, 2021). For this project the IGRF model (from the NOAA website <https://www.ngdc.noaa.gov/geomag/calculators/magcalc.shtml?useFullSite=true#igrfwmm>) was utilized to get the magnetic field strength at an altitude of 300 km (observation altitude of the MSTID) which was then used to appraise Joule heating due to the MSTID.

3.7 Horizontal wind model (HWM14)

The horizontal wind model (HWM) is an empirical model that provides a statistical representation of the horizontal neutral wind of the atmosphere as a function of latitude, longitude, altitude (up to ~ 450 km), day and time (Drob *et al.*, 2015). Satellite and ground-based wind data are used to formulate the model that describes the spatial and temporal variation of the atmosphere by using vector spherical harmonic functions (Hedin *et al.*, 1996). The current version of the model is HWM14, which

provides an improved time-dependent model (Drob *et al.*, 2015). The improvement is mainly for altitudes higher than 120 km. For the HWM14 new data sets are included from six new and two old instruments, and excludes data sets that were included in the previous version HWM07 (Drob *et al.*, 2008). The new data sets include measurements from the equatorial and polar region Fabry-Perot interferometers (FPIs) and cross-track wind measurements from the Gravity field and steady state Ocean Circulation Explorer (GOCE) satellite. The additional data sets improve the gap in latitude and local time coverage (Drob *et al.*, 2015). It is important to note that the HWM14 model has a limitation when it comes to representing high-latitude winds in geographical coordinates, especially when there is less satellite coverage (Drob *et al.*, 2015). Studies show that magnetic coordinates should be used for high-latitude wind rather than geographic coordinates, as the motion of charged particles, which are the main drivers of wind at high latitudes, are organized by the Earth's magnetic field lines (e.g., Emmert *et al.*, 2008; Dhadly *et al.*, 2019). In addition, the HWM14 gives nearly a constant zonal wind for altitudes higher than 350 km due to the exclusion of solar flux parameters in the model, contrary to the HWM93 (Drob *et al.*, 2015). Dhadly *et al.* (2019) developed a high-latitude thermosphere winds (HL-TWiM) empirical model based on the disturbed wind model (DWM07 (Emmert *et al.*, 2008)), which uses magnetic coordination to overcome the limitation of the HWM14. The DWM07 model by Emmert *et al.* (2008) gives data as a function of magnetic latitude, magnetic local time and Kp index. The HL-TWiM model added input parameters, including day of the year and magnetic longitude (Dhadly *et al.*, 2019). The HL-TWiM model also includes additional ground-based data from the high-latitude southern hemisphere, which was an improvement on the HWM14 Dhadly *et al.* (2019). There is a future plan to upgrade the HWM14 by replacing the DWM07 with HL-TWiM to improve the wind data at high latitudes Dhadly *et al.* (2019).

In this project, the neutral wind velocity supplied by the HWM14 was utilized to calculate the Joule heating in a case study presented in Chapter 5. The decision to use the HWM14 was based on the fact that there are no direct measurements of the neutral wind in the area under study. In addition, the new and improved HL-TWiM model was not accessible at the time of the data analysis, whereas the HWM14 is easily accessible. Furthermore, the HWM14 has been used successfully by other researchers for Joule heating calculations (e.g., Billett *et al.*, 2018). The HWM14 model can be accessed via the Pyglow package available at <https://github.com/timduly4/pyglow/>.

3.8 Summary

This chapter describes the instrumentations used for this project. The SuperDARN radar and GPS satellites used to study TIDs characteristics have been introduced in this chapter. The DMSP satellites, magnetometers, and geomagnetic indices used to determine the TIDs source mechanism have been briefly explained. Description of

the horizontal wind model version 2014 (HWM14) and the international geomagnetic reference field (IGRF) models were given. These models will be used to estimate the energy dissipated by an MSTID.

Chapter 4

Data Analysis Methods

For this project, 10 years' radar data from the SANAE SuperDARN were visually surveyed to identify signatures of TIDs. Since the SANAE and Halley radars have a common FOV over a large area, there is the possibility that both radars may observe the same TID event at similar times, which will allow for a bi-static observation of a TID event. In light of that, for the TID events identified in the SANAE HF radar data, measurements from the Halley radar were also obtained where available. All of these events were observed in ionospheric scatter data and in the post-midnight sector in both radars, except for one event which was observed in the afternoon between 13:00 and 20:00 UT. The fluctuation in the power and velocity is easy to identify visually in ionospheric scatter data than ground scatter data since the fluctuation is stronger in ionospheric scatter data, which could be why all the events presented here are from ionospheric scatter data. The Fourier transform and Lomb-Scargle least-squares frequency analysis were used for the spectral analysis of time-series signals that were extracted from different cells (defined by a combination of beams and range gates) of the radar to identify the dominant wave frequencies/periods. A cross-spectral analysis was done to determine the phase difference between signals from different locations, which was then used to estimate the propagation speeds and directions of the observed waves. Detailed analysis of one of the events was done using the multitapering method. This method was utilised to demonstrate the advantage of using multiple windows over a single window in spectral estimation and determination of the waves' instantaneous characteristics. Multitapering analysis allows for the reconstruction of a time series for the dominant frequency band, which can then be used to derive the analytic signal of the waves. The analytic signal was used to estimate the quasi-instantaneous phase and amplitude of the waves. Analytic signals were obtained by applying a Hilbert transform to the reconstructed signals.

The study covered the period 2005-2015 during which 22 possible TID events were identified in the SANAE radar data as observed in the signatures in the range time-intensity (RTI) plots. Of the 22 TID events identified in the SANAE radar data, 9 events are observed simultaneously in the Halley radar data. In addition

to the SANA E and Halley radars, GPS receivers in the FOV of the radars were utilized to supplement the analysis of selected events. The processing of the GPS data is explained here. The result of the multitapering analysis of one of the events is discussed in Chapter 5 and the result of the combination of HF radar data and GPS data are found in Chapter 6. The results showing the characteristics of all TID events are included in Chapter 7.

4.1 Identifying TIDs from radar data

TID signatures are identified in the RTI plots as quasi-periodic enhancements of the backscatter power and/or Doppler velocities propagating towards or away from the radar with time. An RTI plot shows the radar backscatter power, Doppler velocity and spectral width variations with range gate and time. TIDs generated by AGWs are identified in the periodic fluctuations of the backscattered power in the ground scatter or even in the modulation of skip distance of the ground scatter (Samson *et al.*, 1989; Arnold *et al.*, 1998). Variations in the skip distance (distance to the first power return) can be used to determine period and amplitude of AGWs (Arnold *et al.*, 1998). The skip distance is sensitive to propagation of AGWs that it allows to detect AGWs even when the ground scatter is very weak (Karhunen *et al.*, 2006). However, TIDs observed in ionospheric scatter data, which are identified by a fast Doppler velocity and a wider spectral width, are related to gradient drift instabilities (e.g. Ogawa *et al.*, 2009; Suzuki *et al.*, 2009).

The RTI plot in Figure 4.1 shows TID signatures which were observed on 17 March 2013 from beam 13 of SANA E radar (a) and beam 12 of Halley radar (b). Black lines on the backscattered power enhancements and Doppler velocity, shown in the top and middle panels of Figure 4.1, respectively, highlight the TID signature. This event was observed in ionospheric scatter, as in the case of all the other events, since the values of the Doppler velocity and the spectral width are greater than 50 ms^{-1} . The TID signatures in panels (a) and (b) of Figure 4.1 have a positive slope, implying that the TID is traveling away from the radar (i.e. approximately southward according to the geometry of the radars' FOV presented in Figure 3.5).

The SuperDARN radar software toolkit (RST) can be used to read and visualize SuperDARN data. More information on the SuperDARN RST can be found on the Github page <https://github.com/SuperDARN/rst> or <https://superdarn.github.io/rst/> or on zenodo <https://doi.org/10.5281/zenodo.4435297>. The Virginia Polytechnic Institute and State University (also known as Virginia Tech), website <http://vt.superdarn.org/tiki-index.php> provides more SuperDARN visual information, such as RTI, scan and map potential plots. It also provides access to print records of SuperDARN FITACF data. The FITACF 2.5 fitting algorithm is used to produce the FITACF data from the raw ACF data. The SuperDARN data plots used in this project were taken from the Virginia Tech SuperDARN website.

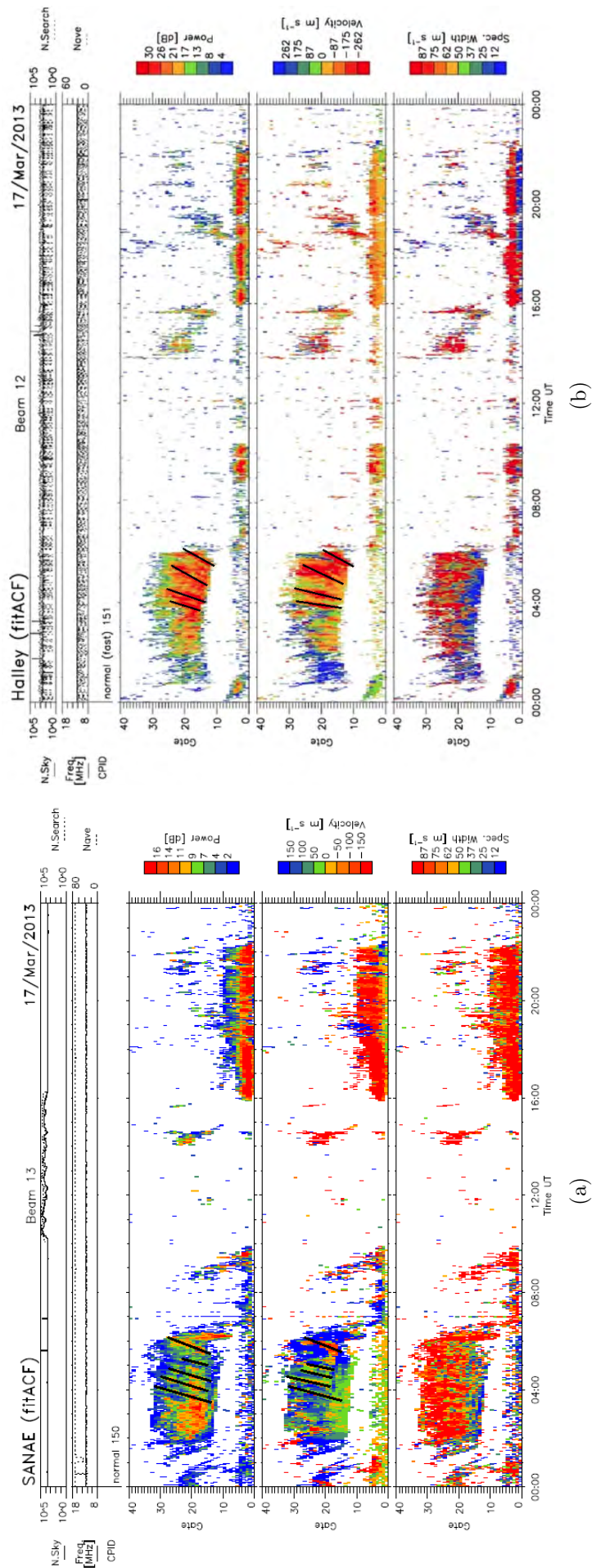


Figure 4.1: RTI plots of backscattered power (top panel), Doppler velocity (middle panel) and spectral width (bottom panel) of the SANA E (left) and Halley (right) radar data for 17 March 2013.

4.2 FFT and CSD

Cross-spectral analysis of time series from different geographical locations across the radar FOV is known to give a reasonable estimate of TID characteristics, such as propagation speed and direction of the TIDs (Samson *et al.*, 1990; He *et al.*, 2004; Ishida *et al.*, 2008; Grocott *et al.*, 2013). In this study the Python package Cross-Spectral Density (CSD) was used to compute the cross-correlation between two signals in the frequency domain. The CSD analysis determined the phase difference between signals, which was then used to calculate the speed and propagation direction of the TIDs. The simplest way to calculate the CSD of two signals is to multiply the Fourier transform of two signals, after taking the complex conjugate of one of the signals. The Fourier transform is used to measure the frequency component of a time series by expressing the signal in terms of a sum of sine waves with different frequencies and amplitudes. For real-world data, which are non-continuous and have a finite length, the discrete Fourier transform is used instead of the continuous Fourier transform. The Fast Fourier Transform (FFT) is a computer algorithm which is used to do a discrete Fourier transform of a time series fast (Bracewell, 1986). The discrete Fourier transform (DFT) of a time series $g(t)$ is estimated by means of the following equation:

$$G(f) = 1/N \sum_{t=0}^{N-1} g(t)e^{(-2\pi ift)/N}, \quad (4.1)$$

where N is the number of data points, $i = \sqrt{-1}$ and $G(f)$ is the DFT of $g(t)$.

The inverse Fourier Transform is given as,

$$g(t) = \sum_{f=0}^{N-1} G(f)e^{(2\pi ift)/N}. \quad (4.2)$$

DFT gives a complex symmetric output with length N , in which half of it represents negative frequency components and the other half are for positive frequencies. The highest possible frequency that can be estimated for a given sampling rate is known as the Nyquist frequency, defined as half of the sampling frequency. Windowing the time series before applying FFT is necessary to minimise errors in spectral estimation. Windows are used to create a smooth transition of the signal to a zero value at the end and beginning of the time series, thereby reducing the spectral leakage that is caused by the finite nature of the signal (Blackman and Tukey, 1958; Ghil *et al.*, 2002). There are different windowing methods, the most common being Hanning and Hamming windows. It was decided to use the Hanning window in this project which is commonly used in similar analysis. The other necessary condition to be fulfilled before doing FFT is that the time series must be evenly sampled with no data gaps. In this study, the spline interpolation method of the Pandas time series package was used to fill in missing data where applicable, before doing the FFT

analysis. This method is similar to that used in studies by Nygrén *et al.* (2015) and Nickisch *et al.* (2016). Prior to doing the FFT, the mean of the data was subtracted from the original signal to reduce the offset of the time series from zero. By subtracting the mean, the appearance of the DC frequency (zero Hz frequency) on the frequency spectrum is minimised.

Following is an example of an FFT and CSD data analysis that was done for 17 March 2013, but using data only from the Halley SuperDARN radar. The full results and discussion of this event are included in Chapter 5. Time series of the backscattered power data extracted from three cells, each cell representing a range gate along a particular azimuth beam, were used for the spectral analysis. Since all the TID events were identified from ionospheric scatter, only cells with this data were used. To make sure ground backscatter data are not included, an algorithm to discard data with a low Doppler velocity (between -50 ms^{-1} and 50 ms^{-1}) and a spectral width of less than 20 ms^{-1} (condition for ground backscatter) was used. The cells used in the analysis of this 17 March 2013 TID event are marked with red stars in Figure 4.2(a). The (b), (c) and (d) panels of Figure 4.2 show time series extracted from cells defined by beam (bm)=9 & gate (G)=21, bm=11 & G=23 and bm=14 & G=21, respectively, (the red lines represent the interpolated data). Only cells with 80% or more of the data available during the time interval of interest (i.e. when the TID signature is visible) were considered for the spectral analysis.

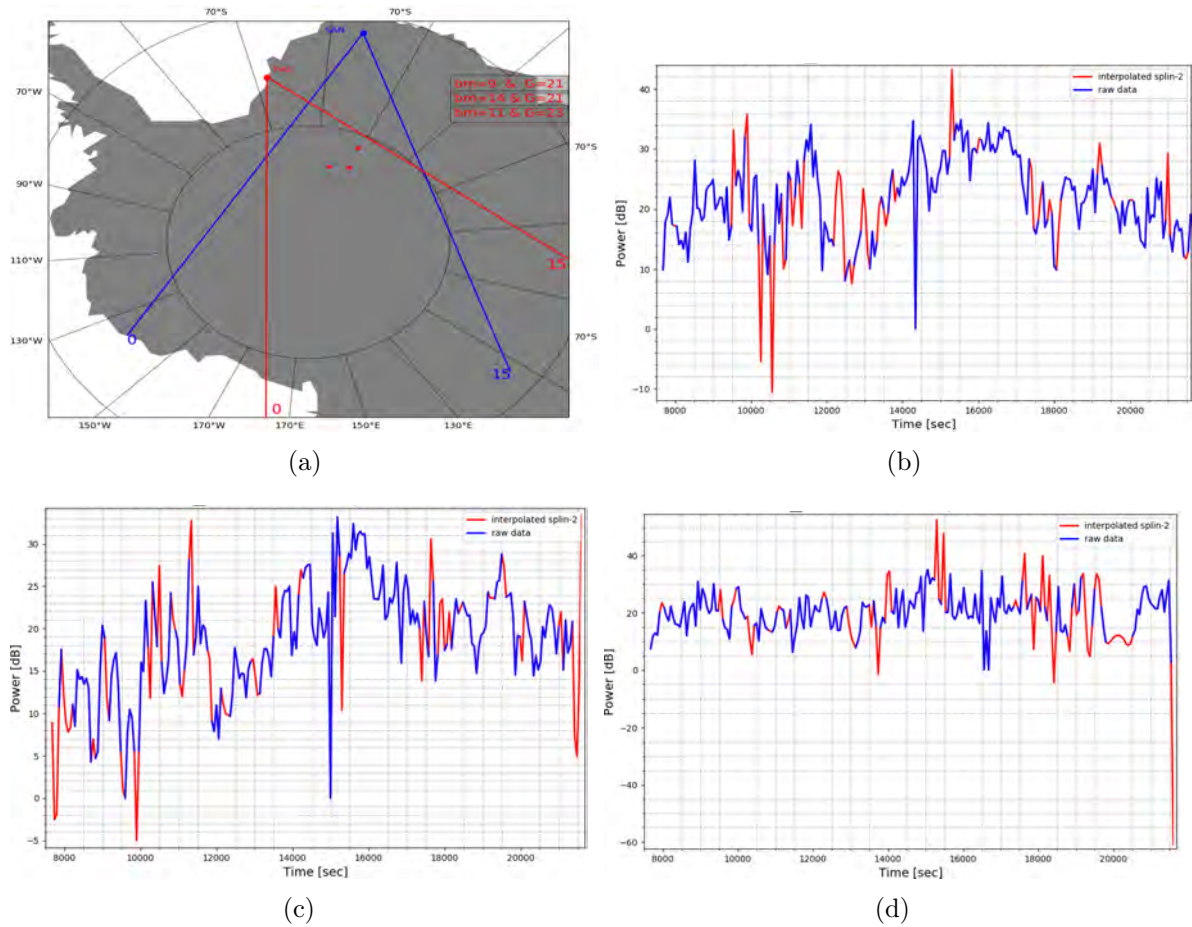


Figure 4.2: Plots showing the geographic location of the three cells used for the spectral analysis (a) and the time series (in blue) and the interpolated data (in red) for cells $bm=9$ & $G=21$ (b), $bm=11$ & $G=23$ (c) and $bm=14$ & $G=21$ (d).

Figure 4.3 presents the time series in Figure 4.2 but with the mean filter and Hanning window applied. Figure 4.4(a) shows FFT plots for cell $bm=9$ & $G=21$ in blue, $bm=14$ & $G=21$ in red, and $bm=11$ & $G=23$ in green. A frequency peak of ~ 0.72 mHz (corresponding to a period of ~ 23 minutes) was identified in the signals shown in Figure 4.4(a), as indicated by the black boxes in the figure. Similarly, the CSD calculated for each pair of signals shows a 0.72 mHz central frequency of a broadband peak (see the black box in Figure 4.4(b)). The CSD was calculated for all available cell combinations to find cell combinations in which similar frequencies were identified. These were then used for phase velocity calculations. The phase difference between each pair of signals, calculated from the CSD, is shown in Figure 4.4(c). However, the focus will be on the phase differences at the common frequency of all signals (0.72 mHz), as indicated by the black box in Figure 4.4(c).

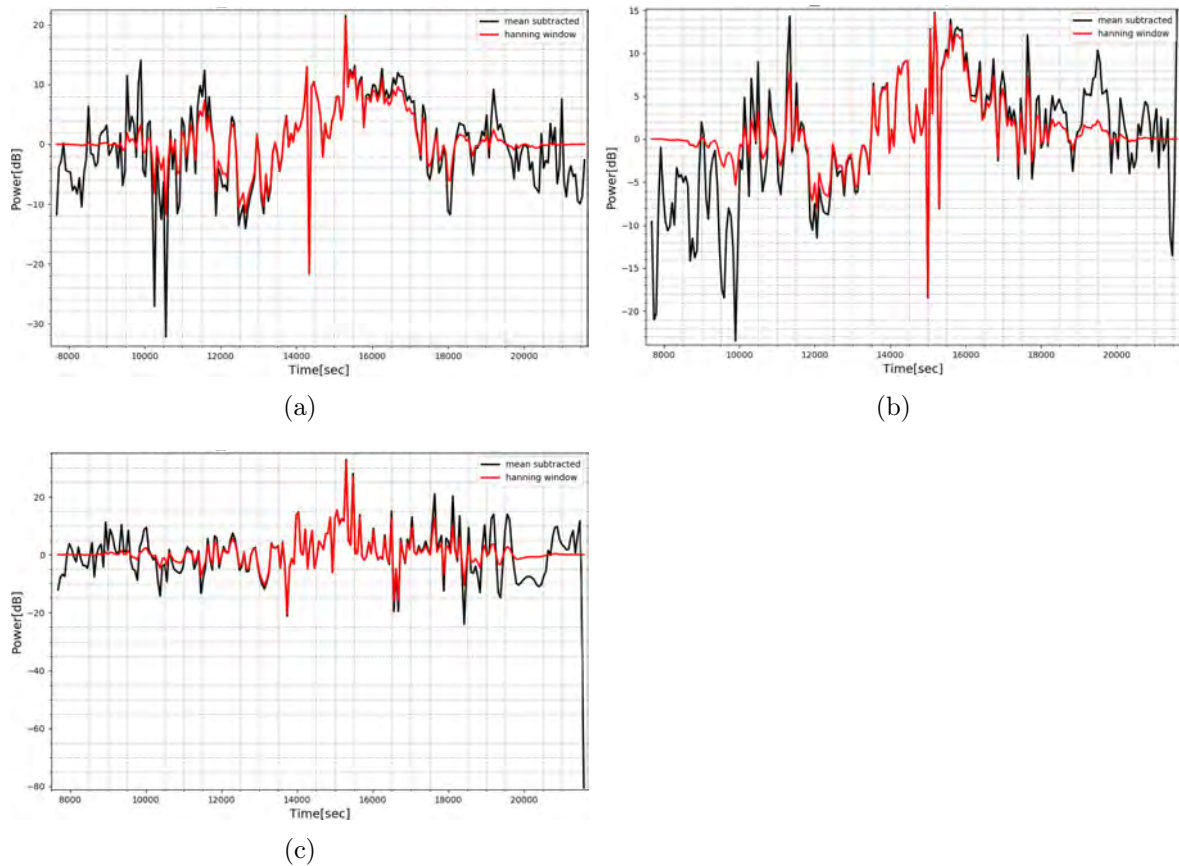


Figure 4.3: Plots of the time series data as used in Figure 4.2 after subtracting the mean (in black) and windowed data using the Hanning window method (in red) for cells $bm=9$ & $G=21$ (a), $bm=11$ & $G=23$ (b) and $bm=14$ & $G=21$ (c)

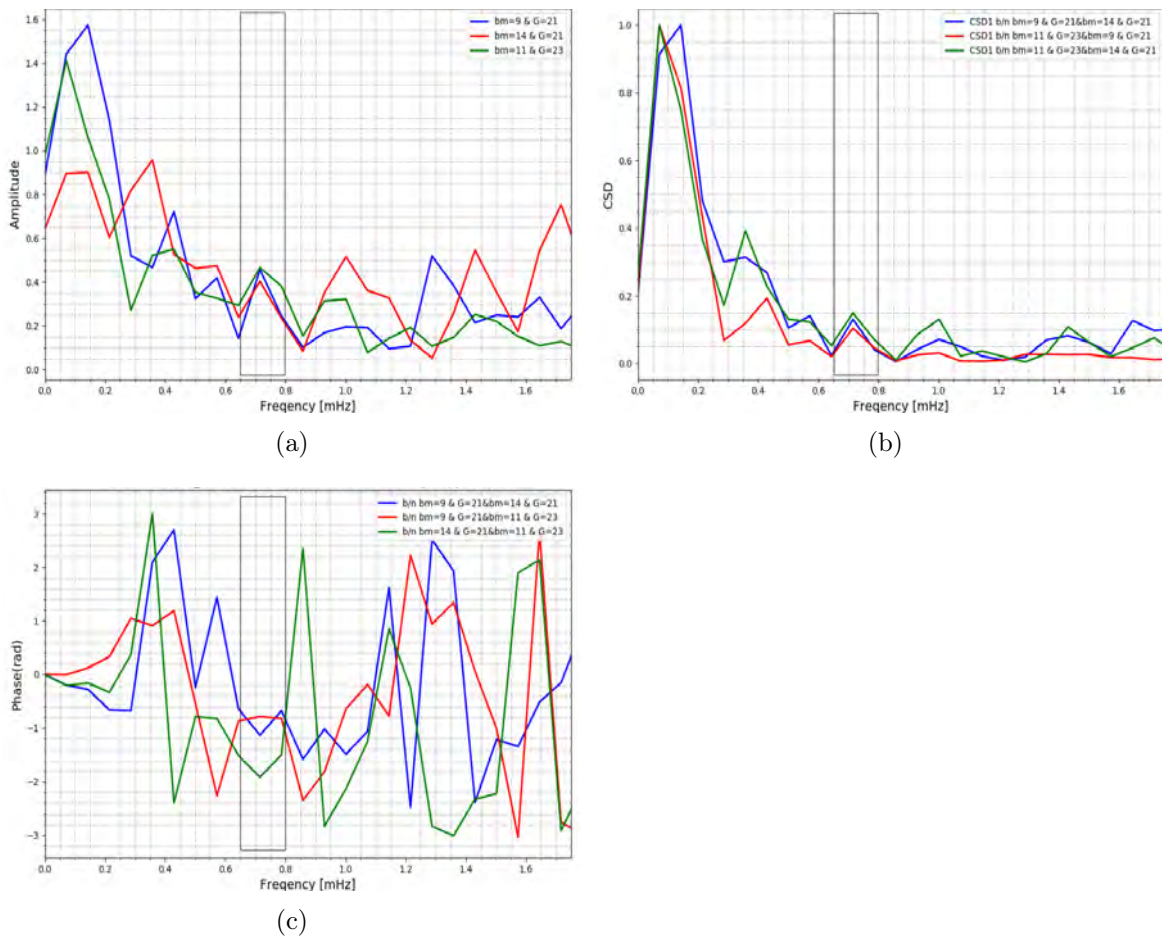


Figure 4.4: Plots of (a) FFT of the time series data shown in Figure 4.3, (b) CSD for each pair of time series and (c) the respective phases derived from the CSD analysis for the 17 March 2013 event using Halley radar data.

The phase differences calculated from the CSD were used to determine the wave number components (k_x east-west direction and k_y north-south direction). A detailed explanation of the method is found in He *et al.* (2004), Ishida *et al.* (2008) and Grocott *et al.* (2013), where it was used to calculate the characteristics of MSTIDs from time series of ground scatter SuperDARN radar data. Equations (4.3), (4.4) and (4.5) below were adapted from He *et al.* (2004) to calculate the phase velocity, wavelength and propagation direction of TIDs:

$$V_{ph} = \omega(k_x^2 + k_y^2)^{-1/2}, \quad (4.3)$$

$$\lambda = 2\pi(k_x^2 + k_y^2)^{-1/2}, \quad (4.4)$$

$$\theta = \tan^{-1}(k_y/k_x), \quad (4.5)$$

where V_{ph} is the phase velocity, ω is the angular frequency, λ is the wavelength and θ is the azimuth angle. ($\theta = 0$ radians indicates northward propagation).

4.3 Lomb-Scargle analysis

The Lomb-Scargle periodogram was developed by [Lomb \(1976\)](#) and [Scargle \(1982\)](#) to do spectral analysis of unevenly sampled data. The Lomb-Scargle method was utilized in this project for events with large data gaps (where more than 20% of the data within a time period of interest is missing). The Lomb-Scargle periodogram for a sampled data set g_i at a sampling time of t_i , for $i = 1, 2, \dots, N$, is calculated by [Scargle \(1982\)](#) as:

$$P_{LS}(\omega) = \frac{1}{2} \left\{ \frac{[\sum_i g_i \cos \omega(t_i - \tau)]^2}{\sum_i \cos^2 \omega(t_i - \tau)} + \frac{[\sum_i g_i \sin \omega(t_i - \tau)]^2}{\sum_i \sin^2 \omega(t_i - \tau)} \right\}, \quad (4.6)$$

where τ is used to ensure time-shift invariance,

$$\tan(2\omega\tau) = \frac{\sum_i \sin 2\omega t_i}{\sum_i \cos 2\omega t_i}. \quad (4.7)$$

A Lomb-Scargle package from Astropy, a collection of software packages written in Python language for use in astronomy, (<https://docs.astropy.org/en/stable/timeseries/lombscargle.html>), was used to analyse events with lots of missing data (e.g. the periodogram in [Figure 4.5\(b\)](#)). Contrary to the FFT power spectrum, which is a complex value, the Lomb-Scargle periodogram is real. Therefore, it is not an easy procedure to get the phase from a Lomb-Scargle periodogram. [Hocke \(1998\)](#) developed a method to estimate the phase and amplitude from the relation of the Lomb-Scargle method to the least-squares fitting. The other method often used is the least-square fitting which also gives the phase and amplitude of a wave ([Vlasov et al., 2011](#); [Negrea and Zabotin, 2016](#)). Here, the slope of the TID signatures was used to estimate the propagation speed. An example of the use of the Lomb-Scargle method is given in [Figure 4.5](#). This figure shows a TID event identified in the SANA RTI data of 15 July 2012 ([a](#)) and the periodogram for gates 39 to 48 of the same data ([b](#)). The slopes of the TIDs signatures, as shown in [Figure 4.5\(a\)](#), were used to estimate the speed. The frequency of the TID together with the speed, which was estimated from the slope, were used to calculate the wavelength.

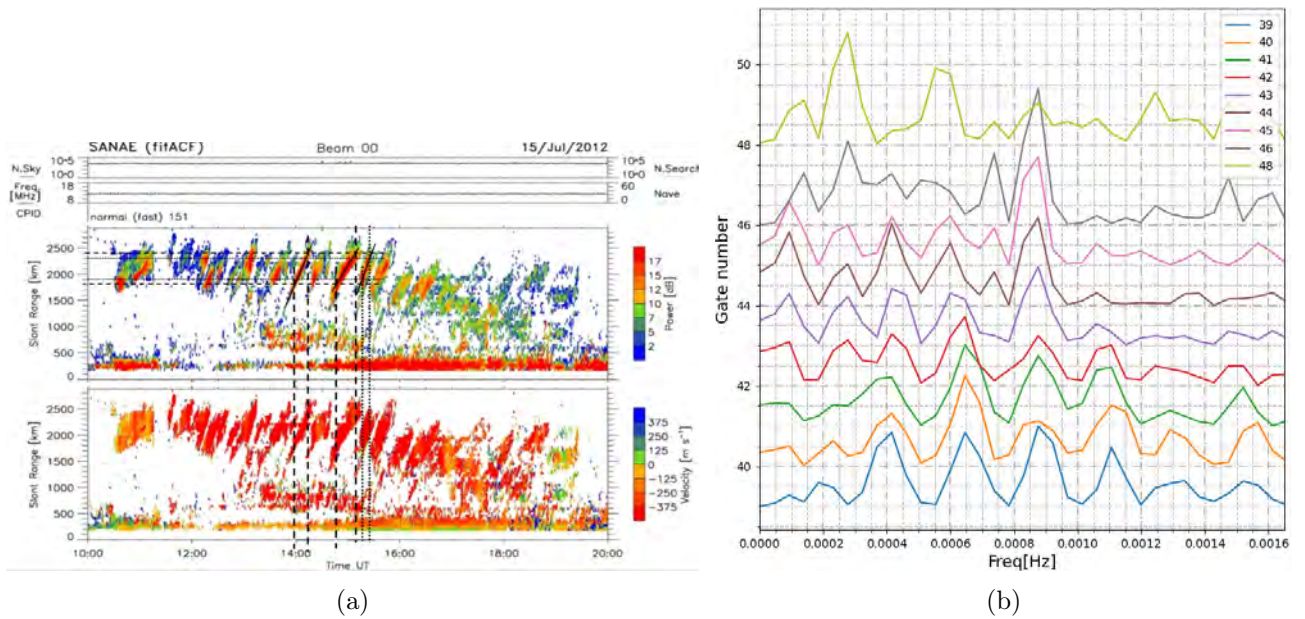


Figure 4.5: The event of 15 July 2012 from beam 0 of the SANAE radar, (a) RTI plot of the backscatter power and Doppler velocity with overlying lines used to calculate the slope and (b) the Lomb-Scargle periodogram for gates 39 to 48.

4.4 Multitaper analysis

The multitaper method (MTM) is used to estimate power spectra based on an orthogonal set of data windows or tapers, particularly the discrete prolate spheroidal sequences (DPSS), which mitigate spectral leakage, bias and smoothing problems (Thomson, 1982). The tapers are mutually orthogonal, with each window emphasising different parts of the data series. The orthogonality of the tapers allows for confidence levels of peaks to be determined. Multiple windowing (tapering) of data has several advantages over single windowing (such as Hanning), among others, in multiple windowing the amplitude data series is effectively reduced in a trade-off to reduce bias due to leakage. Spectral leakages are caused by the finite nature of the signal, which appears as if energy at one frequency leaks into other frequencies.

A combination of multiple windows provides the best possible spectrum. Lower order tapers have minimal leakage (broadband bias). As more tapers are added, the variance or local bias decreases and the peak of interest is smoothed out, or in other words, the resolution of the frequency spectrum is reduced. Therefore, one has to compromise between the resolution of the estimated frequency and the statistical stability of the output (Stephenson and Walker, 2010). The optimal number of tapers is determined by: number of data points (N), the data cadence (dt) and the half bandwidth of the peak of interest ($1/2 W$). W is usually a small multiple of the

frequency resolution. The number of tapers offering an optimal bias is calculated by the Shannon number (k). The number of tapers or Shannon number (k) and the resolution are related by means of the following equation: $k = 2P - 1$, where P is the resolution number (an integer number). Therefore the bandwidth is given by $W = 2Pf_{rayleigh}$, where $f_{rayleigh}$ is the Rayleigh frequency given by $f_{rayleigh} = 1/N \times dt$. Longer data sets can use a larger number of tapers (k) while maintaining the desired frequency resolution. Multitaper estimates arise from the inverse theory solution of the integral equation relating the Fourier transform of the available data of the ideal complete sample (Thomson, 1982). The multitaper estimate is calculated by:

$$s(f) = \sum_{k=0}^{K-1} |d_k(f)y_k(f)|^2, \quad (4.8)$$

where $d_k(f)$ are weights and $y_k(f)$ are the eigencoefficients. The eigencoefficients are Fourier transforms of the data multiplied by a window or taper as given below:

$$y_k(f) = \sum_{t=0}^{N-1} x(t)e^{-i2\pi ft}v_t^{(k)}(N, W), \quad (4.9)$$

where $x(t)$ is the sequence of data sample and $v_t^{(k)}(N, W)$ is the taper, also known as eigenvector, which is derived from discrete prolate spheroidal wave functions. The full derivation of the eigenvectors are found in Thomson (1982). Figure 4.6 shows the three tapers that were used to analyse the 17 March 2013 TID event (the resulting frequency spectrums are shown in Figure 5.4). The first window or taper shown in Figure 4.6 is similar to the Hanning window. Hence, using only one taper in the MTM is the same as using the FFT with a Hanning window.

The singular spectrum analysis -MTM (SSA-MTM) toolkit described in Dettinger *et al.* (1995) and Ghil *et al.* (2002) was used to do the multitapering analysis on the TID event identified in the SANAE HF radar data on 17 March 2013. This is presented in more detail in Chapter 5. In addition to estimating the power spectrum with confidence level against a null hypothesis, the SSA-MTM toolkit provides a tool to reconstruct a signal at a selected frequency band. Figure 4.7 shows the reconstructed signals (in black lines) for cell bm=8 & G=20 (a), cell bm=12 & G=20 (b) and cell bm=10 & G=24 (c) taken from the SANAE radar FOV for the 17 March 2013 TID event. The RTI plot for this event is shown in Figure 5.1(a). A central frequency of 0.78 mHz (period of ~ 21 min) was chosen to reconstruct the signal, since it was identified in all 3 cells with a 95% confidence level (see MTM spectrum plots in Figure 5.4). For comparison, the red curves in Figure 4.7 are the reconstructed signals when the Hanning window is used. The figure clearly shows that the amplitudes of the reconstructed signals with a Hanning window are reduced significantly at the edges/end points, while the centre has the same amplitudes as the MTM reconstructed signal, thus illustrating the clear advantage of the MTM over single windowing. The reconstructed signals (without the Hanning windows) were used

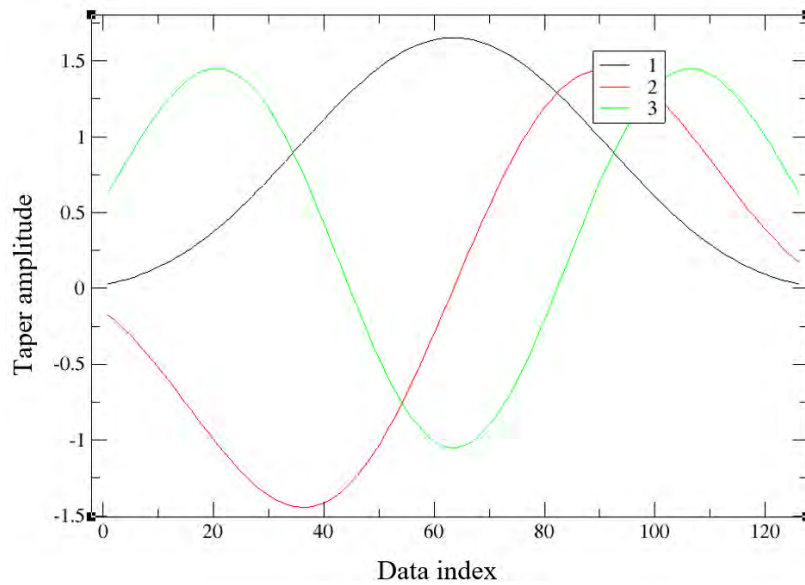


Figure 4.6: The three tapers from the SSA-MTM toolkit that were used to analyse the 17 March 2013 event.

to estimate the instantaneous amplitudes and frequencies with the Hilbert transform method. This will be discussed in the following section. The MTM method has a great advantage, especially when used in conjunction with the complex demodulation method, which is used to estimate the instantaneous propagation speed and direction of the TID. The advantage of using the MTM method in conjunction with the complex demodulation method to determine the characteristics of TIDs, is demonstrated in Chapter 5.

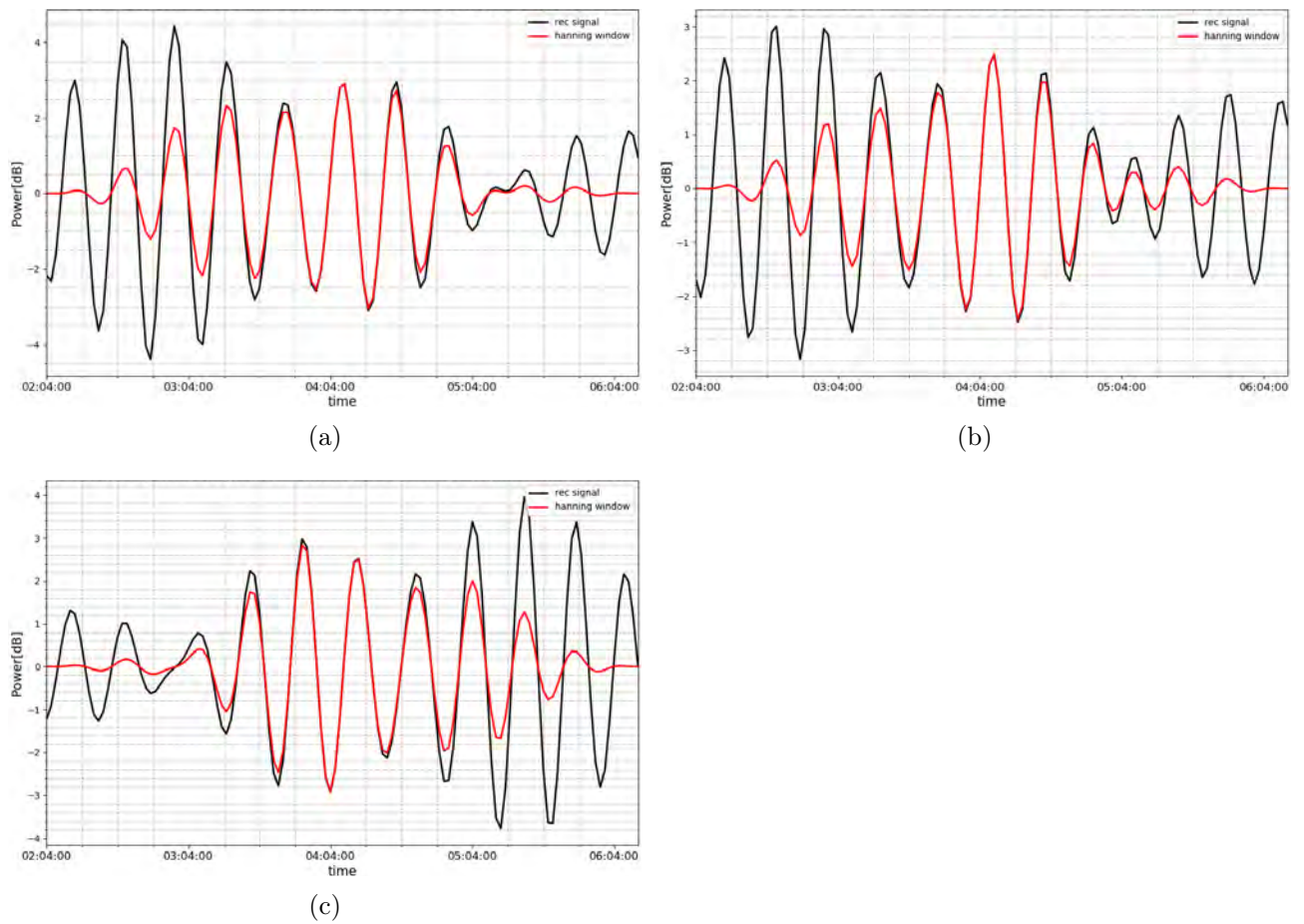


Figure 4.7: Reconstructed data using the SSA-MTM toolkit (in black) and applying a Hanning window on the reconstructed signal (in red) for cells (a) $bm=8$ & $G=20$, (b) $bm=12$ & $G=20$ and (c) $bm=10$ & $G=24$. Data is from SANA E radar FOV for the 17 March 2013 TID event.

4.5 Analytic signals

Analytic signals, which are obtained by complex demodulation, are used to estimate the instantaneous amplitude and phase of a quasi-periodic signal. The analytic signal, $A(t)$, of a real signal, $f(t)$, is made up of real and imaginary parts as seen in equation 4.10. The real part is the same as the original signal, while the imaginary part is derived from the Hilbert transform of the signal (F_{HT}) or the Fourier component of the original signal with $\pi/2$ shift (Bracewell, 1986).

$$A(t) = f(t) - iF_{HT}(t), \quad (4.10)$$

where F_{HT} is the Hilbert transform of $f(t)$ (Bracewell, 1986).

The analytic signal removes the unnecessary negative frequency components, which come with FFT, and keeps only the positive frequency components. The analytic signal can be obtained from the FFT by setting the negative frequency to zero and multiplying the amplitude of the positive frequency by two, and then doing an inverse FFT (Bracewell, 1986; Walker *et al.*, 1992). The analytic signal has the same amplitude as the original signal, but the phase is shifted by $\pi/2$ (Bracewell, 1986). The wave packet structure of a quasi-monochromatic signal can be seen by plotting the amplitude of the analytic signal with time.

The instantaneous amplitude or envelope of the original signal is derived from the magnitude of the analytic signal. The phase information can be calculated by using the imaginary and real components of the analytic signal (i.e. $\theta = \tan^{-1}(\text{Im}/\text{Re})$, where θ is the phase). The derivative of the phase provides the instantaneous frequency. A phase unwrapping algorithm is used to remove the 2π ambiguity of the calculated radian phase. Therefore, the algorithm *unwrap* in Python was used to add and subtract the integer multiple of 2π when the phase gap between consecutive points was greater than π . The phase change rate with time gives the instantaneous frequency (Bracewell, 1986; Walker *et al.*, 1992).

Figure 4.8 shows an example of analytic signals, including the respective envelopes or the instantaneous amplitudes (plotted as red lines), that were calculated for the 17 March 2013 TID event discussed in Chapter 5. The analytic signals are estimated for the 0.78 mHz frequency band (frequency of the MSTID) for the same SANA radar FOV locations given in Figure 4.7. The grey shaded area in Figure 4.8 marks the time interval where all three cells have relatively large amplitudes. A phase change occurs between the wave packets where the amplitude of the wave is small; as a result, a sharp change in the instantaneous frequency will be observed (Walker *et al.*, 1992). However, the instantaneous frequency is relatively constant when the amplitude is large and/or where the instantaneous phase is constant, which is the condition that was used in the calculation of the phase velocity and wavelength of the MSTID. The sharp changes in frequency can be seen in Figure 4.9 outside the grey area, which coincide with the time when the amplitudes were minimal in Figure 4.8.

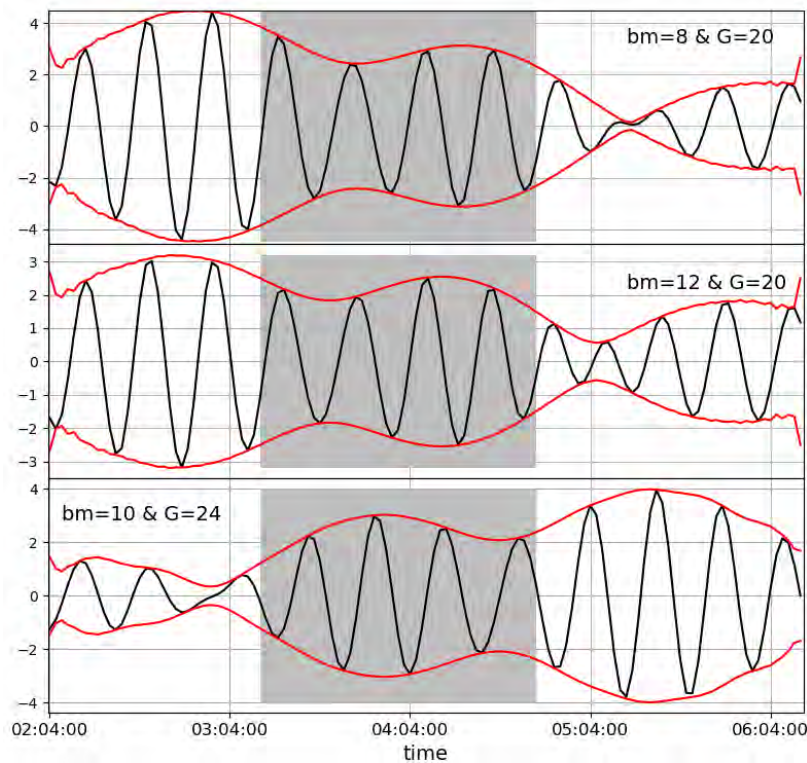


Figure 4.8: Hilbert transform of the reconstructed signals with the envelope (red lines) for cell 1 identified by $bm=8$ & $G=20$ (top panel), cell 2 identified by $bm=12$ & $G=20$ (middle panel) and cell 3 identified by $bm=10$ & $G=24$ (bottom panel) for the 17 March 2013 TID event. The grey shade marks the time interval when the amplitude of all three SANA HF radar cells are large.

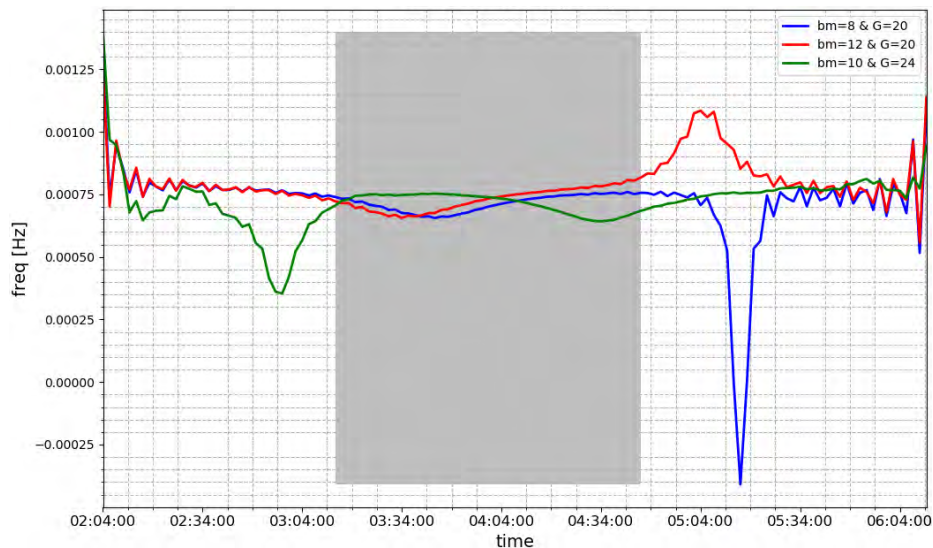


Figure 4.9: The instantaneous frequency for the respective cells where the instantaneous amplitudes are shown in Figure 4.8. The grey shade marks the same time interval as in Figure 4.8

4.6 GPS TEC

GPS allows a derivation of the estimation of the integrated electron density of the ionosphere along the ray path of the GPS signal. TEC measurements derived from GPS signals are known as the slant TEC (STEC), and is measured along each GPS satellite-receiver path. The STEC is mapped to vertical TEC (VTEC) to get the overhead TEC measurements at a geographic location. The VTEC is derived from the STEC based on the assumption that the ionosphere is a thin shell at an altitude of around 350 km (Hofmann-Wellenhof *et al.*, 1992; Misra and Enge, 2006). Figure 4.10 illustrates the geometry that is used to project the STEC measured along the line of sight of the satellite to the VTEC measurement at the ionospheric piercing point. The ionospheric piercing point (IPP) is the geographic location where the GPS signal intercepts the ionosphere at the assumed ionospheric altitude (h_m) (Hofmann-Wellenhof *et al.*, 1992).

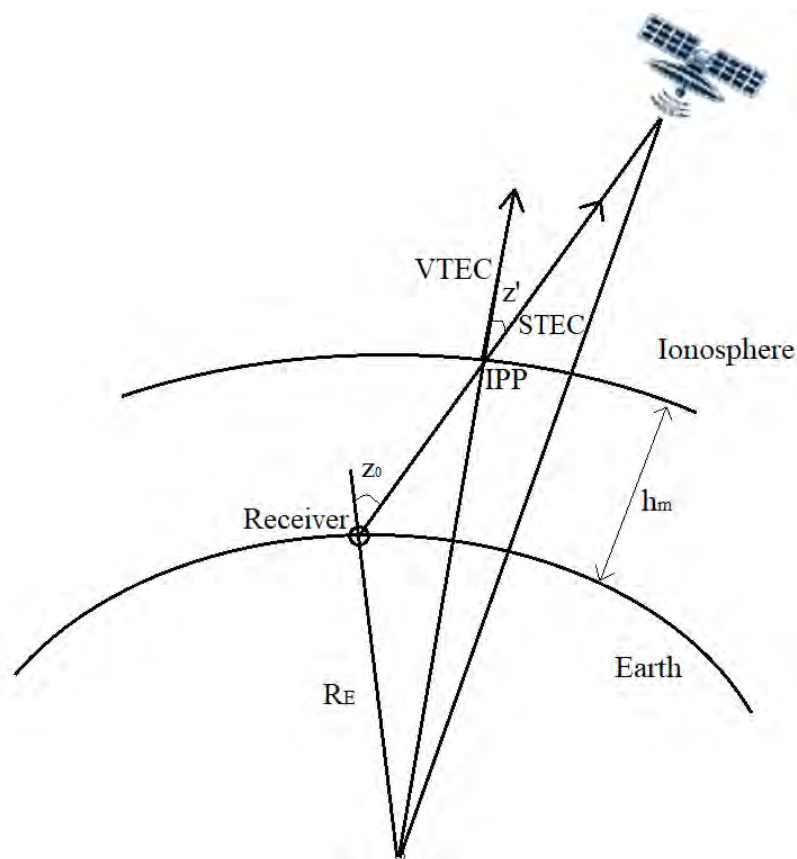


Figure 4.10: Geometry of STEC to VTEC mapping (adapted from Hofmann-Wellenhof *et al.* (1992))

The STEC is related to the VTEC by using the zenith angle of the satellite (z')

at ionospheric altitude, as follows:

$$STEC = \frac{1}{\cos z'} VTEC. \quad (4.11)$$

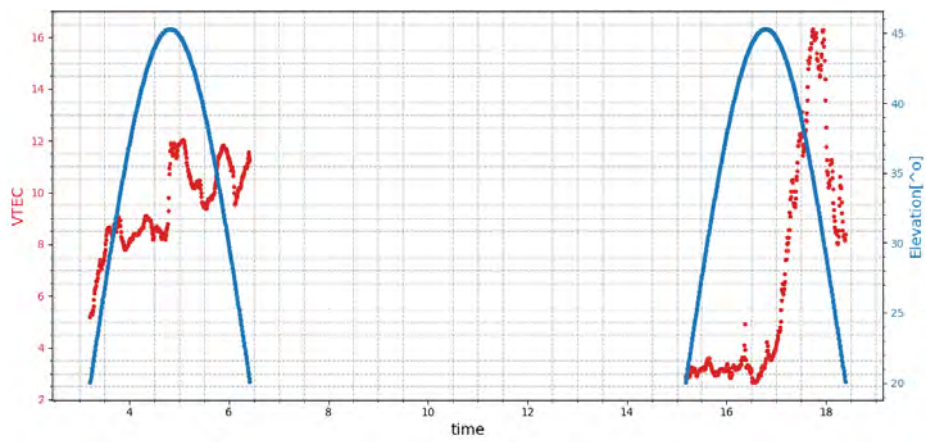
Calculation of z' is derived from the geometry in Figure 4.10 with the aid of the sine rule:

$$z' = \sin^{-1} \left(\frac{R_E}{R_E + h_m} \sin z_0 \right), \quad (4.12)$$

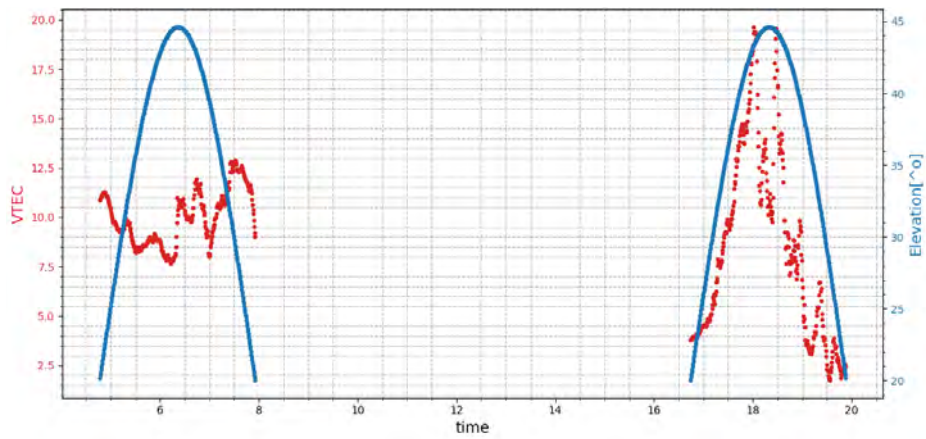
where z_0 is the zenith angle of the satellite at the receiver position, $R_E = 6371$ km is Earth's radius and h_m is the assumed height of the ionosphere, usually assigned a value of 350 km (Hofmann-Wellenhof *et al.*, 1992; Misra and Enge, 2006).

In this project, the GPS-TEC software developed at Boston College was used to derive both STEC and VTEC from the RINEX (receiver independent exchange) observation and navigation data (Seemala and Valladares, 2011; Uwamahoro *et al.*, 2018). The software uses both code and carrier phase measurements at the two GPS frequencies (L1= 1.575 GHz and L2= 1.227 GHz) to estimate receiver and satellite clock errors and biases introduced by the instruments and the medium which the signal traverses (as described in Section 3.3.2), while the RINEX navigation data are used to calculate the elevation and azimuth angles of the satellites. The software uses differential satellite biases published by the University of Bern and receiver biases calculated by minimising the TEC variability between 02:00 and 06:00 LT to determine TEC. A brief description of the procedures to estimate STEC and VTEC by GPS-TEC software can be found in Uwamahoro *et al.* (2018). The RINEX data used for this project have a 30 s time resolution and were downloaded from the UNAVCO data archive (<https://www.unavco.org/data/gps-gnss/gps-gnss.html>).

Figures 4.11(a) and (b) show an example of VTEC data (in red) derived by means of the GPS-TEC software for PRN 1 and 32, respectively, for a TID event on the 15 July 2012 as observed by a receiver located at Amundsen-Scott South Pole, Antarctica (89.9°S, 69.24°W, magnetic latitude 80.49°S). The blue dots in Figure 4.11 indicate the elevation angle of the satellites. An elevation threshold of 20° is used to filter out signals that may experience multipath errors, i.e. signals coming from satellites with elevation angles less than 20° were ignored.



(a)



(b)

Figure 4.11: VTEC and elevation angle versus time plots for PRN (a) 1 and (b) 32 as observed by GPS receiver located at Amundsen-Scott South Pole, Antarctica, on 15 July 2012.

4.6.1 Detrending VTEC

In preparation for further analysis, the VTEC data was detrended to remove the diurnal ionospheric variation and elevation angle dependencies due to the satellite motion (Hernández-Pajares *et al.*, 2006; Valladares and Hei, 2012). Detrending of the data is necessary to remove other dominant perturbations of TEC and to be left with only the perturbations of interest (perturbations within the frequency range of TIDs). Different methods can be used to detrend TEC. The best known methods are the running average (e.g., Tsugawa *et al.*, 2007; Kotake *et al.*, 2006) and polynomial fit (e.g., Valladares and Hei, 2012; Habarulema *et al.*, 2016; Katamzi-Joseph *et al.*, 2019). The former was used in this project.

Figure 4.12 shows plots of the 15-minute running mean (red lines) together with VTEC (black lines) for PRN 1 (a) and 32 (b) as observed at Amundsen-Scott South Pole, Antarctica, on 15 July 2012. The duration of the visibility of these satellites at this station overlaps with the observation time of the TID event observed in the SANAE radar data (see Figure 4.5(a)). The 15-minute running average was used here because the minimum period of the TIDs of interest is 15 minutes i.e. the minimum period for MSTIDs. The detrended VTEC (dVTEC) that was calculated for each PRN by subtracting the 15 minute running average from VTEC, was used to derive the TEC perturbations shown as black lines in Figure 4.12(c) for PRN 1 and Figure 4.12(d) for PRN 32. Perturbations with high magnitude can be seen in both time series at around 18:00 UT. As in the case of the SuperDARN data, the FFT software from Python was used to get the frequency spectrum for dVTEC data. The windowed data using Hanning window are shown using red lines in Figures 4.12(c) and (d) for PRN 1 and 32. The respective frequency spectrum for PRN 1 and 32 are shown in Figures 4.12(e) and (f). A broadband peak with a central frequency of 0.6 mHz (corresponding to a period of ~ 28 minutes) can be seen in the two FFT plots shown in Figures 4.12(e) and (f) for PRN 1 and 32, respectively. It is also important to note the large difference in the amplitudes of the peaks, as can also be seen in the time series (detrended VTEC) in Figures 4.12(c) and (d).

4.7 Summary

This chapter described the methods used to identify and characterise TIDs events from SuperDARN and GPS data. Different signal analysis methods such as FFT, Lomb-Scargle, Multitapering and Analytic signals has been discussed.

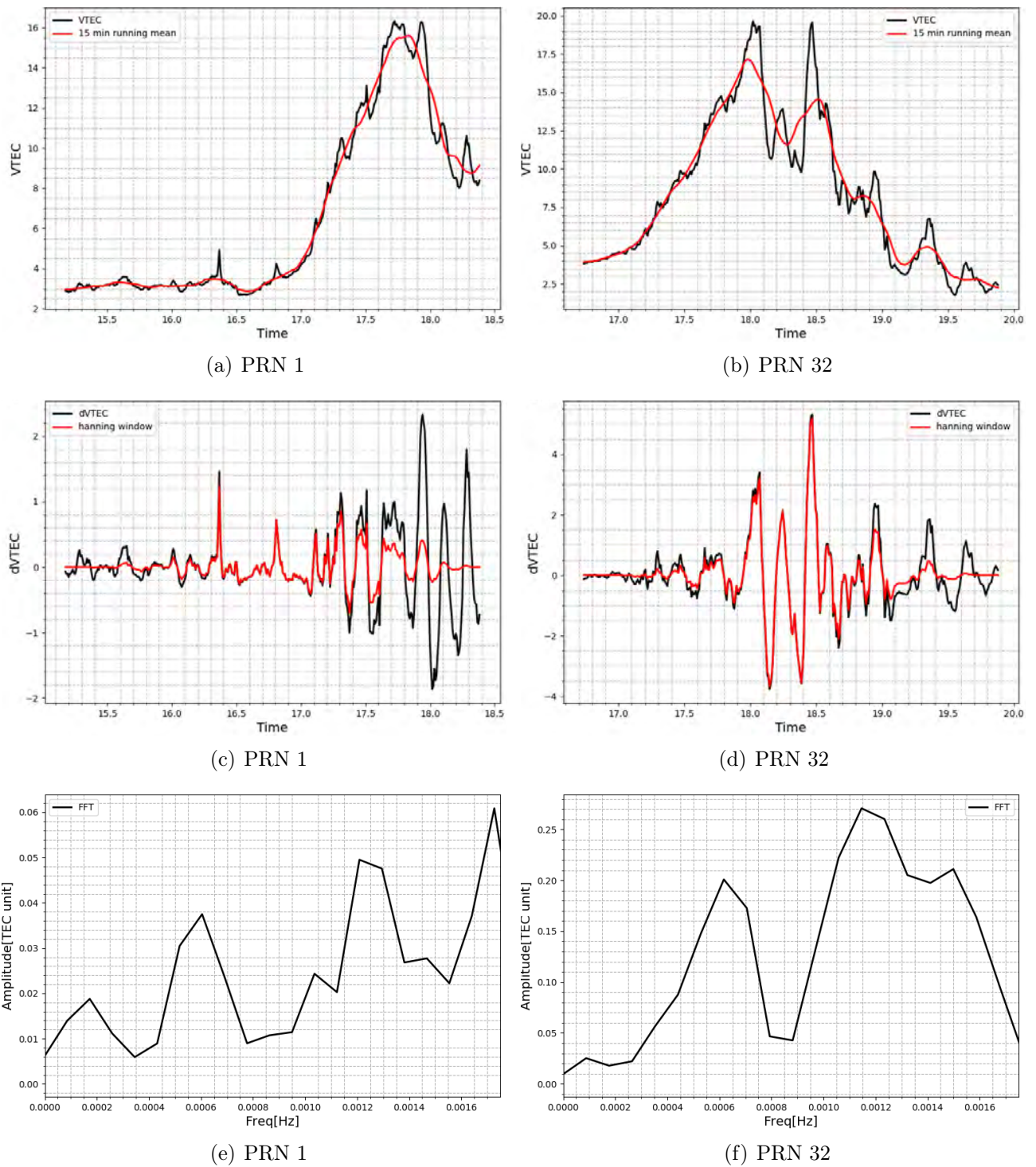


Figure 4.12: These plots show the GPS data processing steps in the study of TIDs. (a) and (b) VTEC (in black) and 15-minute running mean (in red), (c) and (d) $dVTEC$ (in black) and windowed data using Hanning window (in red), and (e) and (f) FFT of the windowed data for PRN 1 and 32, respectively, as observed from Amundsen-Scott South Pole, Antarctica, on 15 July 2012.

Chapter 5

Multitaper analysis of an MSTID event above Antarctica on 17 March 2013

5.1 Introduction

An MSTID was observed concomitantly by SANA E and Halley SuperDARN HF radars on 17 March 2013 02:00-06:00 UT. During this event both SANA E and Halley radars were transmitting at 12.5 MHz, which affords the opportunity to observe a common area from two directions, approximating a bistatic instrument. The event occurred during a geomagnetically quiet time, thus no substorm or storm activity was observed. The MSTID event was observed with periodic fluctuations of both the backscattered power and Doppler velocity parameters of ionospheric scatter from field-aligned irregularities (see Figure 5.1). The strong backscatter power data in the RTI plots represents the scatters from highly dense regions of the ionosphere that are modulated by the propagating MSTID. Similar events were reported by [Ogawa *et al.* \(2009\)](#) and [Suzuki *et al.* \(2009\)](#) with the Hokkaido SuperDARN radar (43.53° N, 143° E). Importantly, these echoes are accompanied by concurrent coherent echoes from the sporadic E region (Es) layers, indicating the existence of E and F region electric field coupling at night. The data from the SANA E SuperDARN radars were subjected to a multitaper analysis, as described in detail in the previous chapter, to elucidate the characteristics of this event (frequency, wavelength and phase velocity). In addition, the energy dissipation by this event was estimated and the driving mechanism behind the observed MSTID was established.

The results presented in this chapter were published in *Polar Science Journal* ([Atilaw *et al.*, 2021](#)).

5.2 Results and discussion

5.2.1 Characteristics of the MSTID

Figure 5.1(a) shows the plot of range gate versus time for beam 12 of the SANAE radar on 17 March 2013 and Figure 5.1(b) for beam 14 of Halley radar on the same day. The MSTID is highlighted by black lines on the backscattered power enhancements. The reader's attention is drawn to the fact that the backscatter power enhancements are concurrent with strong Doppler velocity values away from the radar (red in middle panels of Figures 5.1(a) and (b)). During the MSTID event, the Doppler velocities are greater than 50 ms^{-1} and the spectral widths exceed 50 ms^{-1} . This indicates that the data are ionospheric scatter, and not ground scatter. The black lines that overlay in Figures 5.1(a) and (b) have a positive slope, implying that the MSTID is travelling away from both radars with time, approximately in the direction of the south pole. A better indication of the motion of the phase fronts is given in Figure 5.2, which presents snapshots of the SANAE radar's field of view of the power parameter plotted in geographic coordinates for the period when the MSTID was active. Another important feature of the plots in Figures 5.1(a) and (b) is sporadic E region scatter (having range gates less than 10) that is coincident with the MSTID seen in the F region scatter.

Observations of TIDs in ionospheric backscatter are not commonly reported in the literature, especially at high latitudes such as reported here. Most of the TIDs reported using superDARN are observed in the ground or sea echoes (a signal that is strongly scattered by the ionosphere such that it propagates to Earth from which it can be scattered back along the same path to the radar) (Samson *et al.*, 1990; Bristow *et al.*, 1996; He *et al.*, 2004; Ishida *et al.*, 2008; Grocott *et al.*, 2013). The MSTID presented here is seen in ionospheric scatter (a radar signal returned to radar directly from the ionosphere) that is due to field-aligned irregularities (FAIs). In ionospheric scatter data, Doppler velocities translate to a movement away from or toward the radar along any beam (Samson *et al.*, 1989). MSTIDs similar to this one, as seen in ionospheric scatter, have been reported from other SuperDARN radars (e.g., Ogawa *et al.* (2009); Suzuki *et al.* (2009)).

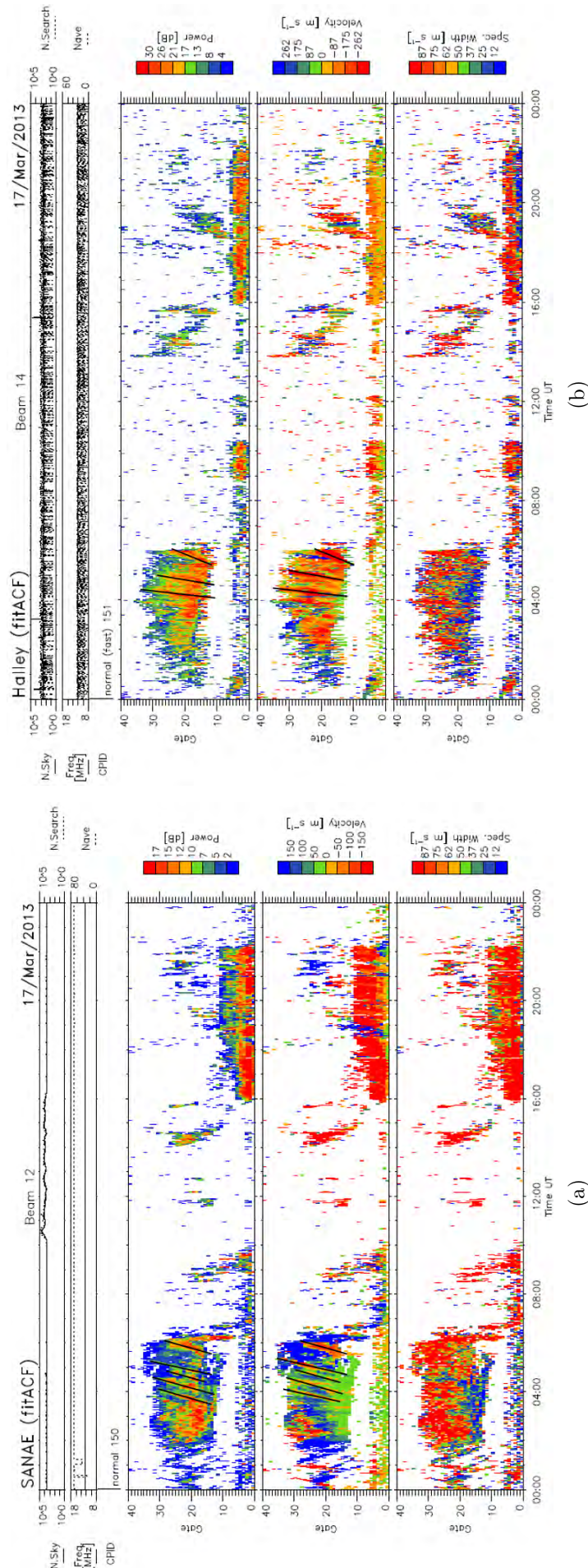


Figure 5.1: Range gate versus time plots of power backscatter (top panel), Doppler velocity (middle panel) and spectral width (bottom panel) from the SANA E (left) and Halley (right) radars on 17 March 2013.

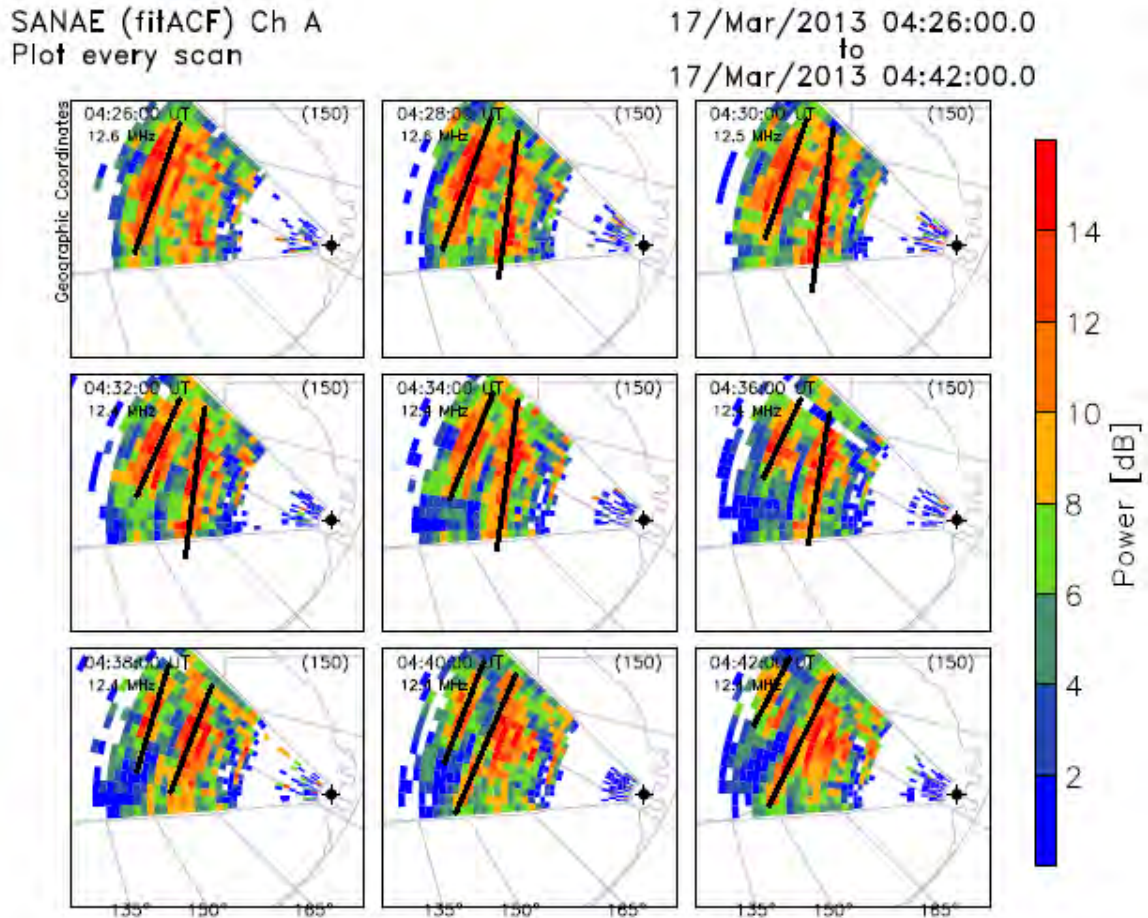


Figure 5.2: Field of view scan plots using geographic coordinates, of the backscattered power for the time period 04:26-04:42 UT plotted in Geographical coordinates. The solid black lines on the figure are used to indicate the wavefronts of the MSTIDs at different timestamps.

The variations in backscatter power of the two radars were analysed using the multitapering method. The multitapering method gives the estimation of the frequency with a confidence level relative to a chosen background noise level. The tapers or windows with different shapes emphasise different parts of the data and help reduce spectral leakage. The multitaper analysis for the SANAE radar is illustrated here. As explained in Section 4.4, the number of tapers used depends on the length of the time series and the sampling rate. In this case, three tapers were applied to the SANAE data which has a 4 hours and 10 minutes length with a 2-minute sampling rate. Time series data of backscattered power was extracted from three cells, each cell representing a range gate along a particular beam. The selected cells are marked by blue stars in Figure 5.3. Only cells with 80% or more of the data available were considered for the spectral analysis. A spline interpolation method was used to replace the 20% or less missing data. The analysis method is illustrated in this section by means of time series data for the period 02:04-06:14 UT.

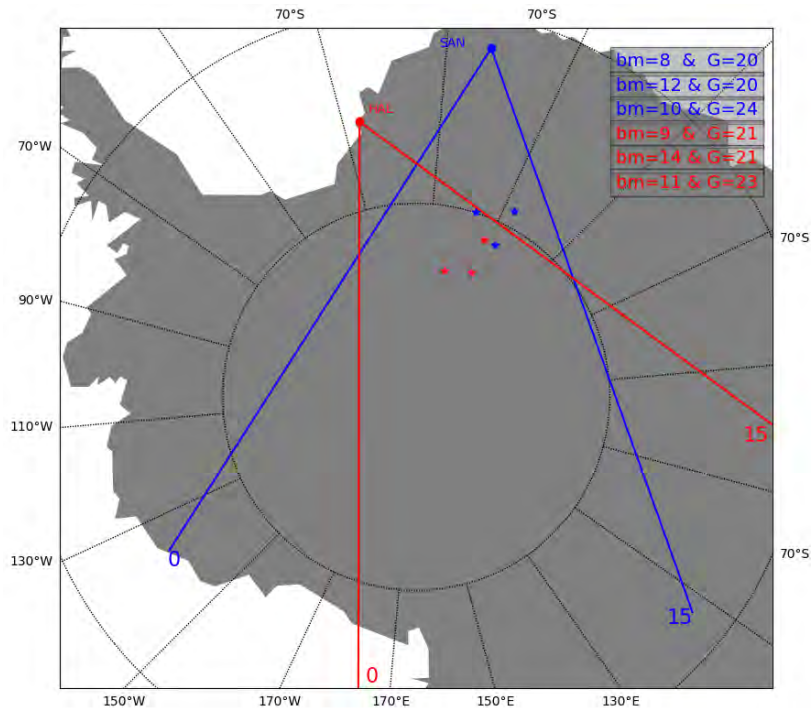


Figure 5.3: The three cells used for cross-spectral analysis from SANAE and Halley are shown in blue and red stars respectively, and the field of view of the respective radars are indicated by the blue and red lines. The beam number and range gate of each cell on the map can be found on the label (e.g., Cell1 $bm=8$; $G=20$, refers to beam number (bm) 8 and range gate (G) 20).

The MTM frequency spectrum for all three cells, with their different confidence levels, are shown in Figure 5.4. This was constructed using three tapers, three being the Shannon number calculated for the characteristics of our data series. A common peak centred around 0.78 mHz, indicated by the black rectangle, is shown in Figure 5.4(d). Each peak has a confidence level greater than 95% above white noise, as can be seen in Figures 5.4(a),(b) and (c). The common peak for the three cells using a Hanning window falls within the broadband of the 0.78 mHz peak, but at a lower frequency of 0.72 mHz. Since the MTM analysis is a more accurate estimation, the analysis obviously continued with the value of 0.78 mHz. The reconstructed signals from the broadband peaks, which represent a time series with a central frequency of 0.78 mHz for each cell, are plotted in red in Figures 5.5(a), (b) and (c), together with the original backscattered power time series. Noteworthy here, is the clearly visible phase difference between these reconstructed signals (see Figure 5.5(d)). Furthermore, the reconstructed signals from the MTM analysis spans the entire event, a clear advantage over other windowing techniques, e.g. the multichannel maximum entropy method, where data is filtered out for much of the start and end periods of the event. In addition, the Hilbert transformation is applied to the reconstructed signals to get the respective analytic signals (Bracewell, 1986).

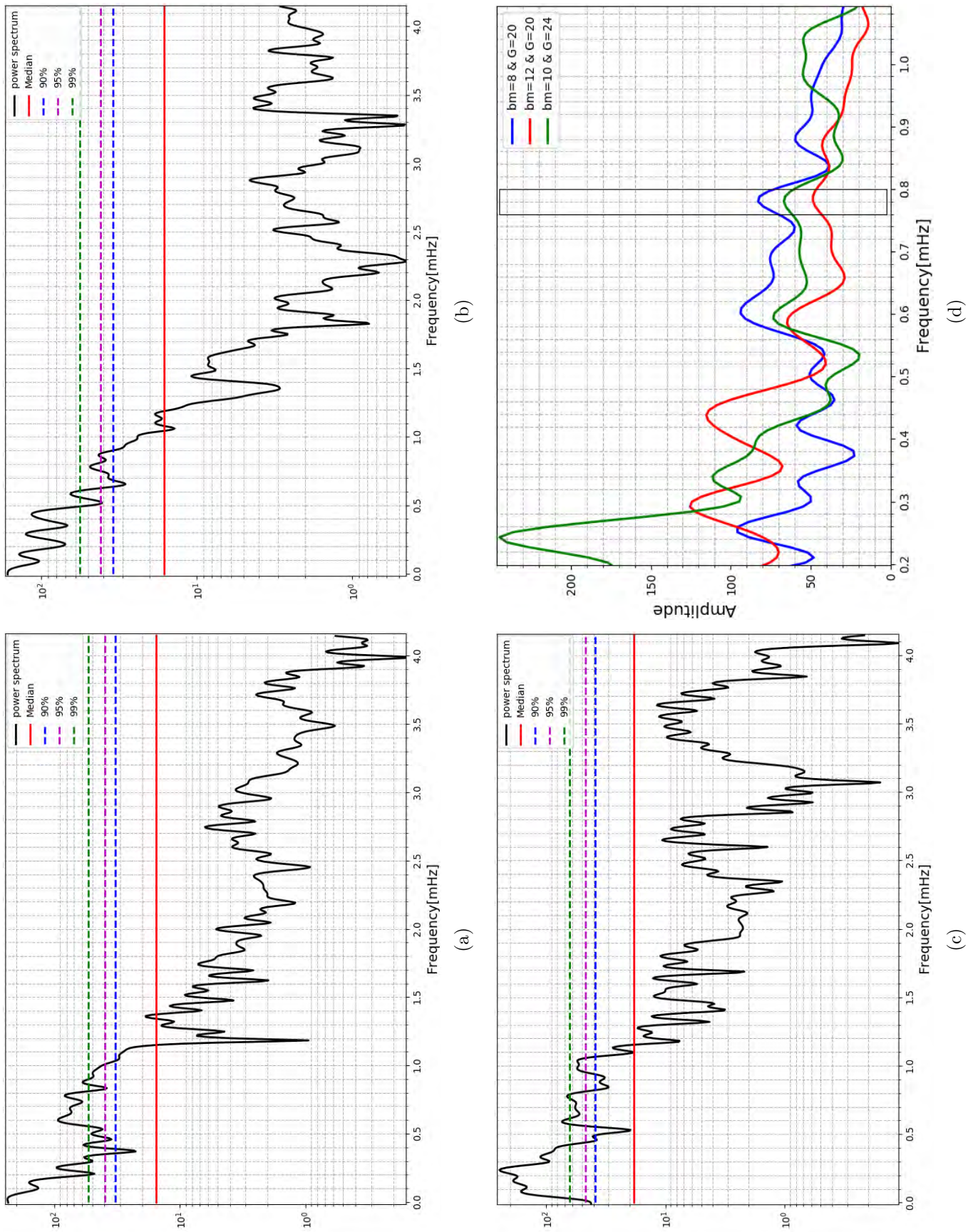


Figure 5.4: MTM spectrum of the time series data taken from 3 different cells, cell 1 (a), cell 2 (b) and cell 3 (c) where the red, blue, magenta and green horizontal lines represent the confidence levels of the median, 90 %, 95 %, 99 % respectively. The MTM spectrum of all three cells are plotted on a single graph (d) with the axis limited to a frequency range between 0.2 and 1.08 mHz.

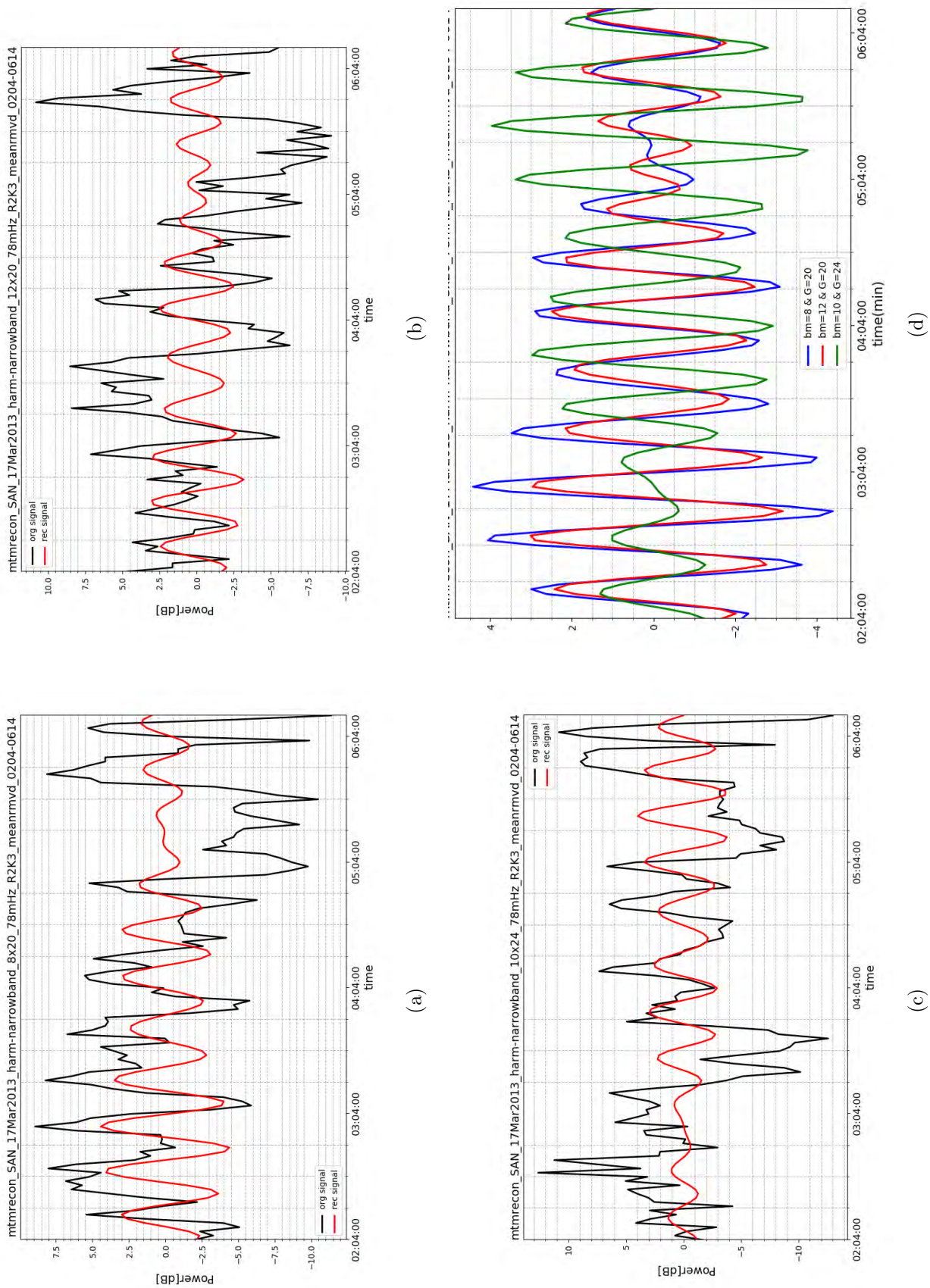


Figure 5.5: Reconstructed signal at the central frequency of 0.78 MHz using the SSA-MTM toolkit. The original signals are plotted in black and the reconstructed signals are plotted in red for (a) cell 1 (bm=8; G=20), (b) cell 2 (bm=12; G=20), (c) cell 3 (bm=10; G=24) and (d) the three reconstructed signals on a single graph/plot.

The Hilbert transform is used to get the analytic signal of the reconstructed signal (which only has real values). The analytic signal is a complex signal with the real part being the same as the reconstructed signal and the imaginary part being the Hilbert transform of the reconstructed signal (more details on Analytic signal and Hilbert transform is found in Section 4.5). An analytic signal gives us an objective estimate of the quasi-instantaneous phase and amplitude of the MSTID for each radar cell. The Hilbert transform analysis for the three cells in the SANAE field of view (marked by blue stars in Figure 5.3) are presented in Chapter 4 Section 4.4. The analytic signals for the three cells, including the respective envelopes or the instantaneous amplitudes (plotted in red lines) are shown in Figure 4.8. The respective instantaneous frequencies for each analytic signal are shown in Figure 4.9. The phase differences for each pair of reconstructed signals, derived from the instantaneous phase, are plotted in Figure 5.6. The grey shaded area in Figure 5.6 marks the time interval where all three cells have relatively large amplitudes (see Figure 4.8). A phase change occurs between the wave packets where the amplitude of the wave is small; as a result, a sharp change in the instantaneous frequency is observed (see Figure 4.9). However, the instantaneous frequency is relatively constant when the amplitude is large and/or where the instantaneous phase is constant, which is the condition used when calculating the phase velocity and wavelength of the MSTID. The wave number components k_x and k_y were calculated, using the phase differences during the active period of the wave packet and the orthogonal distances between the cells. The phase velocity, wavelength and azimuth was then calculated with equations 4.3, 4.4 and 4.5 respectively.

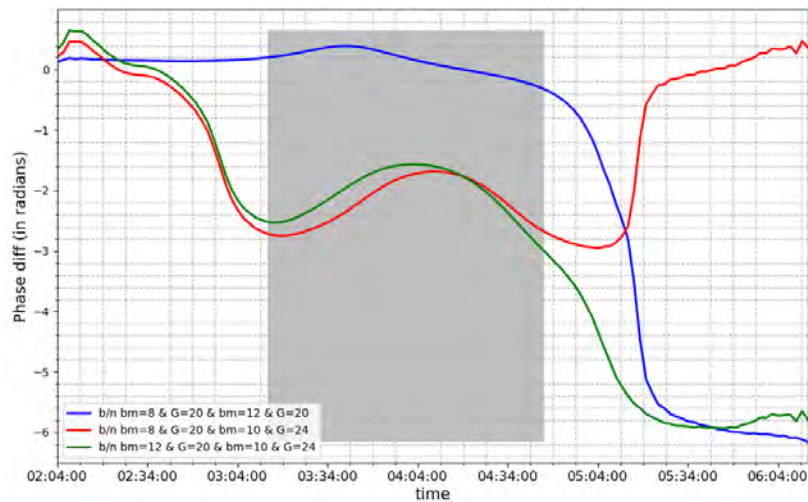


Figure 5.6: The phase differences for each pair of reconstructed signals, derived from the instantaneous phase. The grey shade marks the same time interval as in Figure 4.8

Figure 5.7 demonstrates the three characteristics of the MSTID, namely phase velocity, wavelength and azimuth, for the time interval marked by the grey shade in Figure 5.6 calculated by means of the MTM method. The top panel of Figure 5.7 is a

plot of the MSTID as it appears in the SANAЕ radar’s beam 10 backscattered power data. An important feature here is how well this technique tracks the characteristics during the time interval of the event. The MSTID has a maximum speed of 280 ms^{-1} around 04:04 UT, with a wavelength of 380 km, propagating with an azimuth angle of 146° . The estimated values depict the characteristics of the MSTID for the time interval. The wave signatures are clearly seen on the RTI plot (top panel in Figure 5.7).

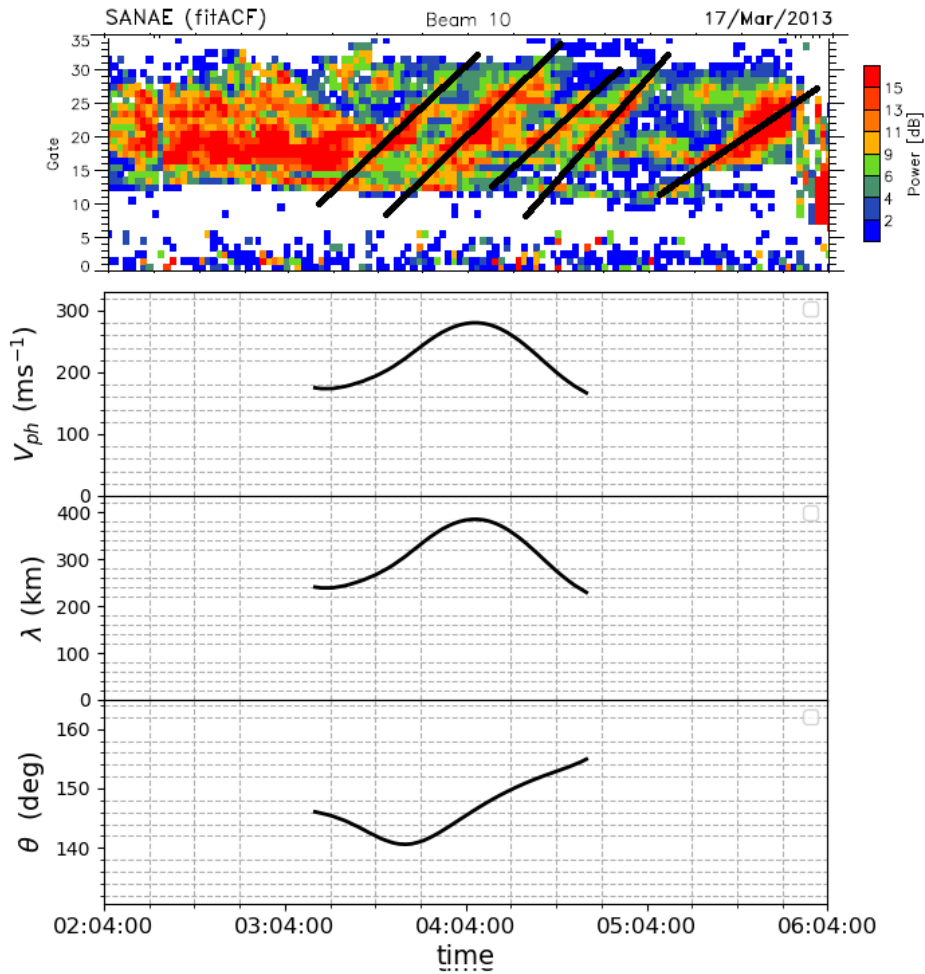


Figure 5.7: RTI plot of the backscatter power from SANAЕ radar beam 10 on 17 March 2013 between 02:04 and 06:14 UT (top panel). Calculated phase velocity (2^{nd} panel), wavelength (3^{rd} panel) and azimuth angle (bottom panel) for the time interval are indicated by the grey shaded area in Figure 5.6.

A similar Fourier analysis was applied to three cells in the Halley radar's field of view. The locations of these cells are shown as red stars in Figure 5.3. Unfortunately, the quality of the data from Halley was not as good as that of SANAE and, as such, the number of returns from targets was fewer. This led to a much shorter period for analysis compared to that of SANAE. MTM windowing was therefore not possible, as the allowable Shannon number was 1, which amounts to the application of a Hanning window. The Fourier analysis of these three cells with a Hanning window is shown in Figure 5.8. With the application of a Hanning window, these plots exhibit the same central frequency (0.72 mHz) as the SANAE data. The CSD analysis for estimating the phase velocity and propagation direction of the Halley data is described in Chapter 4 Section 4.2.

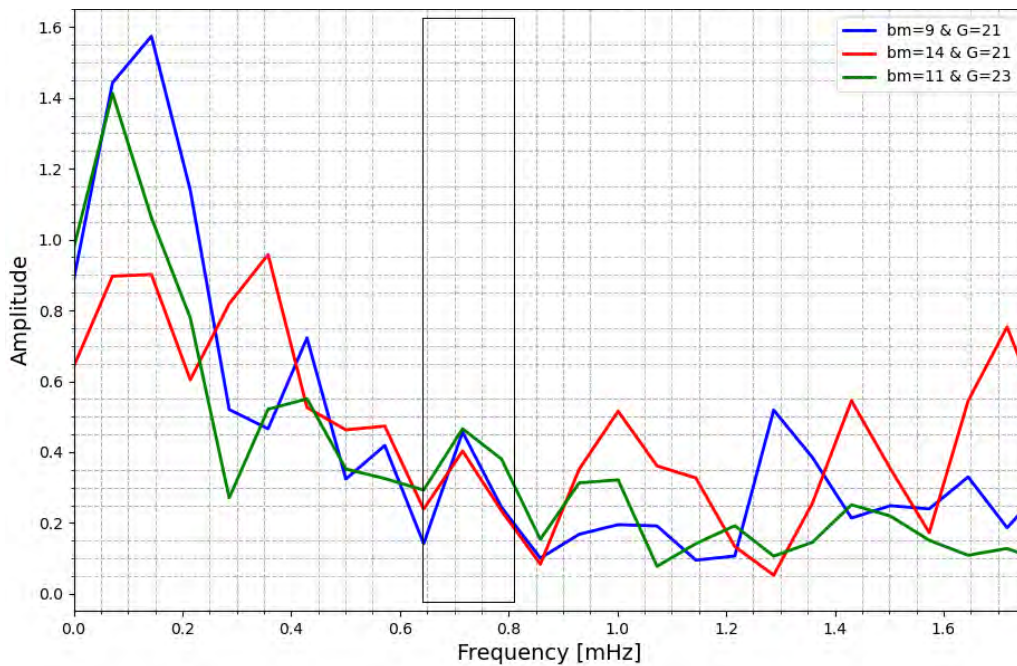


Figure 5.8: FFT of the three cells taken from the Halley radar field of view: in blue cell 1 (beam number 9 and range gate 21), in red, cell 2 (beam number 14 and range gate 21) and in green, cell 3 (beam number 11 and range gate 23).

5.2.2 Estimation of energy dissipation by MSTID

An estimation of the energy dissipated by the MSTID through the Joule heating process is outlined here. The calculation presented here is for 17 March 2013 MSTID event. The amplitude envelope of the analytic signal (derived from the MTM reconstructed signal centred at 0.78 mHz) of the Doppler velocity data was used to calculate the electric field. In order to estimate an order of magnitude of convection Joule heating by the MSTID, the electric field and the magnetic field were used as $\mathbf{V} = \frac{\mathbf{E} \times \mathbf{B}}{B^2}$, which simplifies to $V = \frac{E}{B}$ for altitudes greater than 200 km, where the

ion velocity is in the $\mathbf{E} \times \mathbf{B}$ direction (Brekke, 2013). The direction of the MSTID convection velocity was assumed to be perpendicular to the direction of the phase velocity of the MSTID (Ogawa *et al.*, 2009; Suzuki *et al.*, 2009). The convection velocity is associated with and perpendicular to the polarized electric field, which is generated to maintain the electric current continuity disrupted by the propagation of MSTIDs. The magnetic field was estimated by the IGRF-13 model at 300 km altitude (assumed altitude of the MSTID as observed by the radar). This cell was selected as it exhibited one of the strongest power values in the frequency band of the MSTID. The integrated Pedersen conductance was assumed to be $5 \Omega^{-1}$ for this calculation, as given in Spiro *et al.* (1982) and employed by Stephenson and Walker (2002). Spectral analyses of the Doppler velocity data from all the beams of both the SANAE and Halley radars during the event interval were done in order to identify the area where the MSTID was observed. Only peaks with a frequency of 0.78 mHz with a confidence level above 90% were considered when calculating the area over where the MSTID was observed. The locations of the cells that contributed to the area calculation are plotted in Figure 5.9 for SANAE (in blue) and Halley (in red).

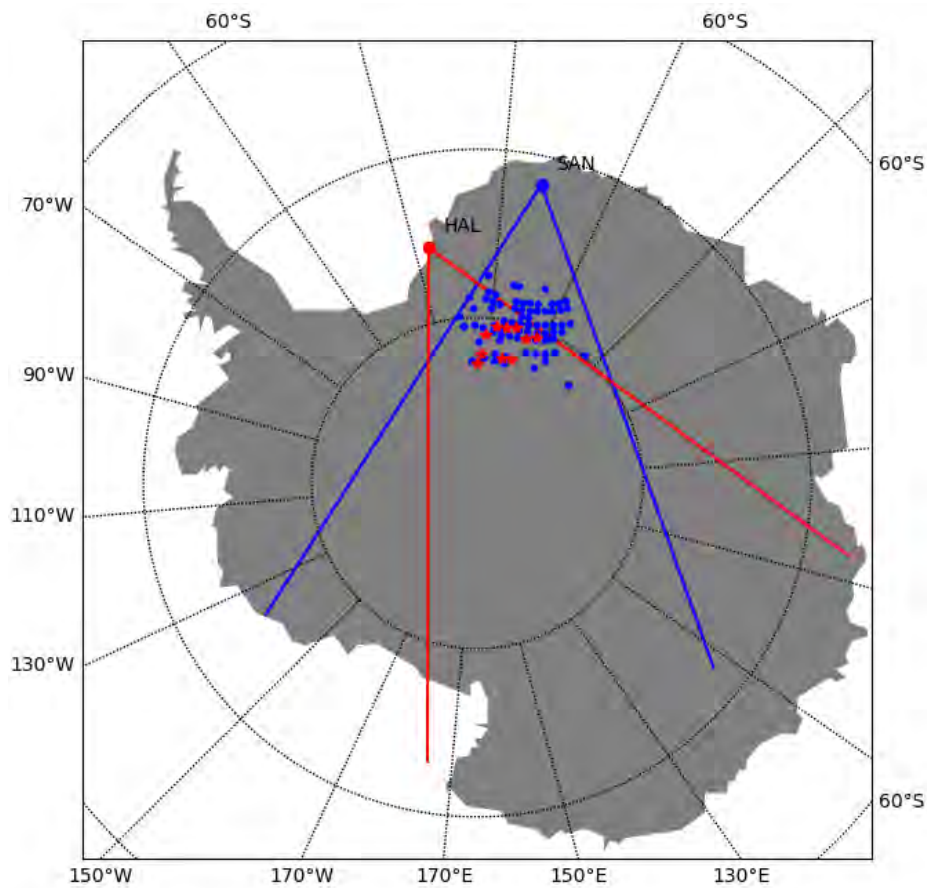


Figure 5.9: The field of view of the SANAE and Halley radars together with the location of cells that observed TIDs with a frequency of 0.72 mHz with a confidence level of above 90%.

Empirical models may be used to estimate the speed of the neutral wind, when no direct measurement of neutral winds are available, as shown by Baker *et al.* (2004) and Billett *et al.* (2018). This was the case for this event. The neutral wind speed at the location of the cells where the MSTID was observed, was determined from the Horizontal Wind Model 14 (HWM14) (Drob *et al.*, 2015). Figure 5.10(a) (top panel) shows the amplitude of the analytic signal of the Doppler velocity taken from a cell at beam 8; range gate 20 (geographic location of the cell 79.96° S and 2.82° E) of the SANAE radar. The method for determining the analytic signal is the same complex demodulation method outlined for the backscattered power of the SANAE data in Section 5.2.1.

Height-integrated Joule heating is calculated by the expression:

$$Q_J = Q_C + Q_{W1} + Q_{W2}, \quad (5.1)$$

where Q_C represents the energy contribution by plasma convection against a zero neutral velocity, Q_{W1} represents the contribution from motion of the neutral wind relative to the plasma and Q_{W2} represents the heating due to neutrals moving against a motionless plasma. Joule heating due to the MSTID was estimated by using the first two terms of Equation 5.1, whereas all the three terms (Q_C , Q_{W1} and Q_{W2}) were used to obtain the background Joule heating, as shown in Figure 5.10(a) and (b), respectively. The terms Q_C and Q_{W1} in equation 5.1 were determined by using the maximum amplitude of the 0.78 mHz MSTID, the magnetic field estimated by the IGRF model and the neutral wind vector as determined by the HWM14. The energy dissipated by the MSTID per unit area during the event is shown in the middle panel. Lastly, the energy dissipation by the MSTID over the area of $636.4 \times 10^6 \text{ m}^2$, where the MSTID was observed, is shown in the last panel of Figure 5.10(a). A maximum of $\sim 55 \text{ kW}$ was estimated to have been dissipated by MSTID. This number is more meaningful when its contribution is assessed in the context of the overall prevailing background Joule heating by convection and neutral winds at that time. To this end the background convection velocity was simulated by averaging the Doppler velocity of the same cell from which the analytic signal representing the MSTID was calculated. A plot of this velocity is seen in the top panel of Figure 5.10(b). The first term in equation 2.25 (Q_C) was evaluated by using this average velocity (165 ms^{-1}) together with the beam direction. A plot of the sum of all three terms of equation 2.25 for the background Joule heating is plotted in the middle panel. Finally, in the last panel of Figure 5.10(b) a plot of the estimated total energy dissipation over the area of MSTID observation is shown. This maximizes at a value of 103 kW. A comparison of the last panels of Figures 5.10(a) and 5.10(b), indicates that the MSTID contributes $\sim 55\%$ of the background Joule heating at that time. At the time when the polarization electric field (calculated from the Doppler velocity shown in the top panel of Figure 5.10(a) and the magnetic field from the IGRF model) is at its maximum value (around 3:30 UT), the heat dissipated due to the MSTID is $\sim 22 \text{ kW}$ and the background Joule heating is $\sim 30 \text{ kW}$, which shows the contribution from MSTID increases to 73%. Its relative contribution is, of course, very sensitive to the relative strength and direction

of the neutral wind. To our knowledge, this is the first estimate of power dissipation by an MSTID.

5.2.3 Source mechanism

On 17 March 2013 an MSTID was observed between 02:00 and 06:00 UT by the SANA E and Halley SuperDARN radars (UT is similar to LT at the location of SANA E radar). This interval, and the eight hours leading up to the event, were characterised by very quiet magnetic conditions with no sub-storms or storms reported. Figure 5.11(a) shows plots of hourly data of solar wind speed, Dst, AE, PCS and Kp*10. where Kp*10 is a mapped version of Kp index from OMNI data set (<https://omniweb.gsfc.nasa.gov/form/dx1.html>). Where Kp values are mapped in such a way that 0+ to 3, 1- to 7, 1 to 10, 1+ to 13, 2- to 17, etc. Figure 5.11(b) gives the Bz, By and Bx components and total magnitude of the magnetic field as derived from the advanced composition explorer (ACE) satellite data. The vertical line indicates the first appearance of the event in the radar data. All indicators characterise a very quiet period (Bz positive or northwards, Dst > -25 nT, PCS 0-2 and AE < 200 nT). Figure 5.12 shows a SuperDARN convection map for the period 02:14–02:16 UT (near the start of the MSTID observation) covering the southern polar region. SuperDARN convection maps are constructed by fitting all ionospheric measurements of Doppler velocities from the operating radars into a spherical harmonic representation of the ionospheric electrostatic potential. This produces a unique representation of the ionospheric convection pattern every 2 minutes (Ruohoniemi and Baker, 1998). The convection velocities (from SuperDARN) and flux of protons and electrons (50 eV - 20 keV) measurements from the polar orbiting environmental satellites (POES) are indicated by a shared colour bar. Both the Heppner Maynard boundary and the estimated equatorward boundary of the auroral oval (from POES) are marked (cyan with black broken lines and red dot-dash line, respectively). The locations of the SANA E (SAN) and Halley (HAL) radars are indicated near, and soon after, magnetic midnight. The radars share a similar magnetic latitude of $\sim 62^\circ\text{S}$. A study by Rodger *et al.* (1983) indicated that a sporadic E layer (Es) was frequently observed in ionosonde data at Halley during both pre- and post-magnetic midnight intervals under both the equatorward and poleward edges of the ionospheric trough. Returns that could be from a sporadic E region are clearly visible from range gates less than 10 in Figures 5.1(a) and 5.1(b) which are RTI plots of single beams of the SANA E and Halley radars. These returns can be placed in a geographical region near the poleward edge of the ionospheric trough (or the equatorward auroral oval boundary, the red dot-dash line in Figure 5.12). The results indicates that instabilities within the Es layer form a polarisation electric field, which is subsequently mapped to the F region, are the causative mechanism for the MSTID in this event (Ogawa *et al.*, 2009; Suzuki *et al.*, 2009; Yokoyama and Hysell, 2010). Figure 5.13 shows the ray trace plot for beam 8 of SANA E radar for 17 March 2013. At the altitude of the MSTID observation (around 300 km) the radar signal encounters the magnetic field

line (in pink) at an angle, which allows up and down movement of the plasma through $\mathbf{E}_p \times \mathbf{B}$. The polarisation electric field estimated from the Doppler velocity of the MSTID (given in Figure 5.10(a)) makes up $\sim 30\%$ of the background electric field. Suzuki *et al.* (2009) estimated the polarisation electric field for an MSTID generated by gradient drift instability to be at least 11% of the effective electric field (i.e. the background electric field plus the contribution from the neutral wind). Since the polarisation electric field contribution calculated here is comparable to that of Suzuki *et al.* (2009), we can deduce that despite the high background electric field in the region of the MSTID, the polarisation electric field could be significant enough to induce $\mathbf{E}_p \times \mathbf{B}$ plasma drifts. Further evidence for this proposition is presented by a Lomb-Scargle periodogram in Figure 5.14 which is a Lomb-Scargle Periodogram (utilized due to many data gaps) of the Es data (gates 1 through 4) from beam 12 of the SANAE radar. A similar frequency as the MSTID (0.78 mHz) is apparent in gate numbers 2, 3 and 4.

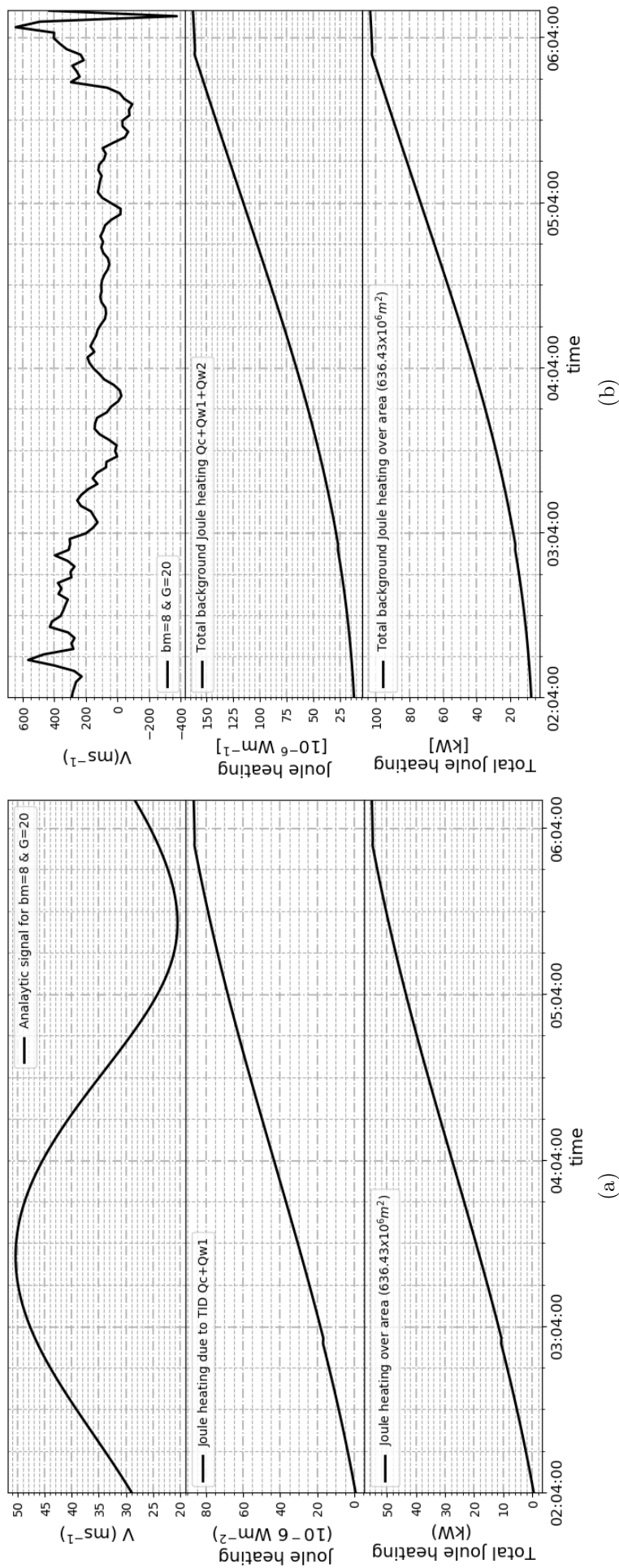


Figure 5.10: Joule heating (a) due to MSTID: the instantaneous amplitude of the Doppler velocity taken from cell with $bm=8$ & $G=20$ (top panel), estimation of energy dissipated per unit area by MSTID ($Q_c + Q_{w1}$) (middle panel) and the total Joule heating over the area where TID was observed ($636.43 \times 10^6 \text{ m}^2$) (last panel), (b) background: same Doppler velocity as cell in (a) (top panel), estimation of the background Joule heating per unit area ($Q_c + Q_{w1} + Q_{w2}$) (middle panel) and the total energy dissipation over the area where the MSTID was observed (last panel)

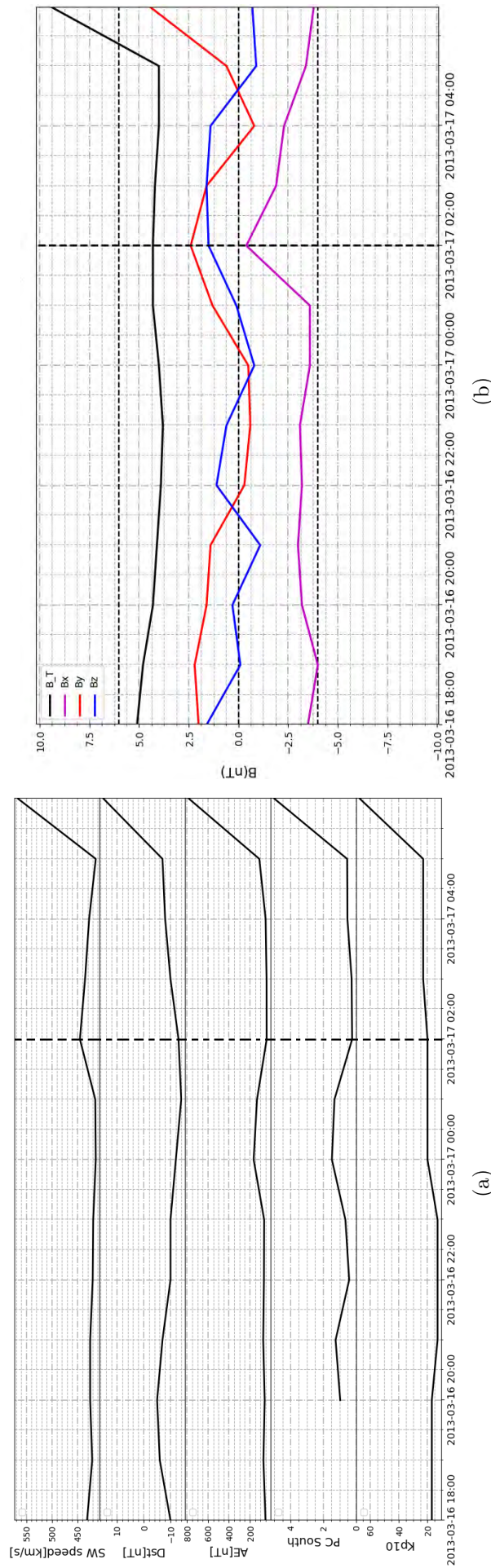


Figure 5.11: Geomagnetic conditions during 16 to 17 March 2013, (a) SW speed (1st panel), Dst index (2nd panel), AE index (3rd panel) PC index for southern hemisphere (4th panel) and Kp10 (5th panel) (b) B_z in blue, B_y in red, B_x in magenta and B_T in black

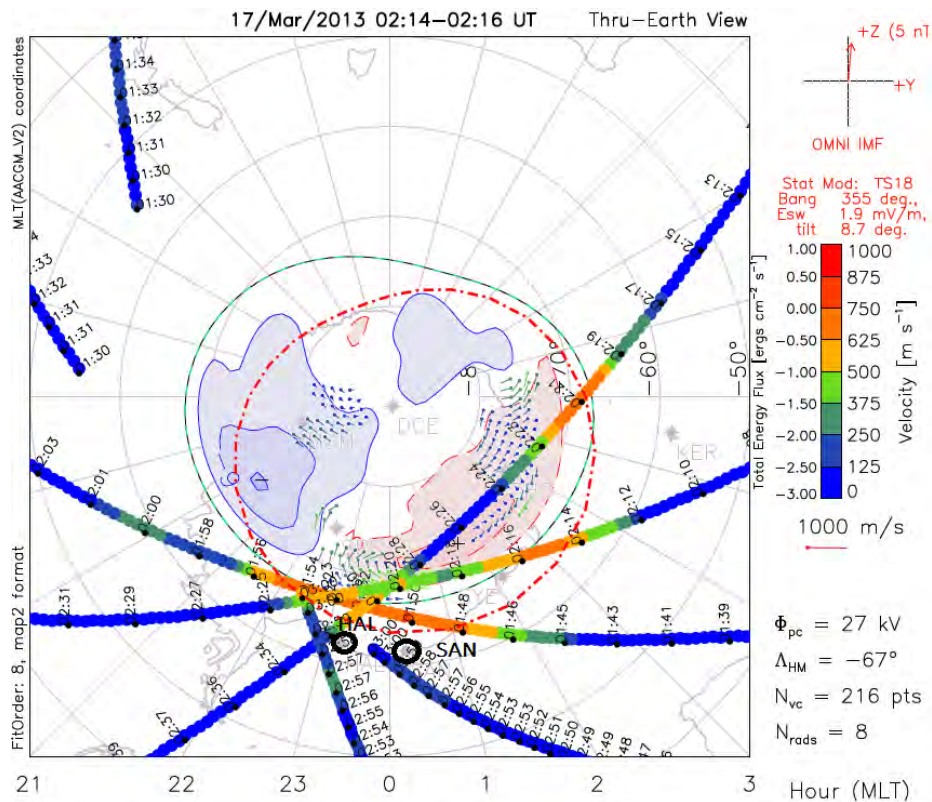


Figure 5.12: Map potential for the time of the event based on the model by [Thomas and Shepherd \(2018\)](#) and produced by RST 4.3 software with FITACF V2.5 data. The total energy flux and the equatorward auroral oval boundary (red dot-dash) from POES are overlaid. Map produced by K. Sterne (Virginia Tech).

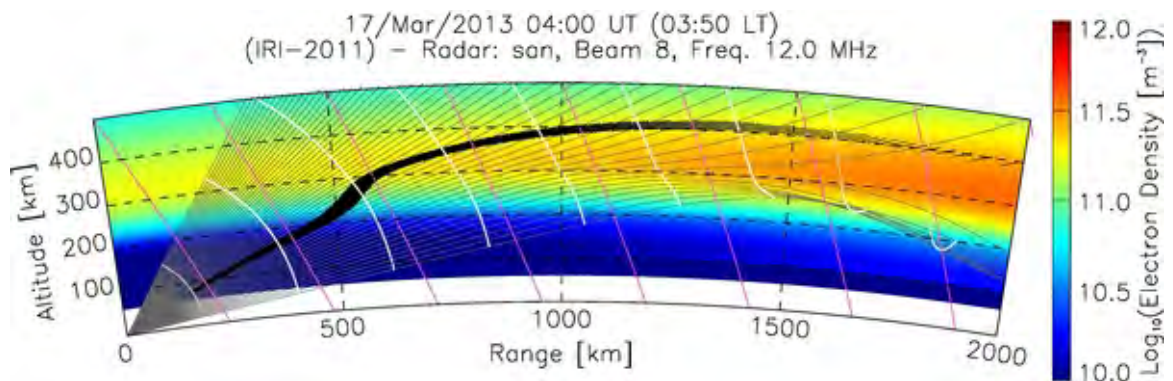


Figure 5.13: Ray tracing plot for SANAE radar beam 8 on 17 March 2013 at 04:00 UT. The pink lines indicate magnetic field lines. The black lines represent segments of computed ray paths where aspect condition is satisfied within 1°.

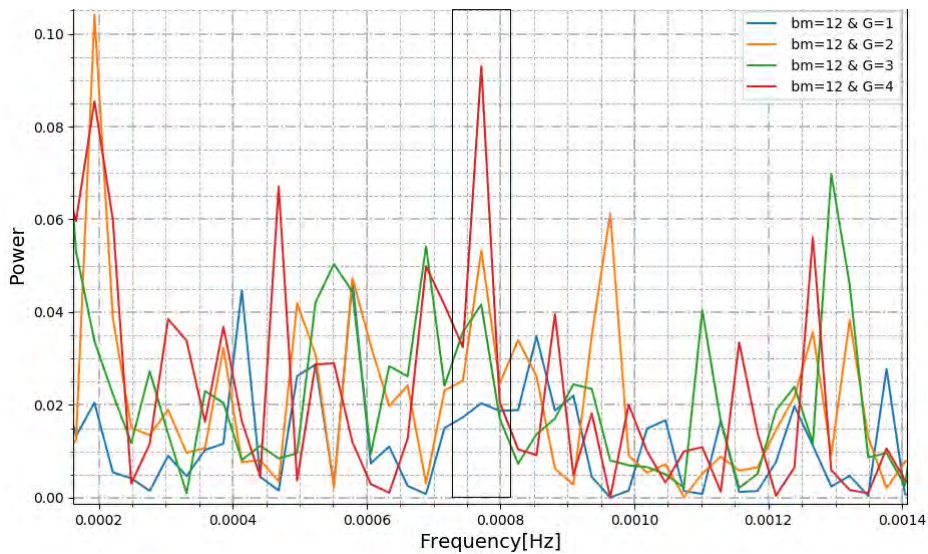


Figure 5.14: Lomb-Scargle periodogram of the backscattered power data from beam 12 and gate number 1 (blue), 2 (orange), 3 (green) and 4 (red).

5.3 Summary

The result of a multitaper analysis of the MSTID event observed on 17 March 2013 was presented in this chapter. The MSTID event was observed in backscatter and Doppler velocity data from both the SANA E and Halley radars for the period between 02:00 and 06:00 UT. The geomagnetic conditions before and during the observation of the event were quiet. The MTM method, together with a complex demodulation method, were used to obtain the analytic signal of the wave, which was used to estimate the instantaneous amplitude, frequency and phase of the MSTID for the duration of the event. Spectral analysis of the SANA E and Halley radar data showed a MSTID with a period of 23 min propagating in southeast direction with a maximum velocity of $\sim 280 \text{ ms}^{-1}$. Joule heating due to the MSTID was estimated by using the Doppler velocity data from the SANA E radar, and estimation of the magnetic field and neutral wind at the altitude where the MSTID was observed.

Chapter 6

GPS data analysis of TID events

6.1 Introduction

A combination of SuperDARN and GPS data have been used to observe TID events simultaneously and study their characteristics (e.g., [Ogawa *et al.*, 2009](#); [Hayashi *et al.*, 2010](#)). [Hayashi *et al.* \(2010\)](#) observed an LSTID event using simultaneous data from the GPS Earth observation network (GEONET) and the Hakkaido radar located in the northern hemisphere. GEONET provides a dense TEC map over Japan that can be used for ionospheric perturbation studies, for example to determine the propagation direction and the speed of TIDs ([Ogawa *et al.*, 2009](#); [Hayashi *et al.*, 2010](#)). TEC maps are used to determine the direction and speed of TID propagation. Over Antarctica, especially in the FOV of the SANA and Halley radars, the GPS network coverage is insufficient to do a similar analysis. Therefore, the analysis in this chapter is limited to the spectral analysis of TEC data in order to determine the frequency of the TID events.

Three events that occurred during different geomagnetic conditions were selected for analysis: 15 July 2012 (a major geomagnetic storm), 17 March 2013 (quiet time event) and 6 April 2015 (substorm event). The four GPS stations selected for this study were AMU2 (geographic location 89.9°S, 69.24°W), CRDI (geographic location 87.41°S, 30.56°W), PECE (geographic location 85.6°S, 111.44°W) and HOWE (geographic location 82.86°S, 120.8°W). These stations were selected for their close proximity to both radars and therefore the IPPs of the satellites observed by them overlap with the field of view of the radars, as illustrated in [Figure 6.1](#) for 16 March 2013. The GPS data used here were downloaded from the UNAVCO data archive (<https://www.unavco.org/data/gps-gnss/gps-gnss.html>) in RINEX (Receiver INdependent EXchange) format. The RINEX data were further analysed using GPS-TEC software to derive VTEC data as described in detail in [Section 4.6](#). VTEC data from the PRNs for the time period during which the radars observed TID events

were selected and detrended using a 15-minute running mean to remove the diurnal ionospheric variation. The detrended data were analysed using FFT for the frequency and period information. An elevation threshold of 20 degrees was used to filter out multipath signals. The frequencies and locations of the PRNs relative to the radars' observation area were compared for similarities between the waves observed from GPS TEC and radar data. The following plots are shown below: time series of VTEC, detrended VTEC (dVTEC) and the respective frequency spectrums. Also included are maps showing the IPP location of the PRNs and the location of the TIDs observed by the SANAE and Halley radars.

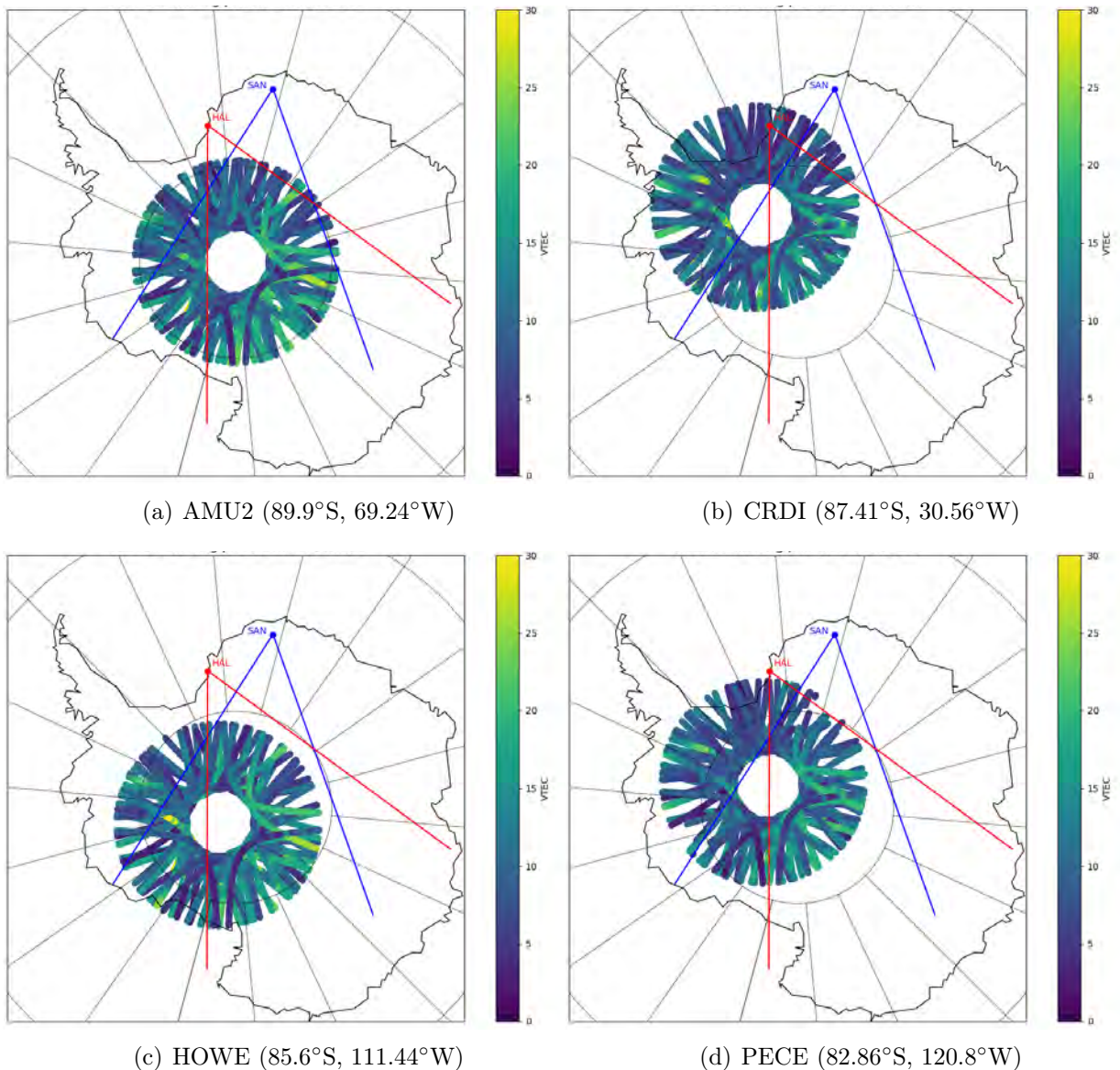


Figure 6.1: VTEC versus IPP latitude and longitude of all GPS satellites observed from station AMU2 (a), CRDI (b), HOWE (c) and PECE (d) on 16 March 2013. Note that coordinates in brackets are geographic coordinates.

6.2 Results and discussion

6.2.1 15 July 2012 event

Signatures of a TID event were observed by both the SANA E and Halley radars between 12:00 and 20:00 UT on 15 July 2012. The RTI plots in Figure 6.2 illustrate the TID signatures that propagated from lower to higher gate numbers with time. This means the TID propagation direction was away from the radar or poleward. Because of data gaps, the Lomb-Scargle method was used to determine the frequency/period of the TIDs, instead of the Fast Fourier transform. The Lomb-Scargle periodogram of the backscatter power data from beam 2 of the SANA E radar and beam 10 of the Halley radar is shown in Figure 6.3. As indicated by the periodogram, more than one wave was observed from the different range gates of the radars. For example, the dominant frequencies from gates 41-45 of beam 2 of the SANA E radar are 0.14, 0.27 and 0.6 mHz, corresponding to periods of 119, 61.7 and 27.7 minutes, respectively (see Figure 6.3(a)). Similarly, waves at gates 28-35 of Halley's beam 14 displayed a dominant frequency of 0.27 mHz (periods of 61.7 minutes) and some gates displayed dominant frequencies of 0.56 and 0.75 mHz (which correspond to periods of 29.8 and 22.2 minutes, respectively).

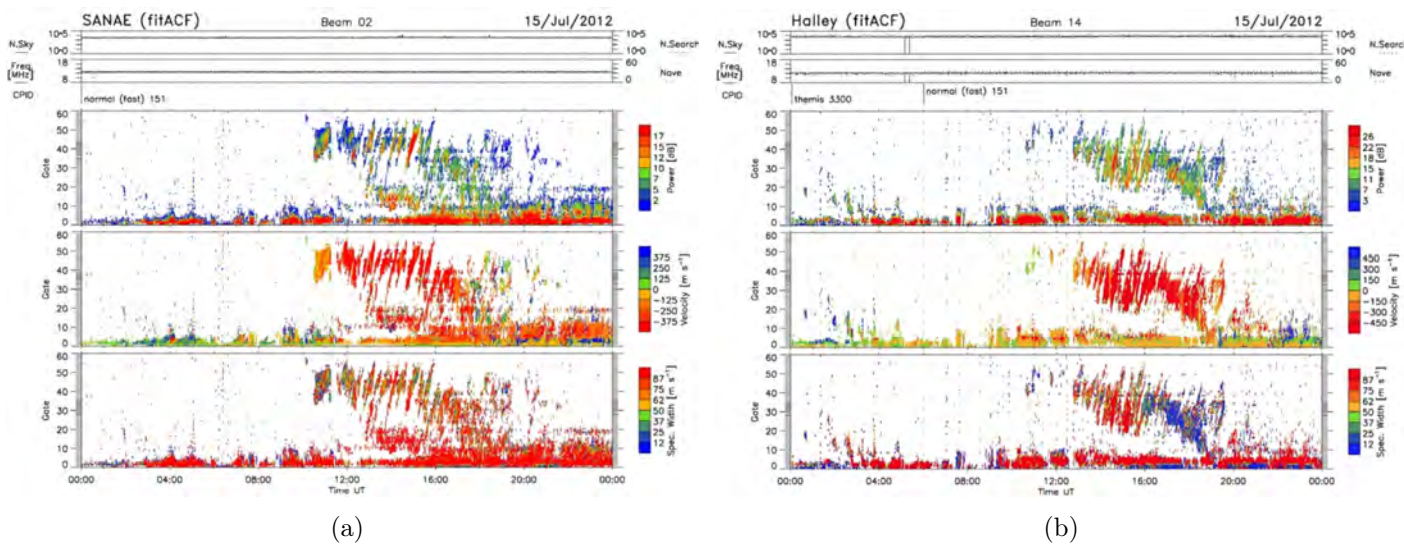


Figure 6.2: RTI plots of backscattered power data (top panel), Doppler velocity (middle panel) and spectral width (bottom panel) for the (a) SANA E and (b) Halley radars on 15 July 2012.

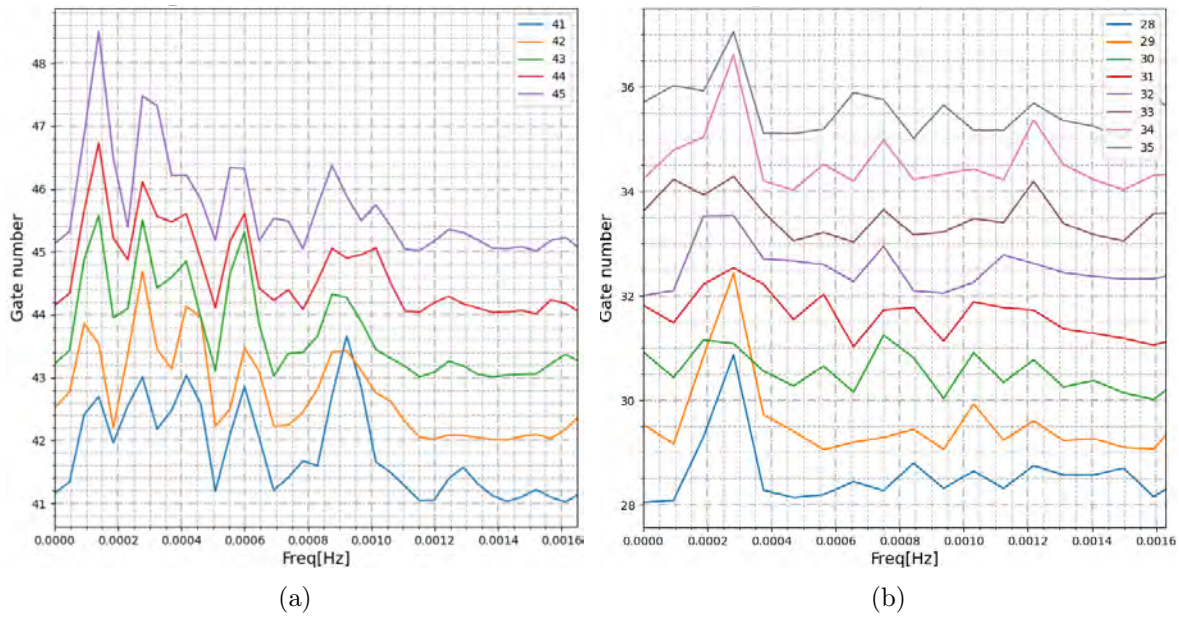


Figure 6.3: Lomb-Scargle periodogram of power measurements by (a) SANA E beam 2, range gates 41 to 45 and (b) Halley beam 14, range gates 28 to 35.

This 15 July 2012 event occurred during an intense geomagnetic storm, as illustrated by the geomagnetic indices and IMF data, shown in Figure 6.4. The storm commenced at around 18:00 UT on 14 July as indicated by an increase in the solar wind speed and B_z turning negative. During the main phase of the storm the solar wind speed, AE, PCS and K_p indices exceeded 600 km/s, 1200 nT, 12 and 7 respectively, while the B_z component and Dst index reached a minimum of -18 and -136 nT respectively. As indicated by the vertical dash lines in Figure 6.4, the TID event commenced at 12:00 UT on 15 July 2012, which was during the main phase of the storm.

Figure 6.5 displays the TEC map and radar data plots for this event as obtained from the VT SuperDARN website (<http://vt.superdarn.org/tiki-index.php?page=DaViT+TEC>). This figure indicates that GPS data coverage was very sparse and most of the data were to the west of the radars with a very small area that overlapped with the radar data. Figures 6.6(a) and (b) shows the time series VTEC data and detrended VTEC (dVTEC) data, respectively, taken from PRNs that were visible from the AMU2 and HOWE stations between 14:00 and 20:00 UT. The ray paths of the PRNs, the fields of view of the radars and the cells that observed the TIDs were plotted on the map in Figure 6.6(c), with the blue and red stars for SANA E and Halley radars. This plot illustrates that the ray paths of these PRNs are not only located closely to the SANA E cells used in the frequency analysis, but also have overlapping paths and time intervals, which suggest that these instruments may be looking at the same wave. The FFT spectrum in panel (d) of Figure 6.6 shows that several frequencies were dominant; however, the frequency of 0.6 mHz (27 minutes period) was detected by all PRNs and was also one of the frequencies that was detected by

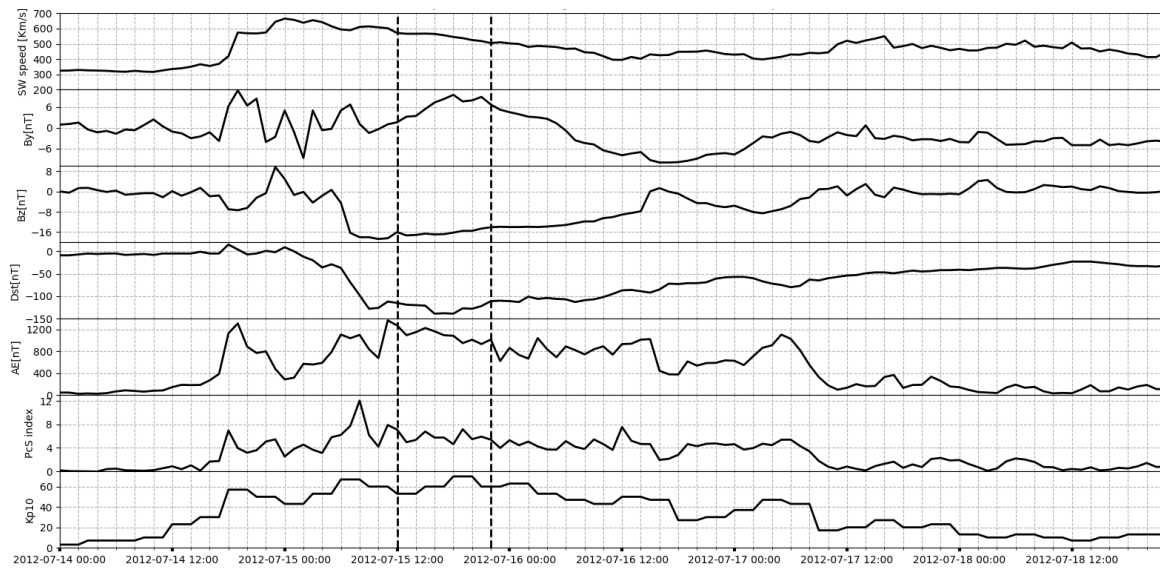


Figure 6.4: Hourly solar wind data (top panel), IMF By (2nd panel), IMF Bz (3rd), Dst (4th panel), AE index (5th panel), PCS index (6th panel) and Kp10 index (last panel) from 14 to 18 July 2012. The vertical dash lines indicate the time period when the TIDs were observed by the SANA E radar.

the SANA E radar.

TOTAL ELECTRON CONTENT 15/Jul/2012 14:55:00.0
 GPS Receiver Network (Millstone Hill) to
 15/Jul/2012 15:00:00.0

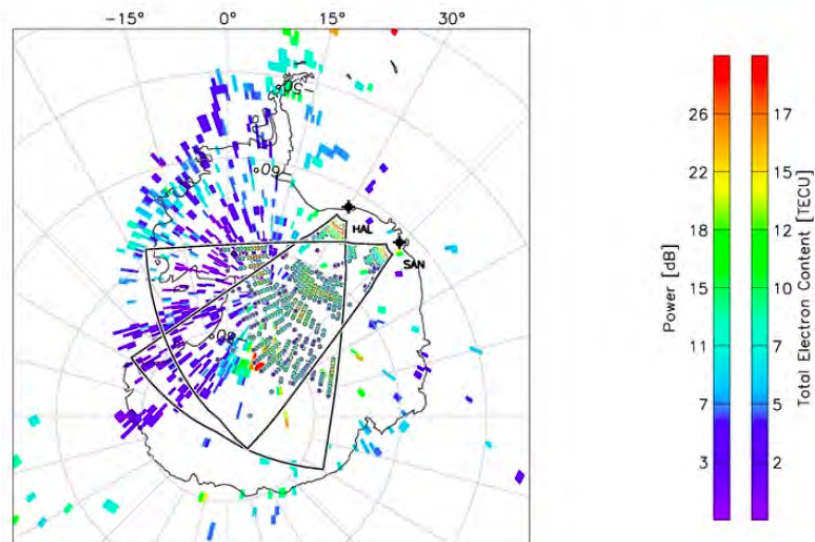


Figure 6.5: TEC map for Antarctica plotted over backscatter power data from SANA E and Halley radars for 15 July 2012 at 15:00 UT. Plot taken from Virginia Tech SuperDARN website. Note that the map displays magnetic coordinates.

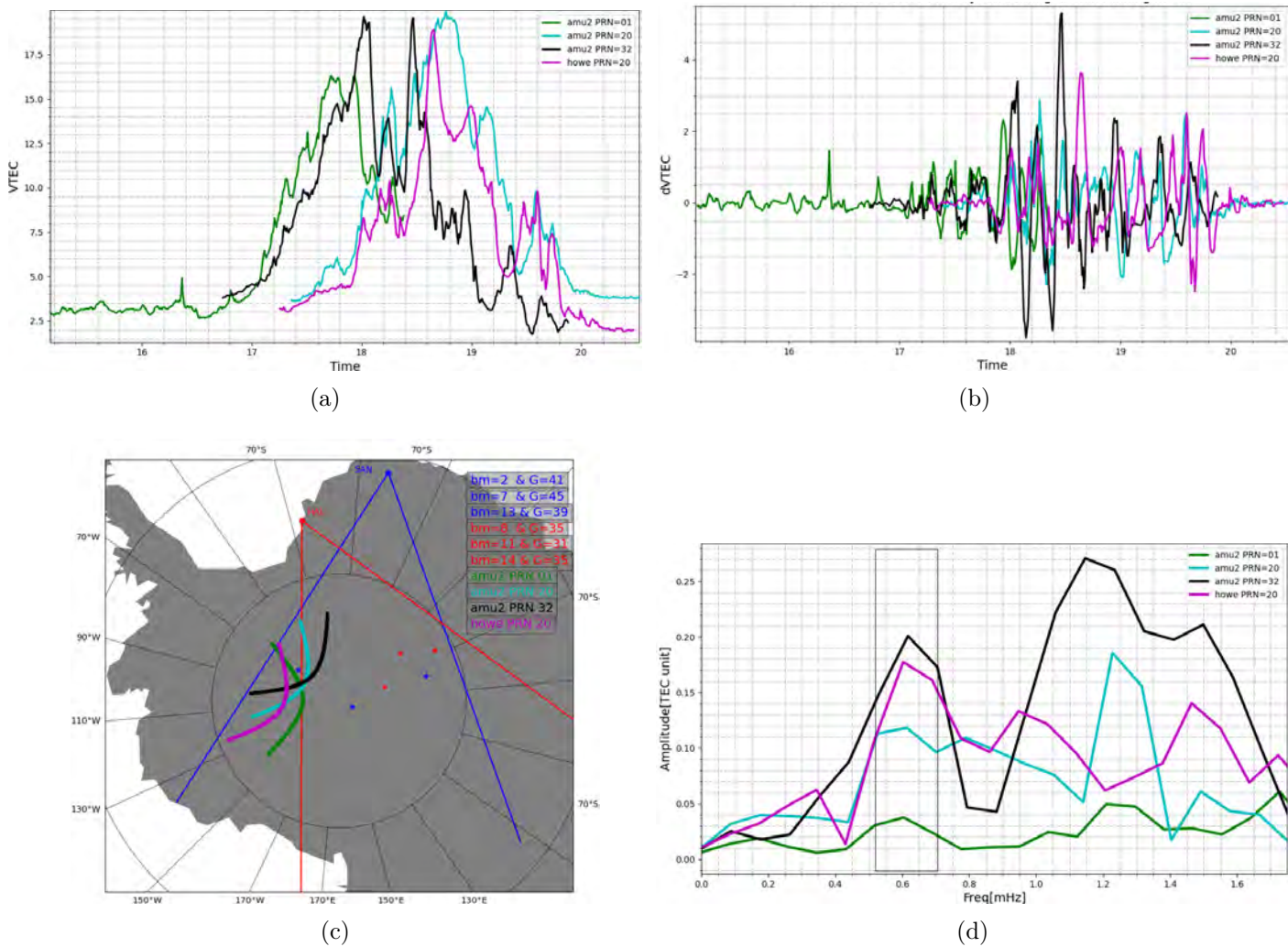


Figure 6.6: Plots showing (a) time series data of VTEC from different PRNs detected by AMU2 and HOWE GPS receiver stations on 15 July 2012, (b) detrended VTEC data, (c) ray path of each PRN with respect to the observation area of the HF radars and (d) FFT of detrended data.

6.2.2 17 March 2013 event

In the previous chapter it was shown that the 17 March 2013 MSTID event occurred post midnight between 02:00 and 06:00 UT during quiet geomagnetic conditions and was observed by both the SANAE and Halley radars. It was found to have an MSTID with period of 23 minutes (frequency of 0.72 mHz) and propagated southeast at a speed of $\sim 225 \text{ ms}^{-1}$. In this section, GPS data is analysed to determine whether this event was observable within the GPS data. Figure 6.7 presents a GPS TEC map and backscatter power data from the SANAE and Halley radars for 17 March 2013 at 03:00 UT (from VT SuperDARN website <http://vt.superdarn.org/tiki-index.php?page=DaViT+TEC>). The variation in TEC value, seen on the map, indicate the area of high and low electron density which is the signature of AGWs/TIDs in the ionosphere. As can be seen from the figure, there are not many areas where the GPS data and radar data overlap, since the backscatter comes from the lower range gates of the radars. Thus, PRNs close to the fields of view of the radar that exhibit frequencies close/similar to the ones in the radar data, will be used instead.

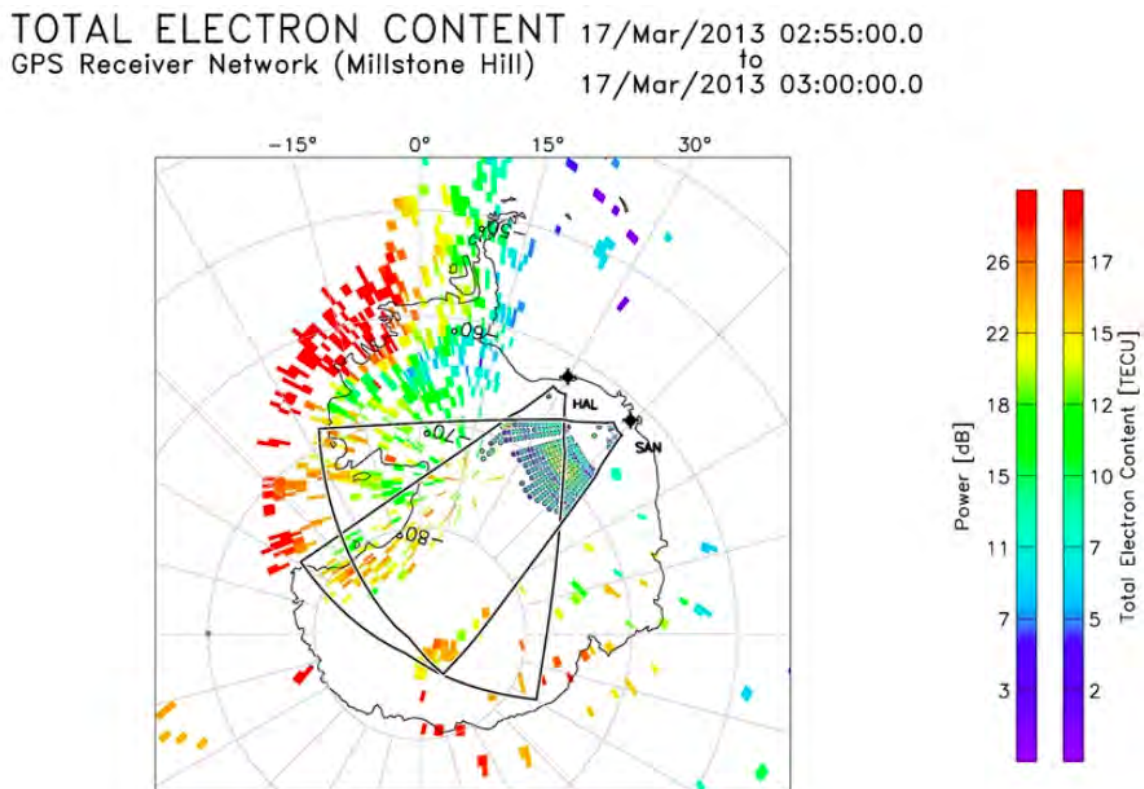


Figure 6.7: TEC map for Antarctica plotted over backscatter power data from the SANAE and Halley radars for 17 March 2013 at 03:00 UT. Plot taken from Virginia Tech SuperDARN website. Note that map uses magnetic coordinates.

Figure 6.8 presents GPS time series data and frequency analysed for time period during which TIDs were observed in the SANAE HF radar data. The VTEC and

detrended VTEC for 4 PRNs, shown in Figure 6.8(a) and (b), exhibit possible signatures of TIDs seen as periodic oscillations of VTEC/detrended VTEC. Note that the IPP locations of the PRNs are within the field of view of SANA E, especially PRN 25 which has a ray path closest to the area where the TID was observed over the CRDI station (see Figure 6.8(c)). An FFT analysis of the GPS data revealed a wave with a frequency of 0.7 mHz (corresponding to a period of 23.8 minutes). This frequency/period agrees with that obtained from SANA E HF radar data and therefore suggests that both instruments observed the same structures.

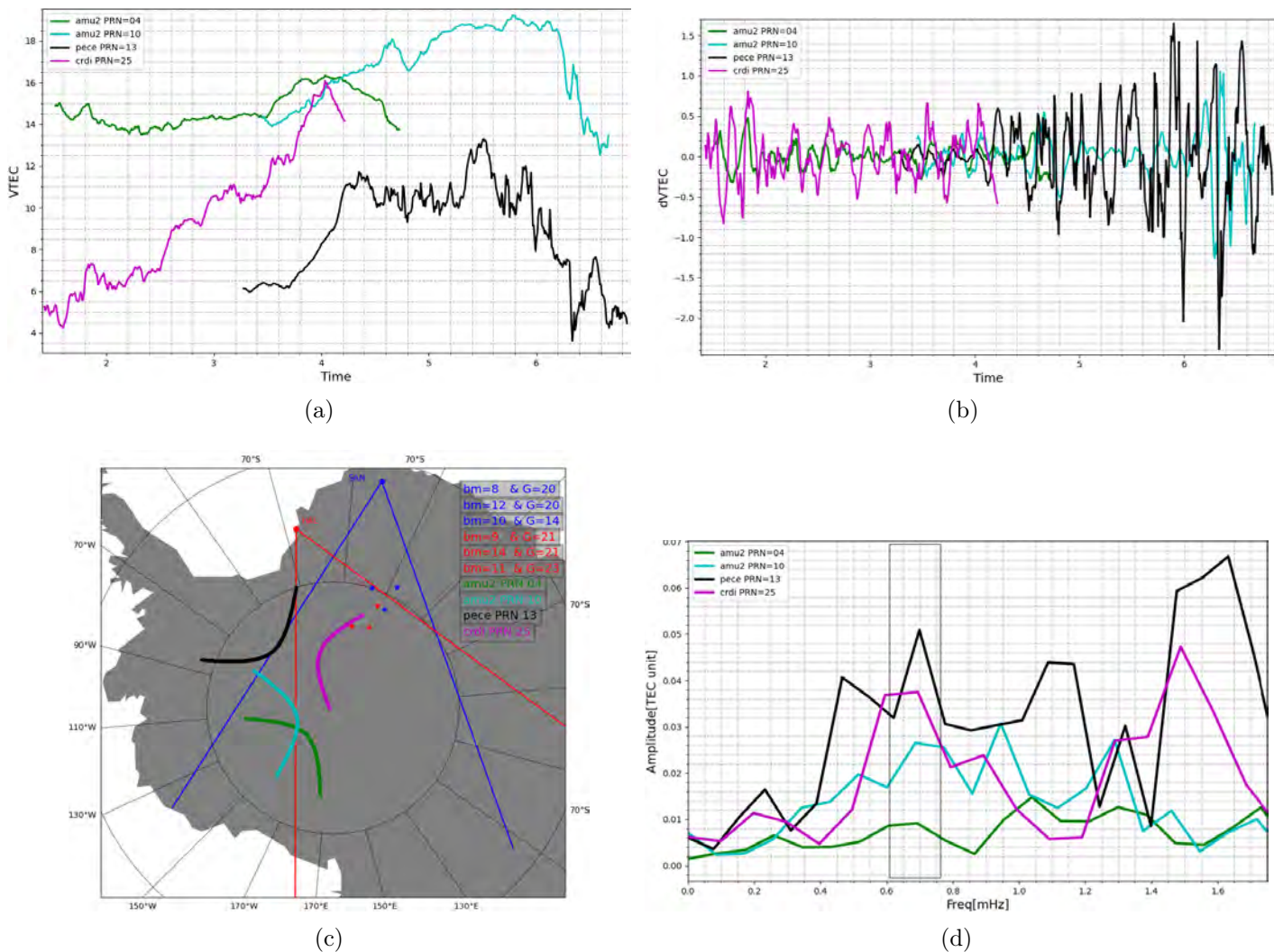


Figure 6.8: Plots showing (a) time series data of VTEC from different PRNs detected over AMU2, PECE and CRDI GPS receiver stations on 17 March 2013, (b) detrended VTEC data, (c) ray path of each PRN with respect to the locations where TIDs were observed by the HF radars and (d) the FFT of the detrended VTEC data.

6.2.3 6 April 2015 event

Figure 6.9 presents an example of TID signatures observed post-midnight in SANA E radar data on 6 April 2015 between 00:00 and 06:00 UT. The frequency analysis of the backscattered power data from the SANA E radar indicates the existence of two dominant frequencies, i.e. 0.38 MHz and 0.55 MHz (equivalent to periods of 43 and 30 minutes, respectively), for most of the beams. FFT plots of selected cells are shown in Figure 6.10. Using Equations (4.3) and (4.5) the phase velocity and propagation direction of the TIDs are determined to be 98 and 109 ms^{-1} for TIDs with frequencies of 0.38 MHz and 0.55 MHz, respectively, and propagates northward.

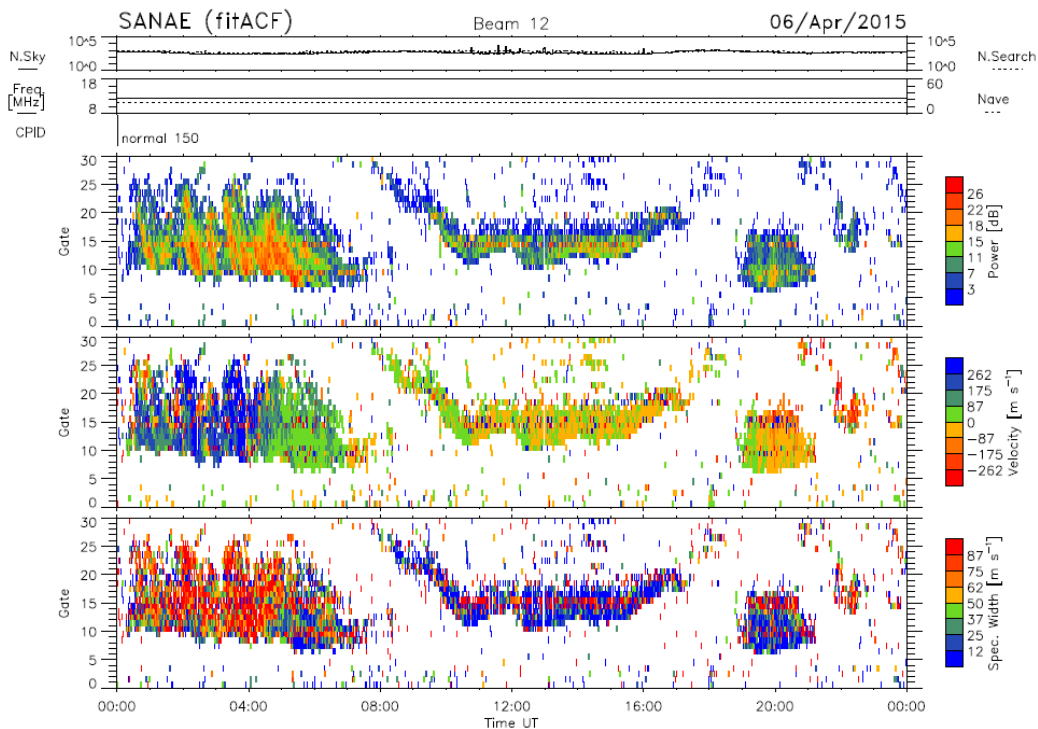


Figure 6.9: RTI plots of backscattered power (top panel), Doppler velocity (middle panel) and spectral width (bottom panel) of data from SANA E radar on 6 April 2015.

The geomagnetic state before the commencement of the event was disturbed condition with multiple AE increments and a high solar wind speed of up to 550 ms^{-1} . Figure 6.11 shows the solar wind conditions and the geomagnetic indices between 2 and 6 April, 2015. The solar wind speed a few days before the event (2-5 April 2015) was higher than the typical solar wind speed, which is usually 300-400 km/s (Tsurutani *et al.*, 2006). These conditions lasted for almost 3 days (see top panel of Figure 6.11). Figure 6.11 also shows that the B_z fluctuated between positive and negative and the AE was $\sim 300 \text{ nT}$ around 23:00 UT on 5 April 2015 (3rd and 4th panels respectively). The IMF B_z fluctuation and a series of AE index activities, in addition to the increase observed in the SW pressure, proton density and temperature, indicate the occurrence of a HSSs and/or a CIRs events.

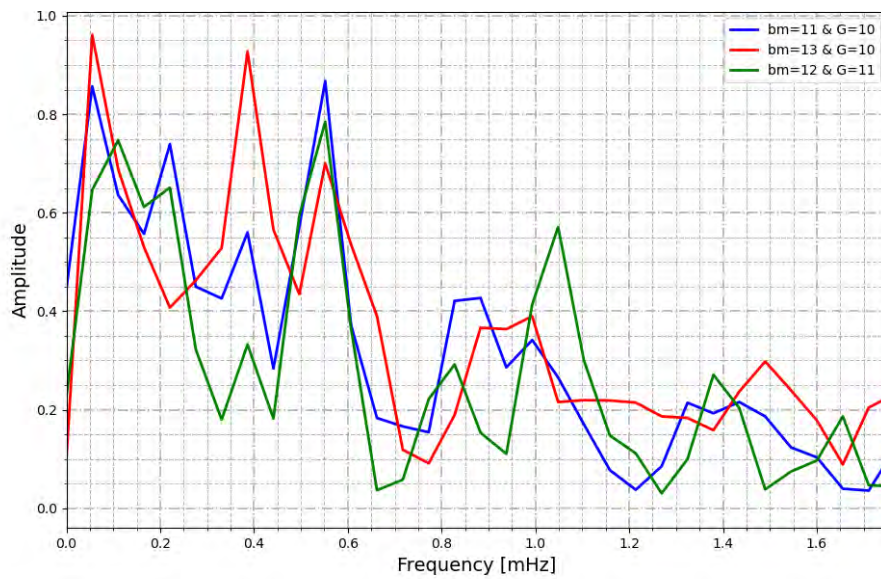


Figure 6.10: FFT plot of backscatter power data from SANAE radar for the period between 01:00 and 06:00 UT on 6 April 2015.

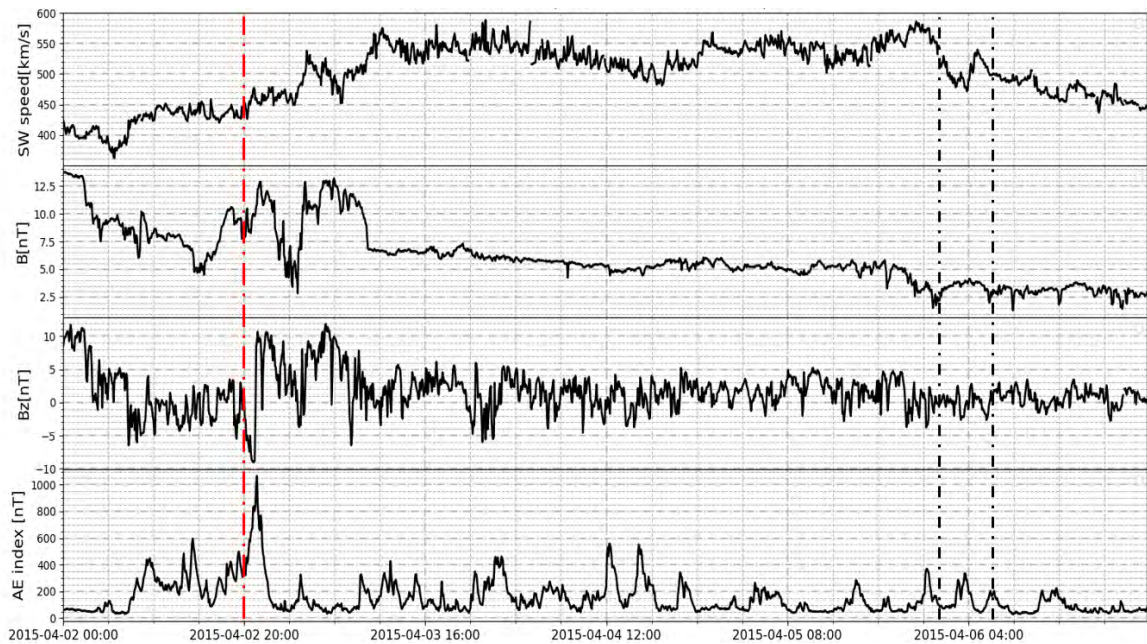


Figure 6.11: Solar wind speed (1st panel), total IMF magnitude (2nd panel), IMF Bz (3rd panel) and AE index (4th panel) for the time period between 02 and 05 April 2015. The start of the HSSs/CIRs event is marked by the vertical red dash line. The vertical black dash line indicates the start and end of the TID event in the SANAE radar data.

As can be seen in Figure 6.12, the ionospheric backscatter data from the SANAE and Halley radars do not coincide. The SANAE backscatter occurs at the lower range

gates at the boundary of the field of view of the Halley radar. The area in which the TIDs were observed was therefore not covered by both radars and thus the results of the Halley radar were not included.

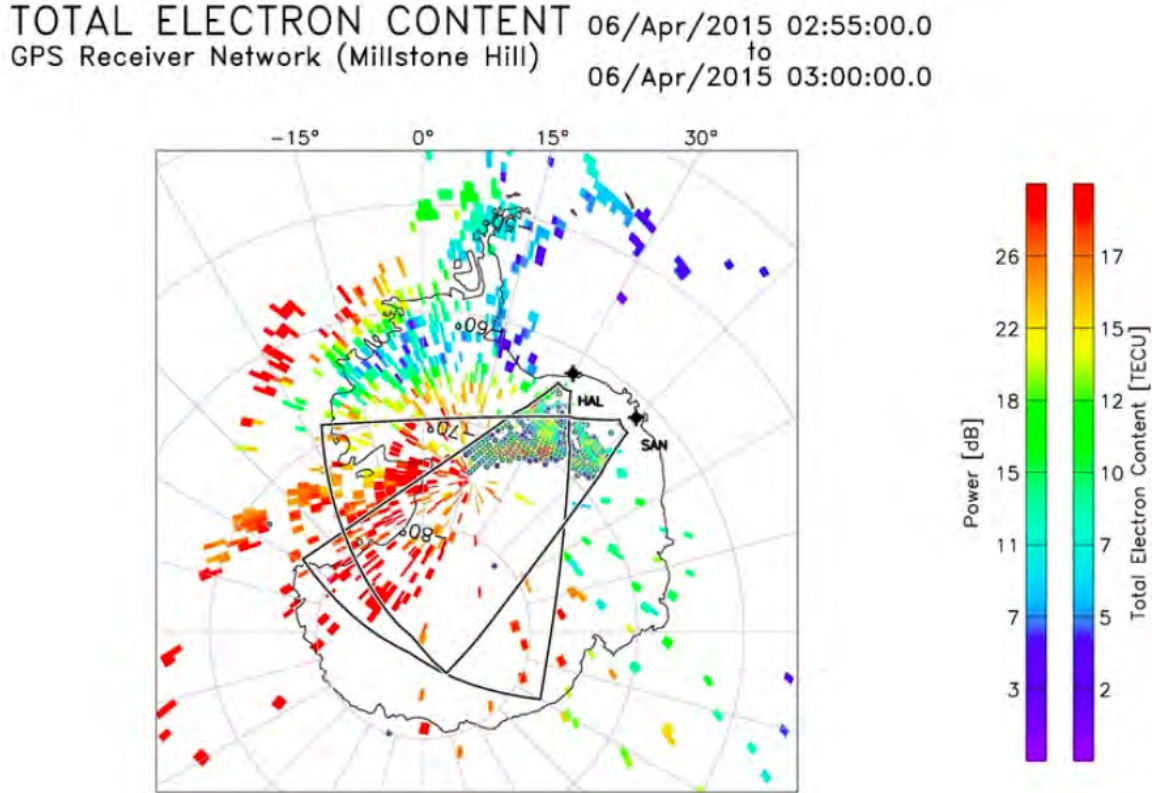


Figure 6.12: TEC map for Antarctica plotted over backscatter power data from the SANA and Halley radars for 6 April 2015 at 03:00 UT. Plot taken from Virginia Tech SuperDARN website. Note that the map uses magnetic coordinates.

Figure 6.13(a) displays time series data of VTEC from PRN 07, 09 and 30 that were detected by the PECE GPS receiver station on 6 April 2015 between 00:00 and 06:40 UT. The PRNs were visible during the period that the TIDs were observed by the SANA radar (see Figure 6.13(a) and (b)). The PRNs have ray paths that are close to each other, as seen in Figure 6.13(c), therefore they probably sample the same general volume of the ionosphere and detect the same wave structures. All the PRNs registered a frequency of 0.55 mHz (equivalent to a period of 30 minutes), as did the radar data (see FFT plot in Figure 6.13(d)).

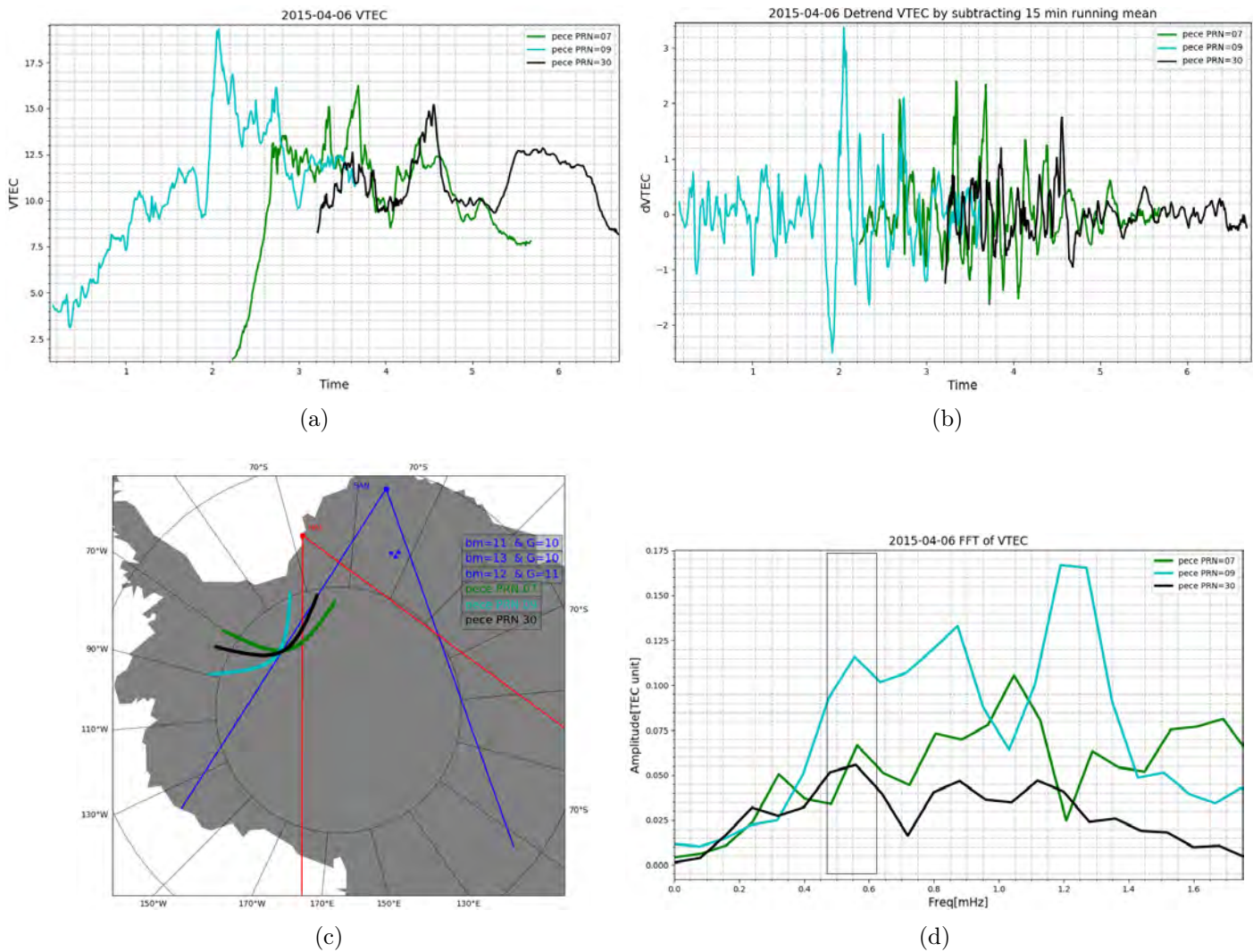


Figure 6.13: Plot showing (a) time series data of VTEC from PRN 07, 09 and 30 that were detected by the PECE GPS receiver station on 6 April 2015, (b) detrended VTEC data, (c) FFT of the detrended data and (d) ray path of each PRN with respect to the locations where TIDs were observed in the HF radar data.

6.3 Summary

This chapter discussed the results of a GPS TEC data analysis of three selected TID events that were observed in SuperDARN data. The events were selected as examples of TIDs observed during different geomagnetic conditions. The first of these events was observed on 15 July 2012 during the main phase of an intense geomagnetic storm. The event was observed by both the SANA and Halley radars with poleward propagating TID signatures. Both the radars and GPS data observed a frequency of 0.6 mHz (corresponding to period of 27 minutes). The second event occurred on

17 March 2013 simultaneously by both the SANA E and Halley radars. This event occurred during a geomagnetically quiet time and was identified by TIDs signatures that depict poleward propagation. A spectral analysis of the radar data detected an MSTID of frequency 0.72 mHz (corresponding to a period of 23 minutes) with an average phase velocity of $\sim 189 \text{ ms}^{-1}$ propagating in southeast direction. GPS TEC data from 4 PRNs that were visible nearby the FOV of the radars during the same time period that the MSTID was observed by the radars, had a frequency of 0.7 mHz (corresponding to a period of 23.8 minutes), very close to that of the radars. The last event that was analysed occurred on 6 April 2015 during a substorm. There was no simultaneous observation by the SANA E and Halley radars of this event, as the backscatter data from each receiver fall under different geographic locations. Consequently, only the results relating to SANA E and GPS TEC were discussed for this event. An MSTID with a frequency of 0.55 mHz (corresponding to a period of 30 minutes) was observed in both the radar and GPS TEC data. The analysis of the radar data showed that the MSTID had a phase velocity of 109 ms^{-1} and propagated northward. Another MSTID with frequency of 0.38 mHz (corresponding to a period of 43 minutes) and phase velocity of 98 m/s was observed from the radar, which has a similar propagation direction as the 0.55 mHz (30 minutes) MSTID. It is important to note that GPS signals comes in a slant direction while the enhancement and depletion of the ionosphere due to the TIDs are in horizontal direction, which might affect the detection of the TIDs using GPS. That means if the TID propagation direction is along the path of the GPS signal the amplitude of TID becomes zero ([Katamzi, 2011](#)).

Chapter 7

Survey of TID events as observed in SANAE HF radar data and their associated source mechanism

7.1 Introduction

In this chapter TID characteristics as observed in SANAE radar will be presented. The study includes TID events that occurred between the years 2005 and 2015, and were identified in visual inspection of the RTI plots. The study aims to give insight into the general characteristics of TIDs over Antarctica during solar minimum and maximum, during the different seasons and times of the day. The study timespan begins with the decline phase of the 23rd solar cycle and continues to the declining phase of the next cycle. The number of sunspots during the two solar cycles is presented in Figure 7.1, which shows that the period from 2005 to 2007 is the declining phase of the 23rd cycle and solar activity was at a minimum from 2008 until 2010. Solar activity then increased until the year 2012 when the first peak of solar maximum was observed. The second and highest solar maximum was observed during mid 2014. From 2015 onward solar activity declines. The SANAE radar is located at geographic latitude of 71.68°S and longitude of 2.85°W, which means the local time and universal time are the same, whereas magnetic local time (MLT)= UT−2 hours.

A total of 22 possible TID event days were identified in the SANAE HF radar data, and 9 of these events were observed simultaneously in the Halley radar data. Some of these events did not show significant signature in the frequency range of TIDs or were not processed due to a significant data gap (more than 50%). Therefore, out of the 22 event days, results for only 16 are reported here. The frequency/period of the TIDs were calculated from both Lomb-Scargle and FFT spectral analyses methods. The FFT method was used for events where 80% of data or more were

available within the time interval of interest, whereas the Lomb-Scargle method was used when the missing data were more than 20% but not exceeding 50%. Table 7.1 lists the 16 event days when TIDs were detected and analysed from the SANA E radar, of which 4 include results from the Halley radar. All events were observed in ionospheric scatter of the radars. The table shows the characteristics of the TIDs, namely the central frequency of broadband peak, period, phase velocity, wavelength, and propagation direction. In addition, geomagnetic condition during and up to 8 hours prior to the start of the event, is listed for each event. Geomagnetic quiet periods are characterized by $Dst > 20$ nT, $kp10 \leq 30$, $AE < 300$ nT and PCS 0–2. For the events that were analysed by means of the Lomb-Scargle method, it was not possible to estimate the propagation direction of the TIDs, because it is not possible to obtain phase information from a Lomb-Scargle periodogram with which to calculate the propagation azimuth. Therefore, the propagation azimuths of these events were roughly estimated using the RTI plots, as either away ($\sim S$) or towards ($\sim N$) the radar. The slopes of the TID signatures from the RTI plots, were used to determine the speed, which was subsequently used to calculate the wavelength (see Section 4.3). The rest of this chapter focuses on discussing the analysis of SANA E HF radar data as this is the main objective of this project.

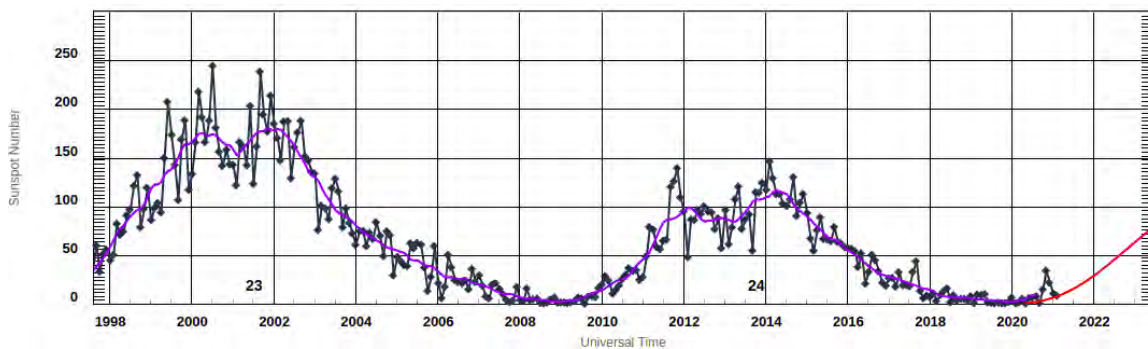


Figure 7.1: Number of sunspots for solar cycles 23 and 24 (credit: <https://www.swpc.noaa.gov/products/solar-cycle-progression>).

Table 7.1: List of TIDs events and their characteristics.

Event day	Radar	Time interval	Frequency (mHz)	Period (min)	V_{ph} (ms^{-1})	λ (km)	Azimuth	Geomagnetic condition
2005/03/01	SANA E	02:00-05:00	0.35	47.62	173	473	NW	substorm
2005/03/03	SANA E	02:00-05:46	0.36	45.66	84	229	SE	HSSs/CIR
2005/03/04	SANA E	03:00-07:00	0.23	72.46	430	1870	away from radar (\sim S)	quiet period
			0.33	50.51	213	645	away from radar (\sim S)	
2005/05/06	SANA E	04:00-08:00	0.35	50.51	186	530	away from radar (\sim S)	quiet period
2005/05/07	SANA E	01:00-13:00	0.44	47.62	285	646	S	quiet period
2007/03/19	SANA E	01:00-05:00	0.2	83.3	65	328	SE	quiet period
			0.55	30.3	70	129	SE	
2007/09/14	SANA E	02:30-06:00	0.4	41.7	333	833	away from radar (\sim S)	quiet period
			0.55	30.3	175	318	away from radar (\sim S)	
			0.7	23.8	95	136	away from radar (\sim S)	
			0.1	166.7	163	1630	away from radar (\sim S)	
2010/03/26	Halley	03:00-06:00	0.27	61.7	100	370	away from radar (\sim S)	substorm
			0.11	151.5	156	1414	NW	
2012/02/27	SANA E	03:30-06:30	0.27	60.2	67	243	N	substorm
2012/03/11	SANA E	00:00-05:00	0.22	75.8	137	623	N	geomagnetic storm
			0.6	27.8	327	546	N	
2012/07/15	SANA E	13:00-16:00	0.1	166.7	750	7500	away from radar (\sim S)	geomagnetic storm
			0.27	61.7	625	2315	away from radar (\sim S)	
			0.56	29.8	434	775	away from radar (\sim S)	
			0.75	22.2	434	579	away from radar (\sim S)	
			0.27	61.7	666	4757	away from radar (\sim S)	
2012/10/27	SANA E	00:30-04:00	0.55	30.3	154	281	N	substorm
2013/03/17	SANA E	02:04-06:14	0.72	23.1	199	274	SE	quiet period
	Halley	02:08-06:00	0.72	23.1	179	248	SE	
2013/03/20	SANA E	02:00-05:00	0.54	30.4	169	309	N	substorm
2013/04/08	SANA E	03:00-06:00	0.18	91.1	54	297	SE	substorm
2015/04/06	SANA E	01:00-06:00	0.38	43.2	98	256	N	substorm or HSSs/CIR
			0.55	30.3	109	198	N	
Halley	Halley	00:30-05:00	0.37	45	243	659	S	

7.2 Results and discussion

7.2.1 Characteristics of TIDs

All events described here were observed in ionospheric scatter data, different from most of the TIDs reported in the literature (e.g. [Samson *et al.*, 1989](#); [Bristow *et al.*, 1994](#); [Ishida *et al.*, 2008](#); [Grocott *et al.*, 2013](#)). One reason for this could be that the SANAE radar has a higher ratio of ionospheric to groundscatter returns than most other SuperDARN radars ([Mravlag, 2007](#)). Also, since these events are picked out by visual inspection, and ionospheric power and velocity variations tend to be larger than those in groundscatter, they are thus easier to identify visually. A recent work by [Gounden \(2022\)](#) showed that there were more ground scatter MSTIDs than ionospheric scatter MSTIDs in SANAE data in 2013 when using automated method, which identify the MSTIDs based on frequency. All events occurred between midnight and 06:00 UT, except for one event on 15 July 2012, which was observed between 14:00 and 20:00 UT. It is important to note that July is in the middle of winter in Antarctica, meaning there is no sunlight.

The characteristics of the TIDs identified in SANAE radar data are presented in histograms in [Figure 7.2](#). As can be seen, 26 TIDs were identified on 16 event days, with some of the events having more than one TID structure. The histograms in [Figure 7.2](#) shows that most of the TID events (65.4%) are MSTIDs with periods between 20 and 60 minutes and phase velocities mostly between 50 to 333 ms^{-1} , except for a few where the velocities exceeded 400 ms^{-1} . The MSTID phase velocities agree with the ones reported by [Crowley *et al.* \(1987\)](#) over Antarctic Peninsula, with MSTID phase velocities of up to 300 ms^{-1} during geomagnetically quiet conditions, but with velocities higher than 300 ms^{-1} during disturbed conditions. On 15 July 2012 multiple waves with frequencies ranging from MSTIDs to LSTIDs and phase velocities $> 400 \text{ms}^{-1}$, were observed during a geomagnetic storm. Unlike the other events, this event was analysed using Lomb-Scargle method due to large data gaps (see RTI plot in [Figure 6.2](#)). Therefore, the estimation of the velocities was based on a slope of the line that traces (using approximate sketch) the strong backscattered power in the RTI plots of different beams. It is known that this method has a large uncertainty, mainly because it is based on visually choosing the best line. Also, the estimation of the velocities of the TIDs by means of one beam provides the velocity component only in the direction of the beam. In addition, since more than one TID structure was identified for this day, it was difficult to relate the estimated velocities to the respective TIDs. Therefore, based on the known characteristics of LSTIDs and MSTIDs (i.e. high velocities for LSTIDs) the estimated velocities were assigned to each TID on the basis of their periods. Based on the estimated periods, velocities and wavelengths of the TIDs, 4 LSTIDs (15.4%) and 17 MSTIDs (65.4 %) were identified from a total of 26 TIDs as observed in the SANAE radar data. Five of the TIDs (19.2%) were too ambiguous to categorise. In addition, it needs to be pointed out that the method that was used to estimate the phase velocity and wavelength, has

been previously used for MSTIDs, but not for LSTIDs (He *et al.*, 2004; Grocott *et al.*, 2013). Therefore, it is possible that the error in the estimated parameters of LSTIDs is due to the method that was used. For the method to work correctly, the phase difference should be calculated using three quasi-equally spaced cells with the distance between the cells being comparable to the wavelength of the TIDs. For LSTIDs this distance has to be in the order of a thousand kilometres, which makes it difficult to find three cells that see the same frequency and have 80% of the data from the SANA E radar FOV over those kind of distances.

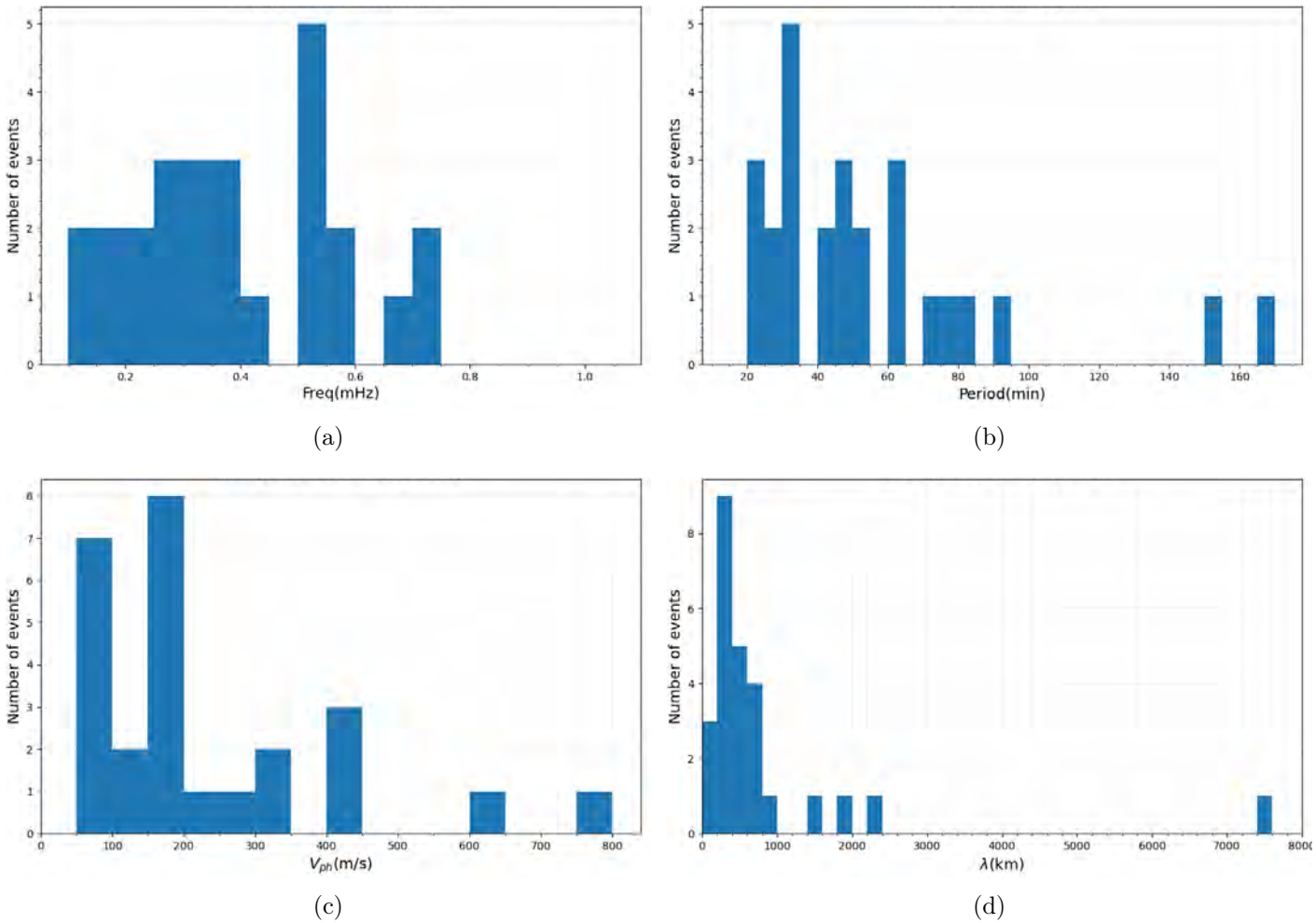


Figure 7.2: Histogram of (a) frequencies, (b) periods, (c) phase velocities and (d) wavelengths for all TIDs events observed between 2005 and 2015.

Figure 7.3 shows azimuth, phase velocity and periods of all TIDs observed by the SANA E radar. Based on the current results, it will be difficult to draw a clear relation between the propagation direction of the TIDs and their source mechanism. As shown in Table 7.1), not all or most events observed during geomagnetic storm or substorm conditions, which have possible source from auroral activity, propagate equatorward (i.e. northward, based on the location of the radars). Commonly TIDs

generated from auroral sources at high latitudes propagate equatorward (Francis, 1975; Hunsucker, 1982). Although not common, a study by Katamzi-Joseph *et al.* (2019) reported high-latitude LSTIDs propagating poleward during substorm activity on 6 January 2014. It is also important to note that, for the events during which TIDs propagated away from the radar ($\sim S$), the direction of the TIDs were determined from the slope of the TID signatures using the RTI plots. A positive (negative) slope in a RTI plot signifies that the propagation direction is away from (towards) the radar, i.e. southward (northward) (see Figure 6.2 for example). Figure 7.3 shows that there are TIDs with longer periods, longer than 1 hour, but phase velocities of less than 200 ms^{-1} . These were also classified as MSTIDs, since their velocities and wavelengths fall within the range of MSTIDs, as was found in to a study by Ding *et al.* (2011). They reported MSTIDs with periods of 20–70 min and phase velocities 50–230 ms^{-1} .

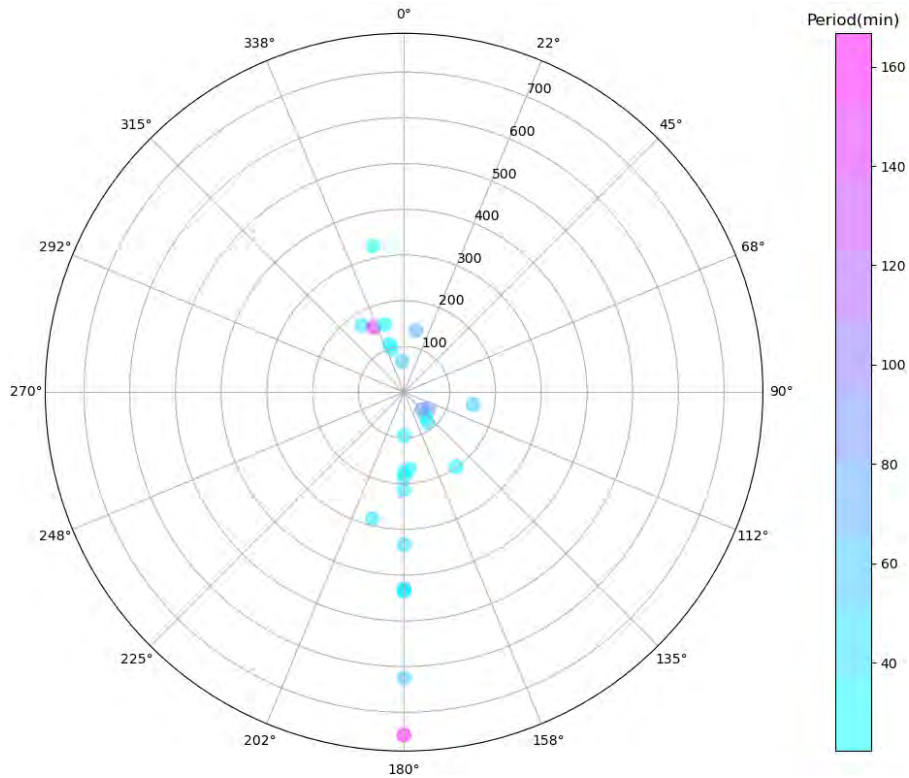


Figure 7.3: Polar plot which shows variation of period and azimuth with phase velocity. The circumference represents the propagation azimuth (with 0° corresponding to northward direction), phase velocity (in ms^{-1}) is represented using the radial distance, and the period is indicated by the colour bar.

7.2.2 Dependence of the occurrence of TIDs on seasonal and geomagnetic activity

The plot (Figure 7.4) of TIDs seasonal occurrence shows that most of the events (46%) were observed during the month of March. The TIDs occurring during the month of March propagated mainly northward and southward. The colour and size of the circles in the polar plots represent the periods and phase velocities in Figure 7.4(a) and (b), respectively, which are also represented by the colour bars. The plot of phase velocity with season shows that the majority of the TIDs observed during the month of March have velocities less than 200 ms^{-1} (see Figure 7.4(b)). Figure 7.3 shows that there was only one day with a TID event during winter; the majority of the events occurred during the equinox season (i.e. from March to May). This trend agrees with the results of a study by Grocott *et al.* (2013) relating to the area near to the Antarctic Peninsula. It was found that majority of the MSTID events were during the equinoxes. However, studies by Ogawa *et al.* (1987) and Bristow *et al.* (1996) over the southern and northern high latitudes, respectively, showed that MSTIDs occur more frequently during the winter season than during summer. These findings which are seemingly contradictory to those of Bristow *et al.* (1996) may be explained by the fact that, unlike the current study, their results were obtained from ground scatter HF radar data. This indicates that the source mechanism is different as TIDs observed from ground scatter are associated with AGWs. Also, the dissimilarity on the seasonal trend obtained in this study compared to that reported by Ogawa *et al.* (1987) could be due to the fact that the studies used different instruments; Ogawa *et al.* (1987) used differential Doppler measurements, which have different capabilities in detecting TIDs. Furthermore, Ogawa *et al.* (1987) pointed out that the results obtained from the differential-Doppler measurements may not represent the actual nature of TIDs/AGWs at ionospheric heights.

Table 7.1 shows that of the 16 event days presented here 6 occurred during quiet geomagnetic conditions and 8 may have been associated with disturbed geomagnetic conditions, since there were substorm or HSS/CIR events that occurred during or within 8 hours before the TIDs events as observed in the SANA E radar data. Figure 7.5 shows that 5 of the events happened during quiet geomagnetic conditions. The 6th event on 17 March 2013 has been discussed in detail (see Figure 5.11). Solar wind speed and the IMF B_y and B_z data confirm that there were no disturbances prior or during the TID events.

Only 2 events reported here occurred during geomagnetic storms, one during the main phase of the 15 July 2012 storm and the other during the recovery phase of the 11 March 2012 storm. A detailed analysis of the 15 July 2012 event, using a Lomb-Scargle periodogram, was done in Chapter 6. Events during geomagnetic storms tend to have multiple frequencies ranging from a medium- to a large-scale TIDs. These could be due to the possibility of multiple sources during geomagnetically disturbed periods.

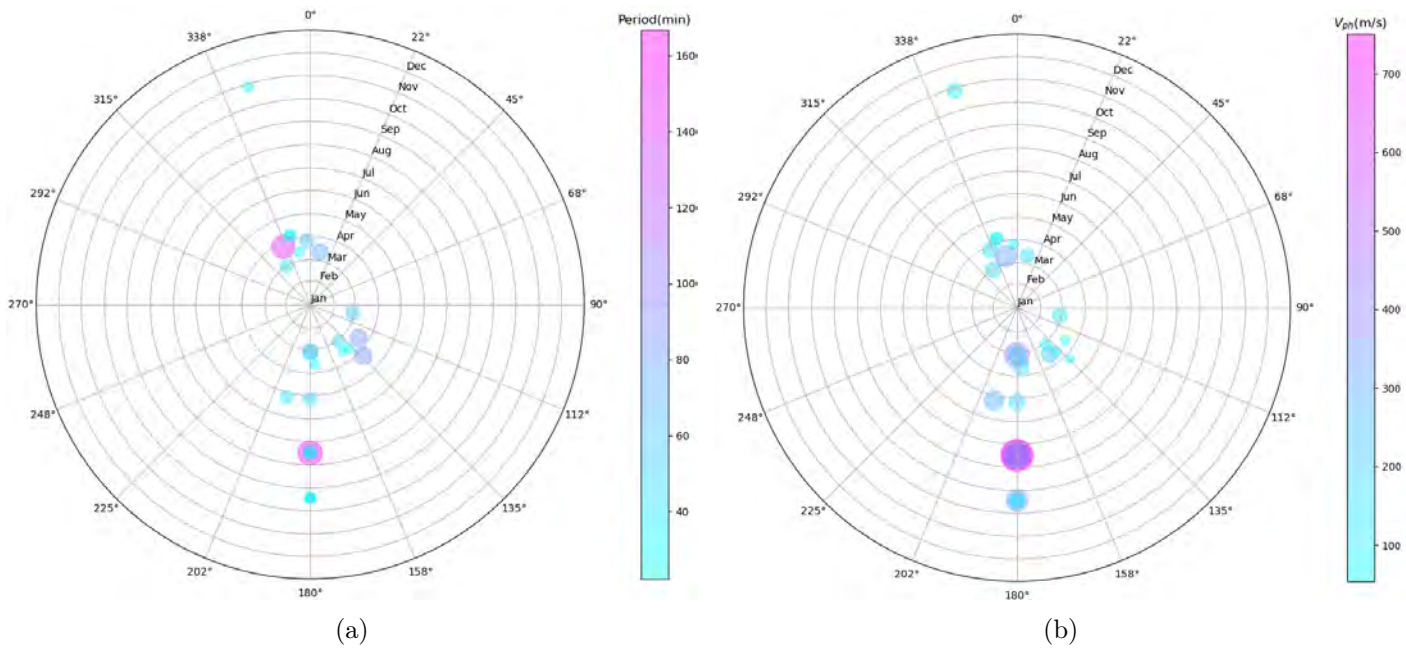


Figure 7.4: Polar plot showing the variation of (a) period and azimuth and (b) phase velocity and azimuth with day of the year (seasonal variation). Note that in this case the radii represent months and the colour bars indicate period and phase velocity of TIDs in (a) and (b) respectively. The size of the circles represent the period in (a) and phase velocity in (b).

It is not possible to statistically determine the solar cycle variation of TID characteristics due to the small number of observed TIDs. However, in general, most of the events (43.7%) reported here occurred during 2012 and 2013, close to the maximum of the moderate solar cycle 24. The other year when TIDs frequently occurred was 2005, which was during the declining phase of the 23rd cycle. In 2005 alone 5 events were identified, and counts for 31% of the total number of events observed by the SANA E radar. From the TIDs detected in this study, the majority were observed during the declining phase (2005) and maximum phase (2012–2013) of the solar cycle.

7.2.3 Source Mechanisms

Based on the geomagnetic condition during and prior to the commencement of the TID event; the events reported here are classified into events observed geomagnetically disturbed periods and events observed during geomagnetically quiet periods. During geomagnetically disturbed periods, possible sources of the TID events were associated with geomagnetic storms or substorms by means of Joule heating and the Lorentz force. For the events occurred during geomagnetically quiet times (see Figures 5.11 and 7.5) source mechanisms such as Joule heating and Lorentz force associated with geomagnetic storm and substorms are excluded from being possible sources of the TID

events. However, these TID events occurred during local nighttime, and some studies found that nighttime MSTIDs are generated by F-region electrodynamics and/or E-F coupled dynamics, in particular Es and polarised electric fields (Perkins, 1973; Kelley and Miller, 1997; Tsunoda and Cosgrove, 2001; Ogawa *et al.*, 2009; Otsuka *et al.*, 2009; Suzuki *et al.*, 2009).

Sporadic E and polarisation electric field

There are several studies which relate nighttime MSTIDs observed during geomagnetically quiet period with Es and polarised electric field (Otsuka *et al.*, 2007; Suzuki *et al.*, 2009; Ogawa *et al.*, 2009). Ionospheric instabilities such as Es instability that acts through electrodynamic processes involving polarised electric fields could develop the MSTIDs. Polarised electric fields are generated perpendicular to the wavefronts of MSTIDs to maintain the electric current continuity that was disrupted by MSTIDs. The polarised electric field maps this perturbation to the F region along magnetic field lines through $\mathbf{E} \times \mathbf{B}$ drifts, which is the reason for the observation of similar waves in the E and F regions.

Some of the events identified from the SANAE radar in this study show similar characteristics to TIDs that are generated by polarised electric fields. One of these events were observed on the 17 March 2013. The MSTID event on 17 March 2013 occurred during a geomagnetically quiet period, with the wavefront aligned in southwest-northeast. In Chapter 5, it was shown that for this event the E-region backscatter power data had frequencies similar to this MSTID (refer to Figures 5.4(d) and 5.14). The other event with similar source mechanism was observed on 19 March 2007. The event occurred just after midnight until 05:00 UT during geomagnetic quiet conditions (see Figure 7.5(d)), which is the time when Es are reported to occur frequently at the latitudes of the SANAE and Halley radars (Rodger *et al.*, 1983). Scatters from Es layer were observed from the radar data and the spectral analysis of the data depicts a similar frequency of an MSTID in F region and Es layer data (see Figure 7.6). As in the case of the 17 March 2013 event, the MSTIDs on 19 March 2007 has a wavefront aligned southwest-northeast with southeast propagation (see Table 7.1). The southeast propagation of the MSTIDs reported here are different from the northwest propagation of MSTIDs in the southern hemisphere mid-latitudes that are due to polarised electric field (e.g., Otsuka *et al.*, 2004; Shiokawa *et al.*, 2005). Figure 7.7 shows a sketch of the MSTID wavefronts together with the direction of the polarised electric fields and neutral wind for the 17 March 2013 event. The direction of the neutral wind was derived from the horizontal wind model (HWM14), which was used in Section 5.2.2. The southeast propagation of the MSTIDs could be due to directional filtering by the neutral wind, which was directed northwest for the case of the 17 March event, as estimated by the HWM14 (illustrated in Figure 7.7). Antiwindward propagation of MSTIDs were observed by Crowley *et al.* (1987) over the Antarctic Peninsula, during magnetically quiet periods.

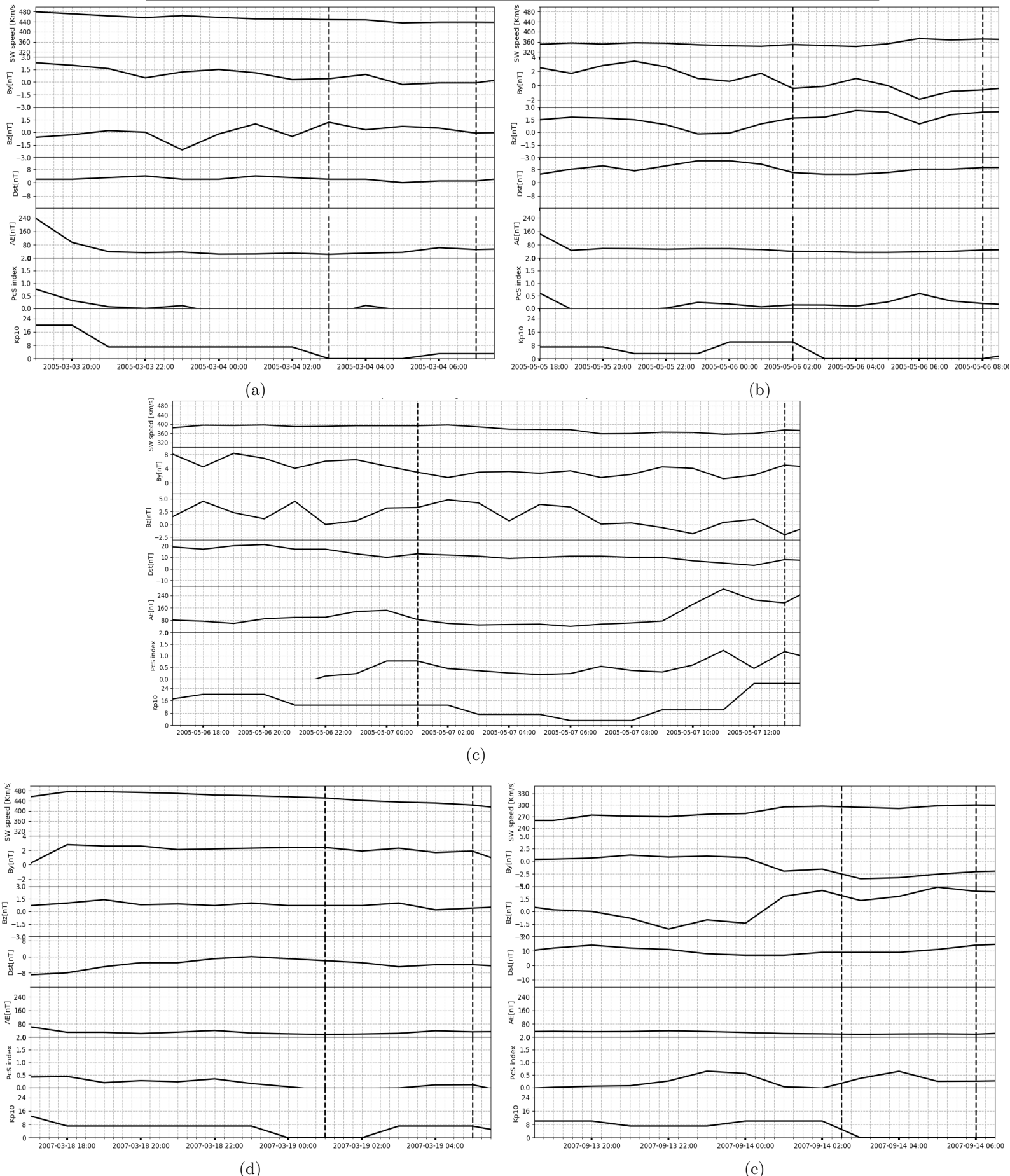


Figure 7.5: Hourly data of solar wind (1st panel), IMF By (2nd panel), IMF Bz (3rd), Dst (4th panel), AE index (5th panel), PC South index (6th panel) and Kp10 index (last panel) for the events on (a) 4 March 2005, (b) 6 May 2005, (c) 7 May 2005, (d) 19 March 2007 and (e) 14 September 2007. The vertical dash lines indicate the starting and ending time of the TID events from the SANA E radar.

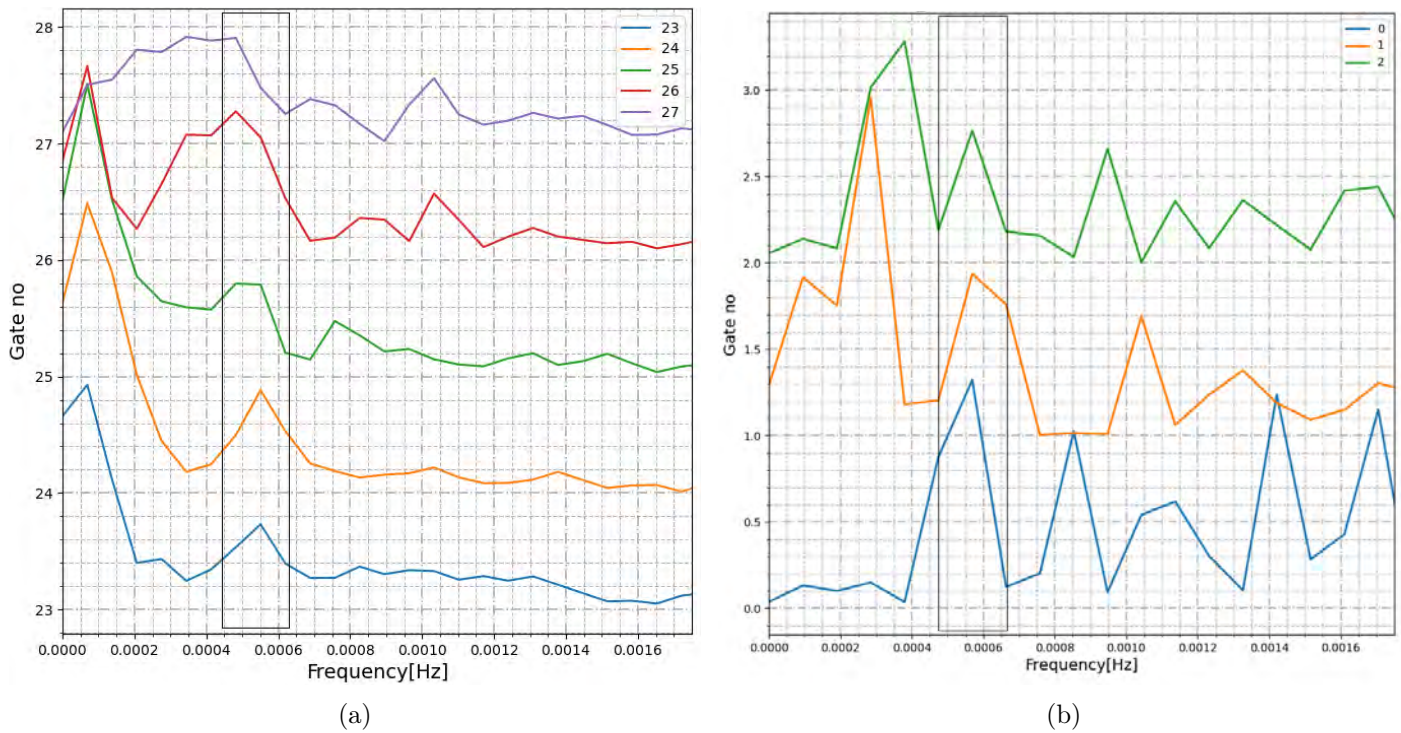


Figure 7.6: Frequency spectrum plots of the 19 March 2007 event (a) using FFT for gate numbers between 23 and 27 and (b) using Lomb-Scargle for gate numbers between 0 and 2.

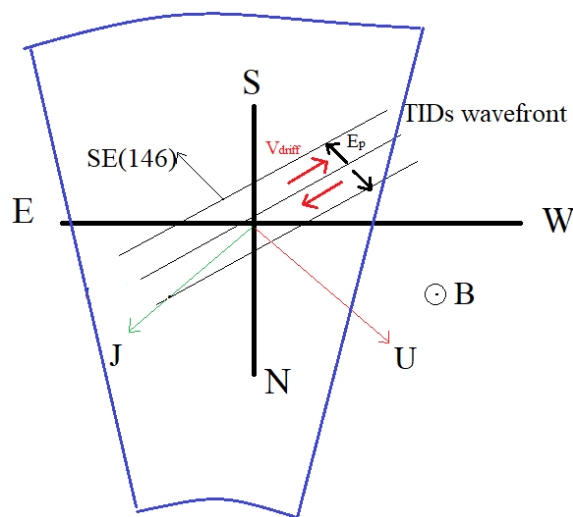


Figure 7.7: Sketch of the propagation direction of the MSTIDs together with the neutral wind (U) and field line-integrated current (J) for the 17 Mar 2013 event. Sketch adapted from Otsuka *et al.* (2009).

Geomagnetic storms and substorms as TIDs generation mechanism

At high latitudes TIDs are thought to be mainly generated through Joule heating and the Lorentz force associated with enhanced auroral electrojets (Chimonas and Hines, 1970; Francis, 1975). Precipitation of energetic particles, which is common at high latitudes, contributes to high-latitude instabilities by depositing heat (Hunsucker, 1982). Both Joule heating and the Lorentz force (force transfer to neutrals through collision) introduce a local time-dependent disturbance into the neutral atmosphere that triggers TIDs at high latitudes (Chimonas and Hines, 1970).

The TID event on 26 March 2010 between 01:00 and 06:00 UT was identified in the SANA E radar data. Figure 7.8 indicates that the TID signatures (strong backscatter power) moved from higher range gate numbers to lower range gate numbers with time, which means that the TID was propagating towards the radar (from higher to lower latitudes or equatorward based on the location of the radar). Two TIDs were identified by means of the spectral analysis of backscatter power data for the 26 March 2010 event (see Table 7.1). An LSTID with a frequency of 0.11 MHz or a period of 151.5 minutes and wavelength of 1414 km propagated northwest with a phase velocity 156 ms^{-1} . The other TID had a frequency of 0.27 MHz (corresponding to a period of 60 minutes), wavelength of 243 km and phase velocity of 67 ms^{-1} . Based on these characteristics, the TID can be classified as an MSTID.

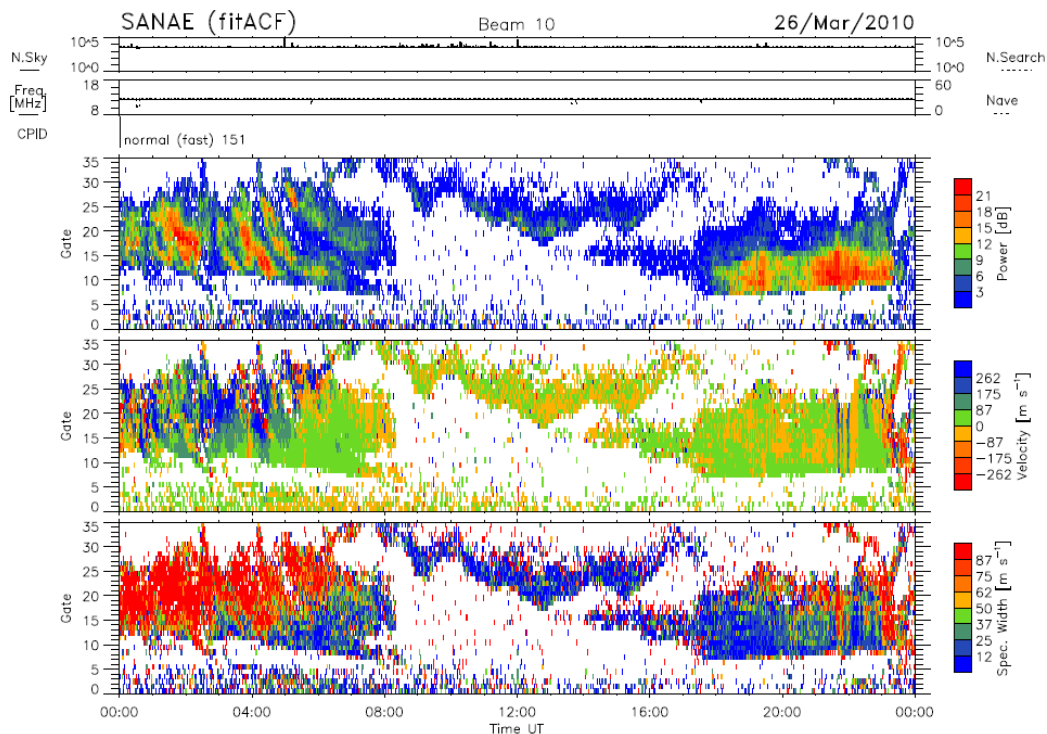


Figure 7.8: RTI plots of backscatter power (top panel), Doppler velocity (middle panel) and spectral width (bottom panel) based on the SANA E radar data of 26 March 2010.

Figure 7.9 shows the geomagnetic conditions prior to the event were quiet, except at 18:00 UT on 25 March (6 hours before the event commenced) when the AE index increased to 300 nT, which could indicate a substorm. The auroral images produced by the Syowa station in the southern hemisphere (69° S, 39.6° E) show high auroral activity before the event (see Figure 7.10). Precipitation activity, as recorded by DMSP satellites as it pass by southern high latitudes, for the time period of the auroral images, are shown in Figure 7.11. DMSP satellites are used to study electron and ion energy flux at mid- and high-latitudes (see Section 3.4 for more information). Satellite data indicates high energy fluxes in the area of the magnetic latitudes and at that time (see Figure 7.11). This suggests that the observed TID event could have been caused by energy deposition into the ionosphere by energetic particle precipitation.

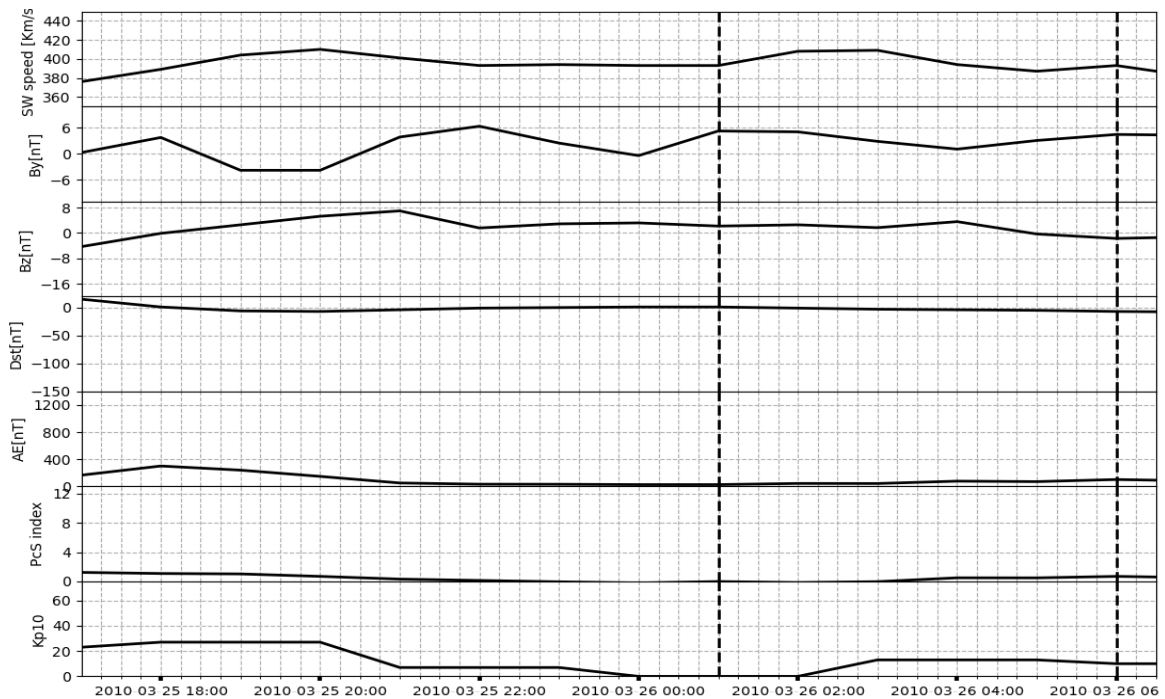


Figure 7.9: Hourly data of solar wind (1st panel), IMF By (2nd panel), IMF Bz (3rd), Dst (4th panel), AE index (5th panel), PC South index (6th panel) and Kp10 index (last panel) for 25 to 26 March 2010. The vertical dash lines indicate the time interval when the TIDs occurred as identified in the SANA E radar.

In the SANA E radar data for 11 March 2012 between midnight and 05:00 UT TID signatures were identified (see Figure 7.12) during the recovery phase of the storm on 9 March 2012. Figure 7.13 shows the geomagnetic conditions between 8 and 13 March 2012. The figure shows that on 8 March 2012 around 10:00 UT there was a sudden impulse, which indicates the arrival of the shock wave on the Earth’s magnetosphere. The storm commenced on 9 March 2012, with the Dst reaching a minimum value of -150 nT around 08:00 UT on 9 March 2013. The maximum AE index recorded for this day was 1785 nT at around 09:00 UT (see Figure 7.13 5th panel). The recovery phase of this storm lasted for almost 2 days (from \sim 16:00 UT

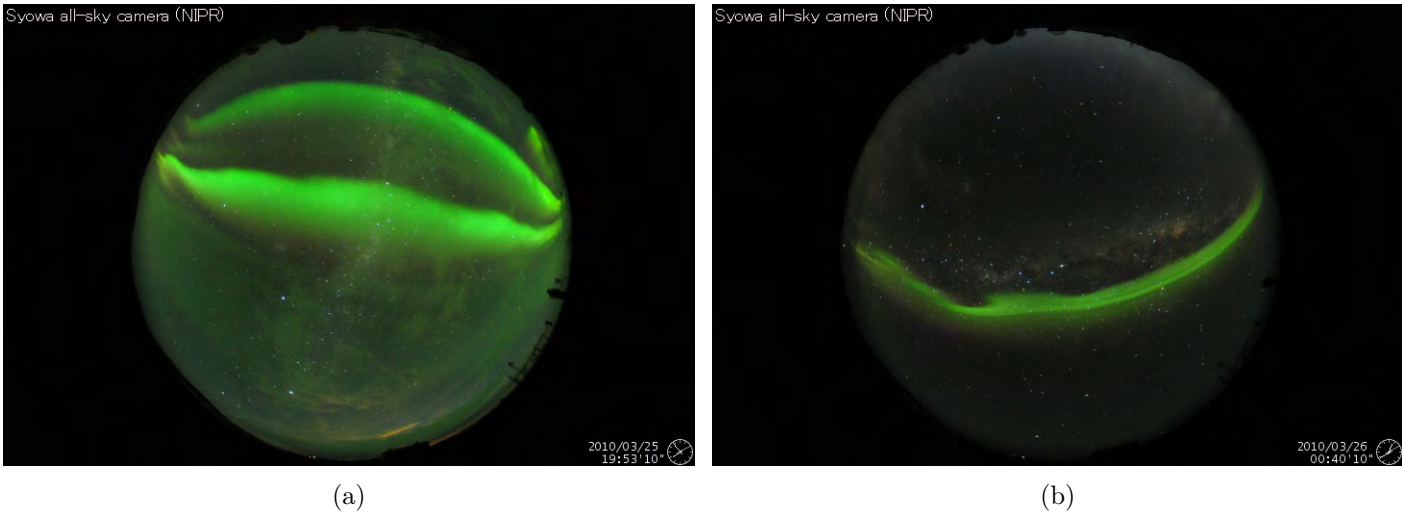


Figure 7.10: Auroral images produced by Syowa station in the southern hemisphere (a) at 19:53 on 25 March 2010 and (b) at 00:40 on 26 March 2010 (http://polaris.nipr.ac.jp/~acaurora/syowa_CDC_QL/).

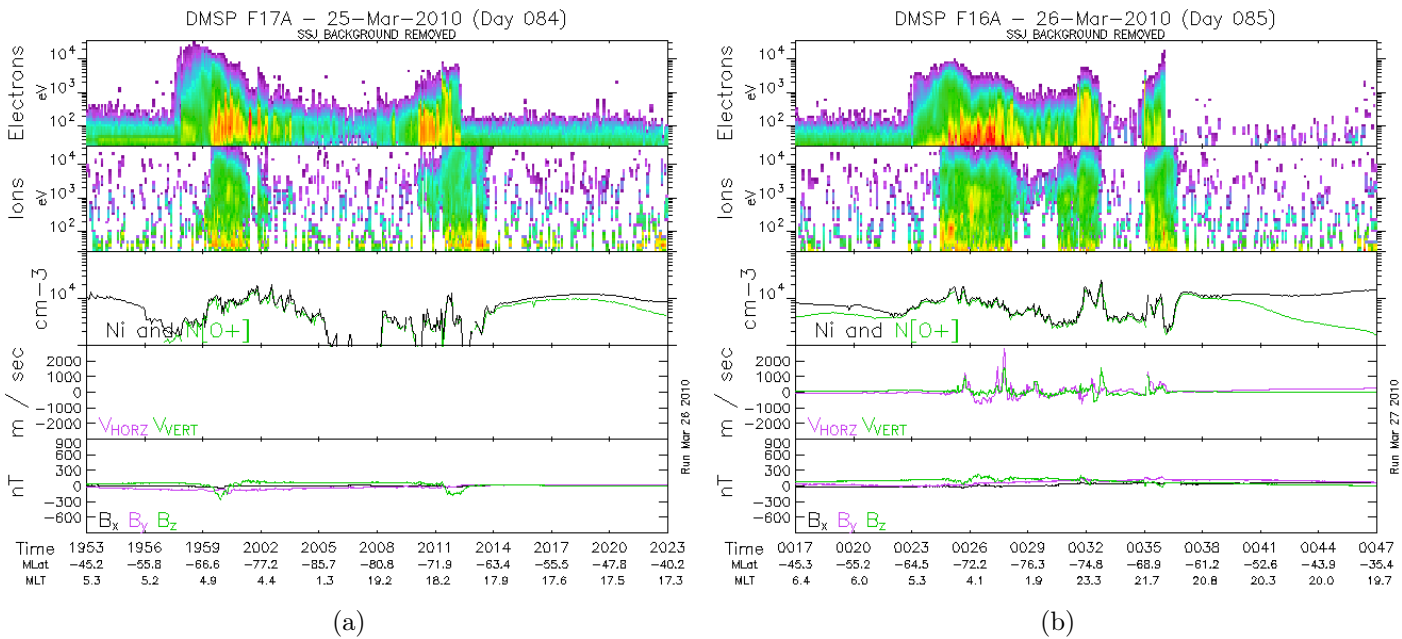


Figure 7.11: Precipitating particle flux data from DMSP satellites (a) F17 for 25 March 2010 and (b) F16 for 26 March 2010. 1st panel Electron flux, 2nd panel Ion flux, 3rd panel Ni and N[O⁺] density, 4th panel vertical and horizontal ion drift velocity and 5th panel magnetic field components (image taken from Boston college space weather data survey site <https://dmsp.bc.edu/html2/index.html>).

on 9 March to ~13:00 UT on 11 March). As listed on Table 7.1, the frequency analysis of this event depicts the existence of two waves with frequencies of 0.22 mHz and 0.6

mHz (corresponding to periods of 75.8 minutes and 27.8 minutes, respectively). The phase velocities and wavelengths of these waves are in the range of MSTIDs, i.e. phase velocities of 137 ms^{-1} and 327 ms^{-1} , and wavelengths of 623 km and 546 km for the TIDs with periods of 75.8 min and 27.8 min, respectively. The propagation directions of the TIDs were northward (equatorward), which is the most common propagation direction for TIDs triggered by geomagnetic storms (e.g. [Bruinsma and Forbes, 2007](#); [Borries *et al.*, 2009](#); [Katamzi and Habarulema, 2014](#)).

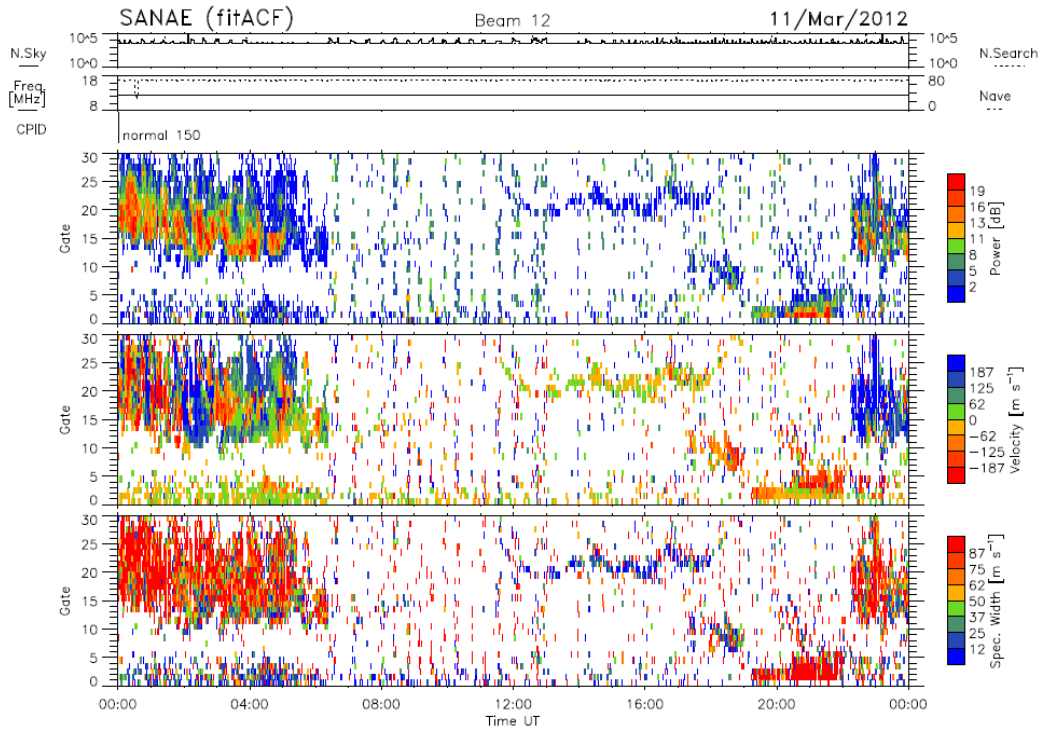


Figure 7.12: RTI plots of backscatter power (top panel), Doppler velocity (middle panel) and spectral width (bottom panel) from SANA E radar from 11 March 2012.

Another event during a geomagnetic storm occurred on 15 July 2012. The spectral analysis of SuperDARN and GPS data for this event, including the geomagnetic conditions, was discussed in Chapter 6. This event occurred during the main phase of an intense geomagnetic storm, with minimum Dst value of -139 nT . Figure 7.14 shows the map potential plot of the southern hemisphere during the time that the TID was observed, which was also during the main phase of the geomagnetic storm. The figure shows a strong convection where the Heppner Maynard boundary (cyan and black line) expanded up to 50° in latitude. Strong flow velocities can be seen in the cusp region within the FOV of the SANA E and Halley radars (indicated using the black circle in Figure 7.14) generated by dayside reconnection, which presumably caused by intense precipitation from the magnetosheath. Multiple waves in the frequency range from 0.1 to 0.75 mHz or in periods from 166.7 to 22.2 minutes were observed during this event. In contrast to the previous storm time TID event (i.e. 11 March 2012 event), this event shows TIDs that propagate southward (poleward).

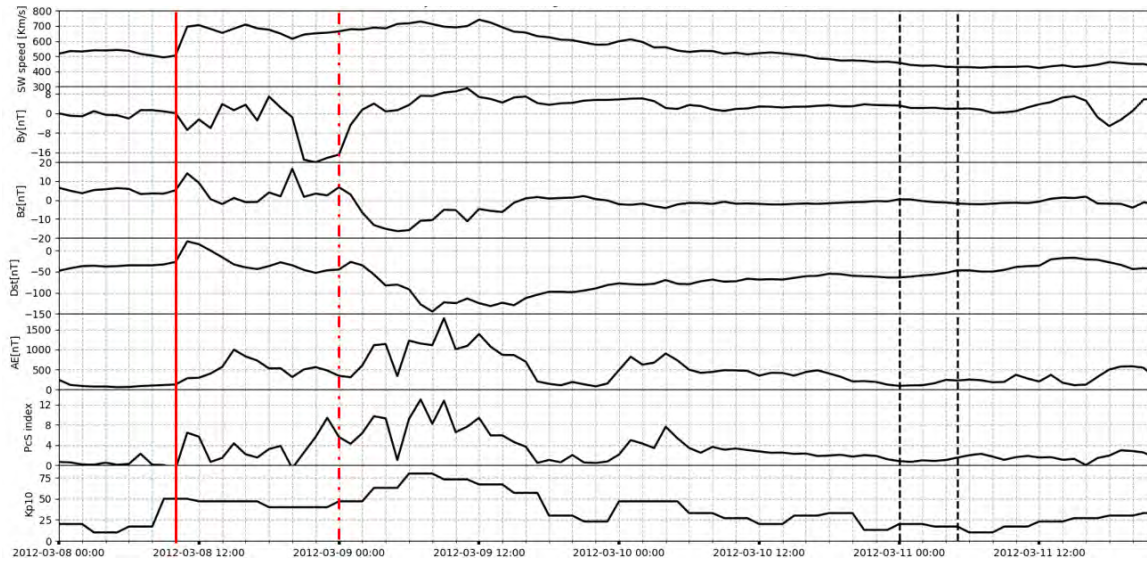


Figure 7.13: Hourly data of solar wind (1st panel), IMF By (2nd panel), IMF Bz (3rd), Dst (4th panel), AE index (5th panel), PC South index (6th panel) and Kp10 index (last panel) for 10 to 11 March 2012. The black dash lines indicate the time interval during which the TIDs observed in the SANA E radar data. The red line indicates the sudden impulse (or arrival of the shock wave) on 8 March 2012 and the red dash line indicates the commencement of the storm on 9 March 2012.

Even if poleward propagating TIDs associated with disturbed auroral/geomagnetic conditions are rare, a number of studies have reported on such TIDs (e.g. [Momani et al., 2010](#); [Katamzi-Joseph et al., 2019](#))

The TID event of 6 April 2015 was associated with HSS and/or CIR events which led to a deposition of high-energy particles, as illustrated by the high plasma flow on the map potential plot in [Figure 7.15\(a\)](#), which coincides with the high energy flux at around 23:00 UT on 5 April 2015 from the DMSP data ([Figure 7.15\(b\)](#)). In addition to increases in the AE index before and during the TID event (see [Figure 6.11](#)), a decrease in the H component magnetic field was observed in the SANA E magnetometer data of 5 April 2015 at around 23:00 UT, as shown in [Figure 7.16](#).

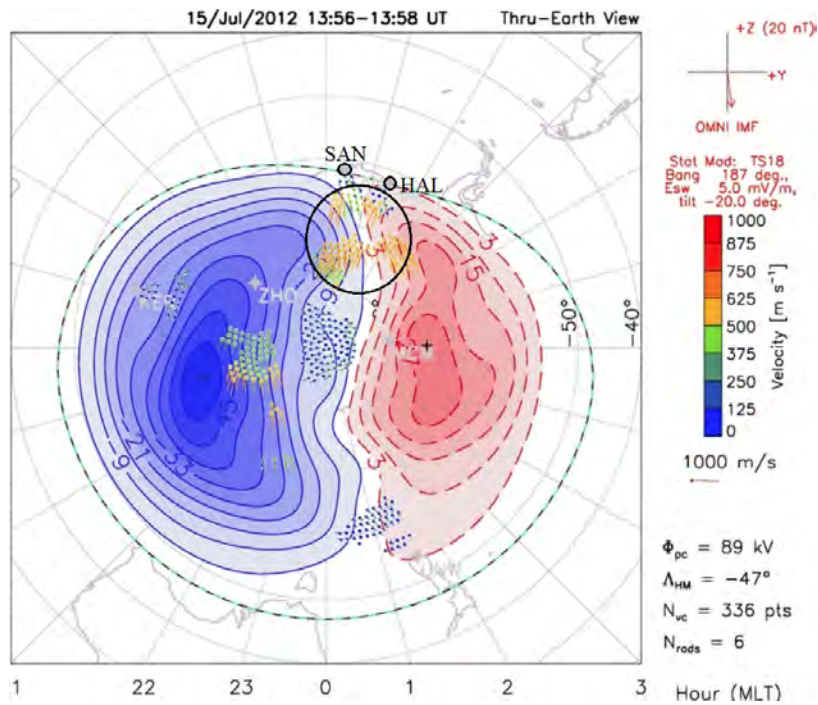


Figure 7.14: Map potential plot for the southern hemisphere between 13:58 and 14:00 UT on 15 July 2012 (image taken from VT SuperDARN website <http://vt.superdarn.org/tiki-index.php?page=DaViT+Map+Potential+Plot>).

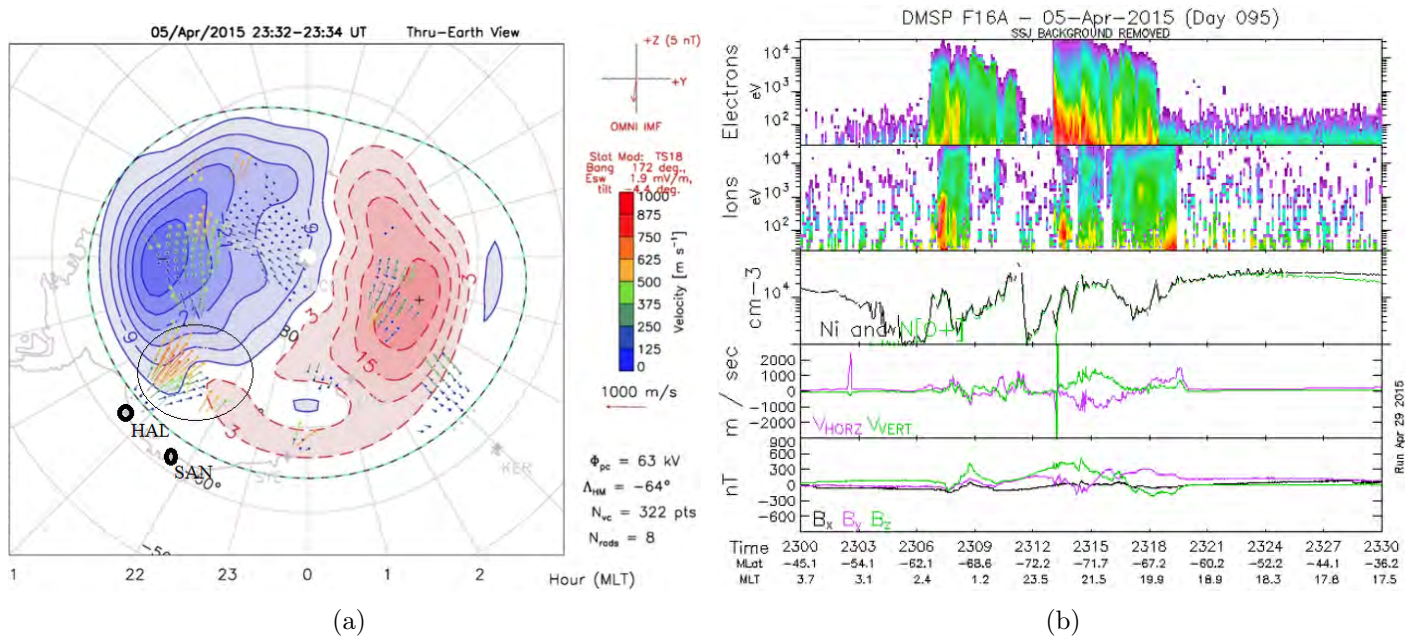


Figure 7.15: Map potential plot for the Southern hemisphere (a) and DMSF data from satellite F16 (b) for 5 April 2015.

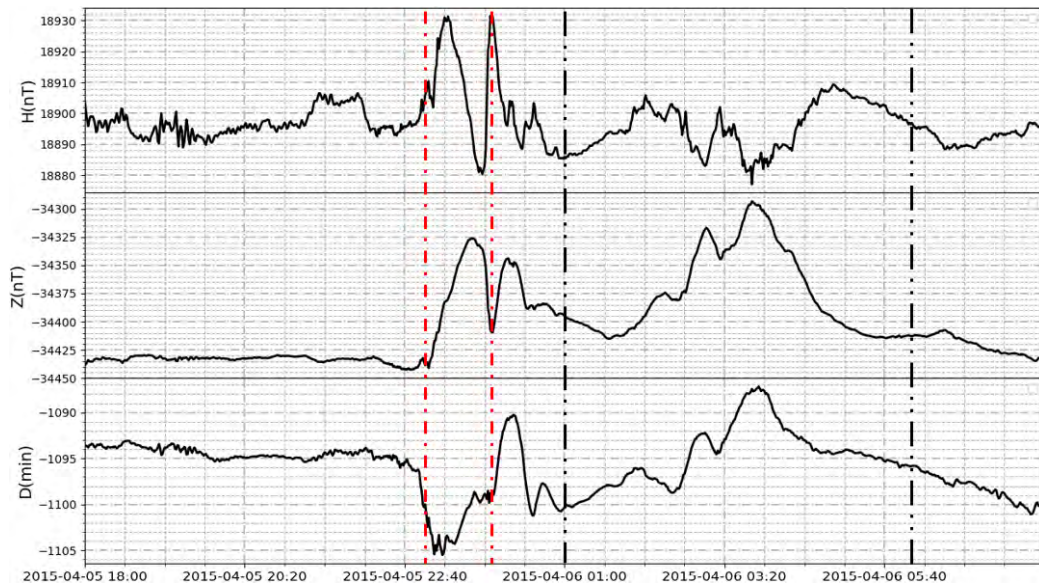


Figure 7.16: Magnetometer data from the SANAE station, showing the H (top panel), Z (middle panel) and D (bottom panel) components of the magnetic field. The red dashed lines indicate the time interval during which the substorm occurred. The black dashed lines indicate the time interval of the TID event as identified in the SANAE radar data.

7.3 Summary

This chapter discussed the characteristics of TIDs identified in the SANAE HF radar data and their possible source mechanisms. A total of 22 events were identified for the period 2005–2015 by means of visual inspection of the RTI plot. Nine of these TID events were also observed in the Halley HF radar data, which were inspected in similar fashion. Of the 22 event days identified, only 16 event days were analysed, since data analysis was done only for those event days for which sufficient data (at least 50%) were available within the time interval of interest. The majority of the TIDs (65.4%) identified in the SANAE radar data were MSTIDs, with periods between 20 and 60 minutes, phase velocities between 50 and 333 ms^{-1} , and wavelengths between 129 and 833 km. The seasonal characteristics of the TIDs shows that 46% of the TID events occurred during the month of March and they propagated in north and southeast direction. Geomagnetic indices data and precipitation data were used to find the possible source mechanisms of the TIDs. The result showed that two of the events may be linked to Es and polarised electric fields since the events were observed during quiet time post midnight and similar frequencies were observed from scatters from F layer and Es layer. For ten events the possible sources of TIDs were observed during geomagnetic storm and substorms, and therefore could have been generated via mechanisms such as Joule heating, the Lorentz force and energetic particle precipitation.

Chapter 8

Conclusion and future work

8.1 Summary and conclusion

Understanding the sources and scale of energy coupling due to TIDs is vital for estimating the upper atmospheric energy balance and for improving atmospheric and/or ionospheric models, because of their important role in energy/momentum distribution. Navigation and communication satellites, as well as radio astronomy instruments, are sensitive to ionospheric irregularities such as TIDs, which can reflect and scatter their signal and introduce error in the measurements. Since at least 1960 TIDs have been studied theoretically and empirically using different ground- and space-based instruments and models. Most of these studies were done at the high and mid-latitudes of the northern hemisphere. Therefore, a climatological study of TIDs in the southern polar region, mainly over SANAE, would narrow the knowledge gap relating to these structures, especially since studies of TIDs above Antarctica are particularly sparse in the literature.

In this project the climatology of the characteristics of TIDs over Antarctica was studied by means of long-term data, covering the period 2005–2015 obtained from the SANAE SuperDARN radar. These were supplemented by the data from the Halley radar, which has a large overlapping FOV with SANAE, and also with GPS TEC data from PRNs close to the FOV over which the TID was detected. Measurement of a common area using two radars as presented in this project are rare in the literature, and the use of multi-instruments provided a unique opportunity for optimal detection and characterisation of TIDs over this region. The use of different signal processing methods, such as MTM, FFT and Lomb-Scargle, for determining the frequency (period) of the waves from radar and GPS TEC data, was demonstrated. The advantage of using multiple windowing spectral analysis with the MTM method over the traditional windowing method in determining TID characteristics, was illustrated using one of the TID events. In particular the analytic signal of the wave from the

MTM method was used to estimate the instantaneous phase velocity and propagation azimuth of the wave, which accurately tracked the change in the characteristics of the MSTID throughout the duration of the event.

The first results chapter, Chapter 5, describes the results of a case study of an MSTID event on 17 March 2013 as identified in the radar data of the SANAE and Halley radars. This has been published (Atilaw *et al.*, 2021). The MTM frequency spectrum of the backscatter power data from the SANAE radar showed a dominant wave at a central frequency of 0.78 mHz of > 95% significance. Complex demodulation of the reconstructed signal of this central frequency allowed for the estimation of the instantaneous amplitude, frequency and phase of the MSTID throughout the duration of the event. A cross-spectral analysis of three cells of the SANAE backscattered power data was used to calculate the MSTID's propagation speed, direction and wavelength by a method incorporating elements from He *et al.* (2004), Ishida *et al.* (2008) and Grocott *et al.* (2013). It was estimated that the MSTID, with a period of approximately 23 minutes, travelled at a phase velocity of 170–280 ms⁻¹ with the maximum phase velocity occurring around 04:04 UT. The change in the speed of the wave was also observed in the change in the slope of the power backscatter and/or Doppler velocity enhancements on the RTI plot (top panel of Figure 5.7). The wavelength and propagation azimuth of the MSTID varied between 240 and 380 km, and 140° and 154° (i.e southeast), respectively, in a similar manner as the phase velocity. The analysis of Halley radar data supports these results, since the data also identifies a MSTID structure with wavelength, velocity and azimuth of 248 km, 178 ms⁻¹, and 130° (southeast), respectively.

Frequency analysis of the SANAE velocity data, together with knowledge of the local magnetic field magnitude allowed for an estimation of the convection polarisation electric field during the period that the MSTID was active. The convection Joule heating was determined from this estimated polarisation electric field, together with an assumed Pedersen conductance. The interaction of the convection with the neutral wind, due to the MSTID, was also calculated. These two contributions were summed over an estimation of the geographic area over which the MSTID had been identified, to provide an estimate of the Joule heating by the MSTID. A maximum of 78 kW was estimated. The Joule heating by the MSTID was compared to the background Joule heating, which was estimated by using the average background convection velocity from the SANAE radar, and the conclusion was that the Joule heating due to the MSTID was almost as important as the background heating during this event. This is an important finding in terms of getting a handle on the importance of TIDs in the energy budget in this climatically sensitive region.

To support and complement TID observations from HF radar, TID event analysis of GPS TEC measurements are offered in Chapter 6. Three events were selected as examples of TIDs under different geomagnetic conditions. The first selected was on 15 July 2012. Both the SANAE and Halley radar data for that date, identifies the TID during the main phase of an intense geomagnetic storm. Spectral analysis of the

radar data from both the SANAE and Halley radar shows the existence of poleward propagating MSTIDs and LSTIDs. The area in which the TIDs were observed by the radars, and the IPPs of the PRNs coincide, since the backscatter of the radars was from higher range gate numbers. MSTIDs with similar periods were observed in the radar data and simultaneously by PRNs that were visible from two GPS receiver stations, namely AMU2 and HOWE. Both the radar and GPS data showed a frequency of 0.6 mHz (corresponding to a period of 27 minutes). For the GPS TEC data only the frequency analysis is done, as it was not possible to determine the velocity and wavelength of the wave, because of the scarcity of GPS data over the FOV of the radars.

The second event that was analysed with radar and GPS measurements, was the TID event of 17 March 2013, which was analysed earlier using the MTM method. As the earlier analysis revealed, this event occurred during quiet geomagnetic conditions and was observed by both SANAE and Halley radars. It had a central frequency of 0.72 mHz (period of ~ 23 minutes). A frequency of 0.7 mHz, which corresponded to a period of 23.8 minutes, was observed in the GPS TEC data of 4 PRNs that were visible near the FOV of the radars during a similar time interval that the MSTID was observed by the radars. The last event, described in this chapter, occurred during a substorm on 6 April 2015. There were no simultaneous observations from the SANAE and Halley radar for this event as the backscatter data from each receiver did not cover the same geographic location. Therefore, only results from SANAE and GPS TEC were discussed for this event. An MSTID with a frequency of 0.55 mHz (period of 30 minutes) was observed in both the radar and GPS TEC data. Further analysis of the SANAE radar data showed that this MSTID was propagating northward (equatorward) with a speed of 109 ms^{-1} .

Chapter 7 presented the characteristics of all TIDs identified visually in the RTI plots of the SANAE HF radar data and their possible source mechanisms over a 10 year period (2005–2015). However, even though 22 TID event days were identified in the 10-year period of the study, the results of only 16 were discussed, due to limited data for the other events. Four of these 16 were also observed in Halley radar data, and therefore their TID parameters were also included. All events reported in this study were identified in ionospheric scatter data, possibly because the SANAE radar has a higher ratio of ionospheric to groundscatter returns (Mravlag, 2007). Another reason could be that it is easier to identify the power and velocity fluctuations from ionospheric scatter data than groundscatter data, since the variations in the former are larger than in the latter. The majority of the TIDs (65.4%) identified were MSTIDs with periods between 20 and 60 minutes, phase velocities between 50 and 333 ms^{-1} , and wavelengths between 129 and 833 km. The characteristics of the MSTIDs are similar to those reported by Crowley *et al.* (1987) and Grocott *et al.* (2013) for TID events observed around the Antarctic Peninsula.

All events reported here were occurred between midnight and 06:00 UT, except for one event, which occurred in the late afternoon during a geomagnetic storm. The

TID occurrence rate was high during equinox with 75% of the event days during March–May, in fact 46% occurred in March and tended to propagate northward and southeastward. Local winter had the least TID activity, with only 1 TID event day identified. Similar observations, by means of the Frank Island HF radar, were reported by [Grocott *et al.* \(2013\)](#) for the region near the Antarctic Peninsula. They reported more frequent occurrences of MSTIDs during the equinoxes. However, the studies by [Ogawa *et al.* \(1987\)](#) and [Bristow *et al.* \(1996\)](#) for the southern and northern high latitudes, respectively, showed that the majority of the MSTIDs occur during winter. This discrepancy in the findings of different studies may be explained as probably being due to the different data types used, as the results presented by [Bristow *et al.* \(1996\)](#) were based on groundscatter data. Only $\sim 38\%$ of the TID event days occurred during geomagnetically quiet periods. Two of these events (19 March 2007 and 17 March 2013) had characteristics similar to those caused by instabilities in the Es layer and polarised electric field ([Ogawa *et al.*, 2009](#); [Suzuki *et al.*, 2009](#); [Otsuka *et al.*, 2009](#)). The other quiet time TID events couldn't be linked to this mechanism, since it was not possible to determine their propagation azimuth or apply spectral analysis to the backscatter data from the Es region due to data gaps, and therefore these events require further investigation. The events during geomagnetic storms indicated the presence of TIDs with multiple frequencies/periods, possibly indicating the existence of more than one source of TIDs during disturbed periods. The preferred propagation direction of the TIDs during disturbed geomagnetic conditions is not clear, this would require further investigation. Both equatorward and poleward propagation of TIDs were observed for the events caused by geomagnetic storms and substorms. On the other hand, all TIDs occurring observed during quiet geomagnetic conditions propagated poleward.

8.2 Future work

This investigation could be improved and complemented by including analysis by other instruments and models. Optical instruments, such as the all-sky imager, can be used to study AGWs in the neutral atmosphere which subsequently propagate to higher altitudes and trigger TIDs. This is important in order to identify the excitation altitudes of TIDs/AGWs and relate them to the source. A reverse ray trace model, such as HINDGRATS (hindcast gravity wave ray tracer) can be used to identify the source of the TIDs. Analyses of data of other SuperDARN radars in the southern hemisphere may provide a better picture of TID characteristics over Antarctica, since there are 14 SuperDARN radars in this region, covering both mid- and high latitudes. Other radars could also have elevation data, which would help in pinpointing sources and providing an even more accurate handle on the TIDs characteristics. The TID events for the 10-year period covered by this project, are very few, since the events were identified by visual inspection of RTI plots. Automatic identification of TIDs using algorithms that detect TIDs in the radar data could improve the statistical

study. It would also be important to know when most of the scatters, both ionospheric and ground scatter, occur from the radar to determine why TIDs occur post-midnight. The majority of TIDs reported in this study occurred between midnight and 06:00 UT. However it is not clear whether it is because there was no scatter from the SANAE radar during other times of the day or because of a genuine characteristic of TIDs over this region. This needs to be explored in more detail and would provide a better understanding of the seasonal and diurnal variation of TIDs over this region. These kind of statistics could also be added to ionospheric models such as NeQuick to help with communication errors and inaccuracies and could also be valuable additional data in empirical climate models.

References

- Abdu, M., Batista, I., Muralikrishna, P., and Sobral, J. A.: Long term trends in sporadic E layers and electric fields over Fortaleza, Brazil, *Geophysical research letters*, 23, 757–760, doi:<https://doi.org/10.1029/96GL00589>, 1996.
- Afraimovich, E., Terekhov, A., Udodov, M. Y., and Fridman, S.: Refraction distortions of transionospheric radio signals caused by changes in a regular ionosphere and by travelling ionospheric disturbances, *Journal of atmospheric and terrestrial physics*, 54, 1013–1020, doi:[https://doi.org/10.1016/0021-9169\(92\)90068-V](https://doi.org/10.1016/0021-9169(92)90068-V), 1992.
- Akasofu, S.-I.: Polar and magnetospheric substorms, Dordrecht, Netherlands, D. Reidel, 1968.
- Alken, P., Thebault, E., Beggan, C., Aubert, J., Baerenzung, J., Brown, W. J., Califf, S., Chulliat, A., Cox, G., Finlay, C. C., *et al.*: Evaluation of candidate models for the 13th generation International Geomagnetic Reference Field, *Earth, Planets and Space*, 73, 1–21, doi:<https://doi.org/10.1186/s40623-020-01281-4>, 2021.
- Arnold, N. F., Jones, T. B., Robinson, T. R., Stocker, A. J., and Davies, J. A.: Validation of the CUTLASS HF radar gravity wave observing capability using EISCAT CP-1 data, *Annales Geophysicae*, 16, 1392–1399, doi:<https://doi.org/10.1007/s00585-998-1392-z>, 1998.
- Aruliah, A., Griffin, E., McWhirter, I., Aylward, A., Ford, E., Charalambous, A., Kosch, M., Davis, C., and Howells, V.: First tristatic studies of meso-scale ion-neutral dynamics and energetics in the high-latitude upper atmosphere using collocated FPIs and EISCAT radar, *Geophysical Research Letters*, 31, 1–4, doi:<https://doi.org/10.1029/2003GL018469>, 2004.
- Atilaw, T. Y., Stephenson, J. A., and Katamzi-Joseph, Z. T.: Multitaper analysis of an MSTID event above Antarctica on 17 March 2013, *Polar Science*, 28, 100643, doi:<https://doi.org/10.1016/j.polar.2021.100643>, 2021.
- Baker, J., Zhang, Y., Greenwald, R., Paxton, L., and Morrison, D.: Height-integrated Joule and auroral particle heating in the night side high latitude thermosphere, *Geophysical Research Letters*, 31, 1–4, doi:<https://doi.org/10.1029/2004GL019535>, 2004.

- Baker, J. B., Ruohoniemi, J., Shepherd, S., McWilliams, K., Greenwald, R., and Bristow, W.: Those DARN Radars: New Directions for the Super Dual Auroral Radar Network, Proceedings of Union Radio-Scientifique Internationale, 2008.
- Baker, K., Greenwald, R., Ruohoniemi, J., Dudeney, J., Pinnock, M., Mattin, N., and Leonard, J.: Polar Anglo-American Conjugate Experiment, Eos, Transactions American Geophysical Union, 70, 785–799, 1989.
- Baker, K., Dudeney, J., Greenwald, R., Pinnock, M., Newell, P., Rodger, A., Mattin, N., and Meng, C.-I.: HF radar signatures of the cusp and low-latitude boundary layer, Journal of Geophysical Research: Space Physics, 100, 7671–7695, doi:<https://doi.org/10.1029/94JA01481>, 1995.
- Balan, N., Skoug, R., Tulasi Ram, S., Rajesh, P., Shiokawa, K., Otsuka, Y., Batista, I., Ebihara, Y., and Nakamura, T.: CME front and severe space weather, Journal of Geophysical Research: Space Physics, 119, 10,041–10,058, doi:<https://doi.org/10.1002/2014JA020151>, 2014.
- Ballatore, P. and MacLennan, C. G.: Significance of the high-latitude geomagnetic index AES-80: comparison with the PC index, Earth, planets and space, 51, 425–430, doi:<https://doi.org/10.1186/BF03352246>, 1999.
- Beach, T. L. and Kintner, P. M.: Simultaneous Global Positioning System observations of equatorial scintillations and total electron content fluctuations, Journal of Geophysical Research: Space Physics, 104, 22 553–22 565, doi:<https://doi.org/10.1029/1999JA900220>, 1999.
- Beer, T.: Atmospheric waves, London, ADAM HILGER LTD, 1974.
- Behlaker, A., Galkin, I., Borries, C., Pintor, P., Altadill, D., Sanz, J., Juan, J. M., Buresova, D., Verhulst, T., Mielich, J., *et al.*: TechTIDE: Warning and mitigation technologies for travelling ionospheric disturbances effects, in: 2019 URSI Asia-Pacific Radio Science Conference (AP-RASC), pp. 1–1, IEEE, doi:[10.23919/URSIAP-RASC.2019.8738350](https://doi.org/10.23919/URSIAP-RASC.2019.8738350), 2019.
- Billett, D., Grocott, A., Wild, J., Walach, M.-T., and Kosch, M.: Diurnal variations in global Joule heating morphology and magnitude due to neutral winds, Journal of Geophysical Research: Space Physics, 123, 2398–2411, doi:<https://doi.org/10.1002/2017JA025141>, 2018.
- Blackman, R. B. and Tukey, J. W.: The measurement of power spectra from the point of view of communications engineering—Part I, Bell System Technical Journal, 37, 185–282, doi:<https://doi.org/10.1002/j.1538-7305.1958.tb03874.x>, 1958.
- Borries, C., Jakowski, N., and Wilken, V.: Storm induced large scale TIDs observed in GPS derived TEC, Annales Geophys, 27, 1605–1612, doi:<https://doi.org/10.5194/angeo-27-1605-2009>, 2009.

- Bowman, G.: Some aspects of large-scale travelling ionospheric disturbances, *Planetary and space science*, 40, 829–845, doi:[https://doi.org/10.1016/0032-0633\(92\)90110-A](https://doi.org/10.1016/0032-0633(92)90110-A), 1992.
- Bracewell, R. N.: *The Fourier transform and its applications*, McGraw-Hill, Singapore, 3 edn., 1986.
- Brekke, A.: *Physics of the upper polar atmosphere*, Springer Science & Business Media, 2013.
- Bristow, W. and Greenwald, R.: On the spectrum of thermospheric gravity waves observed by the Super Dual Auroral Radar Network, *Journal of Geophysical Research: Space Physics*, 102, 11 585–11 595, doi:<https://doi.org/10.1029/97JA00515>, 1997.
- Bristow, W., Greenwald, R., and Samson, J.: Identification of high-latitude acoustic gravity wave sources using the Goose Bay HF radar, *Journal of Geophysical Research: Space Physics*, 99, 319–331, doi:<https://doi.org/10.1029/93JA01470>, 1994.
- Bristow, W. A., Greenwald, R. A., and Villain, J. P.: On the seasonal dependence of medium-scale atmospheric gravity waves in the upper atmosphere at high latitudes, *Journal of Geophysical Research*, 101, 15 685–15 699, doi:<https://doi.org/10.1029/96JA01010>, 1996.
- Bruinsma, S. L. and Forbes, J. M.: Global observation of traveling atmospheric disturbances (TADs) in the thermosphere, *Geophysical Research Letters*, 34, L14 103, doi:<https://doi.org/10.1029/2007GL030243>, 2007.
- Cander, L. R.: *Ionospheric space weather*, Springer, 2019.
- Chimonas, G. and Hines, C.: Atmospheric gravity waves launched by auroral currents, *Planetary and Space Science*, 18, 565–582, doi:[https://doi.org/10.1016/0032-0633\(70\)90132-7](https://doi.org/10.1016/0032-0633(70)90132-7), 1970.
- Chisham, G., Lester, M., Milan, S. E., Freeman, M., Bristow, W., Grocott, A., McWilliams, K., Ruohoniemi, J., Yeoman, T. K., Dyson, P. L., *et al.*: A decade of the Super Dual Auroral Radar Network (SuperDARN): Scientific achievements, new techniques and future directions, *Surveys in Geophysics*, 28, 33–109, doi:[10.1007/s10712-007-9017-8](https://doi.org/10.1007/s10712-007-9017-8), 2007.
- Chisham, G., Yeoman, T. K., and Sofko, G.: Mapping ionospheric backscatter measured by the SuperDARN HF radars—Part 1: A new empirical virtual height model, *Annales Geophysicae*, 26, 823–841, doi:<https://doi.org/10.5194/angeo-26-823-2008>, 2008.
- Chun, F. K., Knipp, D. J., McHarg, M. G., Lu, G., Emery, B. A., Vennerstrøm, S., and Troshichev, O. A.: Polar cap index as a proxy for hemispheric Joule heating, *Geophysical research letters*, 26, 1101–1104, doi:<https://doi.org/10.1029/1999GL900196>, 1999.

- Cierpka, K., Kosch, M., Rietveld, M., Schlegel, K., and Hagfors, T.: Ion-neutral coupling in the high-latitude F-layer from incoherent scatter and Fabry-Perot interferometer measurements, *Annales Geophysicae*, 18, 1145–1153, doi:<https://doi.org/10.1007/s00585-000-1145-0>, 2000.
- Cliver, E. W. and Svalgaard, L.: The 1859 solar–terrestrial disturbance and the current limits of extreme space weather activity, *Solar Physics*, 224, 407–422, doi:<https://doi.org/10.1007/s11207-005-4980-z>, 2004.
- Cosgrove, R. B. and Tsunoda, R. T.: Instability of the E-F coupled nighttime mid-latitude ionosphere, *Journal of Geophysical Research: Space Physics*, 109, 2004.
- Cosgrove, R. B., Tsunoda, R. T., Fukao, S., and Yamamoto, M.: Coupling of the Perkins instability and the sporadic E layer instability derived from physical arguments, *Journal of Geophysical Research: Space Physics*, 109, A06 301, doi:<https://doi.org/10.1029/2003JA010295>, 2004.
- Cowling, D., Webb, H., and Yeh, K.: Group rays of internal gravity waves in a wind-stratified atmosphere, *Journal of Geophysical Research*, 76, 213–220, doi:<https://doi.org/10.1029/JA076i001p00213>, 1971.
- Crowley, G., Jones, T., and Dudeney, J.: Comparison of short period TID morphologies in Antarctica during geomagnetically quiet and active intervals, *Journal of Atmospheric and Terrestrial Physics*, 49, 1155–1162, doi:[https://doi.org/10.1016/0021-9169\(87\)90098-5](https://doi.org/10.1016/0021-9169(87)90098-5), 1987.
- Danskin, D. W.: HF auroral backscatter from the E and F regions, Ph.D. thesis, The University of Saskatchewan (Canada), 2004.
- Davies, K.: *Ionospheric Radio*, 31, United Kingdom, London, Peter Peregrinus Ltd., 1990.
- Davies, K. and Jones, J. E.: Three-dimensional observations of traveling ionospheric disturbances, *Journal of Atmospheric and Terrestrial Physics*, 33, 39–46, doi:[https://doi.org/10.1016/0021-9169\(71\)90180-2](https://doi.org/10.1016/0021-9169(71)90180-2), 1971.
- Davis, T. N. and Sugiura, M.: Auroral electrojet activity index AE and its universal time variations, *Journal of Geophysical Research*, 71, 785–801, doi:<https://doi.org/10.1029/JZ071i003p00785>, 1966.
- De Campra, P. F. and De Artigas, M. Z.: Comparison between indices during geomagnetic disturbances, *Geofisica Internacional*, 43, 113–117, doi:<https://doi.org/10.22201/igeof.00167169p.2004.43.1.221>, 2004.
- Dettinger, M. D., Ghil, M., Strong, C. M., Weibel, W., and Yiou, P.: Software expedites singular-spectrum analysis of noisy time series, *EOS, Transactions American Geophysical Union*, 76, 12–21, doi:<https://doi.org/10.1029/EO076i002p00012>, 1995.

- Dhadly, M. S., Emmert, J. T., Drob, D. P., Conde, M. G., Aruliah, A., Doornbos, E., Shepherd, G. G., Wu, Q., Makela, J. J., Niciejewski, R. J., *et al.*: HL-TWiM empirical model of high-latitude upper thermospheric winds, *Journal of Geophysical Research: Space Physics*, 124, 10 592–10 618, doi:<https://doi.org/10.1029/2019JA027188>, 2019.
- Ding, F., Wan, W., Liu, L., Afraimovich, E., Voeykov, S., and Perevalova, N.: A statistical study of large-scale traveling ionospheric disturbances observed by GPS TEC during major magnetic storms over the years 2003–2005, *Journal of Geophysical Research: Space Physics*, 113, A00A01, doi:<https://doi.org/10.1029/2008JA013037>, 2008.
- Ding, F., Wan, W., Xu, G., Yu, T., Yang, G., and Wang, J.-s.: Climatology of medium-scale traveling ionospheric disturbances observed by a GPS network in central China, *Journal of Geophysical Research: Space Physics*, 116, A09 327, doi:<https://doi.org/10.1029/2011JA016545>, 2011.
- Doherty, P., Coster, A. J., and Murtagh, W.: Space weather effects of October–November 2003, *GPS Solutions*, 8, 267–271, doi:<https://doi.org/10.1007/s10291-004-0109-3>, 2004.
- Drob, D., Emmert, J., Crowley, G., Picone, J., Shepherd, G., Skinner, W., Hays, P., Niciejewski, R., Larsen, M., She, C., *et al.*: An empirical model of the Earth’s horizontal wind fields: HWM07, *Journal of Geophysical Research: Space Physics*, 113, A12 304, doi:<https://doi.org/10.1029/2008JA013668>, 2008.
- Drob, D. P., Emmert, J. T., Meriwether, J. W., Makela, J. J., Doornbos, E., Conde, M., Hernandez, G., Noto, J., Zawdie, K. A., McDonald, S. E., *et al.*: An update to the Horizontal Wind Model (HWM): The quiet time thermosphere, *Earth and Space Science*, 2, 301–319, doi:<https://doi.org/10.1002/2014EA000089>, 2015.
- El-Rabbany, A.: *Introduction to GPS: The Global Positioning System*, Artech House, 2002.
- Elósegui, P., Davis, J., Jaldehag, R., Johansson, J., Niell, A., and Shapiro, I.: Geodesy using the Global Positioning System: The effects of signal scattering on estimates of site position, *Journal of Geophysical Research: Solid Earth (1978–2012)*, 100, 9921–9934, doi:<https://doi.org/10.1029/95JB00868>, 1995.
- Emmert, J., Drob, D., Shepherd, G., Hernandez, G., Jarvis, M. J., Meriwether, J., Niciejewski, R., Sipler, D., and Tepley, C.: DWM07 global empirical model of upper thermospheric storm-induced disturbance winds, *Journal of Geophysical Research: Space Physics*, 113, A11 319, doi:<https://doi.org/10.1029/2008JA013541>, 2008.
- Ferdousi, B., Nishimura, Y., Maruyama, N., and Lyons, L. R.: Subauroral neutral wind driving and its feedback to SAPS during the 17 March 2013 geomagnetic storm, *Journal of Geophysical Research: Space Physics*, 124, 2323–2337, doi:<https://doi.org/10.1029/2018JA026193>, 2019.

- Figueiredo, C., Takahashi, H., Wrasse, C., Otsuka, Y., Shiokawa, K., and Barros, D.: Investigation of nighttime MSTIDS observed by optical thermosphere imagers at low latitudes: Morphology, propagation direction, and wind filtering, *Journal of Geophysical Research: Space Physics*, 123, 7843–7857, doi:<https://doi.org/10.1029/2018JA025438>, 2018.
- Forsyth, C., Rae, I., Coxon, J., Freeman, M., Jackman, C., Gjerloev, J., and Fazakerley, A.: A new technique for determining Substorm Onsets and Phases from Indices of the Electrojet (SOPHIE), *Journal of Geophysical Research: Space Physics*, 120, 10 592–10 606, doi:<https://doi.org/10.1002/2015JA021343>, 2015.
- Francis, S. H.: A theory of medium-scale traveling ionospheric disturbances, *Journal of Geophysical Research*, 79, 5245–5260, doi:<https://doi.org/10.1029/JA079i034p05245>, 1974.
- Francis, S. H.: Global propagation of atmospheric gravity waves: A review, *Journal of Atmospheric and Terrestrial Physics*, 37, 1011–1054, doi:[https://doi.org/10.1016/0021-9169\(75\)90012-4](https://doi.org/10.1016/0021-9169(75)90012-4), 1975.
- Fritts, D. C. and Alexander, M. J.: Gravity wave dynamics and effects in the middle atmosphere, *Reviews of Geophysics*, 41, 3–1 – 3–64, doi:<https://doi.org/10.1029/2001RG000106>, 2003.
- Gao, Y. and Liu, Z. Z.: Precise ionosphere modeling using regional GPS network data, *Positioning*, 1, 18–24, doi:<https://doi.org/10.5081/jgps.1.1.18>, 2002.
- Georges, T.: HF Doppler studies of traveling ionospheric disturbances, *Journal of Atmospheric and Terrestrial Physics*, 30, 735–746, doi:[https://doi.org/10.1016/S0021-9169\(68\)80029-7](https://doi.org/10.1016/S0021-9169(68)80029-7), 1968.
- Georges, T.: Effects of ionospheric motions and irregularities on HF radio propagation, in: *Low-Frequency Waves and Irregularities in the Ionosphere*, pp. 137–151, Springer, doi:https://doi.org/10.1007/978-94-010-3402-9_11, 1969.
- Ghil, M., Allen, M., Dettinger, M., Ide, K., Kondrashov, D., Mann, M., Robertson, A. W., Saunders, A., Tian, Y., Varadi, F., *et al.*: Advanced spectral methods for climatic time series, *Reviews of geophysics*, 40, 3–1–3–41, doi:<https://doi.org/10.1029/2000RG000092>, 2002.
- Gleason, S. and Gebre-Egziabher, D.: *GNSS Applications and Methods*, Artech House, 2009.
- Gounden, H.: Observations of medium-scale travelling ionospheric disturbances (MSTIDs) by the SANA SuperDARN radar for 2013, 2022.
- Greenwald, R., Baker, K., Dudeney, J., Pinnock, M., Jones, T., Thomas, E., Villain, J.-P., Cerisier, J.-C., Senior, C., Hanuise, C., *et al.*: Darn/superdarn, *Space Science Reviews*, 71, 761–796, doi:<https://doi.org/10.1007/BF00751350>, 1995.

- Greenwald, R. A.: History of the Super Dual Auroral Radar Network (SuperDARN)-I: pre-SuperDARN developments in high frequency radar technology for ionospheric research and selected scientific results, *History of Geo-and Space Sciences*, 12, 77–93, doi:<https://doi.org/10.5194/hgss-12-77-2021>, 2021.
- Grocott, A., Hosokawa, K., Ishida, T., Lester, M., Milan, S., Freeman, M., Sato, N., and Yukimatu, A.: Characteristics of medium-scale traveling ionospheric disturbances observed near the Antarctic Peninsula by HF radar, *Journal of Geophysical Research: Space Physics*, 118, 5830–5841, doi:<https://doi.org/10.1002/jgra.50515>, 2013.
- Habarulema, J. B., Katamzi, Z. T., and McKinnell, L.-A.: Estimating the propagation characteristics of large-scale traveling ionospheric disturbances using ground-based and satellite data, *Journal of Geophysical Research: Space Physics*, 118, 7768–7782, doi:<https://doi.org/10.1002/2013JA018997>, 2013.
- Habarulema, J. B., Katamzi, Z. T., Yizengaw, E., Yamazaki, Y., and Seemala, G.: Simultaneous storm time equatorward and poleward large-scale TIDs on a global scale, *Geophysical Research Letters*, 43, 6678–6686, doi:<https://doi.org/10.1002/2016GL069740>, 2016.
- Hamza, A.: Perkins instability revisited, *Journal of Geophysical Research: Space Physics*, 104, 22 567–22 575, doi:<https://doi.org/10.1029/1999JA900307>, 1999.
- Hayashi, H., Nishitani, N., Ogawa, T., Otsuka, Y., Tsugawa, T., Hosokawa, K., and Saito, A.: Large-scale traveling ionospheric disturbance observed by superDARN Hokkaido HF radar and GPS networks on 15 December 2006, *Journal of Geophysical Research: Space Physics*, 115, doi:<https://doi.org/10.1029/2009JA014297>, 2010.
- He, L.-S., Dyson, P., Parkinson, M., and Wan, W.: Studies of medium scale travelling ionospheric disturbances using TIGER SuperDARN radar sea echo observations, *Annales Geophysicae*, 22, 4077–4088, doi:<https://doi.org/10.5194/angeo-22-4077-2004>, 2004.
- Hedin, A. E., Fleming, E., Manson, A., Schmidlin, F., Avery, S., Clark, R., Franke, S., Fraser, G., Tsuda, T., Vial, F., *et al.*: Empirical wind model for the upper, middle and lower atmosphere, *Journal of atmospheric and terrestrial physics*, 58, 1421–1447, doi:[https://doi.org/10.1016/0021-9169\(95\)00122-0](https://doi.org/10.1016/0021-9169(95)00122-0), 1996.
- Hernández-Pajares, M., Juan, J. M., and Sanz, J.: Medium-scale traveling ionospheric disturbances affecting GPS measurements: Spatial and temporal analysis, *Journal of Geophysical Research: Space Physics*, 111, A07S11, doi:<https://doi.org/10.1029/2005JA011474>, 2006.
- Hines, C.: An interpretation of certain ionospheric motions in terms of atmospheric waves, *Journal of Geophysical Research*, 64, 2210–2211, doi:<https://doi.org/10.1029/JZ064i012p02210>, 1959.

- Hines, C. O.: Internal Atmospheric Gravity Waves At Ionospheric Heights, *Canadian Journal of Physics*, 38, 1441–1481, doi:[10.1139/p60-150](https://doi.org/10.1139/p60-150), 1960.
- Hocke, K.: Phase estimation with the Lomb-Scargle periodogram method, *Annales Geophysicae-European Geophysical Society*, 16, 356–358, 1998.
- Hocke, K. and Schlegel, K.: A review of atmospheric gravity waves and travelling ionospheric disturbances: 1982–1995, *Annales Geophysicae*, 14, 917–940, doi:<https://doi.org/10.1007/s005850050357>, 1996.
- Hofmann-Wellenhof, B., Lichtenegger, H., and Collins, J.: *Global Positioning System. Theory and Practice.*, New York, Springer-Verlag Wien, 1992.
- Huang, C.-S., Miller, C., and Kelley, M.: Basic properties and gravity wave initiation of the midlatitude F region instability, *Radio Science*, 29, 395–405, doi:<https://doi.org/10.1029/93RS01669>, 1994.
- Hunsucker, R. D.: Atmospheric gravity waves generated in the high-latitude ionosphere: A review, *Reviews of Geophysics*, 20, 293–315, doi:<https://doi.org/10.1029/RG020i002p00293>, 1982.
- Hunsucker, R. D. and Hargreaves, J. K.: *The High-Latitude Ionosphere and its Effects on Radio Propagation*, New York, Cambridge University Press, 2003.
- Ishida, T., Hosokawa, K., Shibata, T., Suzuki, S., Nishitani, N., and Ogawa, T.: SuperDARN observations of daytime MSTIDs in the auroral and mid-latitudes: Possibility of long-distance propagation, *Geophysical research letters*, 35, doi:<https://doi.org/10.1029/2008GL034623>, 2008.
- Jonah, O., Coster, A., Zhang, S., Goncharenko, L., Erickson, P., de Paula, E., and Kherani, E.: TID observations and source analysis during the 2017 Memorial Day weekend geomagnetic storm over North America, *Journal of Geophysical Research: Space Physics*, 123, 8749–8765, doi:<https://doi.org/10.1029/2018JA025367>, 2018.
- Kalikhman, A.: Medium-scale travelling ionospheric disturbances and thermospheric winds in the F-region, *Journal of Atmospheric and Terrestrial physics*, 42, 697–703, doi:[https://doi.org/10.1016/0021-9169\(80\)90053-7](https://doi.org/10.1016/0021-9169(80)90053-7), 1980.
- Kaplan, E. D. and Hegarty, C. J.: *Understanding GPS: Principles and Applications*, Artech house, 2006.
- Karhunen, T., Robinson, T., Arnold, N., and Lester, M.: Determination of the parameters of travelling ionospheric disturbances in the high-latitude ionosphere using CUTLASS coherent scatter radars, *Journal of atmospheric and solar-terrestrial physics*, 68, 558–567, 2006.
- Katamzi, Z. T.: *Statistical analysis of ionospheric total electron content*, Ph.D. thesis, University of Bath, 2011.

- Katamzi, Z. T. and Habarulema, J. B.: Traveling ionospheric disturbances observed at South African midlatitudes during the 29–31 October 2003 geomagnetically disturbed period, *Advances in Space Research*, 53, 48–62, doi:<https://doi.org/10.1016/j.asr.2013.10.019>, 2014.
- Katamzi-Joseph, Z. T., Aruliah, A. L., Oksavik, K., Habarulema, J. B., Kauuristie, K., and Kosch, M. J.: Multi-instrument observations of large-scale atmospheric gravity waves/traveling ionospheric disturbances associated with enhanced auroral activity over Svalbard, *Advances in Space Research*, 63, 270–281, doi:<https://doi.org/10.1016/j.asr.2018.08.042>, 2019.
- Kelley, M. C. and Heelis, R. A.: *The Earth's Ionosphere : Plasma Physics and Electrodynamics*, California, San Diego, ACADEMIC PRESS, INC., 1989.
- Kelley, M. C. and Miller, C. A.: Electrodynamic waves? A new look at the role of electric fields in thermospheric wave dynamics, *Journal of Geophysical Research: Space Physics*, 102, 11 539–11 547, doi:<https://doi.org/10.1029/96JA03841>, 1997.
- Kelley, M. C., Haldoupis, C., Nicolls, M. J., Makela, J. J., Belehaki, A., Shalimov, S., and Wong, V. K.: Case studies of coupling between the E and F regions during unstable sporadic-E conditions, *Journal of Geophysical Research: Space Physics*, 108, doi:<https://doi.org/10.1029/2003JA009955>, 2003.
- Kil, H.: The morphology of equatorial plasma bubbles-a review, *Journal of Astronomy and Space Sciences*, 32, 13–19, doi:<http://dx.doi.org/10.5140/JASS.2015.32.1.13>, 2015.
- Klobuchar, J. A., Anderson, D., Bishop, G., and Doherty, P.: Measurements of transitionospheric propagation parameters in the polar cap ionosphere, Tech. rep., AIR FORCE GEOPHYSICS LAB HANSCOM AFB MA, 1987.
- Kotake, N., Otsuka, Y., Tsugawa, T., Ogawa, T., and Saito, A.: Climatological study of GPS total electron content variations caused by medium-scale traveling ionospheric disturbances, *Journal of Geophysical Research: Space Physics*, 111, doi:<https://doi.org/10.1029/2005JA011418>, 2006.
- Lanyi, G.: Total ionospheric electron content calibration using SERIES GPS satellite data, *Telecommunications and Data Acquisition Report*, SEE N86-28276 19, 32, 1–12, 1986.
- Lanyi, G. E. and Roth, T.: A comparison of mapped and measured total ionospheric electron content using global positioning system and beacon satellite observations, *Radio Science*, 23, 483–492, doi:[10.1029/RS023i004p00483](https://doi.org/10.1029/RS023i004p00483), 1988.
- Lester, M.: The Super Dual Auroral Radar Network (SuperDARN): an overview of its development and science, *Advances in Polar Science*, 24, 1–11, doi:<https://doi.org/10.3724/sp.j.1085.2013.00001>, 2013.

- Liu, E. X., Hu, H. Q., Liu, R. Y., Wu, Z. S., and Lester, M.: An adjusted location model for SuperDARN backscatter echoes, *Annales Geophysicae*, 30, 1769–1779, doi:<https://doi.org/10.5194/angeo-30-1769-2012>, 2012.
- Lomb, N. R.: Least-squares frequency analysis of unequally spaced data, *Astrophysics and space science*, 39, 447–462, doi:<https://doi.org/10.1007/BF00648343>, 1976.
- Lopez, R. E., Baker, D. N., and Allen, J.: Sun unleashes Halloween storm, *Eos, Transactions American Geophysical Union*, 85, 105–108, doi:<https://doi.org/10.1029/2004EO110002>, 2004.
- Lu, G., Richmond, A., Emery, B., and Roble, R.: Magnetosphere-ionosphere-thermosphere coupling: Effect of neutral winds on energy transfer and field-aligned current, *Journal of Geophysical Research: Space Physics*, 100, 19 643–19 659, doi:<https://doi.org/10.1029/95JA00766>, 1995.
- MacDougall, J., Abdu, M., Batista, I., Fagundes, P., Sahai, Y., and Jayachandran, P.: On the production of traveling ionospheric disturbances by atmospheric gravity waves, *Journal of Atmospheric and Solar-Terrestrial Physics*, 71, 2013–2016, doi:<https://doi.org/10.1016/j.jastp.2009.09.006>, 2009.
- Mannucci, A., Iijima, B., Lindqwister, U., Pi, X., Sparks, L., and Wilson, B.: GPS and ionosphere, in: *URSI Reviews of Radio Science*, 1999.
- Matamba, T. M., Habarulema, J. B., and McKinnell, L.-A.: Statistical analysis of the ionospheric response during geomagnetic storm conditions over South Africa using ionosonde and GPS data, *Space Weather*, 13, 536–547, doi:<https://doi.org/10.1002/2015SW001218>, 2015.
- Mayr, H., Harris, I., Herrero, F., Spencer, N., Varosi, F., and Pesnell, W.: Thermospheric gravity waves: Observations and interpretation using the transfer function model (TFM), *Space Science Reviews*, 54, 297–375, doi:<https://doi.org/10.1007/BF00177800>, 1990.
- McClure, J., Hanson, W., and Hoffman, J.: Plasma bubbles and irregularities in the equatorial ionosphere, *Journal of Geophysical Research*, 82, 2650–2656, doi:<https://doi.org/10.1029/JA082i019p02650>, 1977.
- McNamara, L. F.: *The ionosphere: Communications, Surveillance, and Direction Finding*, Krieger Publishing Company, 1991.
- Mendillo, M.: Storms in the ionosphere: Patterns and processes for total electron content, *Reviews of Geophysics*, 44, doi:<https://doi.org/10.1029/2005RG000193>, 2006.
- Milan, S., Yeoman, T., Lester, M., Thomas, E., and Jones, T.: Initial backscatter occurrence statistics from the CUTLASS HF radars, in: *Annales Geophysicae*, vol. 15, pp. 703–718, Springer, 1997.

- Misra, P. and Enge, P.: Global Positioning System: Signals, Measurements and Performance Second Edition, Lincoln, MA: Ganga-Jamuna Press, 2006.
- Mohinder, S. G., Weill, R. L., and Andrews, P. A.: Global Positioning Systems, Inertial Navigation, and Integration, A John Wiley and Sons, Inc Publication, 2001.
- Moldwin, M.: An introduction to Space Weather, New York, Cambridge University Press, 2008.
- Momani, M. A., Yatim, B., and Ali, M. A. M.: Large-scale traveling ionospheric disturbances observed by GPS receivers in Antarctica, Wuhan University Journal of Natural Sciences, 15, 135–142, doi:<https://doi.org/10.1007/s11859-010-0210-0>, 2010.
- Mravlag, E.: 10 years radar operations at SANAE – a statistical review, SuperDARN workshop, Japan, 2007.
- Mtumela, Z., Stephenson, J. A., and Walker, A. D.: An investigation of the nature of a Pc5 pulsation event using SuperDARN and magnetometer data, South African Journal of Science, 111, 1–7, doi:<http://dx.doi.org/10.17159/sajs.2015/20130391>, 2015.
- Munro, G.: Travelling ionospheric disturbances in the F region, Australian Journal of Physics, 11, 91–112, doi:<https://doi.org/10.1071/PH580091>, 1958.
- Nappo, C. J.: An introduction to atmospheric gravity waves, vol. 85, Academic press, 2002.
- Narayanan, V., Shiokawa, K., Otsuka, Y., and Neudegg, D.: On the role of thermospheric winds and sporadic E layers in the formation and evolution of electrified MSTIDs in geomagnetic conjugate regions, Journal of Geophysical Research: Space Physics, 123, 6957–6980, 2018.
- Negrea, C. and Zobotin, N. A.: Mean spectral characteristics of acoustic gravity waves in the thermosphere-ionosphere determined from Dynasonde data, Radio Science, 51, 213–222, doi:[10.1002/2015RS005823](https://doi.org/10.1002/2015RS005823), 2016.
- Ngwira, C. M., Pulkkinen, A., Leila Mays, M., Kuznetsova, M. M., Galvin, A., Simunac, K., Baker, D. N., Li, X., Zheng, Y., and Glocer, A.: Simulation of the 23 July 2012 extreme space weather event: What if this extremely rare CME was Earth directed?, Space Weather, 11, 671–679, doi:<https://doi.org/10.1002/2013SW000990>, 2013.
- Nickisch, L., Fridman, S., Hausman, M., and San Antonio, G. S.: Feasibility study for reconstructing the spatial-temporal structure of TIDs from high-resolution backscatter ionograms, Radio Science, 51, 443–453, doi:[10.1002/2015RS005906](https://doi.org/10.1002/2015RS005906), 2016.

- Nishitani, N., Ruohoniemi, J. M., Lester, M., Baker, J. B. H., Koustov, A. V., Shepherd, S. G., Chisham, G., Hori, T., Thomas, E. G., Makarevich, R. A., *et al.*: Review of the accomplishments of mid-latitude Super Dual Auroral Radar Network (SuperDARN) HF radars, *Progress in Earth and Planetary Science*, 6, 1–57, doi:<https://doi.org/10.1186/s40645-019-0270-5>, 2019.
- Nygrén, T., Aikio, A., Voiculescu, M., and Cai, L.: Radar observations of simultaneous traveling ionospheric disturbances and atmospheric gravity waves, *Journal of Geophysical Research: Space Physics*, 120, 3949–3960, doi:<https://doi.org/10.1002/2014JA020794>, 2015.
- Ogawa, T., Igarashi, K., Aikyo, K., and Maeno, H.: NNSS satellite observations of medium-scale traveling ionospheric disturbances at southern high-latitudes, *Journal of Geomagnetism and Geoelectricity*, 39, 709–721, doi:<https://doi.org/10.5636/jgg.39.709>, 1987.
- Ogawa, T., Nishitani, N., Otsuka, Y., Shiokawa, K., Tsugawa, T., and Hosokawa, K.: Medium-scale traveling ionospheric disturbances observed with the SuperDARN Hokkaido radar, all-sky imager, and GPS network and their relation to concurrent sporadic E irregularities, *Journal of Geophysical Research: Space Physics*, 114, doi:<https://doi.org/10.1029/2008JA013893>, 2009.
- Ondoh, T. and Marubashi, K.: *Science of Space Environment*, Ohmsha, Ltd., 2001.
- Otsuka, Y., Shiokawa, K., Ogawa, T., and Wilkinson, P.: Geomagnetic conjugate observations of medium-scale traveling ionospheric disturbances at midlatitude using all-sky airglow imagers, *Geophysical research letters*, 31, L15803, doi:<https://doi.org/10.1029/2004GL020262>, 2004.
- Otsuka, Y., Onoma, F., Shiokawa, K., Ogawa, T., Yamamoto, M., and Fukao, S.: Simultaneous observations of nighttime medium-scale traveling ionospheric disturbances and E region field-aligned irregularities at midlatitude, *Journal of Geophysical Research: Space Physics*, 112, doi:<https://doi.org/10.1029/2005JA011548>, 2007.
- Otsuka, Y., Shiokawa, K., Ogawa, T., Yokoyama, T., and Yamamoto, M.: Spatial relationship of nighttime medium-scale traveling ionospheric disturbances and F region field-aligned irregularities observed with two spaced all-sky airglow imagers and the middle and upper atmosphere radar, *Journal of Geophysical Research: Space Physics*, 114, A05302, doi:<https://doi.org/10.1029/2008JA013902>, 2009.
- Perkins, F.: Spread F and ionospheric currents, *Journal of Geophysical Research*, 78, 218–226, doi:<https://doi.org/10.1029/JA078i001p00218>, 1973.
- Rawer, K.: Wave Propagation in the Ionosphere, vol. 5 of *Developments in Electromagnetic Theory and Applications*, Kluwer Academic Publishers, Dordrecht, Boston, London, URL <http://cds.cern.ch/record/1629258>, 1993.

- Ribeiro, A., Ruohoniemi, J. M., Ponomarenko, P., N. Clausen, L., H. Baker, J., Greenwald, R., Oksavik, K., and de Larquier, S.: A comparison of SuperDARN ACF fitting methods, *Radio Science*, 48, 274–282, doi:<https://doi.org/10.1002/rds.20031>, 2013.
- Richmond, A.: Gravity wave generation, propagation, and dissipation in the thermosphere, *Journal of Geophysical Research: Space Physics*, 83, 4131–4145, doi:<https://doi.org/10.1029/JA083iA09p04131>, 1978.
- Richmond, A.: Thermospheric heating in a magnetic storm: Dynamic transport of energy from high to low latitudes, *Journal of Geophysical Research: Space Physics*, 84, 5259–5266, doi:<https://doi.org/10.1029/JA084iA09p05259>, 1979.
- Richmond, A. and Matsushita, S.: Thermospheric response to a magnetic substorm, *Journal of Geophysical Research*, 80, 2839–2850, doi:<https://doi.org/10.1029/JA080i019p02839>, 1975.
- Rodger, A. S., Morrell, C., and Dudeney, J.: Studies of sporadic E (Es) associated with the main ionospheric trough, *Radio Science*, 18, 937–946, doi:[10.1029/RS018i006p00937](https://doi.org/10.1029/RS018i006p00937), 1983.
- Rostoker, G.: Geomagnetic indices, *Reviews of Geophysics*, 10, 935–950, doi:<https://doi.org/10.1029/RG010i004p00935>, 1972.
- Ruohoniemi, J. and Baker, K.: Large-scale imaging of high-latitude convection with Super Dual Auroral Radar Network HF radar observations, *Journal of Geophysical Research: Space Physics*, 103, 20 797–20 811, doi:<https://doi.org/10.1029/98JA01288>, 1998.
- Saba, M. F., Gonzalez, W., and Clúa de Gonzalez, A.: Relationships between the AE, ap and Dst indices near solar minimum (1974) and at solar maximum (1979), *Annales Geophysicae*, 15, 1265–1270, doi:<https://doi.org/10.1007/s00585-997-1265-x>, 1997.
- Saito, S., Yamamoto, M., Hashiguchi, H., Maegawa, A., and Saito, A.: Observational evidence of coupling between quasi-periodic echoes and medium scale traveling ionospheric disturbances, *Annales Geophysicae*, 25, 2185–2194, doi:<https://doi.org/10.5194/angeo-25-2185-2007>, 2007.
- Samson, J., Greenwald, R., Ruohoniemi, J., and Baker, K.: High-frequency radar observations of atmospheric gravity waves in the high-latitude ionosphere, *Geophysical Research Letters*, 16, 875–878, doi:<https://doi.org/10.1029/GL016i008p00875>, 1989.
- Samson, J., Greenwald, R., Ruohoniemi, J., Frey, A., and Baker, K.: Goose Bay radar observations of Earth-reflected, atmospheric gravity waves in the high-latitude ionosphere, *Journal of Geophysical Research: Space Physics*, 95, 7693–7709, doi:<https://doi.org/10.1029/JA095iA06p07693>, 1990.

- Scargle, J. D.: Studies in astronomical time series analysis. II-Statistical aspects of spectral analysis of unevenly spaced data, *The Astrophysical Journal*, 263, 835–853, doi:<https://doi.org/10.1086/160554>, 1982.
- Schunk, R. and Nagy, A.: *Ionospheres: physics, plasma physics, and chemistry*, Cambridge university press, 2009.
- Seemala, G. and Valladares, C.: Statistics of total electron content depletions observed over the South American continent for the year 2008, *Radio Science*, 46, doi:<https://doi.org/10.1029/2011RS004722>, 2011.
- Shiokawa, K., Otsuka, Y., Ihara, C., Ogawa, T., and Rich, F.: Ground and satellite observations of nighttime medium-scale traveling ionospheric disturbance at midlatitude, *Journal of Geophysical Research: Space Physics*, 108, doi:<https://doi.org/10.1029/2002JA009639>, 2003.
- Shiokawa, K., Otsuka, Y., Tsugawa, T., Ogawa, T., Saito, A., Ohshima, K., Kubota, M., Maruyama, T., Nakamura, T., Yamamoto, M., *et al.*: Geomagnetic conjugate observation of nighttime medium-scale and large-scale traveling ionospheric disturbances: FRONT3 campaign, *Journal of Geophysical Research: Space Physics*, 110, doi:<https://doi.org/10.1029/2004JA010845>, 2005.
- Skone, S., Yousuf, R., Coster, A., *et al.*: Performance evaluation of the wide area augmentation system for ionospheric storm events, *Journal of Global Positioning Systems*, 3, 251–258, doi:<https://doi.org/10.5081/jgps.3.1.251>, 2004.
- Spiro, R., Reiff, P. H., and Maher Jr, L.: Precipitating electron energy flux and auroral zone conductances-An empirical model, *Journal of Geophysical Research: Space Physics*, 87, 8215–8227, doi:<https://doi.org/10.1029/JA087iA10p08215>, 1982.
- Spogli, L., Alfonsi, L., Franceschi, G. D., Romano, V., Aquino, M., and Dodson, A.: Climatology of GPS ionospheric scintillations over high and mid-latitude European regions, *Annales Geophysicae*, 27, 3429–3437, doi:<https://doi.org/10.5194/angeo-27-3429-2009>, 2009.
- Stauning, P.: A new index for the interplanetary merging electric field and geomagnetic activity: Application of the unified polar cap indices, *Space Weather*, 5, doi:<https://doi.org/10.1029/2007SW000311>, 2007.
- Stephenson, J. and Walker, A.: HF radar observations of Pc5 ULF pulsations driven by the solar wind, *Geophysical Research Letters*, 29, 8–1, doi:<https://doi.org/10.1029/2001GL014291>, 2002.
- Stephenson, J. and Walker, A.: Coherence between radar observations of magnetospheric field line resonances and discrete oscillations in the solar wind, *Annales Geophysicae*, 28, 47–59, doi:<https://doi.org/10.5194/angeo-28-47-2010>, 2010.

- Sutcliffe, P.: Observations of Pi2 pulsations in a near ground state magnetosphere, *Geophysical research letters*, 25, 4067–4070, doi:<https://doi.org/10.1029/1998GL900092>, 1998.
- Suzuki, S., Hosokawa, K., Otsuka, Y., Shiokawa, K., Ogawa, T., Nishitani, N., Shibata, T., Koustov, A., and Shevtsov, B.: Coordinated observations of nighttime medium-scale traveling ionospheric disturbances in 630-nm airglow and HF radar echoes at midlatitudes, *Journal of Geophysical Research: Space Physics*, 114, doi:<https://doi.org/10.1029/2008JA013963>, 2009.
- Tang, J., Yao, Y., Kong, J., and Zhang, L.: Large-scale traveling ionospheric disturbances using ionospheric imaging at storm time: A case study on 17 March 2013, *Journal of Atmospheric and Solar-Terrestrial Physics*, 145, 12–20, doi:<https://doi.org/10.1016/j.jastp.2016.04.006>, 2016.
- Thébault, E., Finlay, C. C., Beggan, C. D., Alken, P., Aubert, J., Barrois, O., Bertrand, F., Bondar, T., Boness, A., Brocco, L., *et al.*: International geomagnetic reference field: the 12th generation, *Earth, Planets and Space*, 67, 1–19, doi:<https://doi.org/10.1186/s40623-015-0228-9>, 2015.
- Thomas, E. and Shepherd, S.: Statistical patterns of ionospheric convection derived from mid-latitude, high-latitude, and polar SuperDARN HF radar observations, *Journal of Geophysical Research: Space Physics*, 123, 3196–3216, doi:<https://doi.org/10.1002/2018JA025280>, 2018.
- Thomson, D. J.: Spectrum estimation and harmonic analysis, *Proceedings of the IEEE*, 70, 1055–1096, doi:[10.1109/PROC.1982.12433](https://doi.org/10.1109/PROC.1982.12433), 1982.
- Tsugawa, T., Saito, A., and Otsuka, Y.: A statistical study of large-scale traveling ionospheric disturbances using the GPS network in Japan, *Journal of Geophysical Research: Space Physics*, 109, A06302, doi:<https://doi.org/10.1029/2003JA010302>, 2004.
- Tsugawa, T., Otsuka, Y., Coster, A., and Saito, A.: Medium-scale traveling ionospheric disturbances detected with dense and wide TEC maps over North America, *Geophysical Research Letters*, 34, doi:<https://doi.org/10.1029/2007GL031663>, 2007.
- Tsunoda, R. T. and Cosgrove, R. B.: Coupled electrodynamic in the nighttime midlatitude ionosphere, *Geophysical Research Letters*, 28, 4171–4174, doi:<https://doi.org/10.1029/2001GL013245>, 2001.
- Tsurutani, B. T., Gonzalez, W. D., Gonzalez, A. L., Guarnieri, F. L., Gopalswamy, N., Grande, M., Kamide, Y., Kasahara, Y., Lu, G., Mann, I., *et al.*: Corotating solar wind streams and recurrent geomagnetic activity: A review, *Journal of Geophysical Research: Space Physics*, 111, doi:<https://doi.org/10.1029/2005JA011273>, 2006.

- Uwamahoro, J. C., Giday, N. M., Habarulema, J. B., Katamzi-Joseph, Z. T., and Seemala, G. K.: Reconstruction of storm-time total electron content using ionospheric tomography and artificial neural networks: A comparative study over the African region, *Radio Science*, 53, 1328–1345, doi:[10.1029/2017RS006499](https://doi.org/10.1029/2017RS006499), 2018.
- Uwamahoro, J. C., Habarulema, J. B., and Buresova, D.: Highlights about the performances of storm-time TEC modelling techniques for low/equatorial and mid-latitude locations, *Advances in Space Research*, 63, 3102–3118, doi:<https://doi.org/10.1016/j.asr.2019.01.027>, 2019.
- Vadas, S. L.: Horizontal and vertical propagation and dissipation of gravity waves in the thermosphere from lower atmospheric and thermospheric sources, *Journal of Geophysical Research: Space Physics*, 112, A06305, doi:<https://doi.org/10.1029/2006JA011845>, 2007.
- Vadas, S. L. and Fritts, D. C.: Influence of solar variability on gravity wave structure and dissipation in the thermosphere from tropospheric convection, *Journal of Geophysical Research: Space Physics*, 111, A10S12, doi:<https://doi.org/10.1029/2005JA011510>, 2006.
- Valladares, C. E. and Hei, M. A.: Measurement of the characteristics of TIDs using small and regional networks of GPS receivers during the campaign of 17–30 July of 2008, *International Journal of Geophysics*, 2012, doi:<https://doi.org/10.1155/2012/548784>, 2012.
- Vallieres, X., Villain, J. P., Hanuise, C., and Andre, R.: Ionospheric propagation effects on spectral widths measured by SuperDARN HF radars, *Annales Geophysicae*, 22, 2023–2031, doi:[10.5194/angeo-22-2023-2004](https://doi.org/10.5194/angeo-22-2023-2004), 2004.
- Vlasov, A., Kauristie, K., Kamp, M., Luntama, J.-P., and Pogoreltsev, A.: A study of traveling ionospheric disturbances and atmospheric gravity waves using EISCAT Svalbard Radar IPY-data, *Annales Geophysicae*, 29, 2101–2116, doi:<https://doi.org/10.5194/angeo-29-2101-2011>, 2011.
- Waldock, J. and Jones, T.: The effects of neutral winds on the propagation of medium-scale atmospheric gravity waves at mid-latitudes, *Journal of atmospheric and terrestrial physics*, 46, 217–231, doi:[https://doi.org/10.1016/0021-9169\(84\)90149-1](https://doi.org/10.1016/0021-9169(84)90149-1), 1984.
- Waldock, J. and Jones, T.: HF Doppler observations of medium-scale travelling ionospheric disturbances at mid-latitudes, *Journal of atmospheric and terrestrial physics*, 48, 245–260, doi:[https://doi.org/10.1016/0021-9169\(86\)90099-1](https://doi.org/10.1016/0021-9169(86)90099-1), 1986.
- Walker, A., Ruohoniemi, J. M., Baker, K., Greenwald, R., and Samson, J.: Spatial and temporal behavior of ULF pulsations observed by the Goose Bay HF radar, *Journal of Geophysical Research: Space Physics*, 97, 12187–12202, doi:<https://doi.org/10.1029/92JA00329>, 1992.

- Walker, A. D., Pinnock, M., Baker, K. B., Dudeney, J. R., and Rash, J. P.: Strong flow bursts in the nightside ionosphere during extremely quiet solar wind conditions, *Geophysical Research Letters*, 25, 881–884, doi:<https://doi.org/10.1029/98GL00408>, 1998.
- Wanliss, J. A. and Showalter, K. M.: High-resolution global storm index: Dst versus SYM-H, *Journal of Geophysical Research: Space Physics*, 111, doi:<https://doi.org/10.1029/2005JA011034>, 2006.
- Whitehead, J.: Recent work on mid-latitude and equatorial sporadic-E, *Journal of Atmospheric and Terrestrial Physics*, 51, 401–424, doi:[https://doi.org/10.1016/0021-9169\(89\)90122-0](https://doi.org/10.1016/0021-9169(89)90122-0), 1989.
- Williams, P., Crowley, G., Schlegel, K., Viridi, T., McCrea, I., Watkins, G., Wade, N., Hargreaves, J., Lachlan-Cope, T., Muller, H., *et al.*: The generation and propagation of atmospheric gravity waves observed during the Worldwide Atmospheric Gravity-wave Study (WAGS), *Journal of Atmospheric and Terrestrial Physics*, 50, 323–338, 1988.
- Wu, C.-C., Liou, K., Lepping, R., and Meng, C.-I.: Identification of substorms within storms, *Journal of atmospheric and solar-terrestrial physics*, 66, 125–132, doi:<https://doi.org/10.1016/j.jastp.2003.09.012>, 2004.
- Yeh, K., Webb, H., and Cowling, D.: Evidence of directional filtering of travelling ionospheric disturbances, *Nature Physical Science*, 235, 131–132, doi:<https://doi.org/10.1038/physci235131a0>, 1972.
- Yeh, K. C. and Liu, C. H.: Acoustic-gravity waves in the upper atmosphere, *Reviews of Geophysics*, 12, 193–216, doi:<https://doi.org/10.1029/RG012i002p00193>, 1974.
- Yin, P., Mitchell, C. N., Alfonsi, L., Pinnock, M., Spencer, P., De Franceschi, G., Romano, V., Newell, P., Sarti, P., Negusini, M., *et al.*: Imaging of the Antarctic ionosphere: Experimental results, *Journal of atmospheric and solar-terrestrial physics*, 71, 1757–1765, doi:<https://doi.org/10.1016/j.jastp.2009.09.014>, 2009.
- Yokoyama, T. and Hysell, D. L.: A new midlatitude ionosphere electrodynamics coupling model (MIECO): Latitudinal dependence and propagation of medium-scale traveling ionospheric disturbances, *Geophysical Research Letters*, 37, doi:<https://doi.org/10.1029/2010GL042598>, 2010.